External Plasma Interactions with Nonmagnetized Objects in the Solar System

By

Hadi Madanian

Submitted to the graduate degree program in Physics and Astronomy and the Graduate Faculty of the University of Kansas in partial fulfillment of the requirements for the degree of Doctor of Philosophy.

Chair: Professor Thomas E. Cravens

Professor Chris J. Fischer

Professor Steve A. Hawley

Professor Craig A. McLaughlin

Professor JiCong Shi

Date Defended: 10 May 2017

The dissertation committee for Hadi Madanian certifies that this is the
approved version of the following dissertation:

External Plasma Interactions with Nonmagnetized Objects in the Solar System

Chair: Professor Thomas E. Cravens

Date Approved:

Abstract

The absence of a protecting magnetic field, such as the dipole magnetic field around Earth, makes the interaction of solar wind with unmagnetized objects particularly interesting. Long-term evolution of the object's surface and atmosphere is closely tied to its interaction with the outer space environment. The ionospheric plasma layer around unmagnetized objects acts as an electrically conducting transition layer between lower atmospheric layers and outer space. This study considers two distinct types of unmagnetized objects: Titan and comet 67P/Churyumov-Gerasimenko (67P/CG). For many years, Titan has been a key target of the National Aeronautics and Space Administration (NASA) Cassini mission investigations; and the European Space Agency (ESA) Rosetta spacecraft explored comet 67P/CG for more than two years.

Ionospheric composition and primary ion production rate profiles for Titan are modeled for various solar activity conditions. Photoionization is the main source of ion production on the dayside; on the nightside, electron-impact ionization is the main ionization source. This dissertation uses model results and in-situ measurements by the Ion and Neutral Mass Spectrometer (INMS) and the Langmuir Probe (LP) onboard the Cassini spacecraft to show that while the solar activity cycle impacts the primary ion species significantly, there is little effect on heavy ion species. Solar cycle modulates the Titan's ionospheric chemistry. The solar cycle effects of on each ion species are quantified n this work. In some cases, the solar zenith angle significantly overshadows the solar cycle effects. How each individual ion reacts to changes in solar activity and solar zenith angle is discussed in details. A method to disentangle these effects in ion densities is introduced.

At comet 67P/CG, the fast-moving solar wind impacts the neutral coma. Two populations of electrons are recognizable in the cometary plasma. These are the hot suprathermal electrons, created by photoionization or electron-impact ionization, and the cold/thermal electrons. Even though photoionization is the dominant source of ion production, electron-impact ionization can be as high as the photoionization for certain solar events. At 3 AU, electron energy spectra from in-situ measurements of the Ion and Electron Sensor (IES) instrument exhibit enhancement of electron fluxes at particular energies. Model-data comparisons show that the flux of electrons is higher than the typical solar wind and pure photoionization fluxes. The probable cause of this enhancement is the ambipolar electric field and/or plasma compression.

This research also discusses formation of a new boundary layer around the comet near perihelion, similar to the diamagnetic cavity at comet 1P/Halley. At each crossing event to the diamagnetic cavity region, flux of suprathermal electrons with energies between 40 to 250 eV drops. The lower flux of solar wind suprathermal electrons in that energy range can cause this flux drop.

Acknowledgments

First, I would like to thank my parents Mahin and Hossein, my brother Saeid, and my sisters Sharare and Bahare for their love, encouragement, and positive thoughts over the years. They always supported me and had faith in my abilities throughout my education.

My deepest gratitude goes to my advisor, Dr. Tom Cravens, for his invaluable mentorship and support. I have been extremely fortunate to have such an excellent advisor. Thanks also to the RPC-IES and Cassini-INMS teams at Southwest Research Institute for providing the data, in particular Hunter Waite, Jim Burch, and Ray Goldstein for many helpful discussions.

I would like to thank Drs. Craig McLaughlin, Chris Fischer, Steve Hawley, Jack Shi, and Philip Baringer for serving on my dissertation committee. Many thanks to professors and staff members at KU Physics and Astronomy Department. I would also like to thank my colleagues at the Space Physics Group, Ina Robertson, Matt Richard, Ali Rahmati, Shotaro Sakai, Steve Ledvina, Nataly Ozak, Oliver Hamil, and Steven Houston for useful conversations.

A big thank you to my friends and fellow physics graduate students, Peymon, Nesar, Sinan, Keita, Matt, Sam, Frank, Bhupal, Jagaran, James, Will, Ayman, Yuyu, Uzair, and Steven for all the laughs and for making my PhD journey a fun ride.

The work described in this dissertation was supported by Southwest Research Institute subcontracts to the University of Kansas under NASA Prime Contract number NAS7-03001, via the Jet Propulsion Laboratory. SwRI subcontract number D99006L supports Cassini/Titan research and SwRI subcontract number E99054DB supports Rosetta research. Rosetta is a European Space Agency (ESA) mission with contributions from its member states and the National Aeronautics and Space Administration (NASA).

Solar Irradiance Platform historical irradiances are provided courtesy of W. Kent Tobiska and Space Environment Technologies. These historical irradiances have been developed with partial funding from the NASA UARS, TIMED, and SOHO missions.

Table of Contents

List of Figures

List of Tables

1 Introduction

Nonmagnetized objects in the solar system do not possess global intrinsic magnetic fields. Mars, Venus, Pluto, the moon, and small bodies such as comets and asteroids are examples of nonmagnetized objects. Long-term evolution of the object's surface and atmosphere is closely tied to its interaction with the outer space environment. Earth and gas giant planets in the solar system have strong dipole-type intrinsic magnetic fields that surround the planet and extend far beyond their atmospheric boundaries into outer space. In the absence of such protecting layer, external plasma will interact directly with the object's surface or upper atmospheric layers.

For most nonmagnetized objects, the top plasma layer is the first layer of the interaction with outer space that acts as an electrically conducting transition region between outer space and the upper atmospheric levels. This can be a well-developed ionosphere on top of a mesosphere layer (as in Venus, Pluto, and Titan), or a region of highly ionized neutral gas replenished constantly from lower levels (e.g., comets). There are longstanding questions of how modulations of external environments affect the upper plasma layers of these objects, of how fast alteration and recovery of protecting layers occurs under different solar conditions, and of what other effects are at play to protect the surface layer from space's harsh environment in the absence of a protecting magnetic field.

Through this dissertation, I investigate external plasma interaction with comet 67P/Churyumov-Gerasimenko (67P/CG) and Titan, two nonmagnetized objects that are the focus of this research. Along with many interesting aspects of their aeronomy, similarities to the terrestrial environment, and historical importance, the choice of comet 67P/CG and Titan for detailed analysis and modeling was further reinforced by availability of new spacecraft in-situ measurements at the time of my Ph.D. studies. I provide detailed discussion on formation of ionosphere around Titan and comet 67P/CG. I analyze each object by modeling its plasma environment and interactions; and I compare model results with observations.

1.1 Solar Wind

Solar wind plasma is composed of hot, fast-moving charged particles, mainly H^+ (~96 %), He^+ (~4 %), He^{++}, and electrons, to maintain almost perfect charge neutrality. The solar wind also carries with it the Interplanetary Magnetic Field (IMF) and the motional electric field. Due to the large magnetic Reynolds number, the IMF is said to be frozen into the solar wind plasma. The origin of the solar wind is in the corona of the Sun, where the coronal plasma flows along the magnetic field lines. The shape of these fields is determined by the dynamo of the inner layers of the solar atmosphere. Gas dynamics analysis shows that the portion of the plasma flow that becomes transonic near the outer boundary of the solar corona is emitted in the form of solar wind (Figure 1.1). The Sun’s rotational and latitudinal dependent activities result in the spiral shape of the outflowing solar wind, which is known as Parker spirals. High energy charged particles gyrate around the solar wind IMF lines as they move with bulk flow velocity (Cravens, 1997).

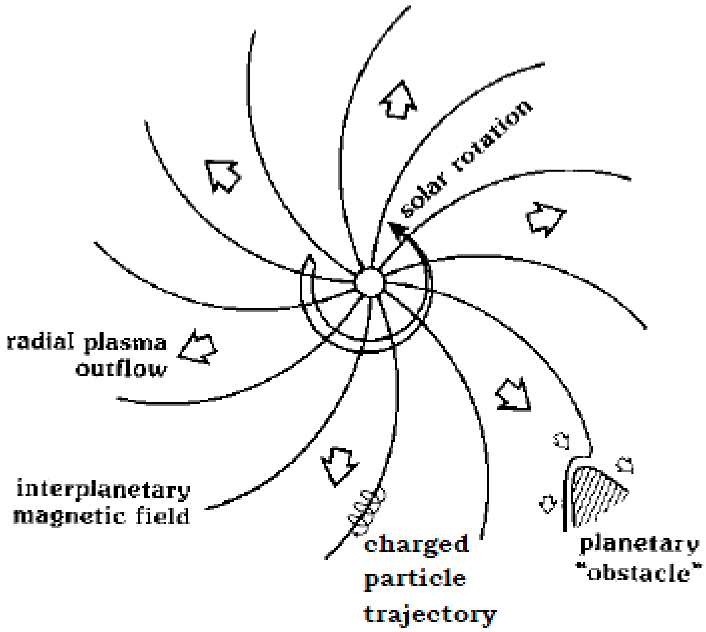

Figure 1.1 - Top-view schematic of the Sun at the center, the solar wind outflow and interplanetary magnetic field, Parker spiral shapes, and gyrating charged particles. The Sun rotation is marked with a counterclockwise vector. Image courtesy: NASA image database.

On average, the solar wind plasma moves with a bulk velocity between 350 and 600 km/s when measured at one astronomical unit (AU). As the solar wind flows outward, properties of the plasma evolve. The plasma density drops as $1/d^2$, where d is the heliocentric distance. At large enough distances, the collisional mean free paths for ions and electrons become large enough (at different rates and distances) for the solar wind plasma to become collisionless. The density and temperature evolve from 10^9 cm^{-3} and 10^6 K at the top of the solar corona, to about 7 cm^{-3} and 10^5 K at 1 AU. Typically, the solar wind electrons are hotter than the ions are, due to their smaller mass. Near the Earth, two populations of electrons are observed: a core Maxwellian distribution with a temperature of $T_c \sim 10^5$ K and a density of $n_c \sim 7$ cm^{-3}, and a hotter halo population with a temperature of $T_h \sim 10^6$ K and a density of $n_h \sim 0.3$ cm^{-3}. Typically, the observed ratio for halo to core electron densities is 1 to 25. The cold core electron population is marginally collisionless but electrons still undergo occasional collisions, while the halo population is entirely collisionless and carries most of the electron heat flux.

Based on the nature of the object, interaction of the solar wind with solar system objects can be separated into four categories (Cravens, 1997):

1. *Lunar* type, in which the solar wind impacts the surface and is absorbed due to absence of an atmosphere and a large-scale magnetic field. The solar wind charges the surface of the objects. The Moon, asteroids, and interplanetary spacecraft are examples of objects with this type of interaction.

2. *Earth* type, which is the case for magnetized objects such as the Earth and gas giants that have an intrinsic magnetic field. The magnetic field around these planets is best approximated by magnetic dipole moments that create an obstacle in front of the fast-moving magnetized solar wind. Through this interaction, the supersonic, superalfvenic solar wind slows down and deflects around the region containing the planet's dipole fields, commonly known as the magnetosphere. The magnetosphere can extend into space for very large distances, encompassing moons and satellites orbiting the planet. Static pressure balance between solar wind dynamic pressure and magnetosphere's magnetic pressure determines the position of the magnetopause. The magnetopause is the limit of planet's magnetosphere and magnetic field. Beyond this boundary, solar wind density becomes increasingly more dominant. Also, transition of the solar wind from supersonic to subsonic speeds produces a bow shock. The region between the magnetopause and the solar wind bow shock is called the magnetosheath, a transitory region from magnetospheric plasma to solar wind plasma.

3. *Venus* type, which is the case for objects with no intrinsic magnetic field but with a rich atmosphere, such as Venus, regions of Mars, and Titan. For these objects, the neutral atmosphere is ionized by solar Extreme Ultraviolet (EUV) and soft X-ray radiation and a dense perfectly conductive ionosphere is present. The solar wind magnetic field induces ionospheric currents, according to Ampere's law. These currents exclude the magnetic field from penetrating into the lower atmosphere. This is known as diamagnetic effect. Therefore, the ionosphere is the actual obstacle to the solar wind flow. The shocked solar wind slows down near the object and the magnetic field piles up in front of the ionosphere. Hence, the ionospheric thermal pressure counterbalances the magnetic field pressure in the solar wind. A bow shock also exists. Titan's interaction in this category, however, is slightly different. Titan's external plasma environment is the slow moving magnetosphere of Saturn rather than the solar wind. Titan's ionosphere still forms but the solar wind bow shock and high ionospheric currents are lacking.

4. *Comet* type, where the solar wind flow interacts with the coma of the comet. Coma formation occurs through sublimation of the neutral species and dust from the nucleus, which creates a radially outflowing envelope whose velocity is typically on the order of 1 km/s. The nucleus gravity for small sized comets is negligible; and therefore, the coma is not bound to the nucleus. Furthermore, in-situ measurements of comets visited so far show that these comets have no intrinsic magnetic fields. For inactive comets, this interaction can become lunar type.

Solar irradiance (not part of the solar wind) is also determined by energy balance and radiative transfer of different layers of the solar atmosphere. A wide range of photon energies are emitted, with highest intensity in the visible range (380-780 nm) and the highest peak at 480 nm. Line emissions observed in this spectrum are evidence of fully ionized plasma in the solar corona, with some highly ionized charge states such as O^{6+} and Fe^{+10}. We are particularly interested in the ~1-100 nm range of the spectrum which includes EUV and soft x-ray photons. These photons have enough energy and substantial flux to ionize atmospheric neutral molecules.

1.2 Comet 67P/Churyumov-Gerasimenko (67P/CG)

Comets have highly elliptical orbits around the Sun. The nucleus of a comet is composed of mixtures of frozen volatiles and dust. Figure 1.2 shows a close-up image of the inactive nucleus of comet 67P/CG that the NAVCAM instrument on the Rosetta spacecraft captured at a distance of 27.5 km on January 1, 2015. Comet 67P/CG has two lobes attached to one another through a thinner neck region. The comet's effective radius is about two kilometers. The two lobes are quite different in outgassing activity, with the larger lobe being more active. Dust jets flowing out from the bigger lobe and neck area are visible in Figure 1.2. With continuous measurements, the Rosetta mission provided a unique space laboratory for studying many space plasma physics phenomena.

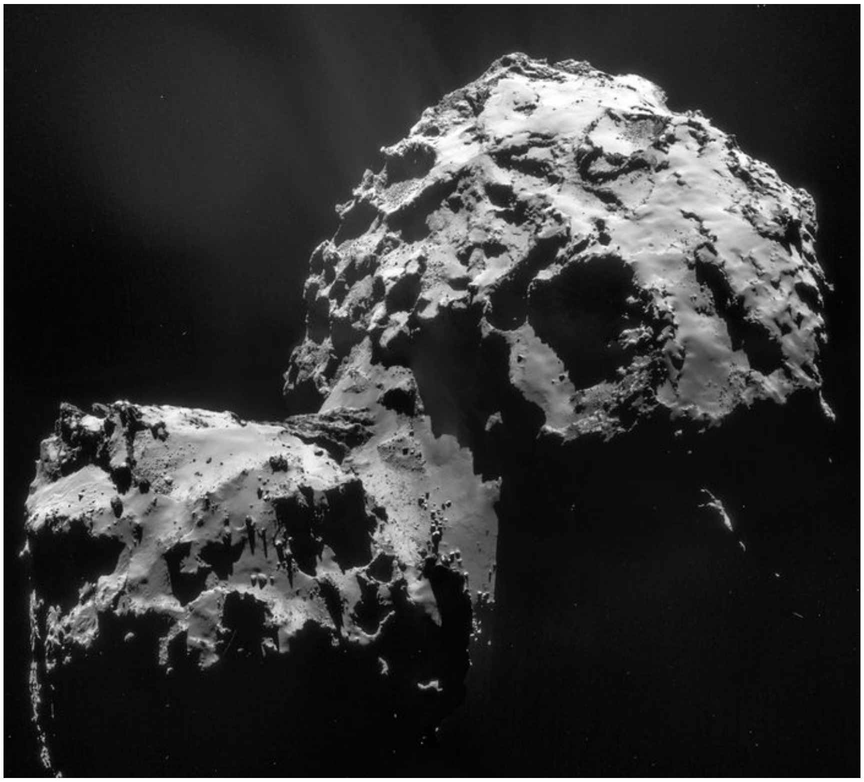

Figure 1.2 - Surface features of the nucleus of comet 67P/CG. The image was captured on January 1, 2015 at 27.5 km by the NAVCAM instrument of the Rosetta spacecraft. Photo courtesy: ESA

1.2.1 Mission to Comet 67P/CG

Comet 67P/CG was the target of the Rosetta mission. Rosetta is a European Space Agency (ESA) mission with contributions from its member states and the National Aeronautics and Space Administration (NASA). Rosetta's initial target was comet 46P/Wirtanen but due to launch failure in 2003 and missing the initial target's orbit, mission planners shifted the mission's attention to comet 67P/CG. The Rosetta spacecraft arrived at the comet in August 2014 and escorted the comet until the end of September 2016. Figure 1.3 illustrates several phases and mission milestones. A series of spacecraft events and maneuvers appears in chronological order at the bottom of Figure 1.3. This figure was designed pre-launch and shows the mission's nominal end date as December, 31, 2015. The mission was extended for nine months beyond that date.

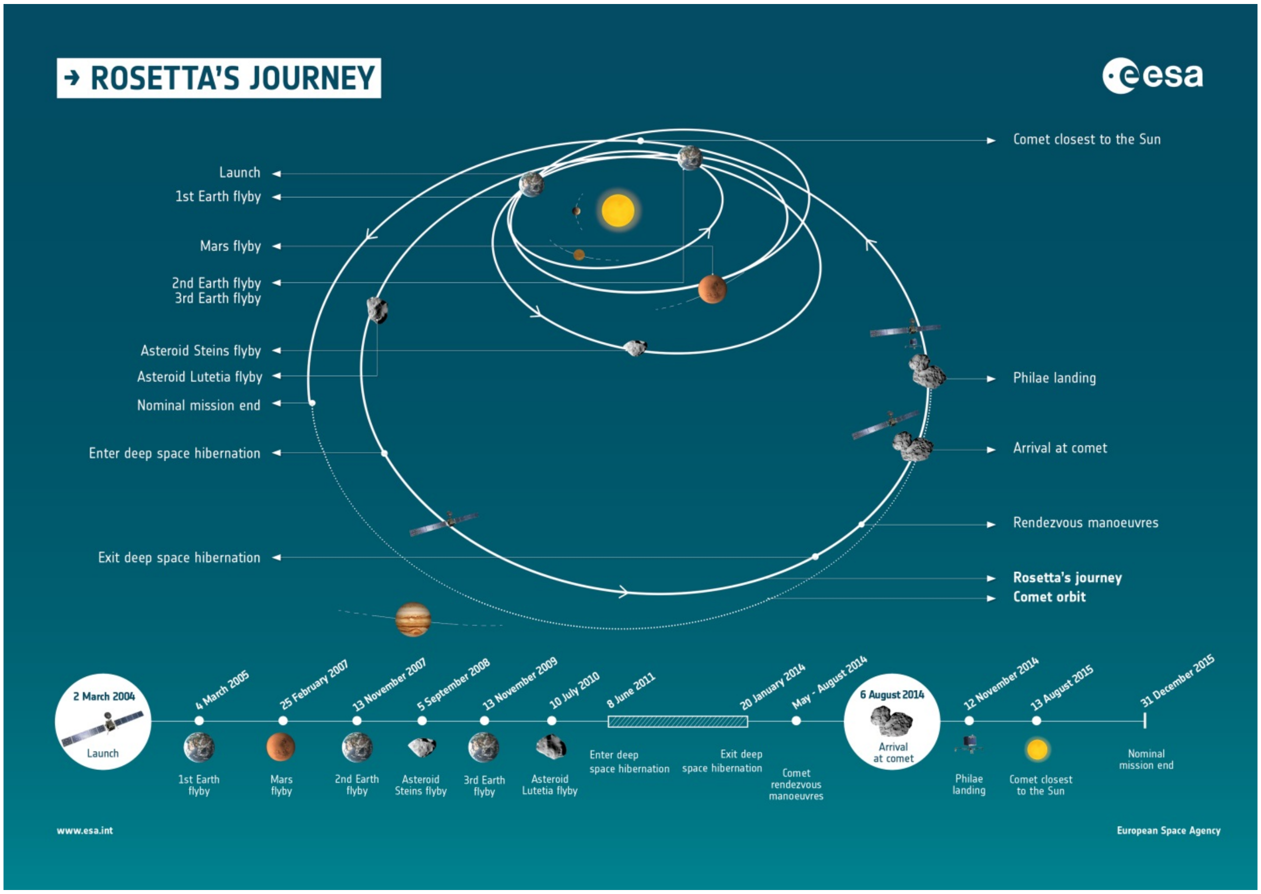

Figure 1.3 - Rosetta spacecraft and comet 67P/CG trajectory around the Sun. A chronological list of events appears at the bottom. The image was designed pre-launch and shows the mission's nominal end date as December 31, 2015. However, the mission was extended until September 30, 2016. Photo courtesy: ESA.

During the two years and one month of the Rosetta mission, many instruments onboard the spacecraft made measurements of the neutral coma, plasma, and nucleus of the comet. Measurements were made at different heliocentric and cometocentric distances, which resulted in observations of a variety of nucleus activity during this time. Along with many remote sensing and imaging experiments, Rosetta carried a full suite of plasma instruments to perform long-term in-situ measurements of the plasma environment around comet 67P/CG. The Rosetta Plasma Consortium (RPC) is a package of five plasma and field instruments, including the Ion and Electron Sensor (IES), the Ion Composition Analyzer (ICA), the Langmuir Probe (LAP) the Mutual Impedance Probe (MIP), and the Magnetometer (MAG) (Carr et al., 2007). The Plasma

Interface Unit (PIU) joint between the other five instruments acts as instrument control, spacecraft interface, and power management unit. A lander (Philae) was also released onto the nucleus surface on November 12, 2014, to provide more details about composition of the nucleus and close-range characteristics (Figure 1.4).

Figure 1.4 – Rosetta spacecraft and Philae lander as it is being mounted on the spacecraft. The high gain antenna is visible in this picture beneath the spacecraft. Adapted from (Glassmeier et al., 2007a).

1.2.2 Solar Wind Interaction with Comets

Interaction of comets with the solar wind is particularly interesting because of their lack of intrinsic magnetic field and their negligible gravity from the nucleus. Over the course of several decades, extensive studies of this interaction have involved remote observations, in-situ spacecraft measurements, and theories, but the emphasis has largely been on active comets in the inner solar system (Cravens and Gombosi, 2004; Gombosi, 2015; Neugebauer, 1987). Previous missions to comets were limited to single flybys as the spacecraft crossed different plasma boundaries near the comets, allowing only snapshots of the cometary environment at specific cometary and heliocentric distances. Flybys of comets 1P/Halley, 21P/Giacobini-Zinner, 26P/Grigg-Skjellerup, and 19P/Borrelly by the ICE, Giotto, VEGA, Suisei, Sakigake, and Deep Space 1 spacecraft all occurred when the comets were near their perihelia and when production rates of dust and neutrals were much higher (≈ 1000 times) than for comet 67P/CG at 3 AU.

Figure 1.5 provides a schematic of the cometary interaction with the space environment. The top-right diagram shows the direction of the solar wind flow (**u**), IMF ($\mathbf{B}_{IMF}$), and the motional electric field (**E**). The neutral coma is shown with H_2O molecules (as the dominant species); however, the real composition can vary and may be a mixture of CO_2, CO and H_2O molecules, with CO_2 density dominant at times. The radially symmetric distribution of the neutral coma is also depicted with blue shaded areas and the XYZ coordinates placed on the comet are arbitrary in this figure. The nucleus sublimation rate depends on comet's activity and is parameterized by the outgassing rate, Q, which is an estimate of the number of molecules leaving the surface per second. A simple model of the total neutral density, n_n, as a function of the distance to the nucleus (r) can be written as follows:

$$n_n(r) = \frac{Q}{4\pi u_n}\frac{1}{r^2} \qquad 1.1$$

where u_n is the outflow velocity. For the most part, photoionization by the EUV and soft X-ray photons is the main source of ion production in the coma, which occurs through this process:

$$h\nu + H_2O \rightarrow H_2O^+ + e \qquad 1.2$$

The figure also shows the charge exchange process that occurs when solar wind ions collide with the cometary neutral species and create new cometary ions:

$$H^+ + H_2O \rightarrow H_2O^+ + H\ (fast) \qquad 1.3$$

The heavy (as compared to solar wind protons) cometary ion production yield of this process is much less than the photoionization. The newly created fast hydrogen atom has a unique energy spectrum, distinct from the neutral coma, and can initiate a second charge exchange process leading to electron attachment to the hydrogen atom and a positively charged ion:

$$H\ (fast) + H_2O \rightarrow H_{fast}^- + H_2O^+ \qquad 1.4$$

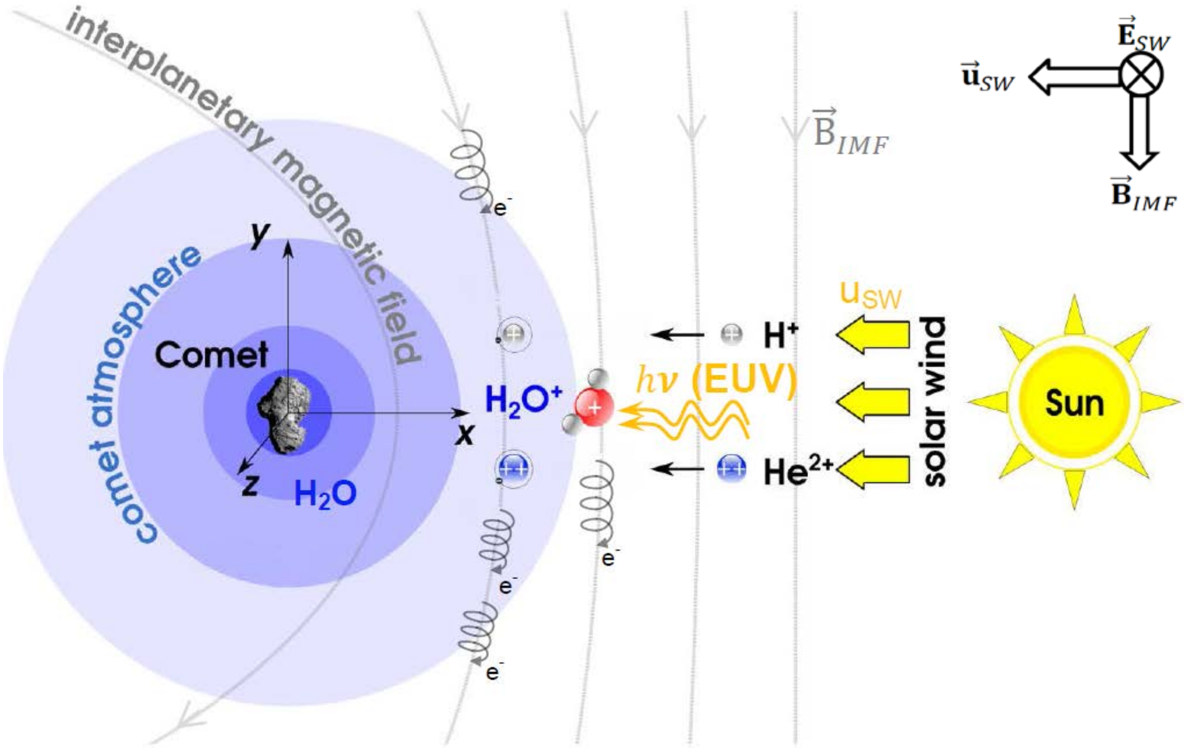

Figure 1.5 - Schematic of the comet-solar wind interaction. The Sun is on the right-hand side. The direction of the solar wind flow and the electric and magnetic fields are specified at the top-right corner. The magnetic field lines are represented with gray lines. Far from the comet, these lines are vertical. Curvature in the field lines (draping) appears at closer distances to the comet. Adapted from Wedlund et al. (2016).

Figure 1.5 also shows the cycloidal path of gyrating electrons along the magnetic field lines. Electron-impact is another main ionization process in which creation of heavy cometary ions and secondary electrons occurs:

$$e + H_2O \rightarrow H_2O^+ + e + e \qquad 1.5$$

New-born cometary ions initially move with the same velocity as the parent neutral species. Compared to the solar wind flow speed, these ions can be considered almost stationary. The cometary ions however, will interact with the Lorentz force in the solar wind, and the motional electric field accelerates the ions in a direction that is perpendicular to the IMF and to the solar wind flow direction. The solar wind motional electric field is given by:

$$\mathbf{E} = -\mathbf{u} \times \mathbf{B}_{IMF} \tag{1.6}$$

The accelerated ions will also gyrate around the magnetic field lines. Therefore, the resultant motion is a cycloidal trajectory. Through this process, cometary ions are picked up by and assimilated into the solar wind, which is why these are called “pickup” ions. Figure 1.6 shows the simulation results of this interaction for comet 67P/CG (Rubin et al., 2014b). In this figure the comet is at the origin, the Sun is to the left and the solar wind is incident from left to right. The motional electric field is in the negative Z direction and the IMF is pointed into the page. The colors correspond to ion densities in logarithmic scale and the white lines in the figure show trajectories of the cometary ion plasma parcels. Figure 1.6 shows results of a hybrid simulation that treats ions as individual kinetic particles, but electrons are a charge-neutralizing fluid. The magnetohydrodynamics (MHD) model is a similar modeling approach to hybrid simulation in which ions and electrons are treated as plasma fluids (i.e., single or multiple fluids). These models are very efficient at simulating large-scale plasma environments. However, the models neglect small-scale single particle interactions and include only a limited amount of details of ionospheric processes.

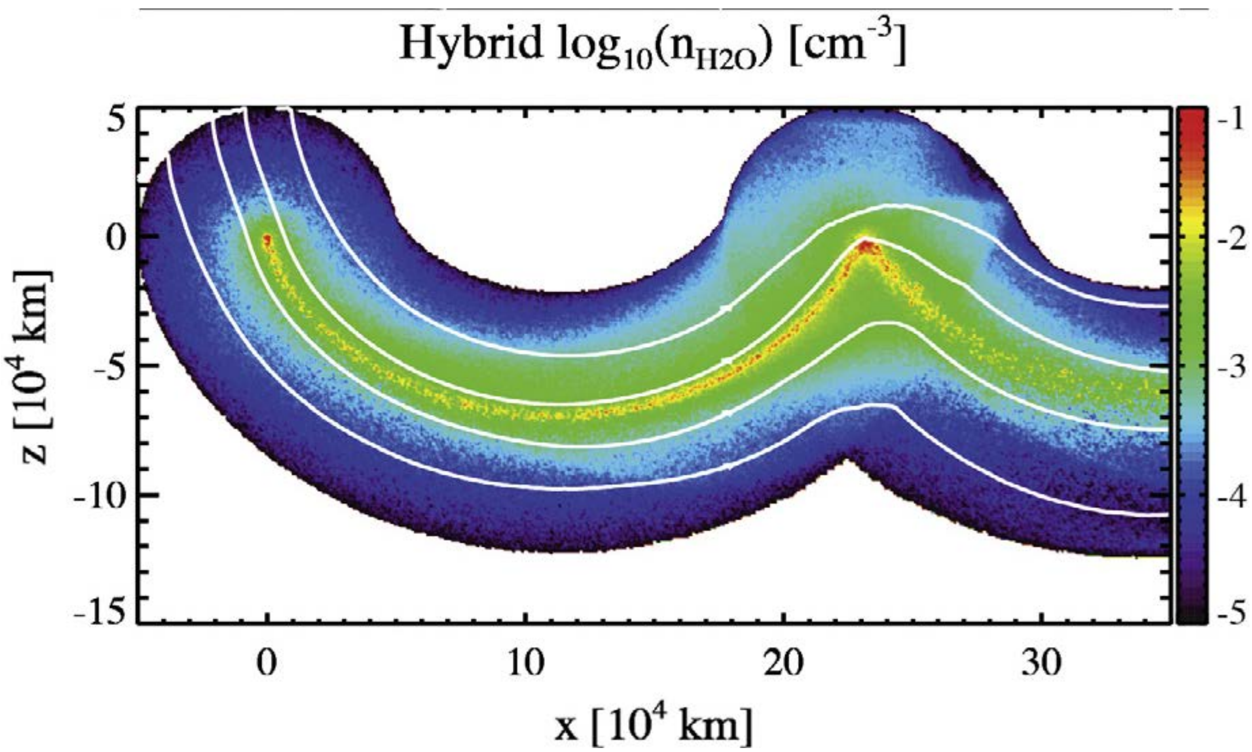

Figure 1.6 - The cycloidal trajectory of the water group cometary ions as they are picked up by the solar wind flow. The comet is at the origin, the Sun is to the left, and the X axis is along the Sun-comet line. The Z axis is perpendicular to the ecliptic plane. The solar wind motional electric field for this simulation is along the negative Z axis and the IMF is pointed into the page. The colors indicate ion densities (in logarithmic scale) and the white lines mark trajectory of the plasma parcels. Adapted from Rubin et al. (2014).

Assimilation of pickup ions will mass-load the solar wind and the momentum conservation will cause the mass loaded flow to slow down. Therefore, areas of the interaction region with higher mass loading rate (i.e., near the ram point) will move slower than areas away from it. Consequently, this causes the solar wind magnetic field lines to drape around the comet (Cravens and Gombosi, 2004; Eviatar and Goldstein, 1988). With substantial mass-loading, a bow shock will also be present upstream of the comet (Coates et al., 1991; Omidi and Winske, 1987).

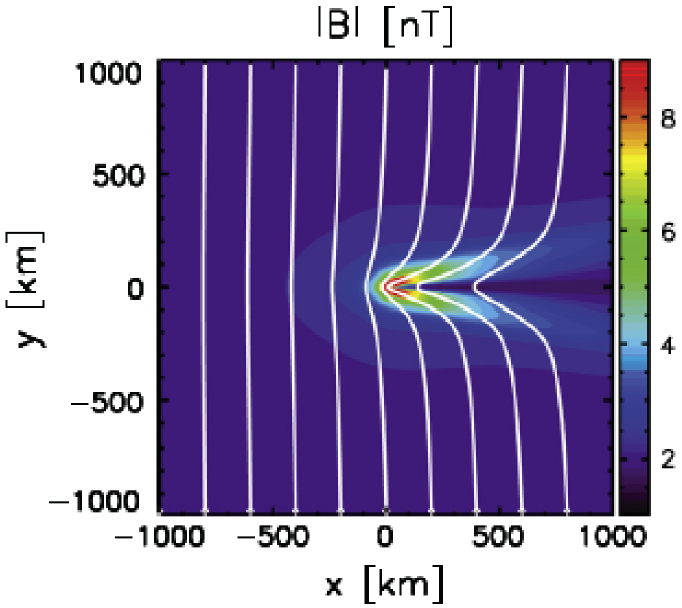

Figure 1.7 - Magnetic field strength and shape in the X-Y plane. The negative X axis is toward the Sun and the Y axis is in the ecliptic plane. The white lines show draping of the magnetic field around the comet (comet is at the origin). Adapted from Rubin et al. (2014).

Figure 1.7 shows the draping of the magnetic field lines around the comet in the X-Y plane as simulated by the hybrid code at a closer range. The comet is at the origin and simulation box size is 2000 × 2000 km. Colors show the magnitude of the magnetic field. The high magnitude of the magnetic field (red colors) upstream from the comet shows the pile up of the magnetic field lines.

1.2.3 Comparison of Comet 67P/CG with Comet 1P/Halley

Much of our understanding of cometary boundaries emerged from analyzing data collected by the Giotto spacecraft’s encounter with comet 1P/Halley on March 14, 1986. The spacecraft entered the diamagnetic cavity at a distance of about 4500 km from the nucleus, where the magnetic field magnitude dropped by 20 nT to almost zero over a distance of 25 km (Neubauer, 1986). Previous research shows that a balance between magnetic pressure gradient force of the solar wind and the ion-neutral drag force in the coma determines the stand-off distance of field free region boundary (see Figure 1.8) (Cravens, 1986; Ip and Axford, 1987; Puhl-Quinn and Cravens, 1995). This distance is known as the diamagnetic cavity boundary or cavity surface distance. Interaction of the unmagnetized outflowing cometary plasma and inflowing magnetized solar wind plasma can also be characterized as a tangential discontinuity in which two scale lengths, the Larmor radius of the outflowing ions and the effective distance of the ion-neutral drag force, are determined to describe structure of the discontinuity (Flammer et al., 1991). Within the stand-off distance in the diamagnetic cavity, ions and neutrals move radially outward and interact with the magnetic field pile-up region. The enhanced magnetic field does not affect the neutral species, while cometary ions are likely to pile up as they approach the region of enhanced magnetic field. Neutral species, however, initiate ion-neutral collisions with inflowing solar wind ions. One should also note that electron-ion recombination is a major loss process for ions in the region just outside the cavity surface.

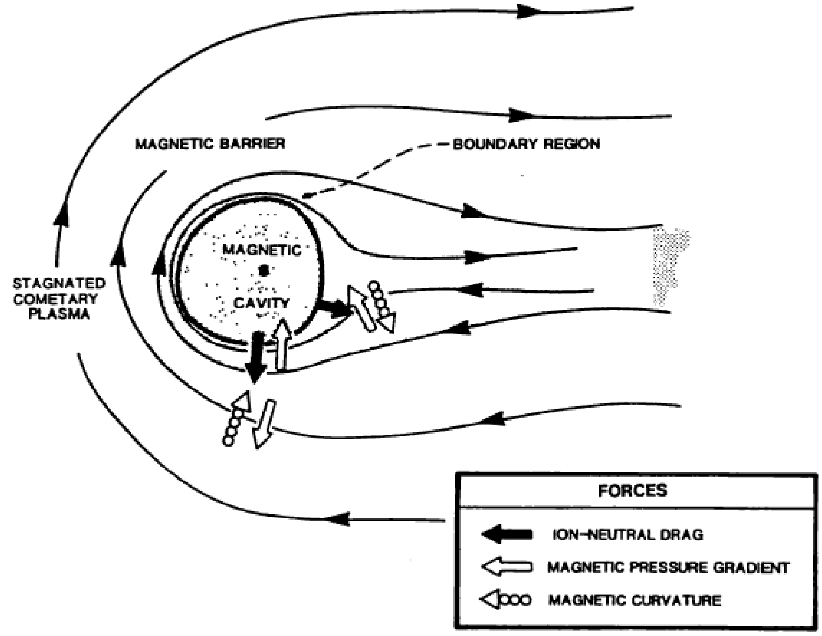

Figure 1.8 - Schematic of the diamagnetic cavity at comet 1P/Halley. The Sun is to the left and the solar wind flow is from left to right. The force balance between the ion-neutral drag force and the magnetic pressure gradient and magnetic curvature are shown with white, black and dotted arrows, respectively. Adapted from Cravens (1986).

Comet 67P/CG has an orbital period of about 6.5 years and a rotational period of about 12.4 hours, which declines after each perihelion passage due to loss of mass. This comet is significantly less active than is comet 1P/Halley. Therefore, plasma boundaries and regions observed at comet 1P/Halley are observable only near perihelion, when the comet is more active and collisional processes in the neutral coma become more frequent. Characteristics of these boundaries can also be quite different.

For comet 67P/CG, at 3 AU and at close proximity to the nucleus, measured flux of suprathermal electrons was much higher than was the regular solar wind (Madanian et al., 2016a). Photoionization of a weak coma, compression and ambipolar electric field contribute to the electron population.

Cometary electron distribution can also be characterized by a combination of two kappa distributions: one for the dense and warm (thermal) electrons and the other explaining the rarefied and hot (suprathermal) population. Based on this characterization, for the active comet 67P/CG near perihelion compared to the inactive comet at 3 AU, density of hot electrons increased by a factor of 10 while the density of thermal electrons increased only by a factor of 3 (Broiles et al., 2016). Kappa indices remained the same while the thermal electrons temperature cooled by a factor of 2. Hence, it was suggested that hot suprathermal cometary electrons are most likely of solar wind origin. Another notable finding was that the warm population itself can have two distinguishable distributions with different temperatures. Impact of extreme solar events such as coronal mass ejections (CMEs) compress the cometary plasma and cause enhancements in suprathermal electron densities, and in the background magnetic field (Edberg et al., 2016).

1.3 Titan

Titan is the largest moon of Saturn, orbiting its parent planet at 20 Saturn radii. Titan's interaction with outer space is quite unconventional because Titan has no intrinsic magnetic field but is protected from the solar wind by residing inside the Saturn's magnetosphere.

The Saturnian system is located at about 9.5 AU from the Sun. Saturn's magnetic field is mostly of dipole shape and is generated by a dynamo of metallic hydrogen fluid in the outer core of the planet. The average magnetopause distance is about 22 Saturn's radii. Therefore, Titan is located inside Saturn's magnetosphere most of the time, with possible excursions into the magnetosheath or even into outer space, where it is exposed to the solar wind. Rare occurrence of these excursion events depends on the solar wind dynamic pressure and Titan's spatial position with respect to the corotating magnetospheric flow. Table 1.1 lists more details about orbital properties of Saturn and Titan.

Table 1.1 - Comparison of orbital properties of Saturn and Titan.

	Saturn	Titan
Radius	R_s= 6.026×10^4 km ^{CT}	R_T= 2576 km
Orbital period	29.4 years	15.9 days
Rotational period	10.5 hours	15.9 days (tidally locked)
Intrinsic magnetic field	5 nT (at Titan)	none
Distance to the Sun	9.5 AU (average)	9.5 AU (20 R_s to Saturn)
Surface gravity	1.05g ^{CT}	0.14g
Main atmospheric constituent	H_2 (96%)	N_2 (95%)
Surface pressure	1 bar ^{CT}	1.6 bar
Surface temperature	95 ºK ^{CT}	97 ºK

CT: Cloud top at 1 bar pressure level

There is continuous loss of Titan’s upper atmosphere to Saturn’s magnetosphere through outflow of neutral gases. Estimated escape rates of the atmospheric gases can be based on a combination of thermal, hydrodynamic, and Jeans escape processes. Titan’s haze layer (Figure 1.9) is a product of chemical processes in the upper atmosphere, which are started by photoionization and ion-neutral reactions in the ionosphere. The Cassini’s Imaging Science Subsystem (ISS) is equipped with a wide-angle and a narrow-angle digital camera. Figure 1.9-left shows a true-color composite image of Titan captured by the ISS on April 7, 2014 at approximately 32,660 km from Titan. Figure 1.9-right shows a true-color image of Titan’s surface captured by the Huygens probe shortly after its landing on January 14, 2005.

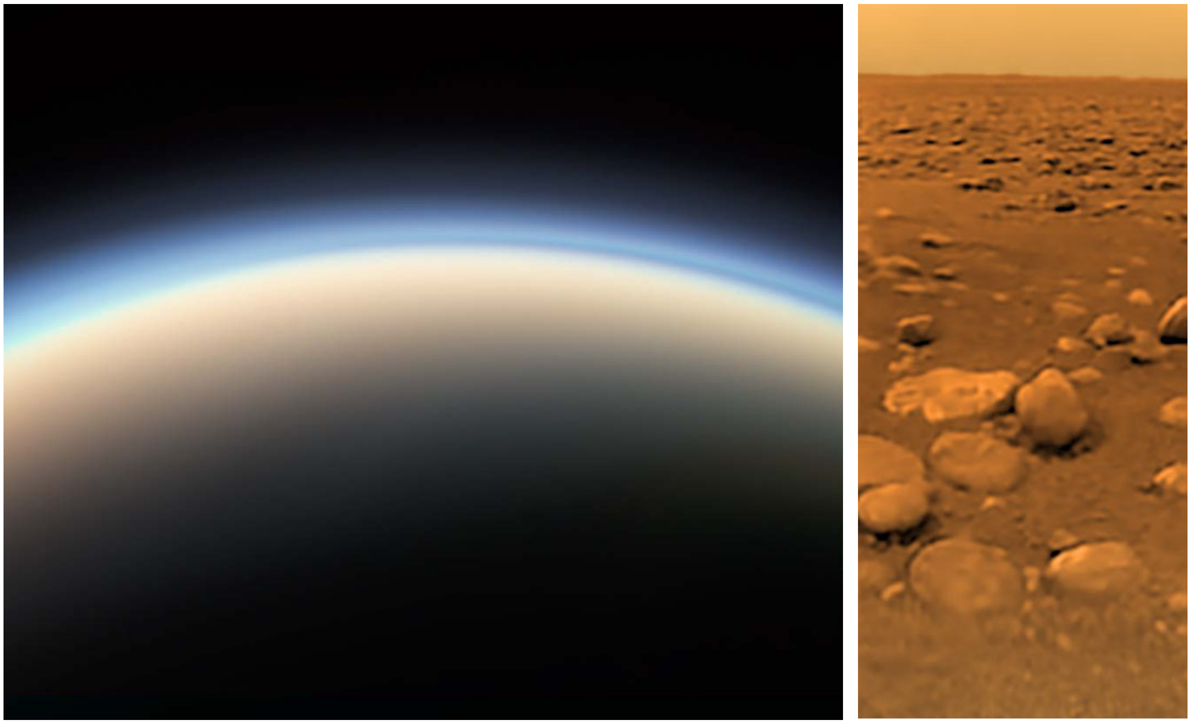

Figure 1.9 – (Left): True-color composite image of Titan captured by Cassini's Imaging Science Subsystem on April 4, 2017. The haze layer is visible in blue. The atmospheric neutral gases extend far beyond the haze layer up to an altitude as high as 3000 km from the surface. (Right): True-color composite image of Titan's surface captured by the Huygens probe on January 14, 2005. The icy stones near the bottom of the image are about 10 – 15 cm wide. Photos Courtesy: NASA.

1.3.1 Missions to Saturn-Titan system

The first detection of Titan's ionosphere occurred during the Voyager 1 spacecraft encounter in 1980 at a closest distance of about 6500 km. The spacecraft provided the Doppler data from ingress and egress radio occultation used in finding atmospheric and ionospheric densities (Bird et al., 1997). This encounter provided information about the draping shape of the magnetic field around Titan (Neubauer et al., 1984).

The Cassini orbiter (and Huygens probe) arrived at the Saturn-Titan system in 2004. The Huygens lander was released on Titan in January 2005. During its descent, the lander made measurements of lower atmospheric levels and provided invaluable images of the surface, which the haze layer usually obstructs. The prime phase of the Cassini mission ended in 2008. Two extensions to the mission (equinox and solstice) expanded the mission timeframe to 2017. The diagram in Figure 1.10 shows the time sequence of different mission phases and the seasonal period of the Titan-Saturn system in its orbit around the Sun for one complete Saturnian year. The red segment on the diagram marks the prime phase of the mission. Blue and yellow indicate the equinox and solstice extensions.

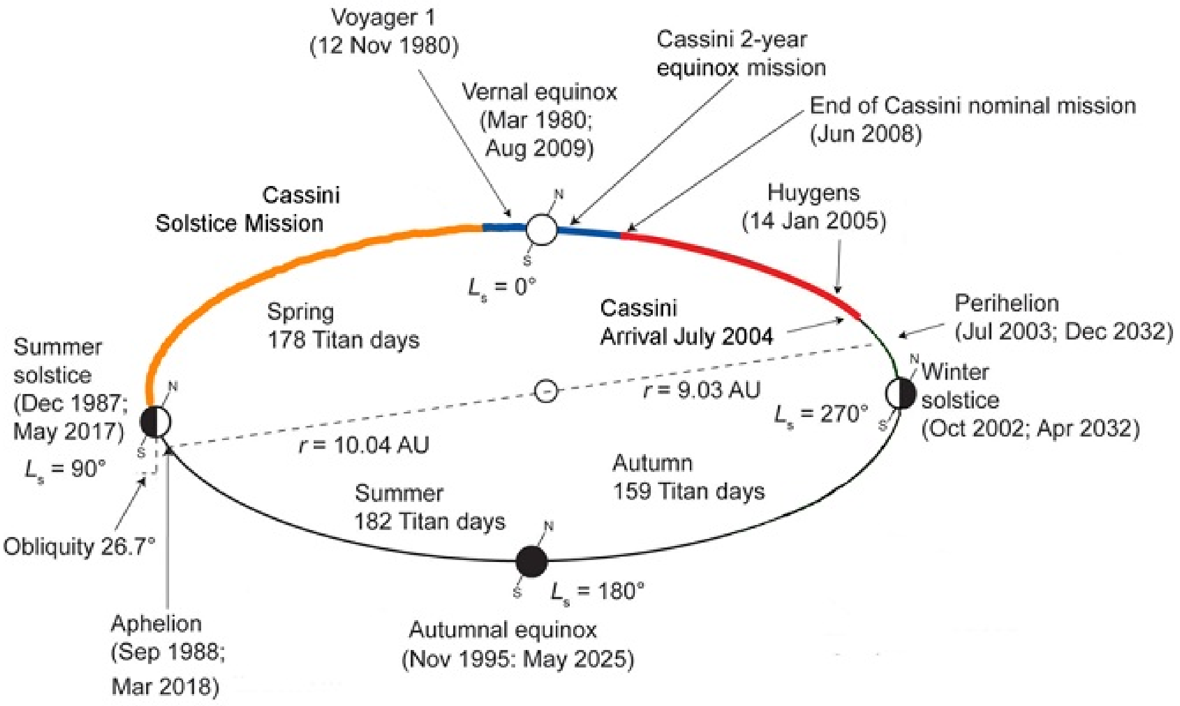

Figure 1.10 - Diagram shows position and date of the Titan-Saturn system orbiting the Sun for one full Saturnian year. The colored segments show different phases of the Cassini mission. The diagram also includes markers of the Voyager 1 flyby and the system’s seasonal changes. Adapted from TSSM report (2009).

With three main platforms, the Cassini spacecraft is suitable for various scientific observations of Titan’s upper atmosphere, middle and lower atmosphere, and surface. Several Titan close encounters were planned in the spacecraft trajectory. These encounters (flybys) are labeled with ‘T,’ representing Titan, followed by the sequence number T5, T40, T113, and so on.

The image in Figure 1.11 depicts the mounting of the 5.7 ton Cassini-Huygens spacecraft prelaunch on the payload adapter. The diagram in Figure 1.12 lists various science experiment platforms. The diagram also lists the instruments that make measurements of the plasma as part of the Particles, Fields, and Waves platform. A more detailed description of the Cassini INMS and RPWS-LP instruments are provided in chapter 3.

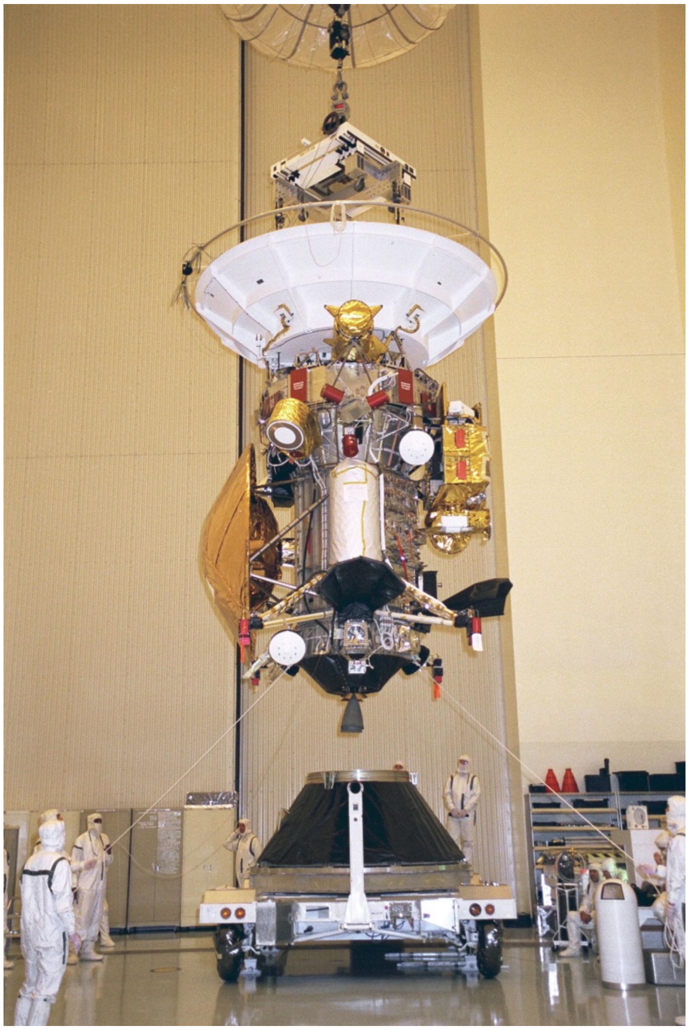

Figure 1.11 - An image of the installation of the Cassini spacecraft and Huygens probe on the payload adapter. The spacecraft weighed 5.7 tons and was launched on October 15, 1997. The white high gain antenna is visible at the top; the golden drum shape on the left side of the spacecraft is the Huygens probe. Photo courtesy: NASA.

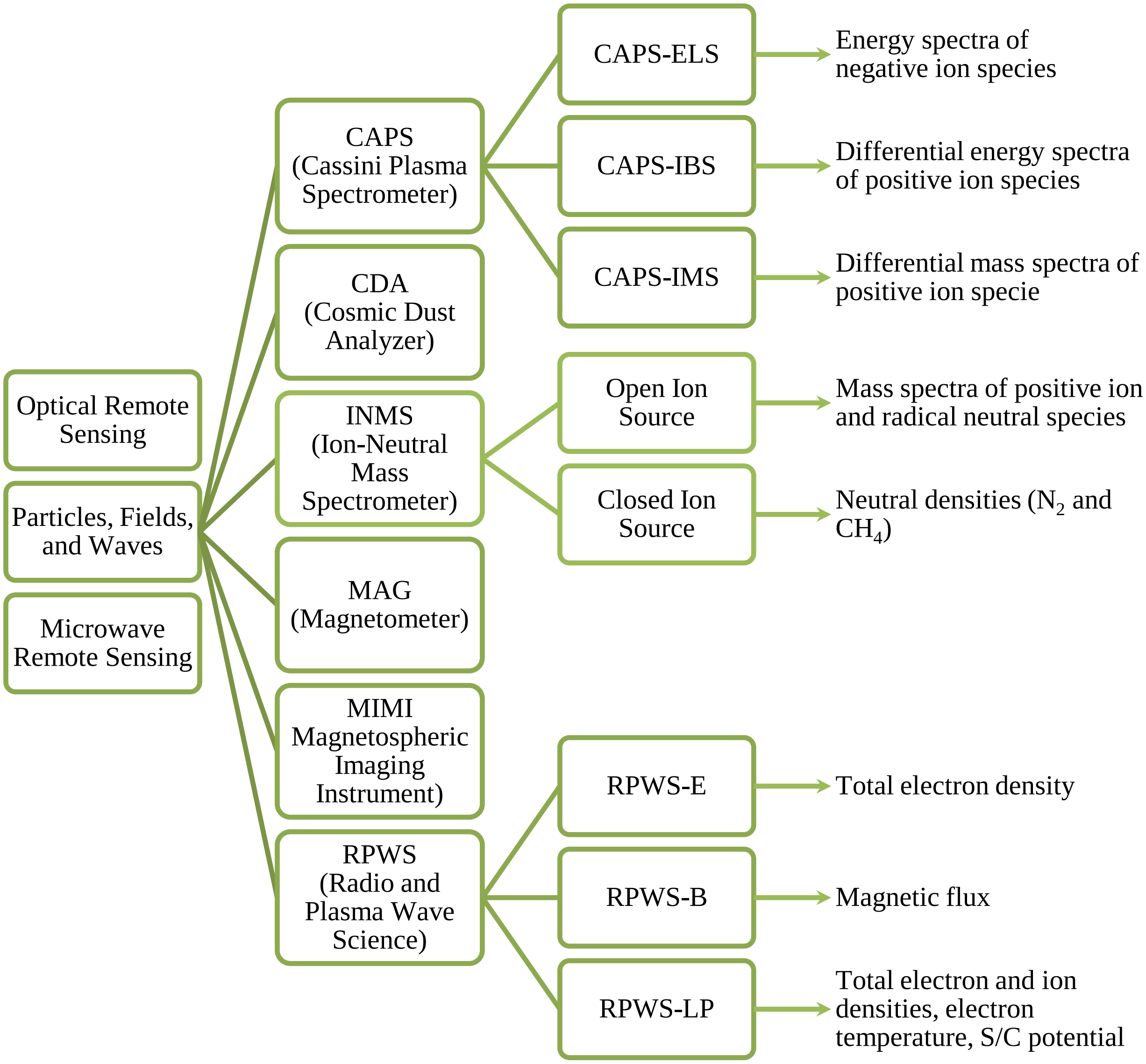

Figure 1.12 – List of science experiments on the Cassini spacecraft. Instruments are categorized under three general platforms, namely: Optical Remote Sensing; Particles, Fields and Waves; and Microwave Remote Sensing. The last column includes a short description of the plasma instruments relevant to this dissertation from the Particles, Fields, and Waves platform.

Along with these missions, there have been ground-based observations to provide primary information about atmospheric composition and densities on Titan. For instance, the observations made by the Infrared Space Observatory (ISO) in 1997 were used for determining abundance of the atmospheric minor neutral species (Coustenis, 1998).

1.3.2 Titan in Saturn’s Magnetosphere

Titan’s interaction with Saturn’s magnetospheric plasma resembles the interaction of Venus with the solar wind, with one major exception: Saturn’s magnetospheric flow is much slower than the solar wind flow and does not form a bow shock upstream from Titan. The figure below shows a schematic of this interaction, where the corotating magnetospheric flow is incident from left and the solar photon flux direction is at an angle β with respect to the flow wake. The nightside hemisphere is colored yellow and the orange ring designates the atmospheric layers. This figure also shows precipitating magnetospheric charged particles as they gyrate along the draped magnetic field line (Coates, 2009).

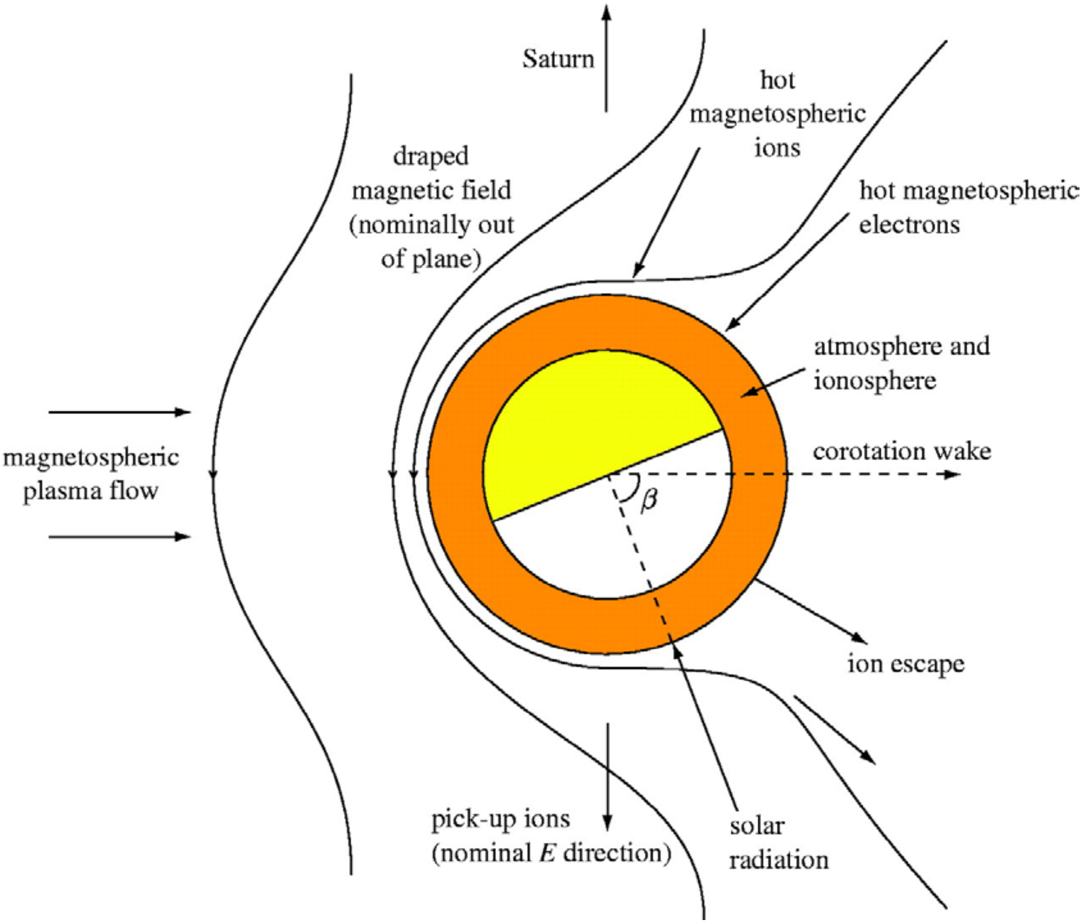

Figure 1.13 - Schematic of the interaction of Titan with the Saturn's magnetospheric flow. The magnetospheric flow is from left to right and the magnetic field is into the page. The magnetic field lines are draped around Titan due to mass loading near Titan. The yellow shaded area shows the nightside hemisphere, and the orange ring indicates the limit of atmosphere and ionosphere layers. Adapted from Coates (2009).

Saturn's dipole magnetic field rotates around the planet at the same speed as the planet's rotational period, which is about 10.5 hours. This causes the magnetospheric plasma to corotate with the planet and directly impacts Titan's upper atmosphere (Figure 1.13). Saturn's magnetosphere is not symmetric in shape and its characteristics vary in time. The plasma consists mostly of energetic H^+, N^+, and O^+ ions and electrons. These particles move with the corotating plasma speed, and carry the frozen-in magnetic field. As the plasma flow encounters an obstacle (i.e., Titan), the energetic charged particles precipitate onto the upper atmosphere, initiating ionization and charge exchange. Multiple studies have investigated variations in the magnetospheric conditions (Bertucci, 2009; Luhmann et al., 2012; Rymer et al., 2009). Based on energy and density of the precipitating electrons and Titan's position with respect to Saturn, Saturn's magnetosphere around Titan can be categorized into four regions as listed below (Rymer et al., 2009):

1. Plasma-sheet region, characterized by high energy and density electron environment. Peak electron energy is from 120 to 600 eV.

2. Lobe-like region, characterized by high energy, low density electron environment. Peak electron energy in this region varies from 150 to 820 eV.

3. Magnetosheath region, characterized by low energy (a few hundred eV), high density electron environment.

4. Bimodal, characterized by two distinct electron populations: an energetic component with electron energies from 200 eV to 3.4 keV, and a less energetic component of electrons with energies ranging from 5.3 eV to 16.3 eV.

Figure 1.14 shows the typical electron flux energy spectrum for each category.

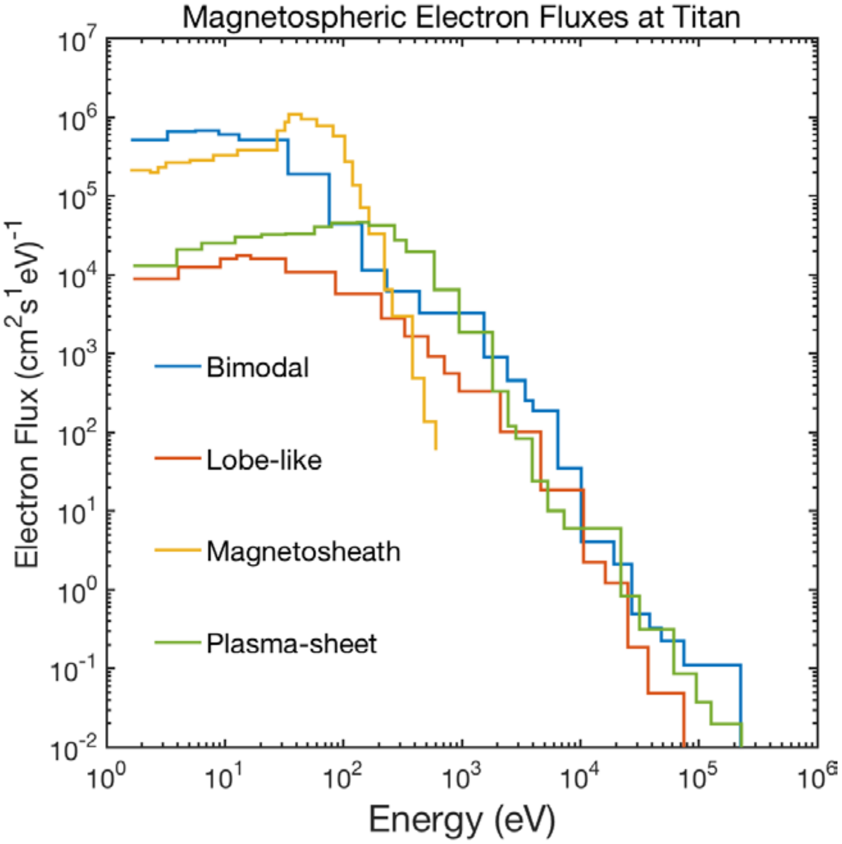

Figure 1.14 – Depiction of the typical electron flux energy spectrum for four types of precipitating electrons in Saturn's magnetosphere at Titan. The flux is in units of 1/(cm^2 s eV). Both axes are in logarithmic scale. Fluxes are measured by the Cassini Plasma Spectrometer-Electron Sensor (CAPS-ELS). The energy range and resolution vary and are set by the instrument detection mode.

Subsequent chapters discuss how orientation of the dayside hemisphere with respect to the Saturn's magnetospheric flow direction is important to determining the interaction between Titan and Saturn. Figure 1.15 depicts five possible scenarios of orientation of the magnetospheric ram direction at different Saturn local times (LT) with the dayside ionosphere. These include the conditions of the Cassini's first flyby of Titan (TA). In this figure, the Sun is to the left and Saturn's magnetic field direction is into the page. Titan's orbit is designated with the dashed circle. The black and white semi-circles represent the Titan's nightside and dayside hemispheres. Orange and green colors, respectively, illustrate the solar and magnetospheric wake regions. The wake regions indicate areas of absence of the relative parameters. Figure 1.15 also shows the motional electric field *E* of the Saturn's magnetospheric plasma at 0:00 LT.

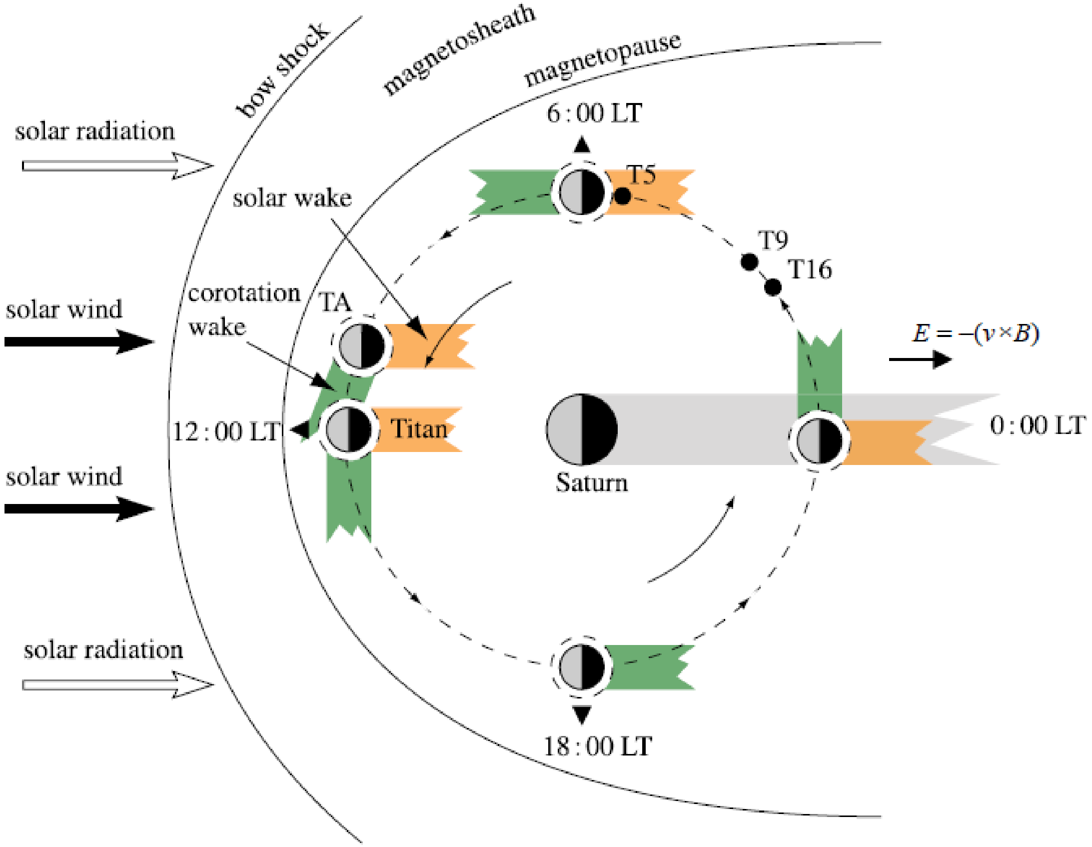

Figure 1.15 – Shows five possible scenarios of Titan's dayside orientation with respect to the Saturn's Local Time (LT). The solar and magnetospheric wakes around Titan are marked with orange and green colors. The Sun is to the left of the image and the Saturn's magnetic field is pointed into the page. Orbital positions of a few Titan flybys are also marked on the figure. Adapted from Coates (2009).

1.3.3 Titan's Atmosphere and Ionosphere

Titan's main atmospheric constituents are nitrogen (~ 98 %), methane (~ 1.6 %), and hydrogen (~ 0.2 %) molecules and small concentration of other hydrocarbons. The minor neutral species such as HCN, C_2H_2, C_2H_4, and C_2H_6 play an important role in the atmospheric chemistry of Titan. Figure 1.16 shows globally averaged neutral density profiles of the three major (N_2, CH_4, H_2) and three minor (C_2H_2, C_2H_4, HCN) neutral species. More details on these profiles, in-situ measurement techniques, and the modeling of minor neutral species appears in Chapters 2 and 3.

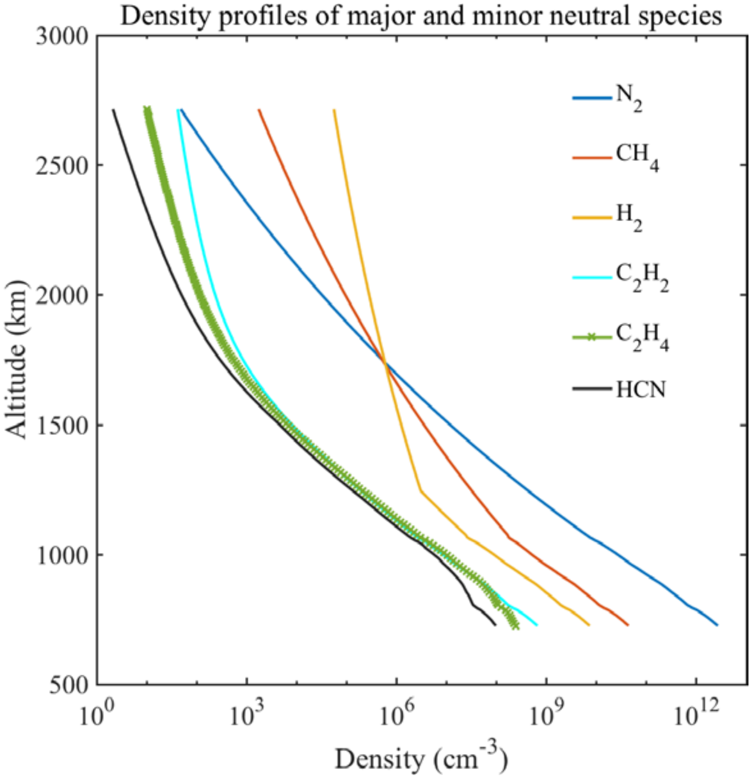

Figure 1.16 - Density profiles of major and minor neutral species at Titan. The major abundant species N_2, CH_4 and H_2 are shown with blue, red, and yellow curves respectively. The minor neutral species C_2H_2, C_2H_4, HCN are shown with cyan, green, and black lines, respectively.

Similar to the comet environment, neutral species in Titan's atmosphere are ionized by solar EUV and soft X-ray radiation or by energetic particles precipitating from Saturn's magnetosphere. Photoionization by solar radiation is the main source of photoion and photoelectron production on the dayside. In this process, the energy of the photoelectron depends on ionization potential of the neutral species and the photon energy. Photoionization rate is a function of ionization cross sections of each species. The incident solar photon flux is also attenuated by neutral species proportional to the photoabsorption cross section and, obviously, atmosphere's column density. Equation set 2.1 lists some preliminary photoionization reactions in the ionosphere.

$$
\begin{aligned}
&h\nu \; + \; N_2 \rightarrow N_2^+ + e \\
&\qquad\qquad \rightarrow \; N + N^+ + e \\
&h\nu \; + CO_2 \rightarrow CO_2^+ + e \\
&h\nu \; + CH_4 \rightarrow CH_4^+ + e
\end{aligned}
\qquad 1.7
$$

On the nightside, impact ionization by high-energy charged particles originating from Saturn's magnetosphere is the main source of ion production. However, magnetospheric contributions might occasionally be important even on the dayside (Cravens et al., 2006; Kliore et al., 2008). An ionospheric plasma layer is created at altitude of maximum ion production. At Titan, this altitude appears to be between 900 and 1400 km. Other ionospheric layers present at lower altitudes, around 650 km and 90 km, are created by meteor showers and cosmic rays, respectively. These layers are not the focus of this research; we only consider the main ionospheric plasma layer in the 900–1400 km region. Figure 1.17 provides an artist's view of the complex chemical environment at Titan.

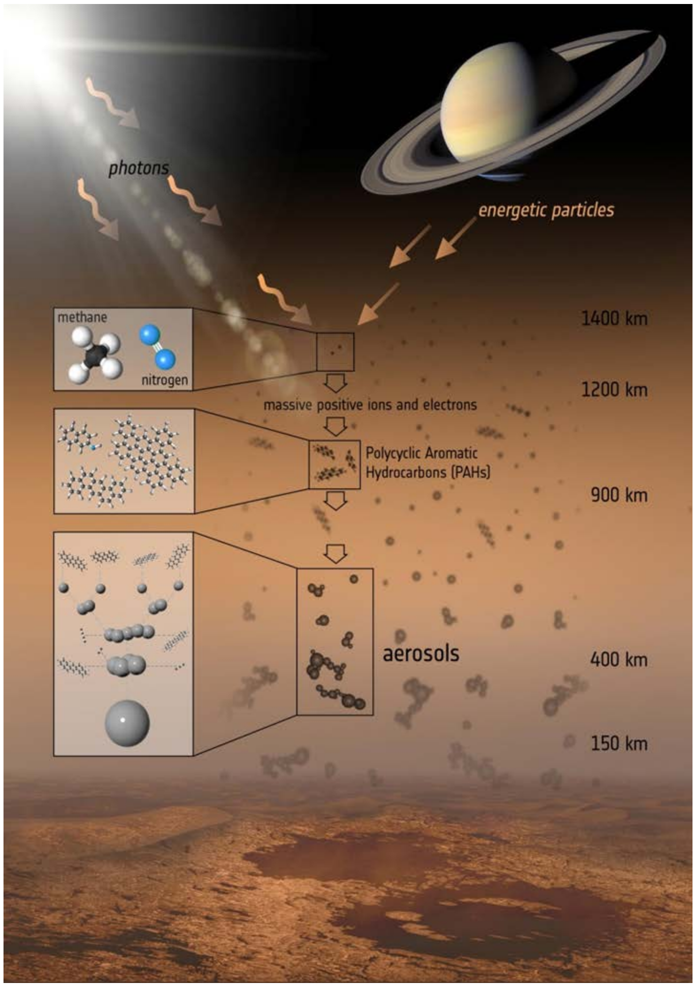

Figure 1.17 - Complex chemical environment of Titan's upper atmosphere and ionosphere. This illustration summarizes the chemistry chain that starts with production of primary ion species by solar photons and Saturn's energetic particles in the ionosphere and ends with aerosol and heavier complex molecules which eventually precipitate on the surface. Photo courtesy: NASA.

The primary ion species take part in a series of ion-neutral chemical reactions to produce heavier, more complex hydrocarbons and nitriles. These heavy species contribute to the chemistry at lower atmospheric levels, to formation of tholin and aerosols, and eventually to surface precipitation of heavy hydrocarbons (Waite et al., 2004). Understanding the ionospheric chemical composition and how it changes under different external factors is essential to studying the physics of the haze layer.

In general, planets with lower surface gravity have a more spread-out atmosphere. The neutral (and thus plasma) densities drop rapidly with increasing altitude by an e-folding length scale known as the scale height. Scale height for ions and neutral species can differ. Beyond a certain distance from the surface, the mean-free-path for binary type collisions is greater than is the plasma scale height; therefore, the plasma becomes collisionless. The altitude at which the plasma becomes collisionless is called exobase boundary. Significant density of ion species above Titan's exobase suggests that the ions can be driven to very high altitudes by a combination of thermal pressure and magnetic forces.

1.4 The Remainder of the Dissertation

The rest of the dissertation focuses on detailed analysis of the upper atmosphere and ionosphere of Titan and comet 67P/CG. To that end, chapter 2 lays out the basis of my modeling efforts to simulate Titan's ionosphere by explaining physical and chemical processes and modeling techniques in the ionosphere. Model components are discussed and modeled ionospheric compositions under variable solar activity conditions are presented. In chapter 2, I will also present results of a simple ion transport model and discuss effects of a transport regime on ionospheric composition.

Chapter 3 explores observations of the Cassini spacecraft at Titan. I will present the Cassini INMS and RPWS-LP in-situ measurements of neutral, ion, and electron densities. The chapter also includes information on Titan flybys and instrument operation. I evaluate ion densities time series over a 10 year period and quantify solar effects on particular ion species. I will outline the long-term effects on the ionosphere under a complete solar cycle and variation of ionospheric peak altitude and background neutral atmosphere.

Description of the plasma environment around comet 67P/CG appears in chapter 4. Information on in-situ measurements made by the Rosetta spacecraft at different phases of the mission is provided. The chapter explains multi-instrument analyses of the cometary plasma at 3 AU and at perihelion. I will present physics of the solar wind interaction with an inactive comet and discuss the existence of two distinguishable populations of electrons around the comet. A kinetic model of electrons is developed to simulate electron distributions and test effects of ambipolar electric field and plasma compression in a sequential manner. Model results are compared with observations in several cases.

Chapter 5 concludes the dissertation where I provide summary of effects of the external plasma environment on Titan and comet 67P/CG. Chapter 5 also explains the new physics we learned from analyzing spacecraft measurements and modeling the plasma environment for each of these objects. Last, chapter 5 offers possible direction for future research.

2 Modeling the Titan’s Ionosphere

This chapter discusses the modeling aspects of the dissertation, with a particular focus on Titan’s ionosphere. Chapter 3 provides comparisons of model results with in-situ measurements of the ionosphere along with analysis of the observations data from multiple instruments on the Cassini spacecraft.

Except for the ion chemistry model, other model components this chapter describes (e.g., solar flux, photoionization, and electron transport) are modified for the comet case. Chapter 4 presents comet modeling results.

My models are developed from and built on several earlier modeling efforts. I acknowledge their contributions (Cravens et al., 2006; Keller et al., 1992; Richard et al., 2015b; Robertson et al., 2009).

2.1 How to Model Planetary Ionospheres

Modeling of planetary ionospheres requires knowledge of the atmospheric neutral composition and knowledge of distance to the parent star. The neutral atmospheric constituents determine ion composition in the ionosphere. Solar extreme ultraviolet (EUV) and X-ray irradiance (wavelength 80-100 nm) can ionize the neutral species. The distance to the Sun, R, determines the amount of incident solar photon flux and solar wind flux the planet receives and is simply proportional to $1/R^2$. For nitrogen dominant atmospheres (such as Earth, Titan, and Pluto) the N_2^+ and N^+ are the dominant primary ion species. For CO_2 rich atmospheres (such as Mars and Venus) the CO_2^+ is the major primary ion species.

At Titan, the primary ion species interact with neutral species at a rate proportional to ion-neutral reaction rate constants. Ion-neutral reaction rates are determined either experimentally or through quantum chemistry models. In the absence of appropriate laboratory and analytical measures, rate constants are estimated by extensive ion-neutral models in a way that brings convergence and chemical equilibrium to the models. A photochemical equilibrium is a state in which ion production and loss rates are nearly equal and where relatively stable ion densities are achieved. In the presence of electrons, ions undergo dissociative electron recombination at a pace that is a function of electron temperature and density. Ion-neutral reactions and electron dissociative recombination are two main ion loss processes at regions of high plasma density. Appendix A provides reaction rate constants for these processes.

In the chemically complex ionosphere of Titan, ion-neutral reactions are the only production source for heavier ion species. At lower altitude heavy hydrocarbons act as nucleation seeds for much heavier compounds and contribute to formation of dust and haze layers.

There are several approaches to modeling the planetary ionosphere. However, none of the current models captures the system's full details. Most of the large scale ionospheric models are based on hydrodynamics fluid theories and cannot predict electron distributions accurately and efficiently. This is mainly due to the simulation box's large scale and limited computation power. Given the size of the system, the number of variables, the scientific objectives, and the details of the physical processes, researchers make certain assumptions and choose a specific set of parameters in their modeling approach.

In our model, ions are considered stationary and ion densities are calculated under photochemical equilibrium (with the exception of ion transport effects, as section 2.3 discusses).

Electrons have more freedom to move in the environment due to their much lower mass. Since we are only interested in spatial and temporal statistically measurable parameters such as particle density, particle flux, and temperature (i.e., collective behavior of the plasma), it is impractical to model the full trajectory of each individual electron. The kinetic description of plasma provides an appropriate formalism to effectively model the electron distribution. In this approach, plasma is assumed to be collisionless. However, collisions do exist and their effects are included by making slight modifications to the electron transport equations. Section 2.2.3 covered these topics in details.

2.2 Model Components

2.2.1 Solar Irradiance Flux Models

To simulate the electron and ion densities in the Titan's ionosphere or comet 67P/CG, one should determine the sources of electron and ion productions. Photoionization is the main source of ion production in both environments. To calculate the production rates from photoionization requires the solar photon flux and the density of neutral species. This section discusses solar irradiance flux models that provide a suitable photon flux spectrum at the top of the atmosphere, $I_\infty(\lambda)$. Several available solar irradiance models are independent of direct solar EUV and X-ray observations. These models use a reference rocket or satellite measurements as an absolute photon flux spectrum and utilize proxies to scale the solar flux to another desired time. The solar activity is tied strongly to the number of dark sunspots on the solar surface. There is a well-established correlation between the solar radio flux at 10.7 cm wavelength (i.e., $F_{10.7}$ index) and the sunspot number. The $F_{10.7}$ index can be readily measured on Earth.

The EUV81 model, also known as HFG, uses a combination of rocket launch data and Atmospheric Explorer-E (AE-E) spacecraft observations of solar irradiance during the solar minimum condition (Hinteregger et al., 1981). Proxies used in the HFG model are combinations of daily $F_{10.7}$ index and its 81-day average. Similarly, the EUVAC model uses the $F_{10.7_p}$ as a proxy defined by:

$$F_{10.7_p} = \frac{F_{10.7} + F_{10.7_A}}{2} \qquad 2.1$$

where $F_{10.7_A}$ is the 81-day average of the $F_{10.7}$ index (Richards et al., 1994). The EUVAC model scales each wavelength bin separately according to the following equation:

$$I_i = F_{74113_i}\left[1 + A_i\left(F_{10.7_p} - 80\right)\right] \qquad 2.2$$

where I_i is the photon flux at bin *i*, the F_{74113} is the measured EUV flux during the solar minimum condition on April 25, 1974, and A_i is the scaling factor for each bin. The bins span the energy spectrum from 50 to 1050 angstroms.

The NRLEUV model is a hybrid model based on physical properties of the solar atmosphere and fractional disk coverage of dark coronal holes to construct the EUV spectrum (Lean et al., 2003). The SOLAR2000 predicts solar flux based on an approach similar to that of the HFG model, using data from the Solar EUV Monitor (SEM) spectrometer onboard the Solar Heliospheric Observatory (SOHO) as a reference spectrum (Tobiska, 2007). A recent model known as the Flare Irradiance Spectral Model (FISM) estimates solar irradiance by utilizing the EUV data from the Solar Extreme Ultraviolet Experiment (SEE) instrument onboard the Thermal Ionosphere Mesosphere Energetics and Dynamics (TIMED) spacecraft, with as many as six different proxies that scale each of the 1-*nm* wavelength bins (Chamberlin et al., 2007). The

Solar Radiation Physics Modeling System (SRPM) also provides high resolution solar spectral irradiance of solar EUV flux (Fontenla et al., 2011; Fontenla et al., 2014). The SRPM is a set of tools that uses solar atmosphere features obtained from images of the solar disk to construct the radiation flux. The two major advantages of the FISM and SRPM are their abilities to predict solar events, such as solar flares and high resolution of the irradiance spectra.

To put these models into perspective, one can compare total EUV irradiance, which corresponds to flux contained in the 5-105 nm wavelength intervals. For NRLEUV, EUV81, EUVAC, SOLAR2000, FISM, and SRPM, total EUV irradiance are 2.11, 2.21, 2.47, 3.78, 2.51, and 2.21 mW/m^2, respectively. These numbers, for all models except SRPM, are the monthly averaged energy flux for solar minimum conditions of September 1986. The SRPM does not provide irradiance data as old as 1986; therefore, the daily average of solar minimum conditions on October 6, 1996 was used instead. Since the goal here is to compare the modeled total EUV flux for solar minimum conditions experienced during the Cassini epoch, using two different time periods is acceptable. Table 2.1 shows a comparison of other features of these irradiance models.

Table 2.1 - Comparison of different solar EUV models at minimum solar activity conditions.

Model	Wavelength range (nm)	Wavelength bins, Emission lines	Proxies	Total EUV Irradiance (mW/m^2)
EUVAC	5-105	37 × 50 Å plus lines	$F_{10.7p}$	2.47*
SOLAR2000	1.8-105	39 × 50 Å plus lines	Lyα, $F_{10.7}$	3.78*
EUV81	1.8-200	866 lines and blends	$F_{10.7}$, $F_{10.7A}$	2.21*
NRLEUV	5-200	1474 lines, variable bin size	I_{CHROM} , $F_{10.7}$, $F_{10.7A}$	2.11
FISM	0.1-190	1nm wavelength bin	$F_{10.7}$, Lyα, 0-4 nm, 36.5 nm, 30.5 nm, MgII	2.51
SRPM	0.12 nm-100 micron	Variable bin size	Solar disk images (no proxy)	2.21

*Adopted from Lean et al. (2003)

We used EUVAC and SOLAR2000 solar irradiance empirical models, which give solar EUV flux as a function of photon wavelength in a manner consistent with our model energy structure (Robertson et al., 2009). As summarized in Table 2.1, the differences between EUVAC and other models are not dramatic. The EUVAC model serves our modeling needs. The SOLAR2000 model was used because it provides excellent wavelength resolution at very low and very high photon energies. The solar photon fluxes are determined for the location of the Earth and are adjusted for other distances in the solar system, either for Titan or for comet 67P/CG.

During the extremely quiet solar minimum 23/24, it should be noted that the EUV flux was lower than observed in the previous solar cycle (Solomon et al., 2013). Figure 2.1 presents two solar flux spectra used in our model (in c.g.s. units) at the time of two Cassini flybys of

Titan, T40 (blue dots) and T86 (red dots). The $F_{10.7}$ indices for T40 and T86 are about 79 and 140 sfu (solar flux unit), respectively. The soft X-ray and EUV energy ranges of the spectrum are labeled with yellow and pink colors at the bottom of the plot. One can observe that the T86 solar photon fluxes are about a factor of 1.5 to 2 times greater than the T40 fluxes, and slightly less than T40 for wavelength less than 1 nm.

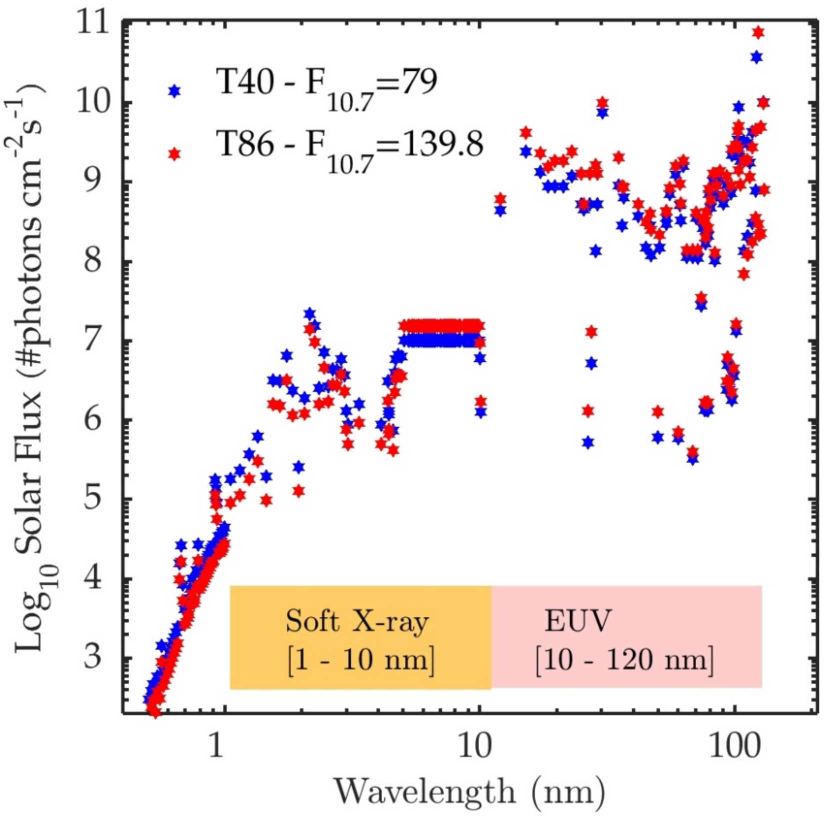

Figure 2.1 - EUVAC generated solar photon fluxes for high (red) and low (blue) solar activity periods at 1 AU. The low solar activity case corresponds to the T40 flyby (January 5, 2008, $F_{10.7}$ = 79 sfu) and the high solar activity data corresponds to the T86 flyby (September 26, 2012, $F_{10.7}$ = 139.8 sfu). The soft X-ray and Extreme Ultraviolet (EUV) wavelength ranges are marked at the bottom of the plot.

2.2.2 Photoionization of Neutral Species

As the photon flux travels through the atmosphere (or the neutral coma), it is absorbed and attenuated by neutral species. The distance traveled by incident flux is various for different solar zenith angles. The solar zenith angle (SZA) is the angle between the direction of the Sun and the nadir line on the surface. At altitude z and solar zenith angle χ, for wavelength λ of the incident irradiance, the weakened solar flux can be calculated by the following equation (Cravens, 1997; Schunk and Nagy, 2009):

$$I(z,\lambda,\chi) = I_\infty(\lambda)\exp\left(-\int_\infty^z \sum_s n_s(z)\sigma_s^a(\lambda)\mathrm{d}r_\lambda\right) \qquad 2.3$$

where $I_\infty(\lambda)$ is the unattenuated flux at the top of the atmosphere, n_n is the neutral density of species s, σ_s^a is the wavelength-dependent absorption cross section of species s, and $\mathrm{d}r_\lambda$ is the change in distance along the path of the photon flux. In this equation the summation is over all available neutral species in the atmosphere or in the neutral coma, integrated from a large distance to the altitude of interest. The value of the integral is a quantity known as the optical depth, τ:

$$\tau = \int_\infty^z \sum_s n_s(z)\sigma_s^a(\lambda)\mathrm{d}r_\lambda \qquad 2.4$$

One can obtain a simplified expression for the optical depth by assuming the atmosphere is plane stratified and in hydrostatic equilibrium:

$$\tau = \sec(\chi)\sum_s n_s(z)\sigma_s^a(\lambda)H_s \qquad 2.5$$

where H_s is the atmospheric scale height, $H_s = K_bT/m_sg$. Therefore, the production rate of primary ion species I, at altitude z is given by:

$$P_I(z) = \sum_n n_n(z) \int_0^{\lambda_I} I_\lambda(z) \sigma_\lambda^i d\lambda \qquad 2.6$$

where λ_I is ionization threshold wavelength, I_λ is attenuated solar flux at altitude z, σ_λ^i is ionization cross section, and n_n is neutral density of at altitude z. The integral segment of equation 2.6 describes ionization frequency and is defined as the ionization rate per unit volume of neutral gas. Figure 2.2 shows photoion production rates for N_2^+ and CH_4^+ calculated by the formalism presented in this section. We calculated the ion production rates for SZA at 40° and $F_{10.7}$ index at 79 sfu.

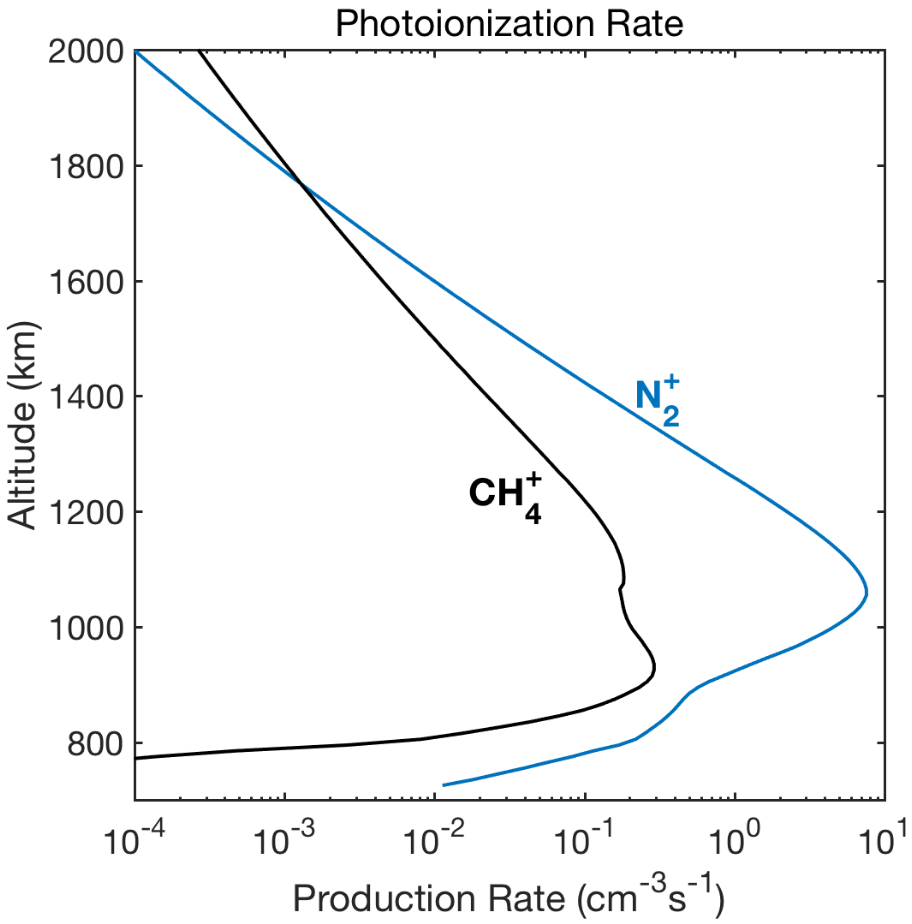

Figure 2.2 – Photoion production rates for N_2^+ (blue) and CH_4^+ (black) versus altitude. Results are for the T40 solar flux presented with blue dots in Figure 2.1. The SZA is 40º.

Photoionization production rates for N_2^+ and CH_4^+ (the two dominant neutral species) are calculated directly, using the photoionization and photoabsorption cross sections of N_2 and CH_4. These two neutral species produce N_2^+, N^+, CH_4^+, CH_3^+, CH_2^+, CH^+, and H^+ ions. However, other minor neutral species in the ionosphere interact with the solar photon flux and produce primary ion species. Cross sections of the minor neutral species are not well defined or documented. However, the primary ion production of these species can be estimated from the corresponding rate constant at optically thin regions of the ionosphere (i.e., vacuum environment) and scaled to other altitudes by an appropriate optical depth ratio. Rate constants for different minor neutral species are available in the literature (Keller et al., 1992).

For each photoion there exists a photoelectron. Therefore, photoelectron production at each altitude is the sum of ion productions of all neutral species. The next section reviews how electrons are transported in plasma.

2.2.3 Electron Transport in the Plasma

Photoelectrons, the byproduct of photoinization, contribute to primary ion production through electron-impact ionization. The photoelectrons or energetic solar wind and magnetospheric electrons with high enough energy (a few tens of eV and higher) collide with neutral species and produce an ion and a secondary electron pairs. For electrons with energies lower than the ionization threshold, the electron-impact may result in excitation of the target neutral species. Similarly, energetic secondary electrons can produce tertiary, quaternary, and more cascades of electrons. Through this process, hot electrons lose energy (become thermalized) and produce ions and lower energy electrons (cold electrons). To quantitatively calculate electron and ion production rates requires electron-neutral collision cross sections for each neutral species. Section 2.2.4 includes these cross sections.

As discussed earlier, electrons in the advanced MHD and hybrid models are treated as a charge neutralizing fluid. In other words, the codes do not take electron effects into account and only follow the ions. However, there is an increasing demand for studying details of electron behavior in space plasma.

In the vicinity of a magnetic field, charged particles gyrate around the field line with gyration radius that is a function of particle energy and field strength. The electron gyroradius is much smaller than that of ions, due to the electron’s much smaller mass. Therefore, the electron’s motion can be regarded as a flux of particles moving along the magnetic field. One can describe the electron transport along the magnetic field by using three commonly cited electron transport models:

1. The diffusion equation model.

2. Models based on two-stream or multistream approximation to the Boltzmann equation.

3. The Monte Carlo model of individual particle trajectory.

Generally, results of the three models are in good agreement under similar modeling criteria (Cicerone et al., 1973).

My models are based on the two-stream electron transport methodology. I present more details of this approach below. We start with deriving the evolution of particle distribution function in single species plasma. Particle position and velocity are denoted by $\mathbf{r}$ and $\mathbf{v}$, respectively. Particle distribution function is presented by $f(\mathbf{X}, t)$, where $\mathbf{X} = (\mathbf{r}, \mathbf{v})$ is a six-dimensional vector. Therefore, in nonrelativistic regime we have:

$$\dot{\mathbf{X}} = \mathbf{U} = (\mathbf{v}, \frac{\mathbf{F}}{m}) \qquad 2.7$$

The number of particles in an arbitrary volume V of the 6-D phase space is given by:

$$N = \int_{\mathrm{V}} f(\mathbf{X}, t) d^6\mathbf{X} \qquad 2.8$$

and the time evolution of the particle number:

$$\dot{N} = \int_{\mathrm{V}} \frac{\partial f}{\partial t} d^6\mathbf{X} \qquad 2.9$$

This quantity can also be calculated directly from the flow rate into the volume, through surface *S*:

$$\dot{N} = -\oint f(\mathbf{X})\mathbf{U}.\,dS = -\int_{\mathrm{V}} \nabla_{\mathbf{X}}\,.\left(\mathbf{U}f(\mathbf{X})\right)d^6\mathbf{X} \qquad 2.10$$

Equating the two equations for $\dot{N}$ gives this result:

$$\frac{\partial f}{\partial t} + \nabla_{\mathbf{X}}\,.\,(\mathbf{U}f) = 0 \qquad 2.11$$

Realizing that the Lorentz force is the only force in the plasma allows for expansion and further simplification of Equation 2.11. The expanded form of this equation is known as the Vlasov equation, given by the following (Nicholson, 1983):

$$\frac{\partial f}{\partial t} + \mathbf{v}.\nabla f + \frac{q}{m}(\mathbf{E} + \mathbf{v} \times \mathbf{B}).\frac{\partial f}{\partial \mathrm{v}} = 0 \qquad 2.12$$

where we used $\frac{\partial}{\partial \mathrm{v}}.(\mathbf{v} \times \mathbf{B}) = 0$, and $\nabla.\mathbf{v} = 0$. The Vlasov equation explains behavior of a collection of charged particles in a collisionless regime. For collisional plasma, $\frac{\delta f}{\delta t}$ must replace the right-hand side of the Equation 2.12 to reflect changes in electron distribution due to collisions. Hence, Equation 2.12 takes on a new name, the Boltzmann equation.

For ionospheric simulations, one can write the Boltzmann equation in terms of particle flux (Φ), particle energy (E), and distance along the magnetic field line (s) (Schunk and Nagy, 2009). We can assume steady-state conditions and neglect the presence of external electric fields or a diverging magnetic field. In this case, the Boltzmann equation simplifies to:

$$\frac{1}{\cos\alpha}\frac{\partial\Phi}{\partial s} = \sqrt{\frac{m}{2E}}\frac{\delta\Phi}{\delta t} \qquad 2.13$$

where α is the pitch angle, or the angle between particle velocity and the magnetic field line. Equation 2.13 enables us to divide the total flux into several equal angular components. For most planetary ionosphere applications, using two streams (up and down) for electron motion provides reasonably accurate results. For upward and downward fluxes we have the following:

$$\frac{d\Phi(\mathrm{E},\mathrm{s})^{+}}{ds} = -\frac{1}{< cos\theta >}\sum_{k} n_k[\sigma_a^k + \sigma_e^k p_e^k]\Phi^{+} + \frac{1}{< cos\theta >}\sum_{k} n_k \sigma_e^k p_e^k \Phi^{-} + \frac{q(E,z)}{2} + \frac{q^{+}}{< cos\theta >}$$

$$2.14$$

$$-\frac{d\Phi(\mathrm{E},\mathrm{s})^{-}}{ds} = -\frac{1}{< cos\theta >}\sum_{k} n_k[\sigma_a^k + \sigma_e^k p_e^k]\Phi^{-} + \frac{1}{< cos\theta >}\sum_{k} n_k \sigma_e^k p_e^k \Phi^{+} + \frac{q(E,z)}{2} + \frac{q^{-}}{< cos\theta >}$$

where the Φ^{-} and Φ^{+} are the flux toward and away from the obstacle (see Figure 2.3), *s* is distance along the field line, n_k is the density of the k^{th} neutral specie, θ is the pitch angle or the angle between direction of electron velocity and the magnetic field line ($< cos\theta >= \frac{1}{2}$ is assumed), σ_a^k and σ_e^k are electron-neutral inelastic and elastic collision cross sections, and p_e^k is backscattering probability for elastic collision, q is primary photoelectron production due to photoionization (results of the photoionization code) and $q^{\mp}$ is electron production rate from ionization by higher energy electrons.

Solar wind or magnetospheric magnetic field lines drape around obstacles (e.g., comet

67P/CG or Titan). A parabola can approximately present such a structure. Figure 2.3 shows typical modeled magnetic field geometry. The obstacle is at the center (parabola's focus), the Sun is to the right, and the parabola is symmetric around Y=0. The vertex is at 10 km for this case, but it can be modified to show more or less draping. The two-stream model only uses half of the parabola (either blue or red segments) to follow the electrons along the field line. The radial distance of points on the field is used to calculate the neutral densities; however, two-stream equations solve electron fluxes as a function of distance (*s*) from the vertex.

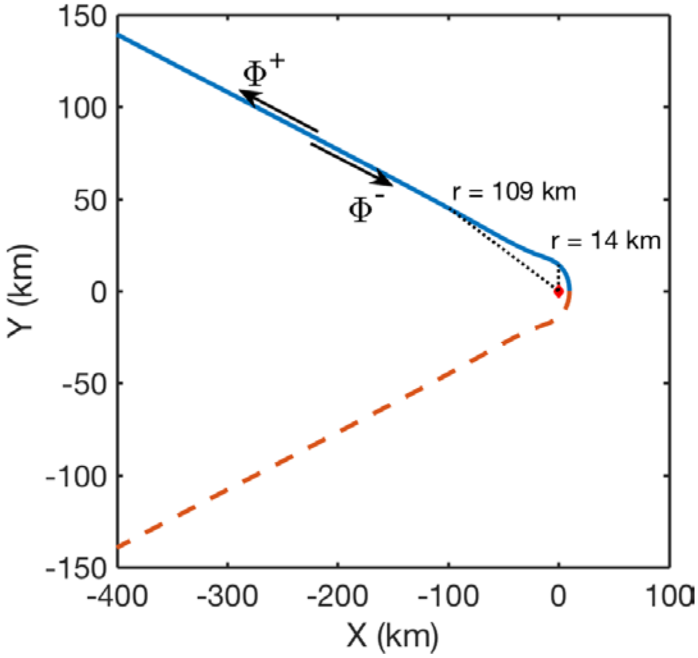

Figure 2.3 – Typical magnetic field geometry used in the two-stream electron transport model. The obstacle is at the origin (or parabola's focus) and the Sun is to the right. The full extent of a parabola is shown with the symmetry axis around Y=0 line. Upward and downward electron fluxes are shown with Φ^+ and Φ^-, respectively.

The advantage of simplifying the electron transport with the two-stream technique is that it is computationally fast and gives reasonable estimates of electron flux. The disadvantages of this approach are loss of information about electron trajectory and details of pitch angle distribution, and the ability to model only energy loss processes.

Two-stream equations are solved for each energy bin, starting with the highest energy. After each inelastic collision, the fraction of electrons cascading to lower energies are stored accordingly. This process is repeated for all altitudes at the current energy loop. The model then solves the two-stream equations for the next energy with knowledge of additional fluxes from previous energy bins. We design the energy grid structure to enable discretization of the equations. Bin widths can vary depending on variation levels of other energy dependent parameters (e.g., cross sections, photon flux).

We also consider electron-electron Coulomb collision, which plays an important role in thermalizing the suprathermal electrons. For this process to be efficient, a population of cold thermal electrons must be present. Otherwise, thermalizing the suprathermal electrons with other suprathermal electrons would be very inefficient. Therefore, an artificial background thermal population of cold electrons (E<<1 eV) is brought into the model. Knowledge of the abundance of cold electron population is achieved in two ways:

1. Through measurements made by plasma instruments. The Langmuir Probe is the instrument that measures the plasma's bulk density by measuring the currents in a probe at different biased voltages. Chapter 3 provides more detail on the plasma instruments.

2. By assuming a cold fully ionized neutral atmosphere. In the absence of in-situ measurements, thermal electron population is determined by calculating the equilibrium density of the cold electrons at a constant temperature (100 K):

$$n_{e_{cold}} = \sqrt{\frac{P_e}{L_e}} \qquad 2.15$$

where P_e and L_e are electron production and loss rates, respectively, calculated by:

$$P_e = f_{ion} n_n$$

$$L_e = \alpha \left(\frac{300}{T}\right)^{\beta} \tag{2.16}$$

f_{ion} is the ionization frequency due to photoionization and needs scaling for heliocentric distance. In equation 2.16, n_n is the neutral density, α is the electron recombination coefficient, β is the temperature dependence parameter, and T is the electron temperature. Appendix A.2 lists α and β values for various ion species at Titan.

By calculating electron flux at each energy step and each altitude, one can augment new ion production rates from electron-impact ionization by multiplying electron flux by the neutral densities and corresponding cross sections. Figure 2.4 shows results of the two-stream model for electron-impact ion production for N_2^+ and CH_4^+. Primary suprathermal electrons are from photoionization rates presented in Figure 2.2. No boundary flux was included for these runs.

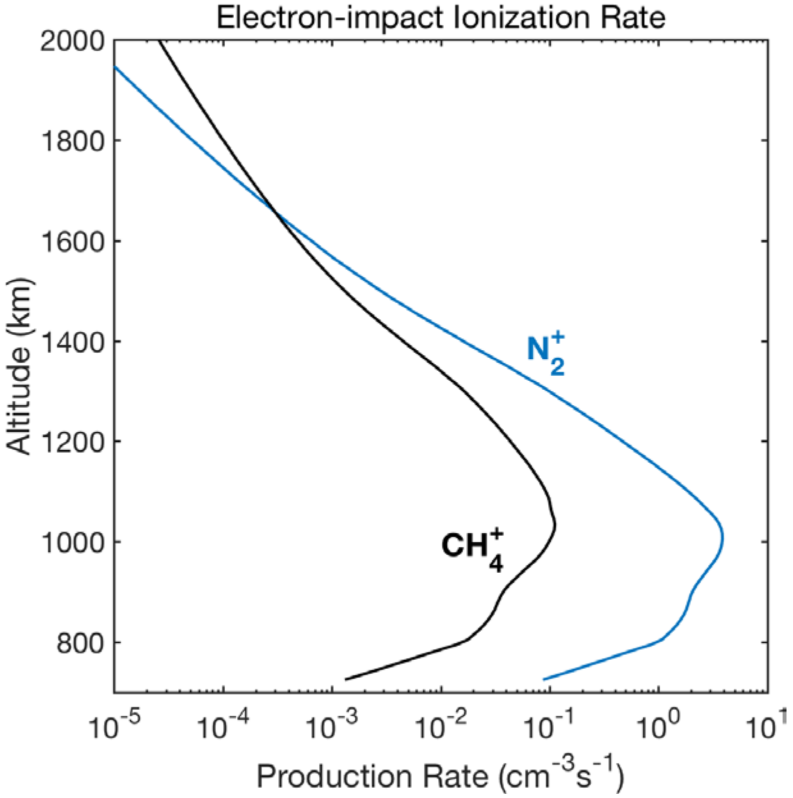

Figure 2.4 – Electron-impact ion production rates for N_2^+ (blue) and CH_4^+ (black) versus altitude.

Incident external plasma, such as solar wind or magnetospheric electrons, is implemented in the model in the form of a downward flux at the highest altitude (i.e., upper boundary condition). At Titan, the contribution of the precipitating magnetospheric electrons to the total ion production is generally less than 15%.

Therefore, total ion production at each altitude is the sum of photon and electron-impact ionization in all energies. Figure 2.5 shows modeled N_2^+ production rate profiles (in $cm^{-3}s^{-1}$) which include photoionization and electron-impact ionization rates. The models simulate different SZA and solar activities, as each panel on the figure indicates. The two-stream model includes a boundary flux in the form of bimodal magnetospheric electrons (see Figure 1.14).

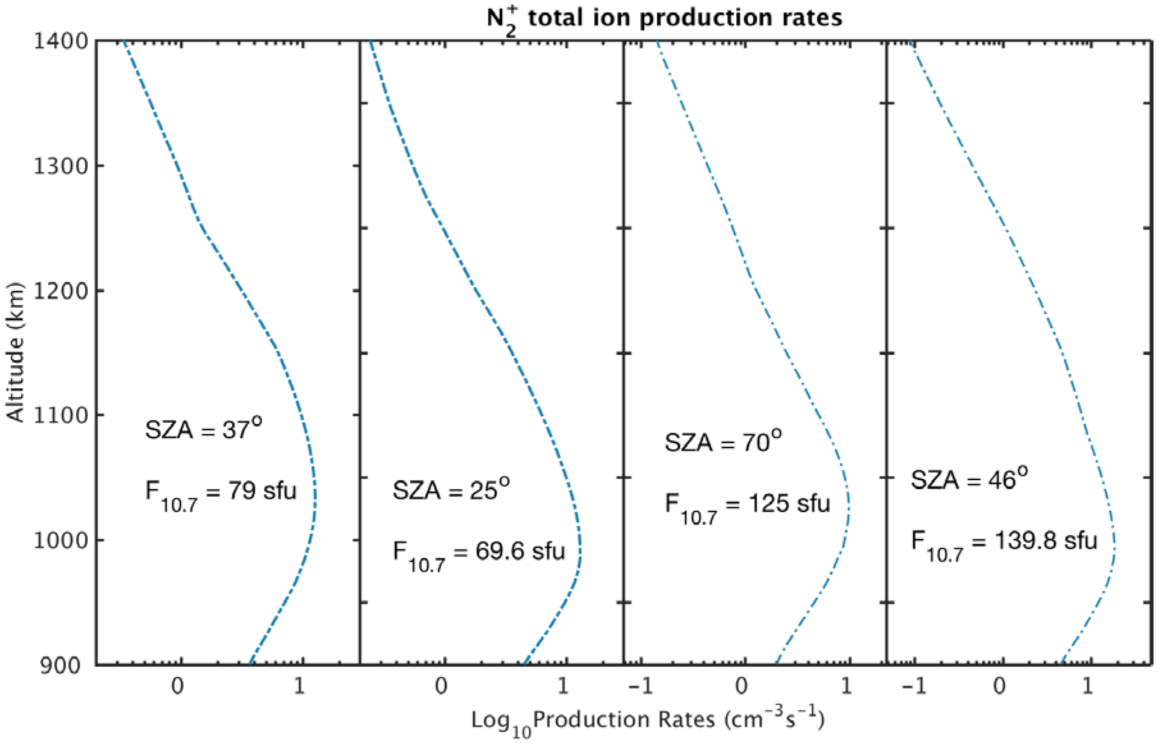

Figure 2.5 - Shows modeled N_2^+ ion production rate profiles for four different configurations of solar zenith angle (SZA) and solar activity.

2.2.4 Cross-Sections

As discussed in the previous sections, the collision cross sections are important to accurately calculating electron and ion production rates. In this section, I present photoabsorption, photoinization, and electron-impact ionization data used in my models. These cross sections were compiled in earlier studies (Gallagher et al., 1988; Gan et al., 1992; Richard, 2013). At Titan, nitrogen and methane provide the majority of the primary ion production, so these are the only species presented here.

Figure 2.6 shows photoabsorption cross sections of N_2 and CH_4 in units of cm^{-2} as a function of the wavelength of the incident photon in nanometers (nm). Blue data points show N_2 cross sections and red circles show CH_4. To avoid clutter on the graph, CH_4 cross section values are reduced by a factor of 10.

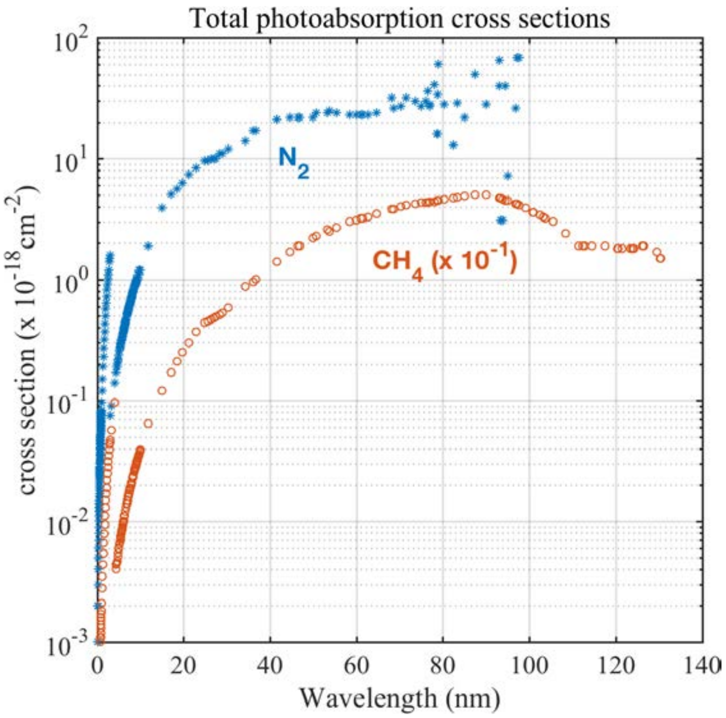

Figure 2.6 - Photoabsorption cross sections of N_2 and CH_4 as a function of the incident photon wavelength in nm. CH_4 cross section values (red circles) are reduced by a factor of 10 to avoid clutter on the graph. The ordinate is in units of 10^{-18} cm^{-2}.

After ionization, each neutral molecule may end up at a number of possible ion final states determined by fractional probability of that state and the energy of the incident photon. Figure 2.7 presents total photoionization cross sections summed over all possible final states. Equation 2.6 uses these data to calculate the photoion production rates. Energy of the photoelectron at each collision can be determined by subtracting the selected final state ionization potential from the photon energy.

Figure 2.8 provides the cross sections for the electron-impact ionization process. Similar to photoionization, fractional probability of the ion final states are required for determining the energy of the secondary electrons.

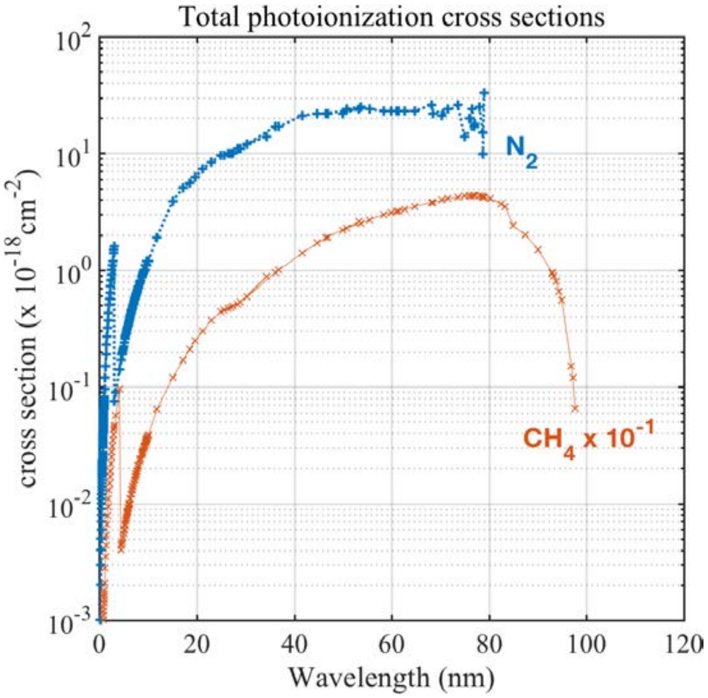

Figure 2.7 - Total photoionization cross sections of N_2 and CH_4 as a function of the incident photon wavelength in nm. The CH_4 cross section values (red circles) are reduced by a factor of 10 to avoid clutter on the graph. The ordinate is in units of 10^{-18} cm^{-2}.

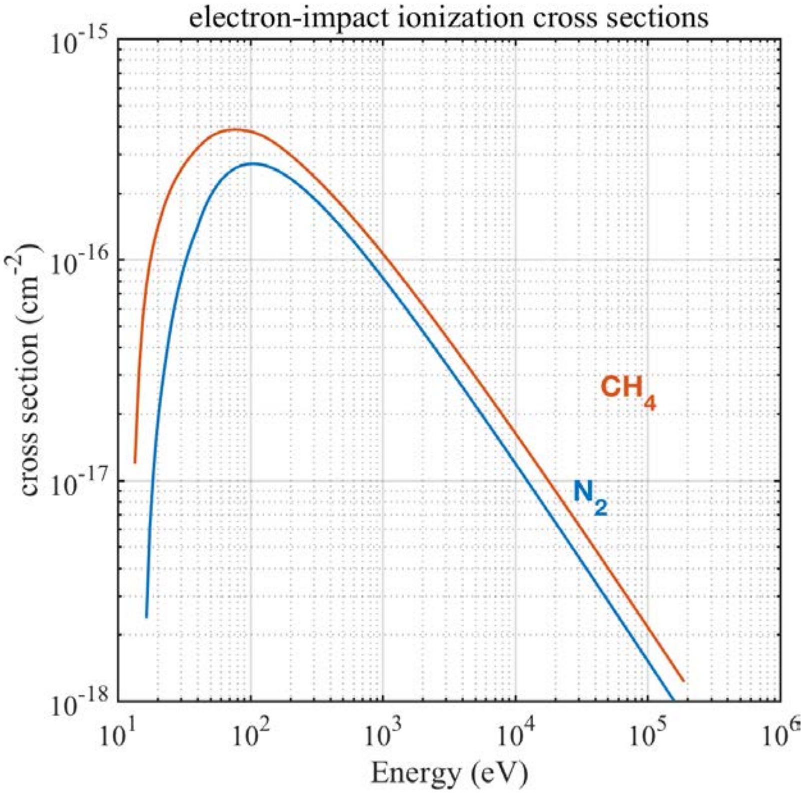

Figure 2.8 - Electron-impact ionization cross sections of N_2 and CH_4 as a function of incident electron energy in eV. The ordinate is in units of cm^{-2}. Cross sections for N_2 and CH_4 are presented by blue and red curves, respectively.

For certain populations of suprathermal electrons, collision with the neutral species can be elastic. This represents no loss of energy. Electrons may change direction after the collision, based on certain backscattering probability. Figure 2.9 illustrates electron-neutral elastic collision cross section for CH_4 and N_2 peaks at around 10 eV and 2 eV, respectively, for incident electron energy.

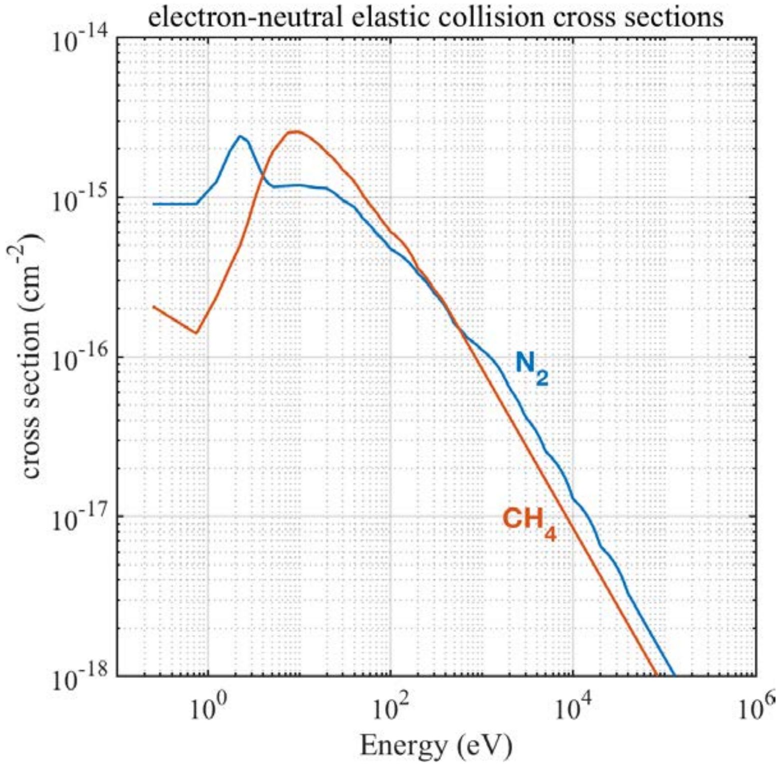

Figure 2.9 - Electron-neutral elastic collision cross sections of N_2 and CH_4 as a function of incident electron energy in eV. The ordinate is in units of cm^{-2}. Cross sections for N_2 and CH_4 are presented by blue and red curves, respectively.

2.2.5 Photochemical Model

Knowledge of Titan's main atmospheric constituents and primary ion productions allows formation of many chains of ion-neutral chemistry. Equation set 2.17 shows several initial chemical reactions in Titan's ionosphere.

$$
\begin{aligned}
&N_2^+ + H_2 \rightarrow HN_2^+ + H && k = 2.0 \times 10^{-9}\ cm^3/s \\
&N_2^+ + CH_4 \rightarrow CH_3^+ + N_2 + H && k = 1.04 \times 10^{-9}\ cm^3/s \\
&CH_3^+ + CH_4 \rightarrow C_2H_5^+ + H_2 && k = 1.1 \times 10^{-9}\ cm^3/s \\
&C_2H_5^+ + HCN \rightarrow HCNH^+ + C_2H_4 && k = 5.0 \times 10^{-9}\ cm^3/s \\
&CH_4^+ + HCN \rightarrow HCNH^+ + CH_3 && k = 3.23 \times 10^{-9}\ cm^3/s \\
&N_2H^+ + HCN \rightarrow HCNH^+ + N_2 && k = 7.4 \times 10^{-10} cm^3/s \\
&HCNH^+ + \text{other neutral species} \rightarrow \text{higher mass ion species}
\end{aligned}
\qquad 2.17
$$

Measurements of reaction rates for available ion and neutral species and ideal conditions takes place in a lab. Quantum chemistry analysis of the reaction is another way of deriving the reaction rate constants. However, for some reactions no reaction rate is available from either of these methods. For those reactions, comprehensive ion-neutral chemistry models give estimates of the range of reasonable rate constants, so that the whole chemistry model convergence on various ion densities and a photochemical equilibrium is reachable.

Photochemical equilibrium is a state in which production rate for each ion equals the loss rate. The model must solve a continuity equation for each ion species and neutral species, if one wants to consider neutral-neutral reactions. Neutral-neutral reactions are important in lower levels of the atmosphere for the formation of haze layer and heavy hydrocarbons that precipitate on the surface. We are interested in the ionospheric chemical composition and our chemistry model omits neutral-neutral reactions. For ion species i, the continuity equation is define by:

$$\frac{dn_i}{dt} = P_i - L_i \qquad 2.18$$

In this equation, n_i is the ion's number density and P_i and L_i are total production and loss rates, respectively. The right-hand side of this equation is the net production, P_{net}. In photochemical equilibrium$P_{net} \approx 0$. The model must satisfy the photochemical equilibrium condition for all ion species in a self-consistent manner. The Newton-Raphson numerical technique allows for solving the continuity equation for all ions concurrently (Press et al., 2007). In this technique, Equation 2.18 is solved for each ion and ion densities, production and loss rates are updated before the next iteration. The number of iterations and the tolerance limit are defined by the user. Tolerance limit determines how much net production from all ions can deviate from zero (i.e., absolute equilibrium). Appendix A.1 provides a list of ion-neutral reaction rate constants used in our model. The rate constants have been compiled from several studies based on lab measurement, analytical calculations, as well as data from the UMIST astrochemistry database (Anicich, 2003; McEwan and Anicich, 2007; Vuitton et al., 2006; Vuitton et al., 2007). Figure 2.10 illustrates a snapshot of the complex chemistry in Titan's ionosphere.

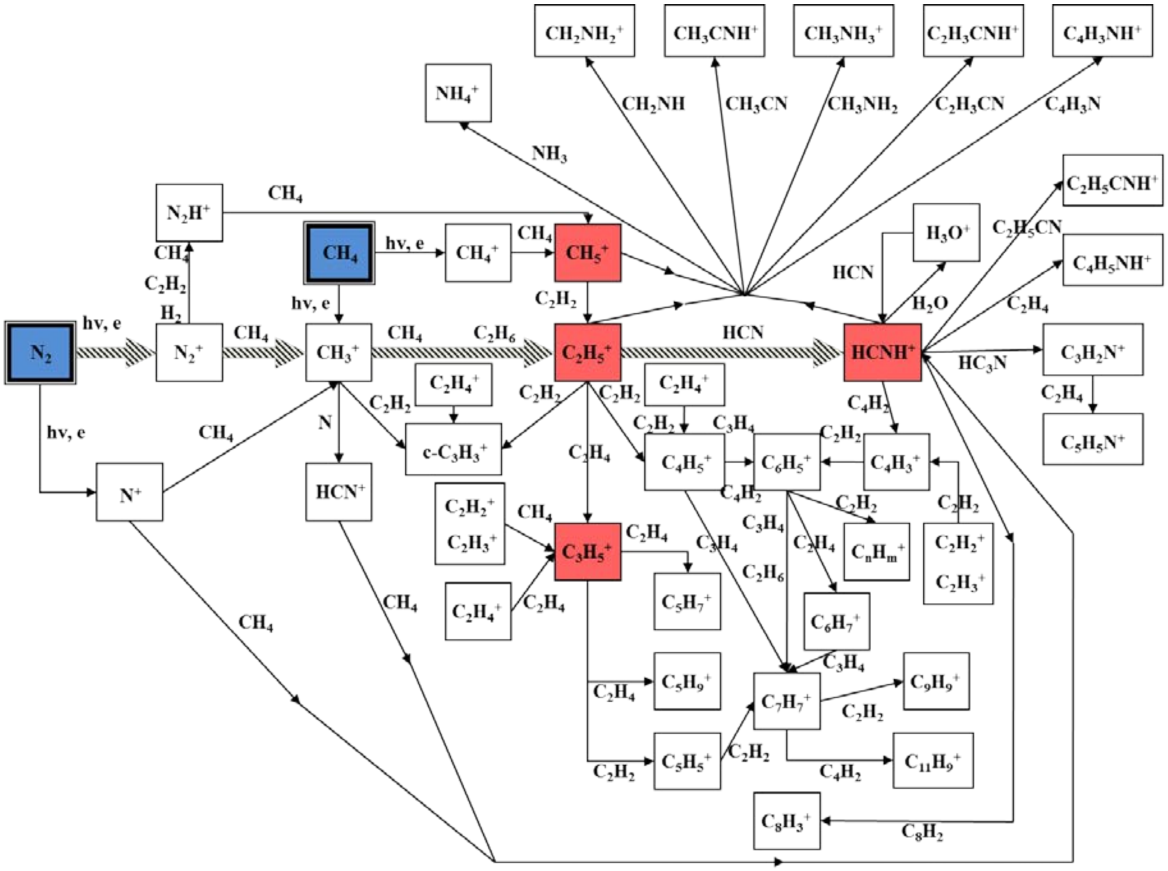

Figure 2.10 - Snapshot of some ion-neutral chemical reactions in the Titan's ionosphere. Blue boxes represent the two most abundant neutral species. Red boxes represent the most abundant ion species. This snapshot tends to show only the strongest reaction links. Many other chemical reactions, hydrocarbons, and electron dissociative recombination are not shown. The image is adapted from Richard et al. (2015).

The minor neutral species play important roles in the chemistry of heavy ion species in the ionosphere. Combined ion-neutral chemistry models have provided estimates of these neutral species (Bell et al., 2010; Keller et al., 1998; Krasnopolsky, 2009; Krasnopolsky, 2014; Muller-Wodarg et al., 2003; Toublanc et al., 1995). These models strive to obtain reasonable ionospheric densities by adjusting the mixing ratio of minor neutral species and the estimated reaction rates. Therefore, the resultant ionospheric densities can be highly sensitive to certain chemical reactions and neutral mixing ratios. Densities of some minor neutral species can be derived directly from measurements (Cui et al., 2009; Magee et al., 2009; Waite et al., 2005;

Waite et al., 2007). Our model uses the INMS derived mixing ratios at select altitude as an anchor point to scale the modeled mixing ratio profiles by Krasnopolsky (2009). Table 2.2 summarizes neutral mixing ratios of different neutral species used in the current study and previous research.

Table 2.2 - Mixing ratio of minor neutral species from various studies.

	This study 1065 km	Richard 2015 1065 km[1]	Robertson 2009 1100 km[2]	Vuitton 2007 1100 km[3]	Westlake 2012 1050 km[4]	Magee 2009 1050 km[5]
H_2	2.8×10^{-3}	3.7×10^{-3}	6.1×10^{-3}	4.0×10^{-3}	-	$(3.38\pm0.23)\times10^{-3}$
C_2H_2	1.05×10^{-3}	3.5×10^{-4}	4.6×10^{-4}	2.8×10^{-4}	3.42×10^{-4}	$(3.42\pm0.14)\times10^{-4}$
C_2H_4	8.0×10^{-4}	4.0×10^{-4}	2.4×10^{-4}	1.0×10^{-3}	3.91×10^{-4}	$(3.91\pm0.16)\times10^{-4}$
HCN	4.9×10^{-4}	2.48×10^{-4}	6.04×10^{-4}	2.0×10^{-4}	2.44×10^{-4}	$(2.44\pm0.10)\times10^{-4}$
C_2H_6	2.5×10^{-5}	4.47×10^{-5}	0.29×10^{-4}	1.2×10^{-4}	-	$(4.75\pm0.74)\times10^{-5}$
H_2O	2.6×10^{-7}	3.2×10^{-6}	0.29×10^{-6}	$< 0.3\times10^{-6}$	-	-
NH_3	2.4×10^{-7}	4.92×10^{-5}	-	6.7×10^{-6}	3.0×10^{-7}	-
CH_2NH	1.2×10^{-6}	9.5×10^{-6}	10.2×10^{-6}	1.0×10^{-5}	1.5×10^{-6}	-
HC_5N	7.0×10^{-7}	2.1×10^{-6}	-	1.0×10^{-6}	-	-

[1](Richard et al., 2015b), [2](Robertson et al., 2009), [3](Vuitton et al., 2007), [4](Westlake et al., 2012), [5](Magee et al., 2009)

Figure 2.11 shows modeled density profiles for the major ionospheric species CH_3^+, CH_5^+, $HCNH^+$, $C_2H_5^+$, and $C_3H_5^+$. Densities are modeled for four select Titan flybys T40 (black), T48 (blue), T83 (green), and T86 (red). The first panel from the left shows CH_3^+ density profiles. More than 90% of the CH_3^+ density comes from the reaction of N_2^+ with CH_4. Since CH_4 is an abundant neutral species, CH_3^+ production rate is nearly equal to N_2^+ production rate. The second panel from the left shows CH_5^+ ion density profiles, for which the majority of production (about

88%) is from the reaction of the N_2H^+ ion and CH_4. The loss of CH_5^+ ion species takes place mainly through reactions with minor neutral species and electron dissociative recombination. The third panel from the left shows $HCNH^+$, the most abundant ion species in the ionosphere. The reaction of minor neutral HCN with several ion species makes up the bulk production of the $HCNH^+$. The density profiles of $C_2H_5^+$ appear in the fourth panel from the left. The majority of the CH_3^+ density is consumed through its reaction with methane to produce more than 85% of the $C_2H_5^+$ density. This reaction is also the largest loss process for the CH_3^+ ion species. The $C_2H_5^+$ is the second most abundant ion species in the ionosphere. The first panel from the right in Figure 2.11 shows $C_3H_5^+$ density profiles. This ion is lost mainly through electron dissociative recombination. Dissociative recombination is the main loss mechanism for most of the heavy ion species.

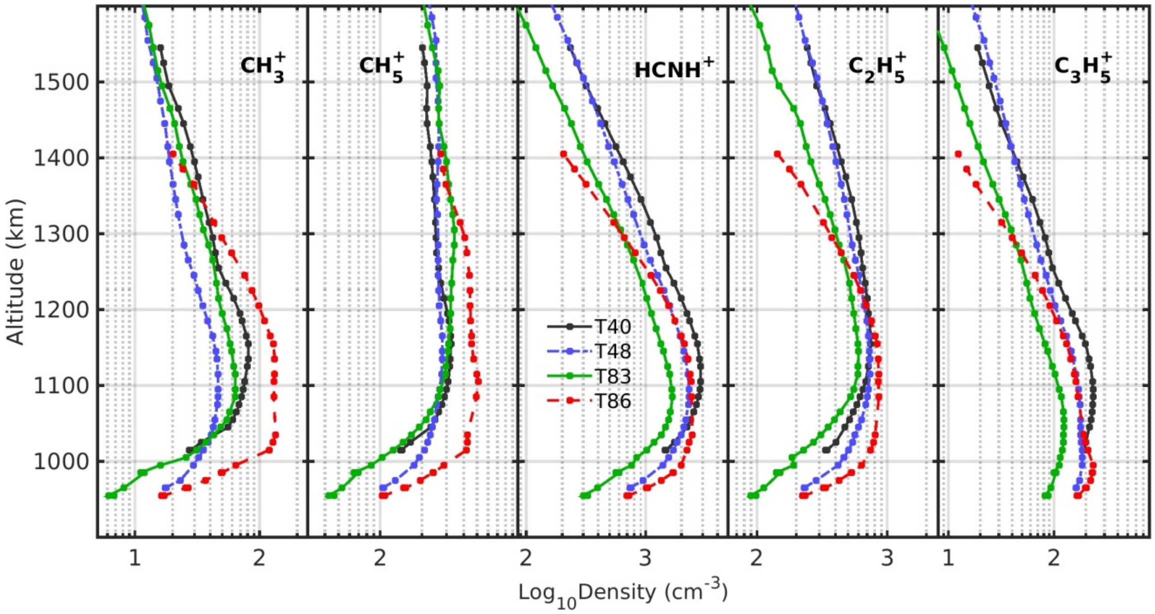

Figure 2.11 - Density profiles for several major ion species in the Titan's ionosphere.

We revisit this figure in chapter 3, where I discuss the Cassini spacecraft measurements and compare the model results with in-situ measurements under different ionospheric conditions.

We analyzed the mixing ratio of minor neutral species and sought to identify reaction paths that play more important roles in production of ionospheric species and illustrate the outstanding model-observation discrepancy. Our priority was $HCNH^+$, which is overestimated in the models. Figure 2.12 illustrates ion densities in mass range 10-99 atomic mass units (amu or Dalton) at 1065 km. Green bars represent the INMS densities from the T40 flyby and are included for comparisons as we make changes to the chemistry model. Modeled densities are based on major neutral species measurements during T40 flyby. Minor neutral mixing ratios in this figure, are similar to values in the first column of Table 2.2. In several ion masses, observation and model densities differ significantly.

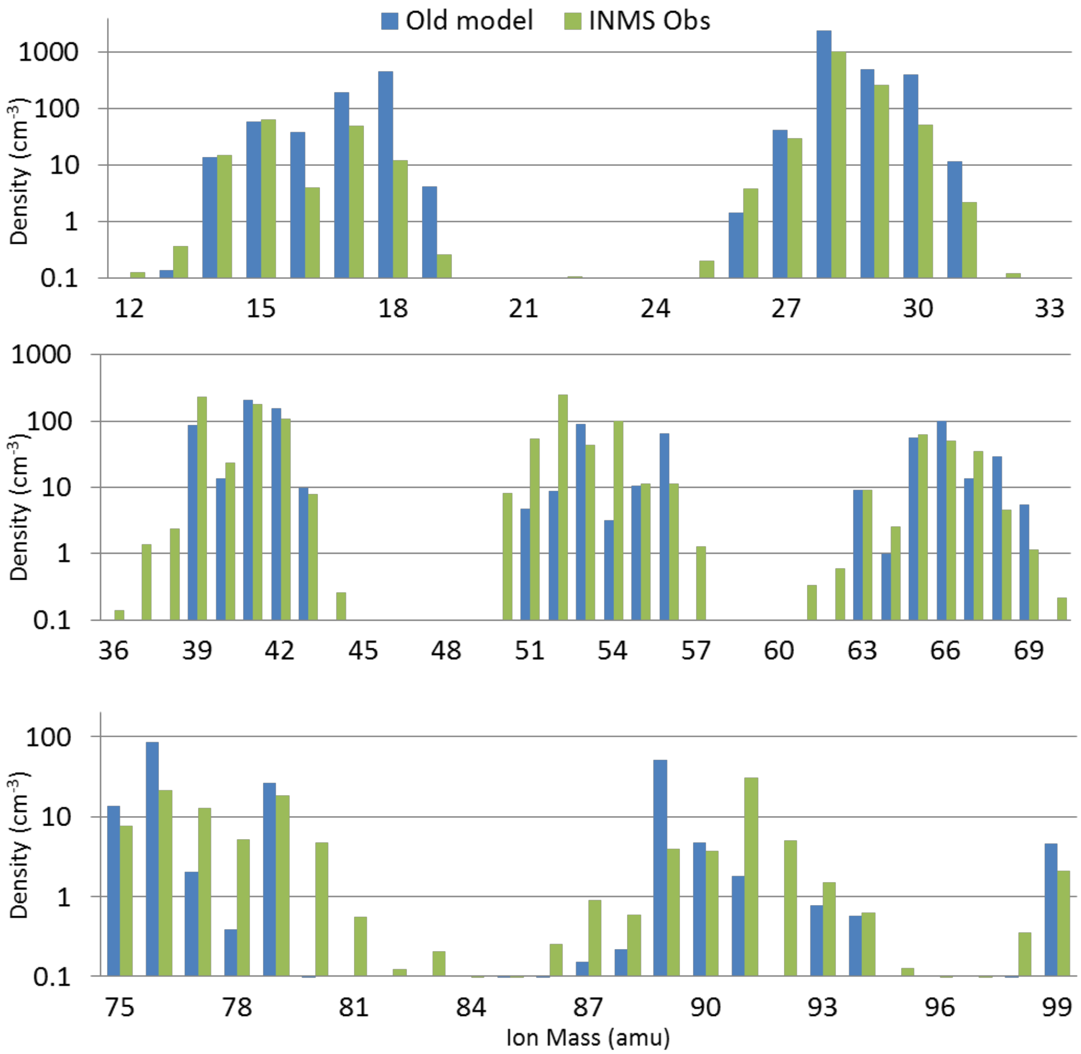

Figure 2.12 – INMS-measured and modeled ion densities for ion mass range 10-99 amu at 1065 km. Green bars represent INMS densities and are included for comparison purposes. Blue bars represent modeled densities. Mixing ratios for this model run are based on values in Table 2.2.

Next, we changed the current minor neutral mixing ratios according to correction factors in Table 2.3 and included several new reactions to leverage high density of $HCNH^+$ ion in the model. Equation set 2.19 lists these reactions. Notably, while all these reactions are exothermic, their feasibility under Titan's ionospheric conditions remains a topic of debate (Westlake et al., 2012). We also reduced the abundance of ammonia significantly in an effort to achieve a better agreement for mass channel 18. Ammonia is also the main loss term for $HCNH^+$. To compensate for the lower NH_3 mixing ratio, we increased the mixing ratio of neutral species involved in the reactions in equation set 2.19. Figure 2.13 shows the new ionospheric composition.

Table 2.3 - Change in mixing ratio

species	mixing ratio	correction factor
H_2	2.8×10^{-3}	0.75
C_2H_2	1.05×10^{-3}	3
C_2H_4	8.0×10^{-4}	2
HCN	4.9×10^{-4}	2
C_2H_6	2.5×10^{-5}	0.5
H_2O	2.6×10^{-7}	0.08
NH_3	2.4×10^{-7}	0.01
CH_2NH	1.2×10^{-6}	0.125
HC_5N	7.0×10^{-7}	0.125

$$\begin{aligned} &HCNH^{+} + H_2 \rightarrow CH_2NH_2^{+} && k = 1.0\times10^{-12}\ cm^3/s \\ &HCNH^{+} + C_2H_2 \rightarrow HC_3NH^{+} && k = 5.0\times10^{-10}\ cm^3/s \\ &HCNH^{+} + C_2H_4 \rightarrow C_3H_3NH^{+} && k = 5.0\times10^{-11}\ cm^3/s \end{aligned} \qquad 2.19$$

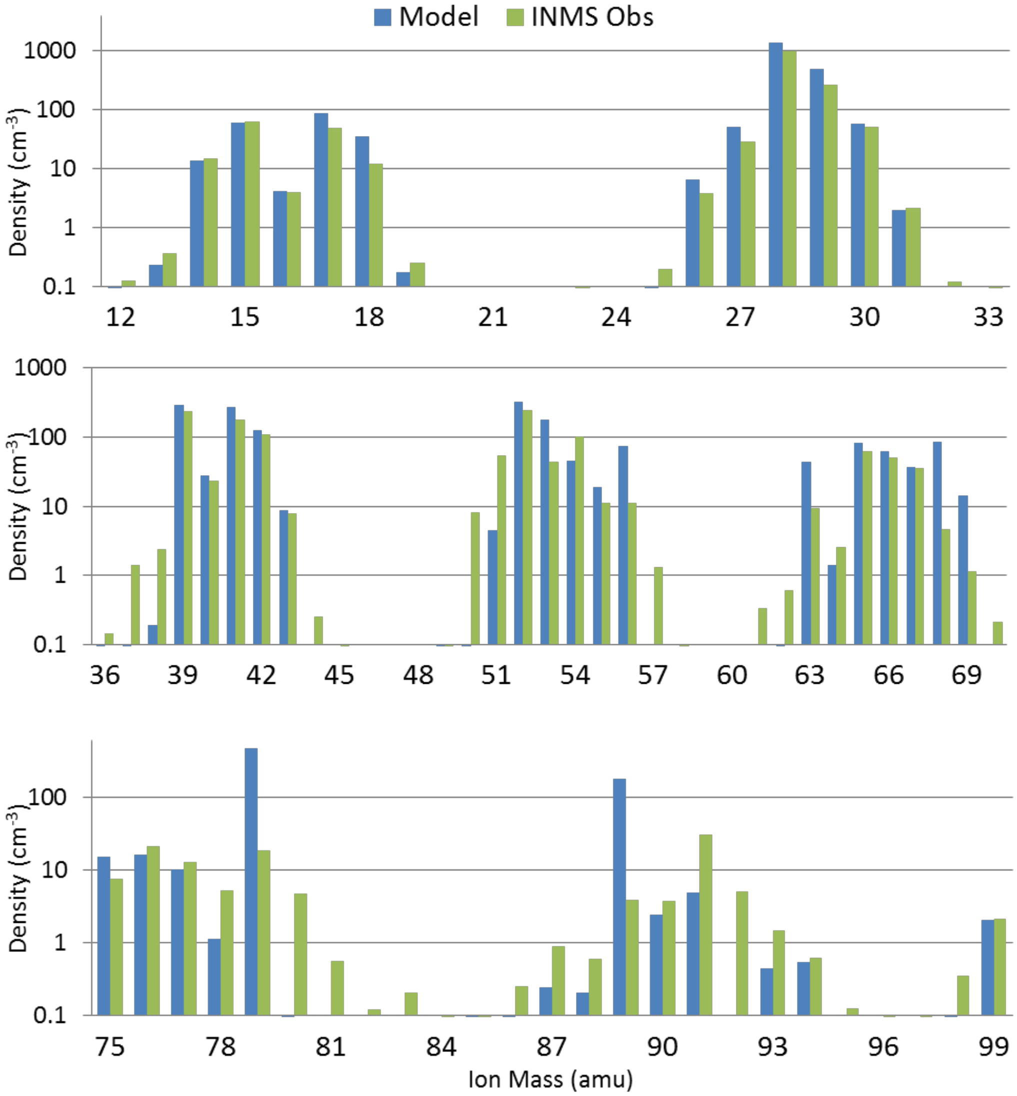

Figure 2.13 – Similar to Figure 2.12 but after including the changes in mixing ratios as listed in Table 2.3 and adding new reaction shown in 2.19. The INMS densities are shown with blue bars and modeled densities are in green.

The chemistry seems to improve agreement between model and observation, especially for ion masses between 10 to 35 amu. However, some heavy ion species in the model now differ markedly from the INMS observations. In other words, the problem is shifted from low mass ions to heavier ions. One may address the high density of some heavy ion species by improving electron dissociative recombination rates, which are now well known at present.

2.3 Ion Transport

To this point, our assumption in the photochemical model has been that, upon creation, the ion species remain stationary. This assumption is completely valid at low altitude and near the peak of the ionosphere, where the chemistry controls ionospheric properties. At lower altitudes in most planetary ionospheres, ion–neutral collisions and high neutral densities limit flow of plasma so that chemistry dominates the density structure. At high ionospheric altitudes, however, ion transport becomes increasingly significant. Only at high altitudes is transport time comparable or shorter than are the chemical lifetimes of some ion species. Previous studies show that ionospheric transport effects start to prevail over the chemistry at altitudes above 1400 km, which invalidates photochemical equilibrium assumption (Cravens et al., 2010; Ma et al., 2006).

2.3.1 Chemical versus Transport Lifetime

Ion chemical lifetime is proportional to the inverse of the ion loss rate, which consists of chemical loss from ion-neutral collisions and ion loss due to electron dissociative recombination. Dissociative recombination is the main loss process for heavy terminal ion species with long chemical lifetimes, while ion-neutral reactions control the chemical lifetimes of lower mass ions. By implication, when electron abundance in the ionosphere is high (dayside ionosphere), heavy terminal ion species have shorter lifetimes compared to those on the nightside. Figure 2.14 shows chemical lifetime profiles of several ion species, estimated from the photochemical model based on conditions (SZA, neutral densities, etc.) of the T40 flyby.

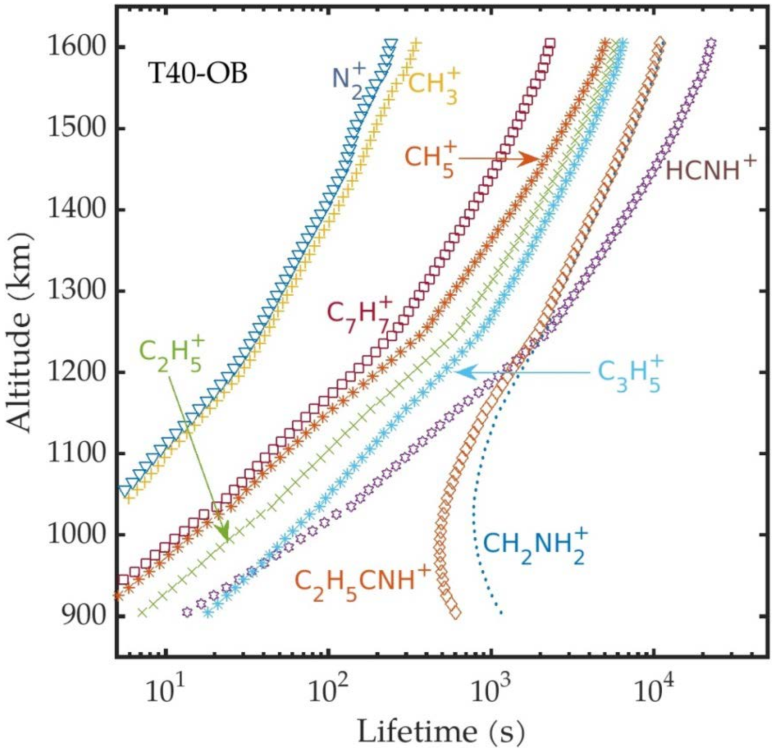

Figure 2.14 - Chemical lifetime profile of several ion species estimated by the photochemical model. The model is tuned to reflect conditions of the T40 flyby for SZA, neutral atmosphere, and solar flux.

Heavy terminal ion species such as HCNH$^+$, $CH_2NH_2^+$, $C_2H_5CNH^+$ have long chemical lifetimes (more than 3 hours at altitudes above 1400 km). These ions have longer lifetimes than do heavy mass (but still reactive) ion species such as $C_2H_5^+$ and $C_3H_5^+$. The highly chemically reactive ion species such as N_2^+ and CH_3^+ are controlled purely by the chemistry and have very short lifetimes. One exception to this pattern is the $C_7H_7^+$ ion species produced via two main reaction paths, the reactions between $C_6H_5^+$ with CH_4 (44%) and $C_5H_5^+$ with C_2H_2 (47%). This heavy ion shows unexpectedly short lifetimes (Figure 2.14). Understanding of loss processes for this ion and many other heavy terminal ion species of this type is lacking. Furthermore, knowledge of dependence of the electron dissociative recombination on electron temperature is unclear and requires more investigation.

As a first attempt, and to test the effective timescales and sensitivity of different ion species to the ion productions and chemistry, we monitored ion densities in the photochemical equilibrium model in time. Figure 2.15 shows densities of several ion species and electrons in time at 1105 km altitude. After reaching a stable ionosphere at around 1000 s, we reduced primary ion productions to 10% of initial values for 500 seconds. The primary ion species (e.g., N_2^+) reflect the immediate effects of this change, while ion species in the middle of the chemistry chain (such as CH_5^+, and $C_2H_5^+$) show an exponential drop and recovery. The heavier ion species with long chemical lifetimes at the end of the chemistry chain (such as $HCNH^+$ and electrons), which are produced after numerous reactions, exhibit modest, and slow changes in density. The model does not directly estimate electron densities. Instead, electrons are the sum of all the ion densities, which is a characteristic of quasi-neutral plasma. Since a significant portion of the ion population at equilibrium comes from heavier ion species, electrons represent the collective behavior of those ion species well.

Different ion species react differently to the transport because different ions have different chemical lifetimes. Light ions, with short chemical lifetimes (i.e., a few hundred seconds or less), show small-scale structure in their profiles. Long-lived ions (i.e., typically heavy ions) showed smooth unperturbed profile shapes.

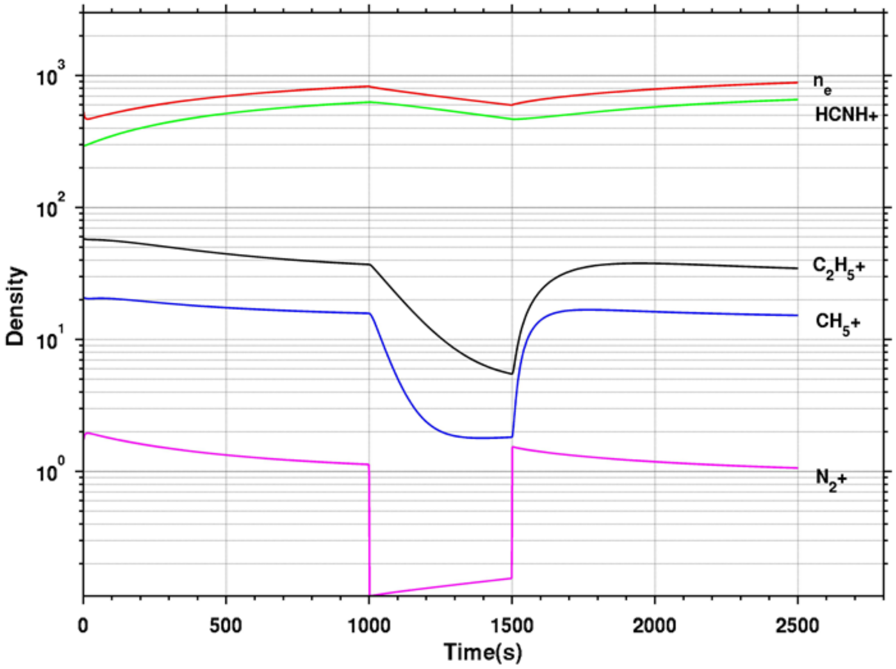

Figure 2.15 - Time series of the density of several ion species and electrons. Primary ion production was reduced to 10% of its initial value between 1000 and 1500 seconds. The terminal ion species $HCNH^+$ and electron densities show a modest drop during this time.

Ion transport time is defined as the time required by ions with a certain velocity to travel a certain length scale (e.g., atmospheric length scale). An ion parcel's velocity is determined from various forces acting on the parcel. Depending on Titan's position with respect to Saturn and the Sun, different pressure gradient forces can influence the ionosphere. Origins of these forces can be the magnetic pressure gradient from the impinging magnetosphere, thermal pressure gradient between dayside and nightside ionospheres, or neutral wind flows from lower atmospheric layers.

Determining these forces and their impacts, in the scale of the Titan-Saturn system is beyond the scope of this dissertation. However, several previous studies of plasma transport in Titan's ionosphere investigated the effects of magnetosphere interaction with Titan's ionosphere and estimated the ionospheric plasma velocities (Ledvina and Cravens, 1998; Ma et al., 2004;

Muller-Wodarg et al., 2008). These models aim mainly at simulating large scale interactions. Therefore, small scale phenomena such as ionospheric chemistry and collisions are kept at minimum. The degree to which such effects are accounted for depends on the available computation power.

Several other studies used Cassini measurements to estimate the Titan's ionospheric wind velocities empirically (Cravens et al., 2010; Cui et al., 2010). For example, Cravens et al. (2010) empirically estimated flow speeds using the magnetic field, electron densities, electron temperatures, and neutral density measurements. Figure 2.16 shows estimated horizontal and vertical flow velocities during the T5 flyby, along with results of MHD modeled flow velocities and estimates of magnetic and thermal pressure gradients.

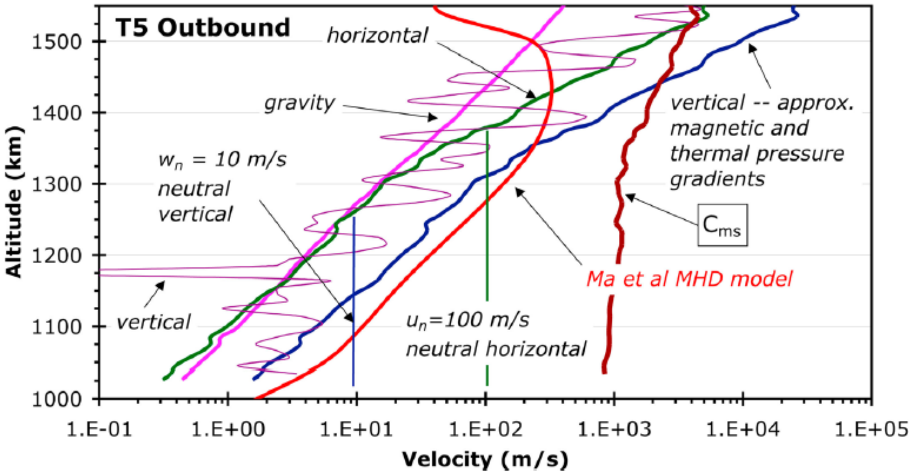

Figure 2.16 - Empirically estimated flow velocities during the T5 flyby. The green line shows the horizontal flow velocity profile used in the time-dependent ionosphere model, which the next section discusses. Taken from Cravens et al. (2010).

2.3.2 Time-Dependent Photochemical Model

Next, we simplify the transport problem by assuming there is no vertical transport and that flow takes place only horizontally and along fixed latitudes. Consequently, flow trajectories are on a spherical shell and SZA is the only varying atmospheric variable along the ion path, which leads to different ion production rates. Here, we derive a formalism to incorporate this process into the model we start with the continuity equation in the spherical coordinate system.

$$\frac{dn}{dt} = P_{net} \tag{2.20}$$

Or similarly:

$$\frac{\partial n}{\partial t} + u_\theta \frac{\partial n}{\partial s} + n\left[\frac{1}{r^2}\frac{\partial}{\partial r}(r^2 u_r) + \frac{1}{rsin\theta}\frac{\partial}{\partial \theta}(sin\theta u_\theta) + \frac{1}{rsin\theta}\frac{\partial u_\theta}{\partial \varphi}\right] = P_{net} \tag{2.21}$$

One can disregard the first term on the left-hand side of the equation due to steady state assumption for small scale perturbations. Based on the assumption we made earlier, the only nonzero ion velocity component is along $\hat{\theta}$ and the first and third terms in the bracket are zero because there is no vertical (i.e., along the radius) and zonal transport. Equation 2.22 can be rewritten as follows:

$$\frac{\partial n}{\partial t} = P_{net} - \frac{n u_\theta}{r\, tan\theta} \tag{2.22}$$

where we assumed $u_\theta$is constant and took advantage of $\partial t = \frac{\partial s}{u_\theta}$. The last term on the right-hand side of this equation shows divergence in u_θ that pressure gradient forces cause.

2.3.3 Changes in the Ionospheric Composition under Transport Effects

As an initial attempt to study the transport, we used the horizontal flow velocity profile presented in Figure 2.16. We ran the model for specific SZA and at select altitudes. The results for this run appear in Figure 2.17 for day-to-night (represented by purple squares) and night-to-day (represented by inverse blue triangles) flows. Note that ion velocities in Figure 2.16 are for day-to-night flows. Nonetheless, we tested feasibility of an inverse flow with the models to see the effects of night-to-day transport near the dusk and dawn regions. For comparisons, we over-plotted the global photochemical equilibrium at SZA=60º (black solid line) and the INMS densities (diamonds) in this figure. INMS densities are from various flybys, which had observations at the specified altitudes and occurred when the SZA at that altitude was 60 ± 5 degrees.

Figure 2.17 illustrates transport effects on CH_3^+ (left) and $C_3H_5^+$ (right). These two ions are good examples of short-lived and long-lived ion species.CH_3^+ densities show no significant change from photochemical equilibrium under transport, even at high altitudes where the ionospheric flow speed is about 2 km/s. From Figure 2.14 we learned that chemical lifetime of CH_3^+ at 1500 km is around 100 seconds. The transport velocity at this altitude is around 1500 m/s (Figure 2.17). Horizontal length scale along which, ion production rate undergoes significant change is simply the arc length of a circle segment with central angle of 30º. We assumed ion parcels move from SZA 60º to ~90º. At 1500 km from Titan's surface, the corresponding arc length is around 2000 km. Therefore, the ion transport time for this length scale is around 1300 s, much longer than the chemical lifetime. Chemistry will use up the CH_3^+ before any transport occurs. Fore $C_3H_5^+$ however, chemical lifetime is around 2000 s, comparable to the transport time. Therefore, transport is much more effective for this ion. Figure 2.17-right illustrates that at altitude 1400 km and above, $C_3H_5^+$ densities deviate from the photochemical equilibrium starting.

As the vertical green line on Figure 2.16 indicates, speeds are slower than 100 m/s at altitudes below 1400 km, which makes the transport effects barely noticeable. For small horizontal flow velocities on the order of a few meters per second, the transport effect is insignificant and chemical lifetimes of ions are much shorter than the transport time scale. Therefore, photochemistry controls ionospheric densities rather than transport.

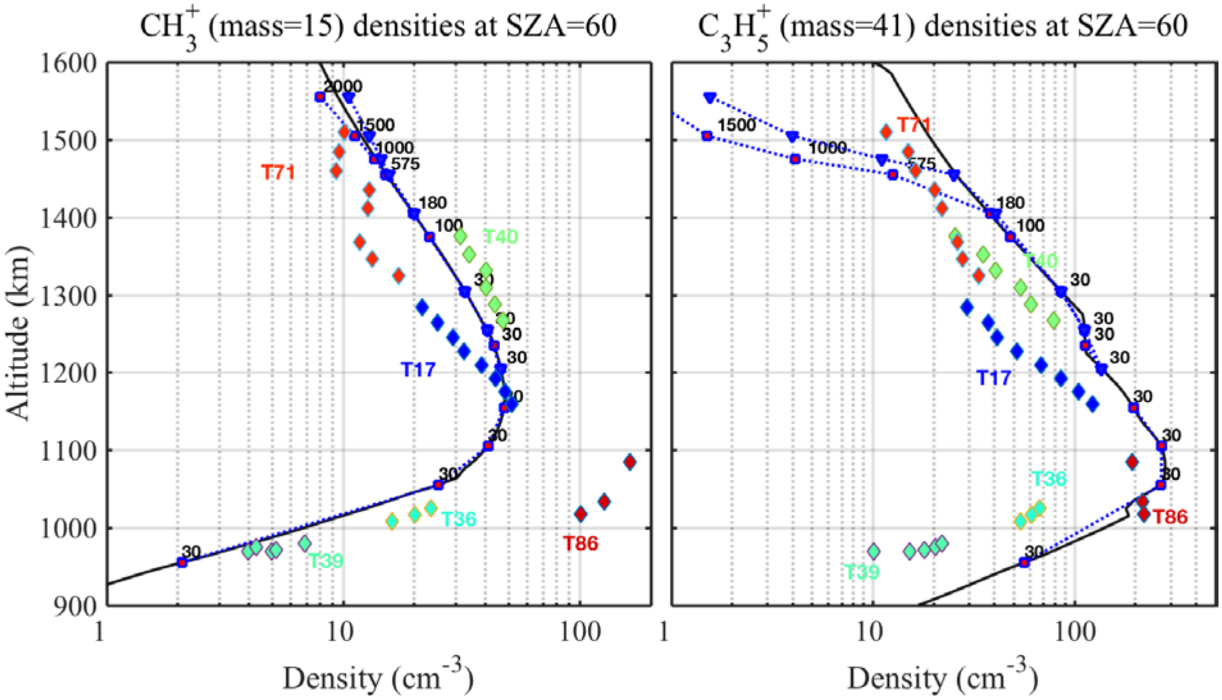

Figure 2.17 - Density profiles of short-lived ion species CH_3^+ (left) and long-lived ion species $C_3H_5^+$ (right) at 60° SZA. The purple boxes are day-to-night flow and the blue triangles are reversed flow. Velocities are indicated on each plot next to data point in m/s. The black solid curve is the photochemical equilibrium ion density output. Diamonds show the INMS measurements from multiple flybys, as colors indicate.

Next, we look at a wider range of SZAs and altitudes, and at how movement of the ion parcel around Titan affects density of each ion species. We compiled a lookup table for ion production rates at 35 different SZAs equally space from 0° to 120°, and 200 altitudes and used this table as an input to the time-dependent photochemical model. Figure 2.18 shows spectrograms of CH_5^+ density as a function of SZA and altitudes, with transport (left) and without transport at photochemical equilibrium (right). To create plots for the time-dependent (dynamic) model, we aggregated model results at 35 SZAs and at 10 altitude levels from 1000 to 1500 km. Horizontal flow velocities are the same as those we used in Figure 2.17. We created the spectrogram for photochemical equilibrium by running the photochemical model for a range of SZAs from 0º to 120º, with slightly lower SZA resolution for angles below 80º.

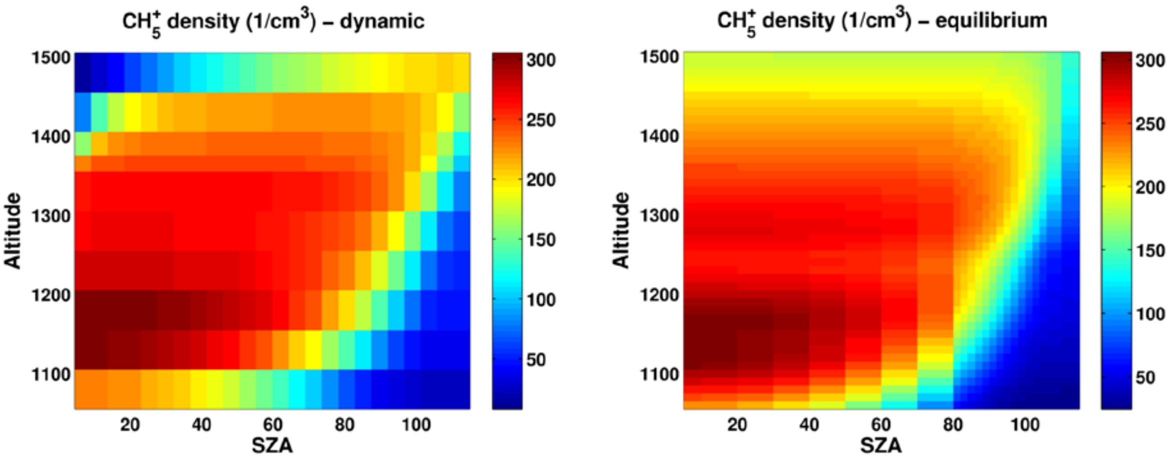

Figure 2.18 - (left) Density spectrogram of the CH_5^+ ion species with ion transport (i.e., dynamic), and (right) Density spectrogram of the CH_5^+ ion species in photochemical equilibrium. The dynamic plot is obtained from the time-dependent photochemical model which employs the horizontal transport regime presented in Figure 2.16.

Comparison of CH_5^+ density spectrograms in the dynamic mode with the equilibrium mode in Figure 2.18 suggests that the adopted transport regime does not affect the densities at low altitudes. However, at higher altitudes above 1400 km with faster flow speeds, there is a depletion of ion densities at low SZAs and these are shifted towards SZAs greater than 100°.

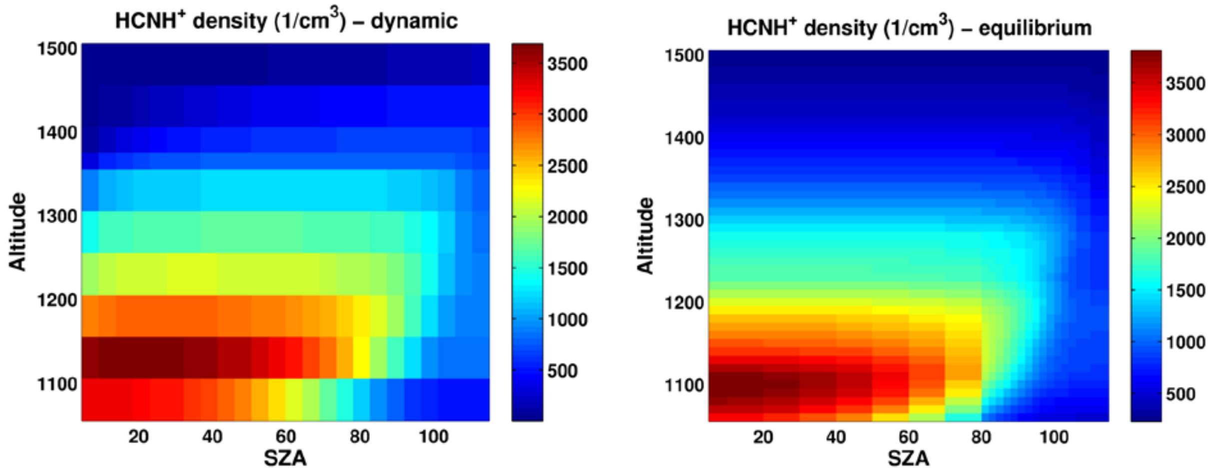

Figure 2.19 - Similar to Figure 2.18, except for $HCNH^+$ ion. The density of this terminal ion species shows no substantial changes.

For $HCNH^+$, transport did not have much effect on densities (Figure 2.19). At low altitudes, chemistry is dominant over transport effects. At high altitudes where transport speeds are noticeable, $HCNH^+$ densities are inherently small and show hardly any significant change.

2.4 Concluding Remarks

This chapter discusses the methodology for efficiently modeling a planetary ionosphere along with different components of the model for the Titan's ionosphere. I presented each segment of the model and explained how these contribute to simulating the ionosphere state under various circumstances. To put these components into perspective, Figure 2.20 provides a cross-linked diagram of the model's elements. The green circles to the left indicate that the input parameters are provided by instrument measurements.

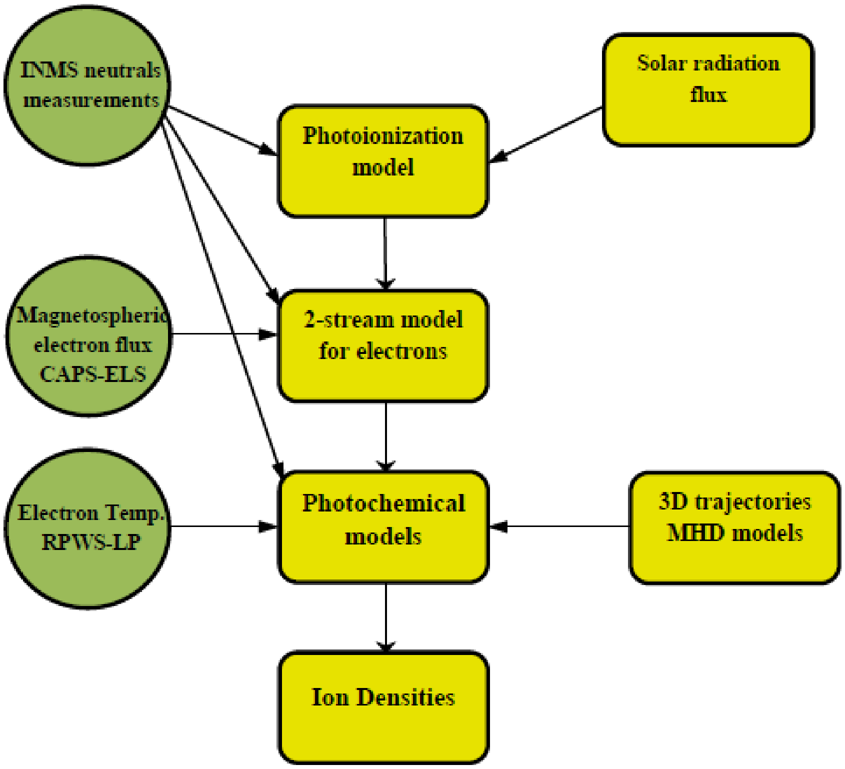

Figure 2.20 - Shows various components of the model discussed in this chapter. Connections between model segments show where they contribute.

My models are effective in predicting the ionospheric composition at Titan under various SZAs, solar flux, and atmospheric conditions. Most of the predicted ion densities are comparable to other modeling efforts. However, compared to in-situ measurements, the model in this chapter and other modeling efforts tend to overestimate certain ion densities (e.g., $HCNH^+$). This overestimation has been a long standing issue with Titan's ionosphere. In our attempt to address this issue, we modified the mixing ratio of minor neutral species and introduced new exothermic reactions that consume $HCNH^+$. The new model seemed to offer better model-data agreement for low mass ion species, while heavier ion densities became more deviant from INMS observations.

Ion transport certainly affects ion densities at high altitudes. Our simple one-dimensional transport model showed that the light ion species can actually be transported from the dayside to the nightside ionosphere.

3 Cassini Observations of Titan

The Cassini spacecraft arrived at Titan in 2004 during the declining phase of solar cycle 23 and has probed the moon's atmosphere during a quiet solar minimum into solar cycle 24. The mission has been extended twice since the end of its primary phase in June 2008. The instruments that are operational at each Titan flyby vary depending on scientific objectives of the flyby, position of the instrument on the spacecraft, geospatial properties of the flyby, and the limit of the data transfer bandwidth. This chapter presents the Cassini spacecraft observations of the ionospheric plasma densities for multiple flybys of Titan. The measurements span over 10 years which give us an opportunity to investigate the effects of the solar cycle on the ionosphere. The chapter's underlying goal is to investigate effects of the solar cycle on Titan's ionosphere.

3.1 Instruments Overview

3.1.1 The Ion and Neutral Mass Spectrometer (INMS)

The INMS instrument (Waite et al., 2004), which is emphasized in this chapter, can measure ionospheric and atmospheric constituents in three detection modes. These modes are: closed source neutrals (CSN), open source neutrals (OSN) and open source ions (OSI). In the neutral measuring modes, neutral species enter the instrument through the closed or open source inlets. Two electron guns inside the chamber ionize the neutral species and a set of electrostatic focusing lenses direct the ionized molecules into the quadrupole switching lenses. These lenses can switch between open and closed sources (depending on the detection mode) and electrostatically deflect and transmit the particles into a radiofrequency quadrupole mass analyzer. An unbiased voltage across the switching lenses can dramatically reduce ion transmission efficiency and measured densities (Mandt et al., 2012). The quadrupole mass analyzer diverts the ions' path based on their mass-to-charge ratio. The sorted ions are then focused into the secondary electron multipliers and counted at the multiplier's anodes. For ion measurements in OSI mode, ion species go through the same path but without being impacted by the electron guns.

The difference between CSN and OSN is that in the OSN mode, a cylindrical ion trap prevents ions from contaminating the neutral beam. The CSN mode is used for detection of nonreactive species such as N_2 and CH_4 while the OSN modes are designed to detect reactive neutrals such as H_2O. The reactive and nonreactive here depends on the stickiness of the species to the antechamber walls of the instrument. Figure 3.1 shows a schematic of the INMS instrument.

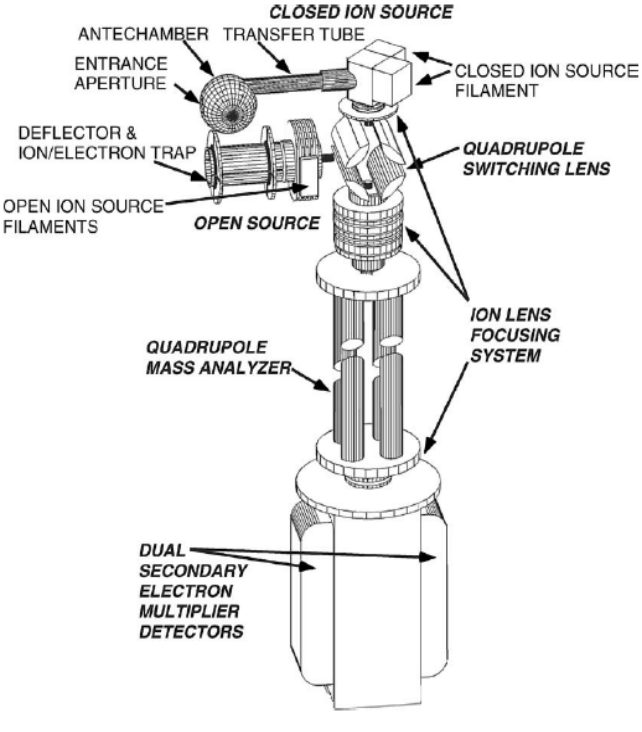

Figure 3.1 - A schematic of the INMS principal components. See text for description of each component. Adapted from Waite et al., (2004).

After 10 years of operation, reanalyzing the original calibration models and detector gain sensitivity of the INMS, specifically for Titan observations, showed a possible gas leakage from the ion source enclosure (Teolis et al., 2015). The ram pressure of the inflowing gas into the enclosure enhances the density of the sampled species in a known manner, especially when the spacecraft ram direction is along the field of view of the INMS. The leakage causes the enhancement to be lower than what was originally used in the calibration models. Consequently, the densities of the measured species were too low. Additionally, reduction in the electron multiplier gain was not accounted for in the pre-launch calibrations. Teolis et al. (2015) performed a cross calibration of the INMS neutral mass densities with measurements that the Cassini Attitude and Articulation Control System (AACS) and Navigation (NAV) made. AACS and NAV both use spacecraft drag data and aerodynamics models to calculate the ambient mass densities. As a result, a new correction factor of 2.2±0.23 for neutral densities and a new correction factor of 1.55±0.21 for ion densities were reported. These correction factors are incorporated in the results shown in this chapter.

3.1.2 The Radio and Plasma Wave Instrument (RPWS) – Langmuir Probe (LP)

The RPWS-LP (Gurnett et al., 2004) is another source of data for this study. This instrument measures the plasma current over a range of bias voltages applied to a sphere (probe) and provides current-voltage (I-V) curves of the surrounding plasma. For a positive bias voltage the current is directly proportional to the electron number density. In the negative bias voltage regime an electrostatic potential barrier exists and only those electrons with higher kinetic energy contribute to the current. In this case, the electron temperature is inversely proportional to the slope of the logarithmic I-V curve. The spacecraft charging has always been an issue that interferes with the Langmuir probe measurements because it creates an offset in the measured currents. The spacecraft potential can be estimated from the shape of the I-V curves. However, to minimize disturbances due to plasma shielding of the charged spacecraft, the distance of the probe to the spacecraft body should be significantly larger than the Debye shielding length of the plasma. This imposes a lower limit on the electron densities the probe can measure (Gurnett et al., 2004; Wahlund et al., 2005). Figure 3.2 shows a photo of the Langmuir probe installed on the Cassini spacecraft.

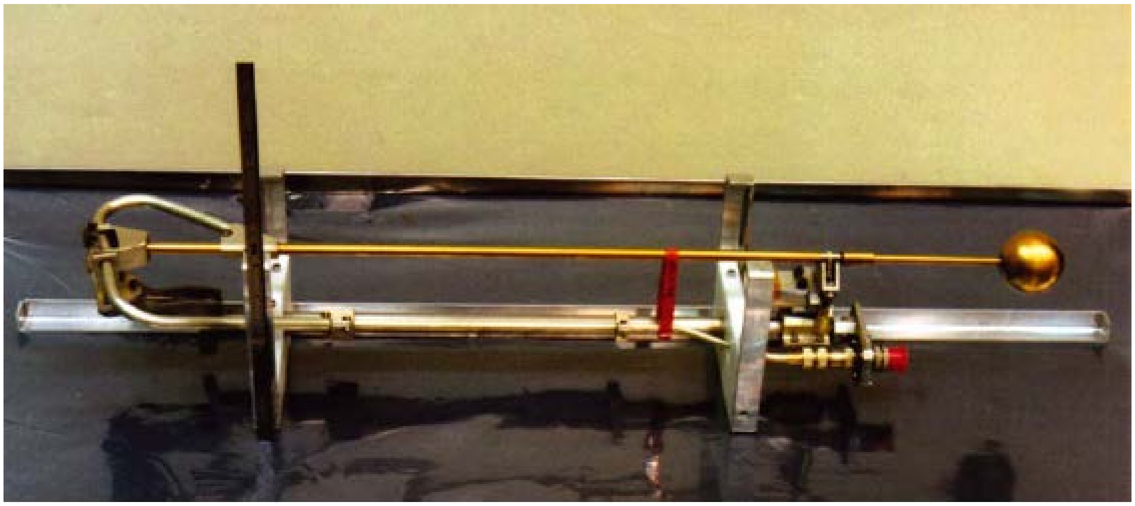

Figure 3.2 - Image of the Langmuir probe and boom assembly. Adapted from Gurnett et al. (2004).

The INMS instrument requires specific spacecraft pointing and flyby geometry to be able to provide reliable ionospheric measurements. The majority of flybys are not suitable for optimum INMS operation. Particularly for the open source mode, the accuracy of the measured densities is highly sensitive to the angle between the spacecraft velocity and the inlet openings (ram angle). The smaller ram angles result in higher pressure of gas in the antechamber and, therefore, more efficient measurements. In many flybys of Titan, however, the RADAR instrument, that provides maps of the surface structures and other information about the lower atmosphere, and the associated high gain antenna had to be pointed towards the surface which would orient the spacecraft such that increases the ram angle of the INMS. Therefore, only a subset of the Titan flybys contains relevant data on the ionospheric species.

3.2 Titan Flybys

The INMS ion measurements and RPWS-LP electron measurements from 21 flybys and INMS neutral measurements from 33 flybys, spanning the period from April 2005 to September 2015 are used. Table 3.1 shows specific details of these flybys. Columns (from left to right) show flyby sequence (T followed by the sequence number), date of the flyby, solar $F_{10.7}$ index in solar flux units (sfu), 81-day averaged $F_{10.7}$, altitude, latitude, and SZA at the closest approach. The last column marks the usable ion data segments for each flyby (i.e., inbound or outbound, or full flyby).

Usable segments of the data were identified by examining the INMS data for each of these flybys. Flybys with ‘N’ in the last column only include neutral density data while flybys with ‘*’ only have the ion densities available. For the ion density data, the ingress part of flybys T50, T65, T83, T100 and T104 is used rather than egress for which, the data had multiple outliers or densities were unusually low. By contrast, for flybys T5, T26, T32, T39, T51, T57, and T113 only the egress data is used. Ingress and egress parts of flybys T17, T18, T36, T40, T48, T59, T71, T86, and T95 are both reliable. This gives a total of 21 flybys for ion density profiles. For the neutral density data, which incorporate up to 33 flybys, the only criterion was for the ram angle to be less than 30°. Sixteen flybys include ion and neutral measurements.

Table 3.1 - Information on the Cassini Titan flybys used in this chapter.

Flyby	Date	$F_{10.7}$ (sfu[1])	$F_{10.7}$A	Altitude (km)[2]	Latitude[2]	SZA[2]	Ion Data Segment[3]
T05	16 Apr 2005	84.9	92.8	1026	73.66	127.6	OB

T16	22 Jul 2006	72.6	77.3	949.9	84.8	105.1	N
T17	7 Sep 2007	84	77.6	1000	22.92	44.9	Full[*]
T18	23 Sep 2006	72	77.64	960	73.23	91	Full
T19	9 Oct 2006	75.2	79.3	980	63.37	82.3	N
T21	12 Dec 2006	92.2	85	1004.8	40.7	123.8	N
T23	13 Jan 2007	83.8	82.1	1000.3	30.3	53.1	N
T25	22 Feb 2007	74.8	76	1000.4	30.4	161.2	N
T26	10 Mar 2007	71.6	73.9	980	29.08	152.1	OB
T27	36 Mar 2007	73.7	73.5	1009.9	41.1	143.9	N
T28	10 Apr 2007	69.9	73.4	990.9	50.3	137.1	N
T29	26 Apr 2007	76.5	73.9	980.8	59.4	129.8	N
T30	12 May 2007	71.5	73.9	959.2	68.5	121.7	N
T32	13 Jun 2007	70.4	73.1	964.8	84.89	106.5	OB
T36	2 Oct 2007	67.7	67.7	973	-59.88	66.9	Full
T39	20 Dec 2007	74.5	74.9	970	-69.66	60.9	OB
T40	5 Jan 2008	79	75.3	1014	-11.52	37.2	Full
T41	22 Feb 2008	71.8	72.1	999.7	-34.8	30.2	N
T42	25 Mar 2008	79.4	71.2	999.4	-27.1	21.2	N
T48	5 Dec 2008	69.6	68.8	960.6	-9.98	25.3	Full
T49	21 Dec 2008	69.1	69.2	970.6	-43.8	82.5	N
T50	7 Feb 2009	70.1	69.6	966.8	-33.46	136.3	IB
T51	27 Mar 2009	69.1	69.4	962.6	-30.05	84.2	OB
T55	21 May 2009	71.5	65.6	965.7	-22.1	141.4	N
T56	6 Jun 2009	70.1	69.3	967.7	-32.1	135	N
T57	22 Jun 2009	67	68.9	955.1	-42.51	127.4	OB
T58	8 Jul 2009	71.3	68.1	965.8	-52.52	119.8	N
T59	24 Jul 2009	67.8	67.7	956.2	-62.61	111.8	Full
T61	25 Aug 2009	67.6	68.8	960.7	-19.5	85.9	N
T65	12 Jan 2010	89.2	81	1074	-82.36	94.8	IB
T71	7 Jul 2010	72.7	77.5	1003.7	-56.27	82	Full
T83	22 May 2012	125	121.7	955	72.53	70.7	IB
T84	7 Jun 2012	151.9	128.4	959.3	38.8	74.5	N
T86	26 Sep 2012	139.8	118.6	956	62.46	46.4	Full
T95	14 Oct 2013	129.3	129.1	961	7.8	25	Full[*]
T100	7 Apr 2014	140.9	147.4	963	37.1	59.5	IB[*]
T104	21 Aug 2014	118.3	130	964	34.7	12.1	IB[*]
T113	28 Sep 2015	125	106	1035.6	-0.79	42	OB[*]

1: 1 sfu (Solar Flux Units): $10^{-22}\ Wm^{-2}Hz^{-1}$

2: At closest approach

3: OB: Outbound; IB: Inbound; Full: Both in and outbound; N: Only neutral densities

[*] Only ion densities are available

It should be noted that the T32 flyby was one of the rare cases when Saturn's magnetopause was pushed inward inside the orbit of Titan and Titan's ionosphere experienced a magnetosheath plasma environment. Flybys T83 and T86 occurred when Titan was positioned directly between Saturn and the Sun and around the time of the first peak of solar cycle maxima. These flybys together with two flybys at solar minimum condition, namely T40 and T48, are used for the more detailed ion production modeling. Figure 3.3 shows geometrical schematics for most of the flybys in Titan-solar Orbital System (TOS) and Titan Interaction System (TIIS) coordinates. The four flybys emphasized for the modeling are shown in color. The left panel shows flybys in TOS coordinates, where the horizontal axis is the distance along the Titan orbit in units of Titan radius (R_T) and the vertical axis shows the distance from the ecliptic plane. The Sun is positioned out of the page and along the positive x-direction. The right panel of Figure 3.3 shows the geometry of the same flybys in TIIS coordinates, where the vertical axis shows the distance along the line connecting the center of Titan to the center of Saturn, and the horizontal axis shows the distance along the corotational flow velocity. In both panels of the figure, outbound legs of the flybys are shown as solid lines, inbound legs are shown with dashed lines, and the flyby sequence is displayed next to each line.

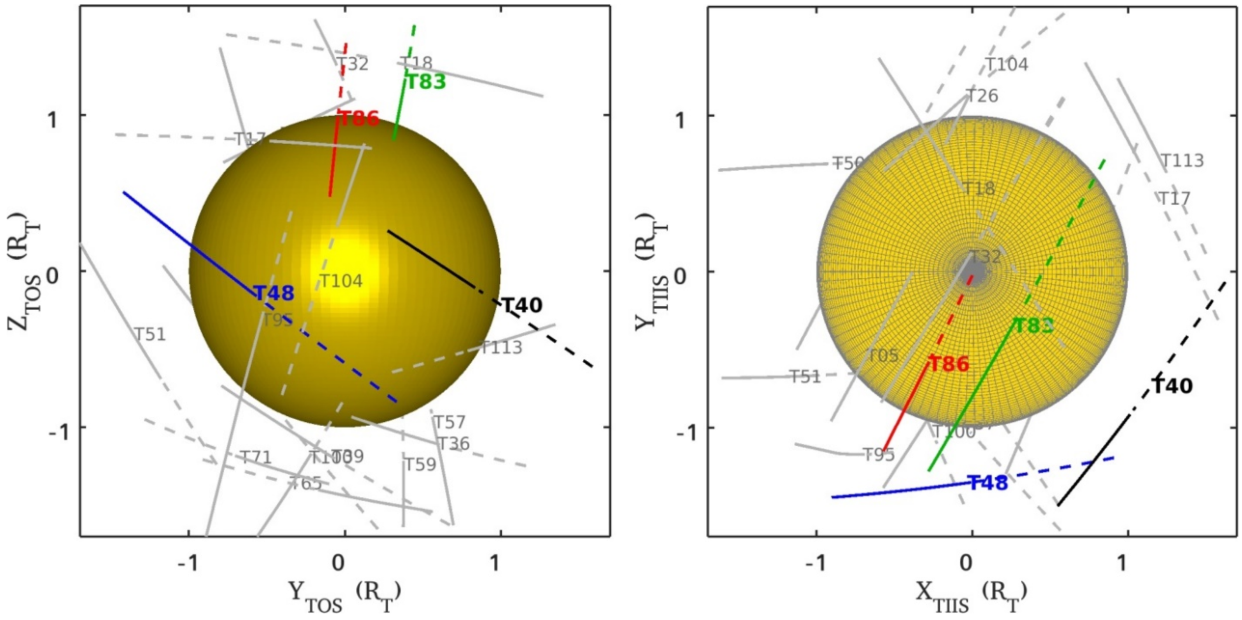

Figure 3.3 - (Left) Titan flybys in TOS (Titan-solar Orbital System) coordinates where the x-axis is directed towards the sun, the y-axis points to the orbit direction and the z-axis completes the right-handed coordinate system. The flyby sequences are marked next to each flyby trajectory. The inbound segment of each flyby is shown with a dashed line and the outbound leg with a solid line. Four of the flybys (T40, T48, T83, T86) emphasized in the modeling section are marked with black, blue, green and red colors, respectively. (Right) Here we show the flyby geometries in TIIS (Titan Interaction System) coordinates, in which the x-axis is along the corotational flow direction, the y-axis points from Titan to Saturn, and the z-axis completes the right-handed coordinate system. The axes in both plots are in units of Titan radius (R_T).

3.3 Neutral Density Data

3.3.1 Major Neutral Species

This section presents INMS density measurements of major neutral species. Nitrogen (N_2), methane (CH_4), and hydrogen (H_2) are the primary neutral species in Titan's upper atmosphere, with small concentrations of more complex hydrocarbons and nitrile compounds (Cravens et al., 2005; McEwan and Anicich, 2007; Waite et al., 2005; Yung et al., 1984). The major neutral density profiles are directly measured by INMS. Figure 3.4 shows the measured density profiles of the major neutral species for two flybys, T40 and T86. The N_2 gas is the dominant neutral species below ~1600 km and near the peak of the ionosphere. At altitudes above 2000 km the H_2

becomes the dominant neutral, which contributes greatly to Titan's outgassing to the Saturn's magnetosphere. The gap in the T40 data from 1500 - 2200 km (1400 - 2500 km in T86) is due to changes in INMS operations modes.

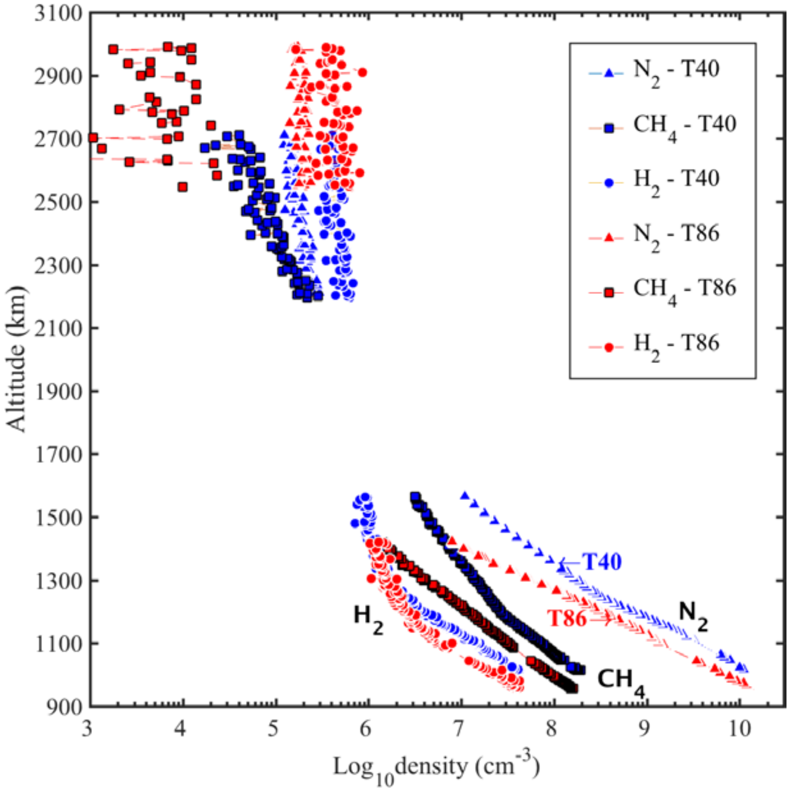

Figure 3.4 - Density of major neutral species (N_2, CH_4 and H_2) measured by INMS in CSN mode. Densities for the T40 flyby are shown in blue and the red markers are for the T86 flyby. The triangles represent N_2, squares represent CH_4, and circles are for H_2. The difference in the densities of the three species, between the T40 and T86 flybys at an altitude of 1050 km is about a factor of 2.

The gap in the data in Figure 3.4 is caused by change in the detection mode of the instrument. To maximize the scientific observations the ground team practiced various combinations of mass tables (arrangement of active mass channels) during each flyby.

The density profiles of N_2 and CH_4, from 33 flybys are presented in Figure 3.5. Data points with ram angle greater than 30° are filtered out because high ram angles may cause inaccurate measurements by the instrument. Data points are color-coded by the $F_{10.7}$ index and the colorbar to the right shows the corresponding values. Panel (a) of Figure 3.5 shows the nitrogen density for altitudes between 900 and 1800 km. The snippet in panel (b) is an expanded view of the densities for altitudes between 950 and 1200 km. The blue dashed line on this plot shows the averaged densities versus altitude (every 30 km) for low solar activity flybys for which the $F_{10.7}$ was less than 120 sfu, and the red dashed line represents altitude-averaged densities of the higher solar activity flybys with the same altitude interval. The dotted horizontal line is drawn at 1050 km for comparisons. Similar plots for methane are pictured on the right hand side. Panel (c) shows the methane density profiles for the altitude range 900-1800 km and the bottom plot (panel d) is a close-up view of the profiles between 950 and 1200 km. A consistent drop in the densities of major neutral species for higher solar activity is evident, particularly for altitudes between 900 and 1200 km. For high altitudes above 1500 km, this drop is less obvious. At an altitude of about 1050 km, the drop in the densities between low and high solar activity measurements is about 70% for methane and 50% for nitrogen. This can explain the drop in peak altitude of the ionosphere (to be discussed in section 3.5).

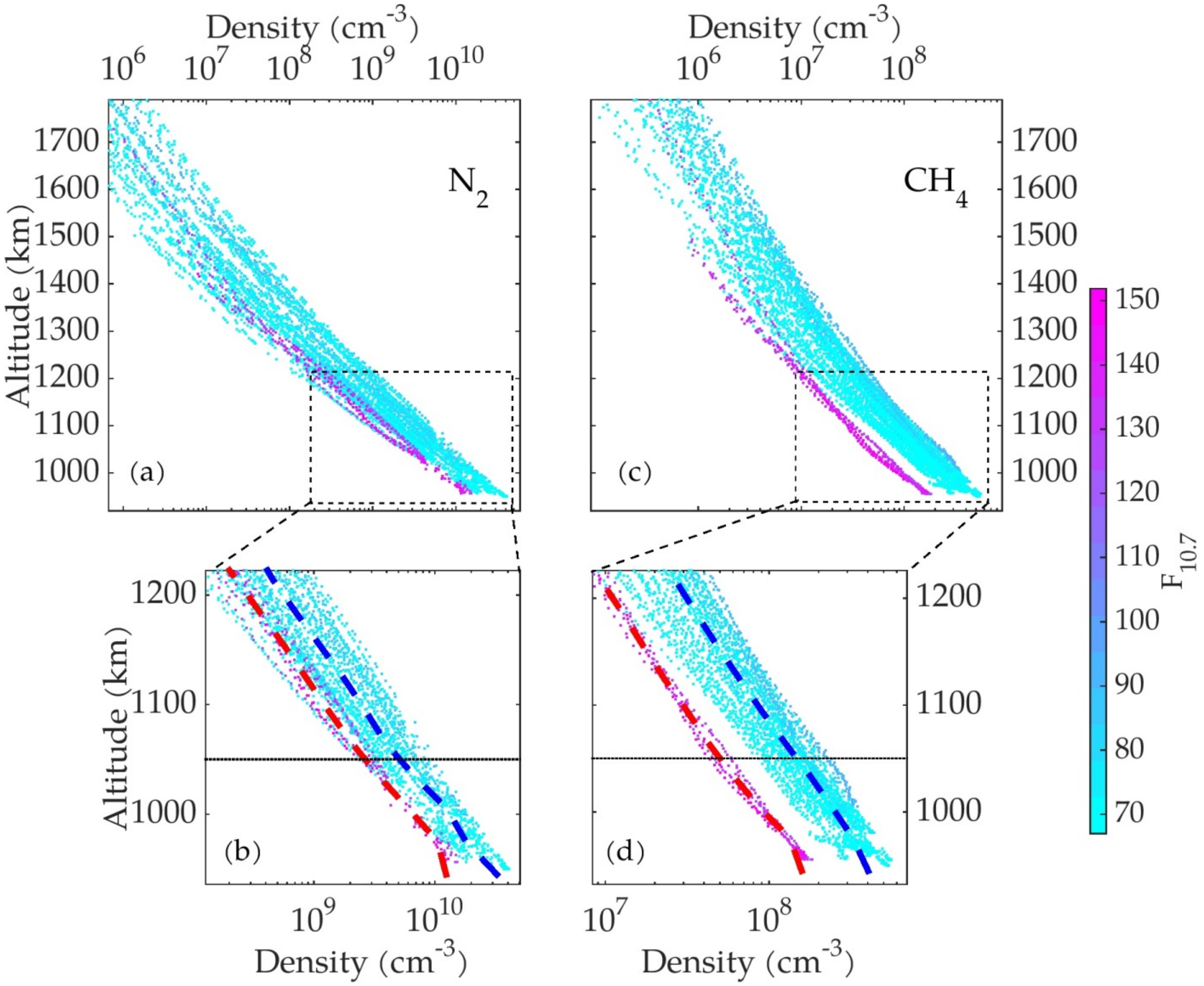

Figure 3.5 - Density profiles of nitrogen (upper left) and methane (upper right) measured by INMS closed source mode. Data points are color coded by the $F_{10.7}$ index. The snippet below each plot shows the densities near the peak of the ionosphere and the average density of low solar activity flybys ($F_{10.7} < 120$) and high solar activity flybys are over-plotted with blue and red dashed lines, respectively.

The possible latitudinal dependence of the neutral (and ion) observations was also studied. Methane densities are plotted versus latitude in Figure 3.6, where an evenly distributed methane densities across latitudes is observed. The flybys are colored by the $F_{10.7}$ index and high solar activity flybys show a clear decrease in the density, as was illustrated previously. The current available data show that observations during high solar activity only covered the northern latitudes. Future studies should see whether densities show the same distribution at southern latitudes. However, we do not expect to see higher densities at low latitudes (Coustenis et al., 2013).

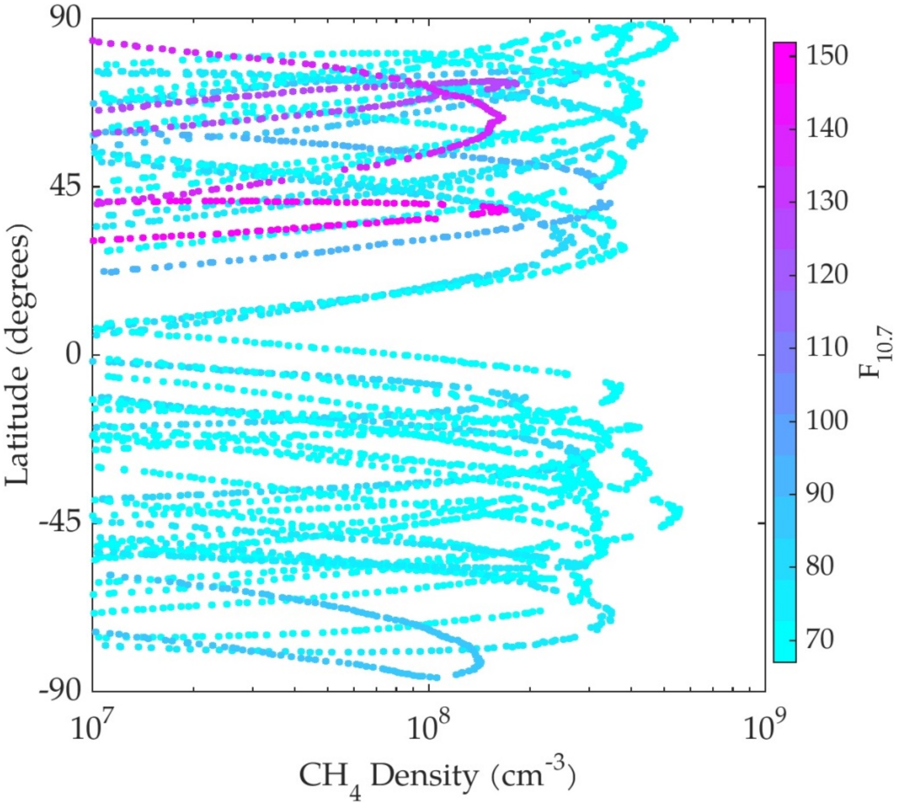

Figure 3.6 - Density profiles of methane measured by INMS versus latitude. Data points are color coded by the $F_{10.7}$ index. Data points with ram angle less than 30° are filtered out. Flybys at high solar activity show a decrease in density.

The outflow of methane from the thermosphere to the magnetosphere can be considered as another source of thermospheric depletion (Bell et al., 2010; Cui et al., 2012). However, a study of INMS data from 32 flybys and showed that the methane escape rate is neither solar driven nor temperature dependent, but is a sporadic phenomenon seen often on the nightside. Therefore, it is important to consider possible solar cycle effects on neutral atmosphere, especially near the peak of the ionosphere.

3.3.2 Minor Neutral Species

Densities of some minor neutral species can be derived directly from the INMS measurements. Many other species are deduced from combined ion-neutral chemistry models. These minor neutral species are particularly important for the production of higher mass ion species, but information on their dependence on solar activity has not been studied.

One chemically important minor neutral species in the Titan's ionosphere is HCN, a major coolant through rotational line emissions. However, no apparent inverse correlation has been observed between HCN abundance and the temperature of the neutral species (Cui et al., 2016). HCN abundance typically decreases with increasing altitude and remains at a constant level above 1200 km. At altitudes 600-800 km, HCN densities show increase with increasing solar zenith angle. At higher altitudes, this trend becomes significantly less noticeable. The most likely cause of this decline in abundance is photo-dissociation of the HCN molecules. This also means that the HCN abundance is depleted on the dayside, especially at altitudes below 1000 km.

Figure 3.7 shows the dependence of the HCN mixing ratios on the solar activity level and the solar zenith angle near the pick of the ionosphere. The HCN mixing ratio data is from a recent study by Cui et al. (2016), who retrieved the HCN mixing ratios from INMS data for 41 Titan flybys. The right panel in Figure 3.7 shows the HCN mixing ratio as a function of $F_{10.7}$ index at 1050 km altitude. At this altitude, the mixing ratios seem to be decreasing at higher solar activity, while showing no apparent correlation with the SZAs as presented in the left panel.

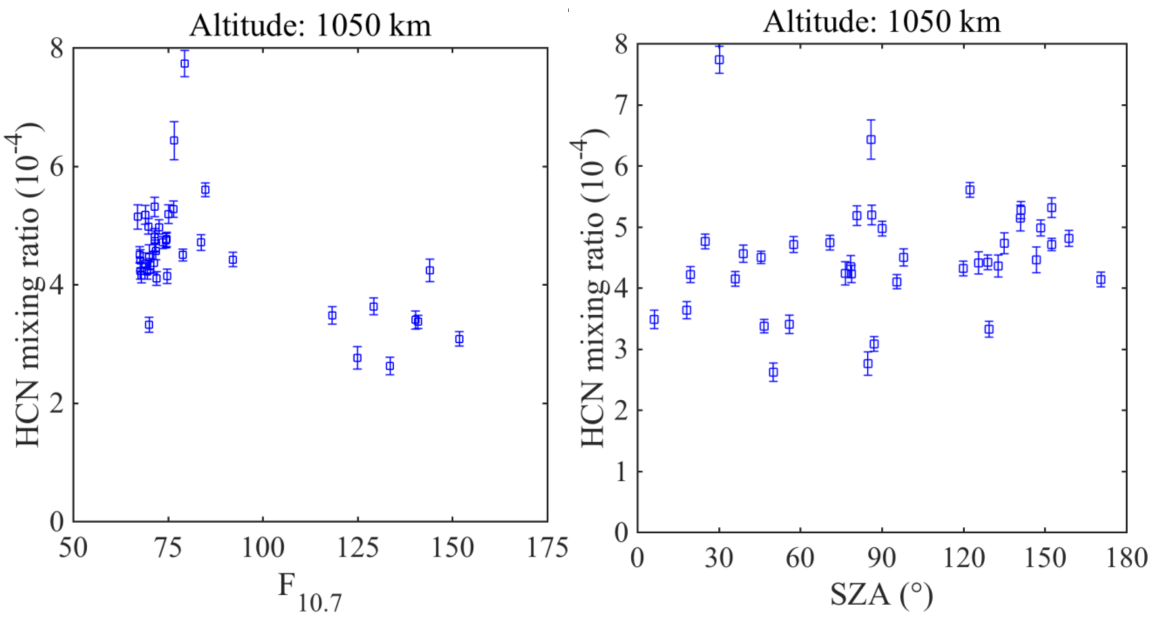

Figure 3.7 - HCN mixing ratio versus solar index $F_{10.7}$ (left) and HCN mixing ratio versus solar zenith angle (right). The mixing ration data is from Cui et al. (2016).

3.4 Primary Ion Species Analysis

In this section, we focus on the density and production rate of CH_3^+. The schematic in Figure 3.8 illustrates the main production and loss reactions for CH_3^+ ion. The contribution percentage to total production or loss for each reaction is indicated in parentheses. About 90 percent of CH_3^+ production comes from the reaction of N_2^+ with CH_4. The abundance of CH_3^+ relates directly to N_2^+ production, either from photoionization or from particle ionization.

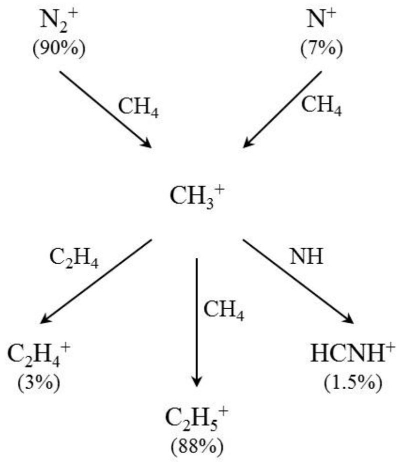

Figure 3.8 - The main production and loss reactions of CH_3^+. The neutral species involved in each reaction is also indicated. Most CH_3^+ production comes from the reaction of N_2^+ with methane. The major loss process is through reaction with methane and production of $C_2H_5^+$.

Figure 3.9 shows INMS density profiles for mass channel 15, which corresponds to CH_3^+. Flybys are color-coded based on the daily $F_{10.7}$ index. The colorbar shows the corresponding value. Nightside observations are included for context and are shown with triangles. The data show a clear density enhancement for higher solar activity.

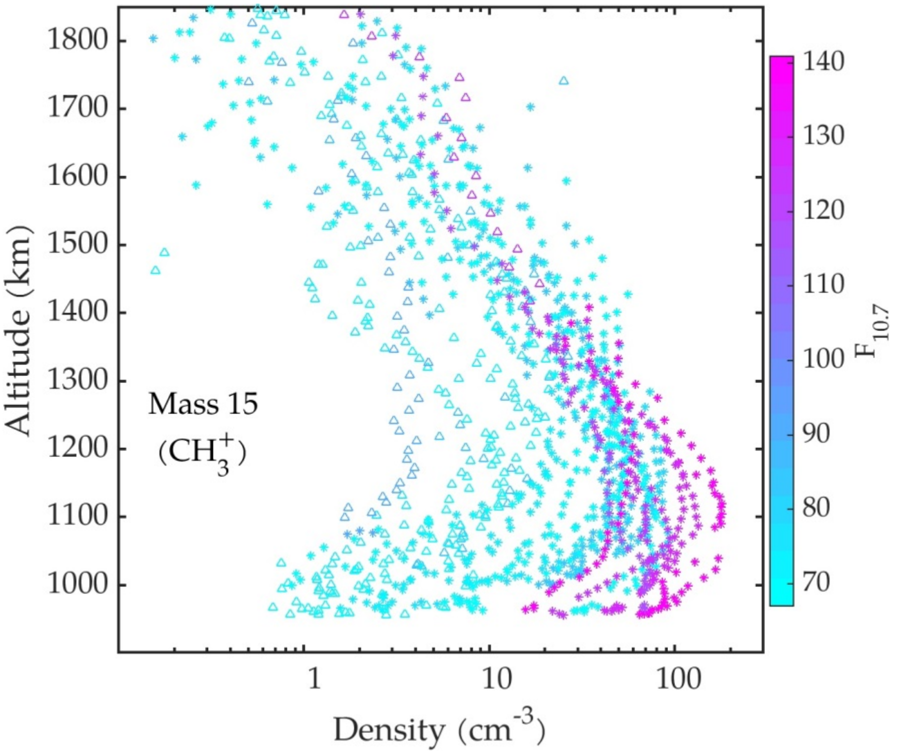

Figure 3.9 - Density profiles of CH_3^+. Profiles are color coded based on the $F_{10.7}$ index. Nightside observations (SZA > 100°) are shown with triangles. CH_3^+ is an "almost" primary species and is directly produced by the primary species N_2^+.

To help determine the effect of solar zenith angle on ion production we binned the CH_3^+ data into a matrix consisting of 10 solar zenith angle bins, starting from 10° up to 110°, and 40 altitude bins between 950 km and 1750 km. The data are binned for two separate ion datasets, distinguished by their $F_{10.7}$ (i.e., less than and greater than 120 sfu). The results are shown in Figure 3.10 in which the data is color-coded by SZA. The legend next to each panel shows the SZA values. The error bars correspond to the counting statistics at each bin.

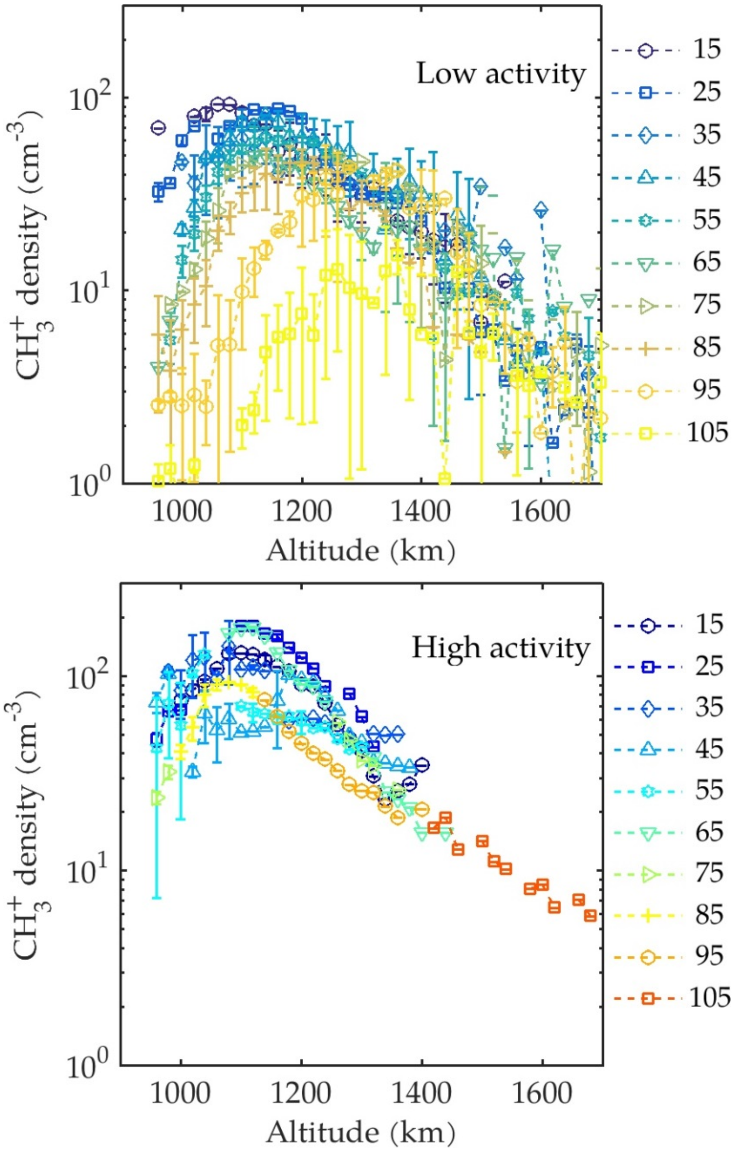

Figure 3.10 - Shows the CH_3^+ densities. Data have been sorted in to 40 altitude bins ranging from 950 km to 1750 km and 10 SZA bins ranging from 10° to 110°. Error bars present the counting statistics at each bin. The color of the points corresponds to the SZA value and the legend next to each plot shows the mid-point of the SZA bins.

At low solar activity, ion densities decrease with increasing SZA and altitude of the density peak moves to higher altitudes as expected. However, at high solar activity the altitude of peak density remains about the same. It should be noted that there are fewer observations for high solar activity periods than for low activity, as the list of flybys in Table 3.1 shows. A major gap in the available data includes the period from early 2010 to mid-2012 (nearly 30 months), when there is no usable Titan flyby.

The INMS mass channel 28 is strongly populated by $HCNH^+$. Therefore density of N_2^+ cannot be measured directly by the INMS because it has a very short lifetime and reacts quickly with neutral species and particularly methane, to produce CH_3^+. Hence the value of CH_3^+ is used as a proxy for N_2^+ production rates. Densities of CH_3^+ and CH_4 measured by INMS can be used to give an empirical estimate of the N_2^+ production rate, which amounts to over 95% of the total ion production rate (Richard et al., 2015a; Sagnières et al., 2015). A two-reaction chemistry scheme is adopted in which all the CH_3^+ is produced from N_2^+ and then lost by the methane reaction (see section 2.3). The N_2^+ empirical production rate is given by (with a small correction factor very close to unity):

$$P_{N_2^+} = P_{CH_3^+} \approx k_{CH_3^+,CH_4}[\mathrm{CH_3^+}][\mathrm{CH_4}] \qquad 3.1$$

where P stands for the production rate, $k_{CH_3^+,CH_4}$ is the reaction rate between methane and CH_3^+, and quantities in the brackets are the INMS measured densities.

Figure 3.11 shows N_2^+ production rate profiles for T40, T48, T83, and T86 from the empirical INMS-based method. Recall that T40 and T48 are for lower solar activity. These can be compared with the theoretical production rates in the previous section 2.3. Overall, there is a good agreement between theoretical and empirical (INMS) N_2^+ production rates for low and high solar activity. Peak theoretical N_2^+ production rates for T40, T48, T83 and T86 are 12.78, 13.05, 9.81, and 18.68 $cm^{-3}s^{-1}$, respectively. T83 N_2^+ production rates are lower than those for the rest of the flybys despite the high $F_{10.7}$ index, due to the high solar zenith angle for this case. Solar zenith angle is an important variable that needs to be tracked.

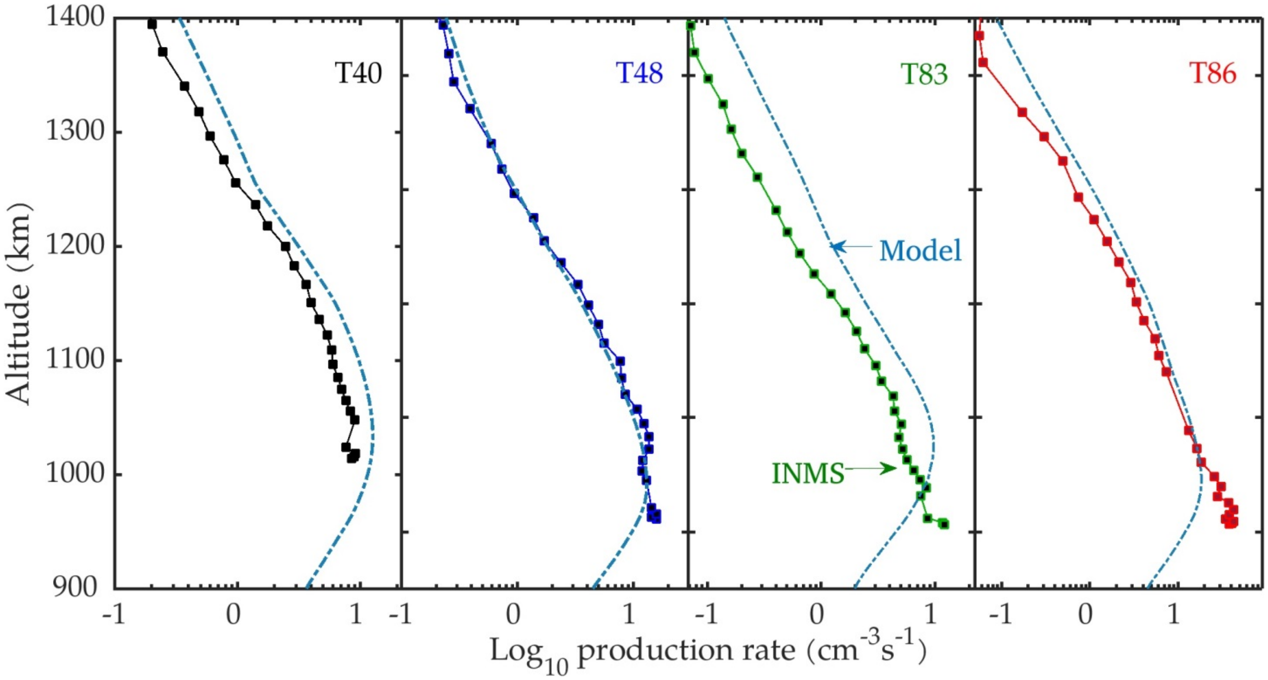

Figure 3.11- Shows the N_2^+ production rates from empirical estimates (squares) and the theoretical model (dashed lines), for the T40, T48, T83 and T86 flybys. The empirical production rates have been estimated from INMS data using a method similar to that introduced by Richard et al. (2015). For the T83 flyby, the inbound segment of the data has been used while the T40, T48, and T86 panels show outbound segments. Solar zenith angles at closest approach for T40, T48, T83 and T86 are 37, 25, 70 and 46 degrees, respectively.

3.5 Ion Density Data

3.5.1 INMS Ion Density Variations

This section presents the ion densities measured by INMS during both high and low solar activity periods are presented, starting with the former. Figure 3.12 shows the INMS ion density profiles for several species for the inbound leg of the flybys T83, T100, and T104, and outbound leg of the flybys T113, T95, and T86. These flybys have $F_{10.7}$ greater than 120, and are all dayside flybys except T83 which is near the terminator region. The solar zenith angle-altitude coverage of these flybys appears in Figure 3.12.

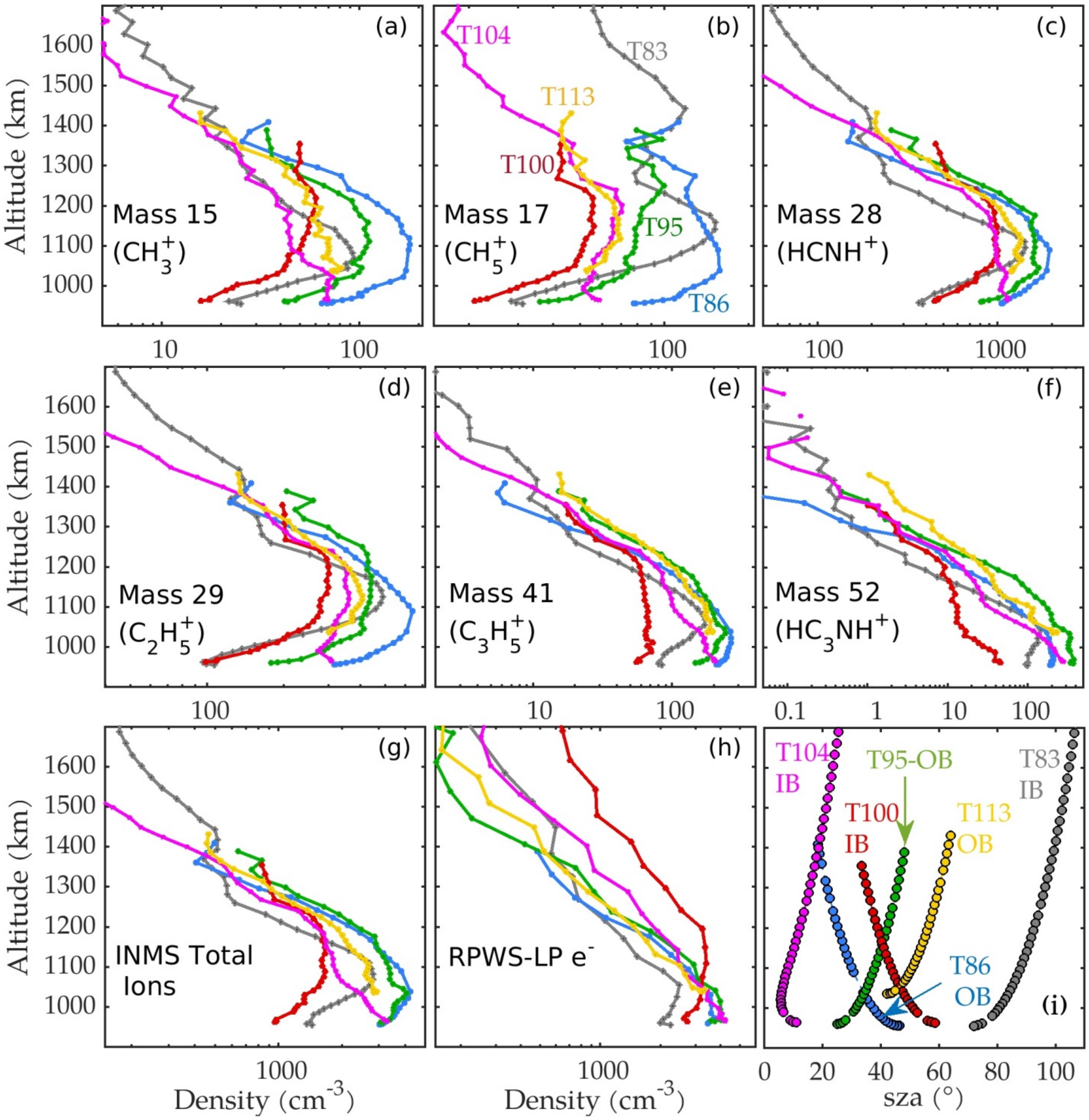

Figure 3.12 - Shown are the ion and electron density profiles and SZA coverage between 900 and 1700 km for six flybys: T83 (grey), T86 (blue), T95 (green), T100 (red), T104 (purple), and T113 (green). Panels (a) through (h) show the density profiles of CH$_3^+$, CH$_5^+$, HCNH$^+$, C$_2$H$_5^+$, C$_3$H$_5^+$, HC$_3$NH$^+$, total INMS ion densities, and RPWS-LP electron densities, respectively. Data segments shown here are for the inbound parts of the T83, T100, and T104 flybys and for the outbound parts of the T86, T95, and T113 flybys. Solar zenith angle-altitude coverage of these flybys is shown in panel (i).

Several important and representative species are shown here, including INMS densities for six mass channels, the total ion density, and the electron density measured by RPWS-LP versus altitude. Panel (a) in Figure 3.12 shows mass channel 15 density (almost all the counts are the CH_3^+ ion species), which was shown earlier for all available flybys. NH^+ ions also make a very small contribution to this mass channel. Panel (b) shows the density for mass channel 17 for which the main ion species is CH_5^+. Panels (c) through (e) show the density profiles of mass channels 28, 29, and 41, corresponding predominantly to $HCNH^+$ and $C_2H_5^+$, and $C_3H_5^+$ ion species, respectively. Using a 1-D photochemical model, Dobrijevic et al. (2016) evaluated the contribution of several species to the mass 28 and 41 channels (i.e., N_2^+ and $C_2H_4^+$ to channel 28 and CH_2CNH^+ to channel 41) and showed that these mass channels are indeed populated mostly by $HCNH^+$ and $C_3H_5^+$. $C_3H_5^+$ has a relatively long chemical lifetime and is produced through chemical reaction of major ion species, mainly $C_2H_5^+$, with the important minor neutral species acetylene and ethylene. Mass channel 52 densities are shown in panel (f). Ion species HC_3NH^+, $C_2N_2^+$, and $C_4H_4^+$ are associated with this mass channel with most of the counts believed to come from HC_3NH^+. Panel (g) is the density of all ion species measured by INMS (atomic mass less than 100 amu). About one third of the total ion density in Titan's ionosphere comes from $HCNH^+$. Panel (h) shows the electron density profiles measured by the Langmuir probe part of the RPWS. In Titan's ionosphere, quasi-neutrality dictates that the density of positive and negative charged particles be the same. That is, the total positive ion density equals the total negative ion density (including very heavy species and aerosols) plus the electron density. Panel (i) shows the SZA-altitude coverage of the flybys for inbound or outbound.

The T86 flyby had the second highest $F_{10.7}$ index among the flybys in Table 3.1. Combined with low SZAs throughout the flyby, this can explain the significantly higher densities observed during this flyby. Based on this figure it appears that the electron density profiles of high solar activity flybys (panel h) are not as sensitive to solar flux variations as ion species are.

This observation is, most likely, related to the long chemical lifetime of the electrons. Below an altitude of about 1050 km the electron density is less than the total ion density due to the presence of negative ions (Coates et al., 2007).

Figure 3.13 is the same as Figure 3.12, except for the low solar activity flybys. The outbound legs of flybys T17, T36, T39, T40, and T48 are used to show the density profiles for INMS mass channels 15, 17, 28, 29, 41, and 52, along with INMS total ion density and RPWS-LP electron density. The T39 flyby (green curve) shows a sudden decrease in density for most ion species above 1300 km. Therefore, one should use the high altitude data caution. This could be caused by dynamical effect associated with rapid cross track ionospheric winds (Mandt et al., 2012). Peak altitudes for T48 densities are lowest, which makes sense because the solar zenith angle for this flyby is the lowest (i.e., about 25°).

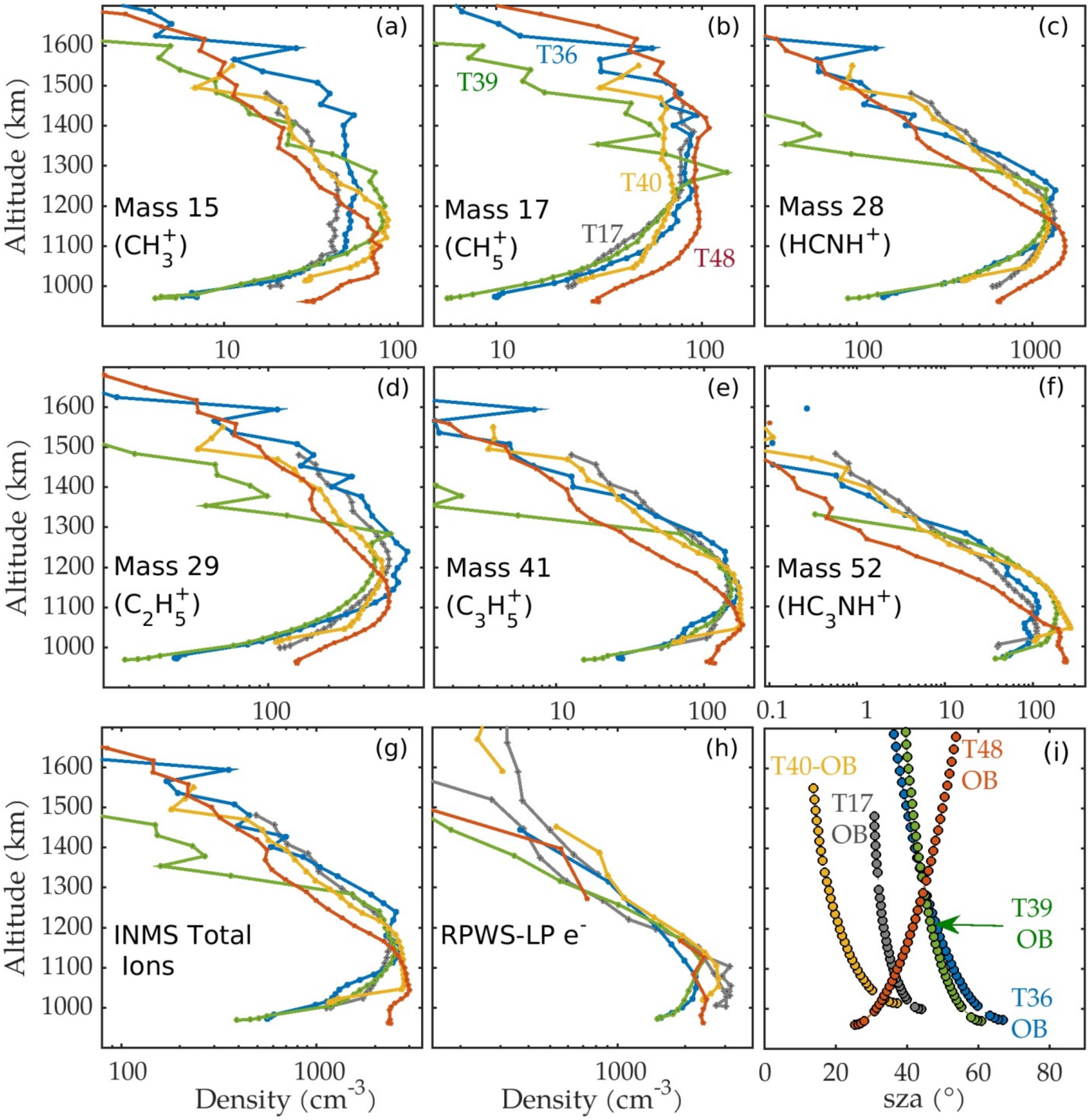

Figure 3.13 - Shows the density profiles for five flybys, T17 (grey), T36 (blue), T39 (green), T40 (yellow), and T48 (red) between 900 to 1700 km. Panels (a) through (h) show density profiles of CH_3^+, CH_5^+, $HCNH^+$, $C_2H_5^+$, $C_3H_5^+$, HC_3NH^+, total INMS ions, and RPWS-LP electrons, respectively. Panel (i) provides solar zenith angle-altitude coverage of these flybys. Data segments shown here are the outbound part of the flybys. The legend at the top-right corner describes the color, corresponding segment. The SZA at closest approach for each flyby.

Panel (g) in Figure 3.12 and Figure 3.13 shows the INMS total ion density (mass to charge ratio less than 100 Daltons). The total ion density is particularly important because it provides a general overview of the state of the ionosphere. A similar binning process (shown in Figure 3.10) is applied to the total ion densities at low and high solar activity. The results appear in Figure 3.14 where the data are sorted into 10 SZA bins and 40 altitude bins. We can make the following observations:

1. The total ion density is somewhat enhanced at high solar activity (peak values of ≈ 4000 cm^{-3} versus 3300 cm^{-3} for lower solar zenith angles).

2. For larger SZAs peak densities become smaller and are observed at higher altitudes.

3. The peak altitudes are lower, overall, for the high activity than they are for the lower activity.

4. The density falls off with altitude, as expected, up to about 1400 km, above which point more "irregularities" are apparent.

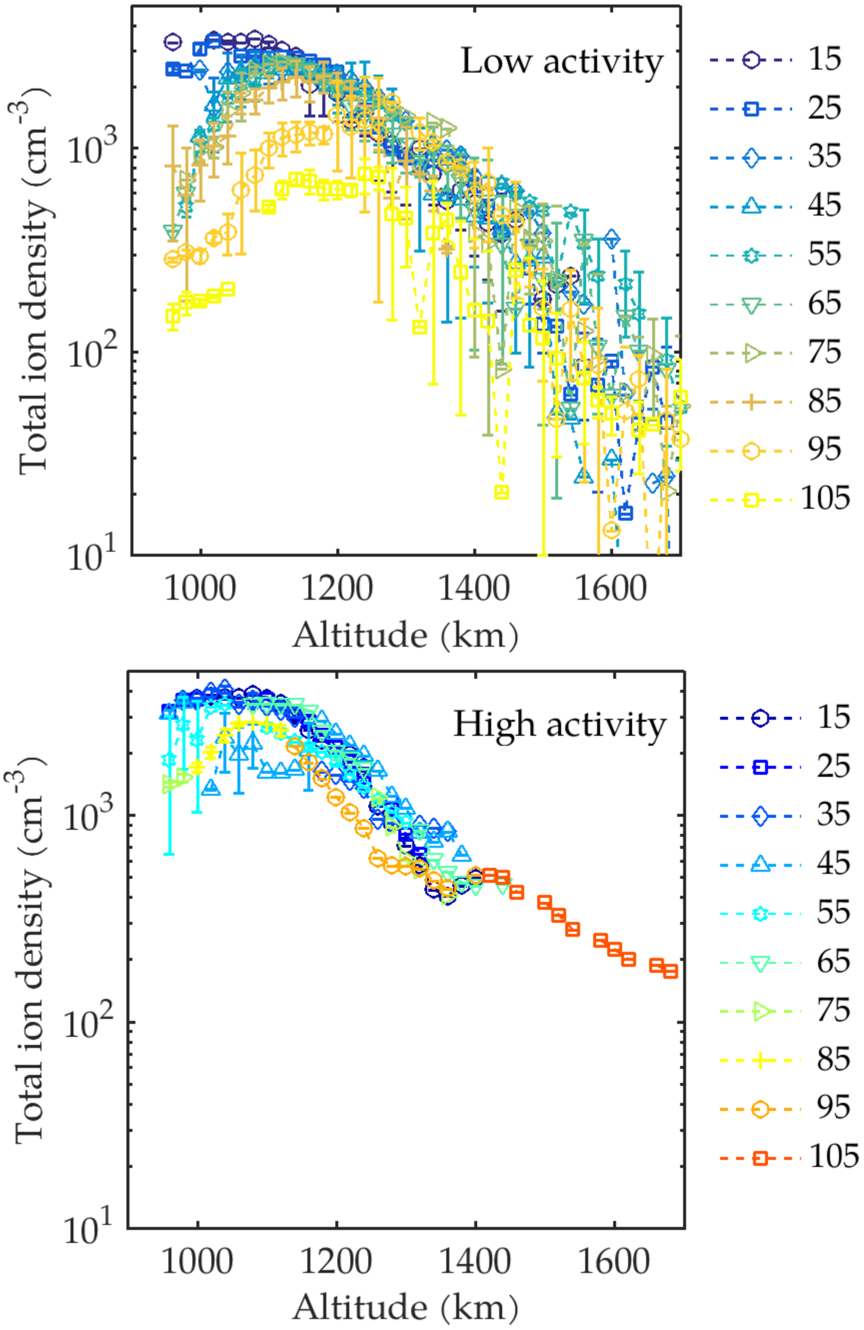

Figure 3.14 - Total ion densities. Data have been sorted in to 40 altitude bins ranging from 950 km to 1750 km and 10 SZA bins ranging from 10° to 110°. The error bars present the counting statistics at each bin. The color of the points corresponds to SZA value. The legend next to each plot shows the mid-point of the SZA bins.

Next, we consider peak densities of a few ion species versus altitude and solar zenith angle and for different solar activity, looking for differences in long-term behavior between primary species such as CH_3^+ and more “terminal” species such as $HCNH^+$, for which electron dissociative recombination is important. For example, one can argue that the electron temperature increases at higher solar activity due to increased energy deposition. However, for heavy ions, the temperature dependence of electron recombination coefficient is not yet well defined (Galand et al., 2014). Figure 3.15 shows distribution of the peak density versus peak altitude for ion species in mass channels 15, 16, 17, 28, 29, and 41. The nightside flybys (solar zenith angle > 100^o) are shown with triangle markers (included for context) while the dayside flybys are marked with circles. Data points are color-coded consistently, based on the $F_{10.7}$ index of the flybys.

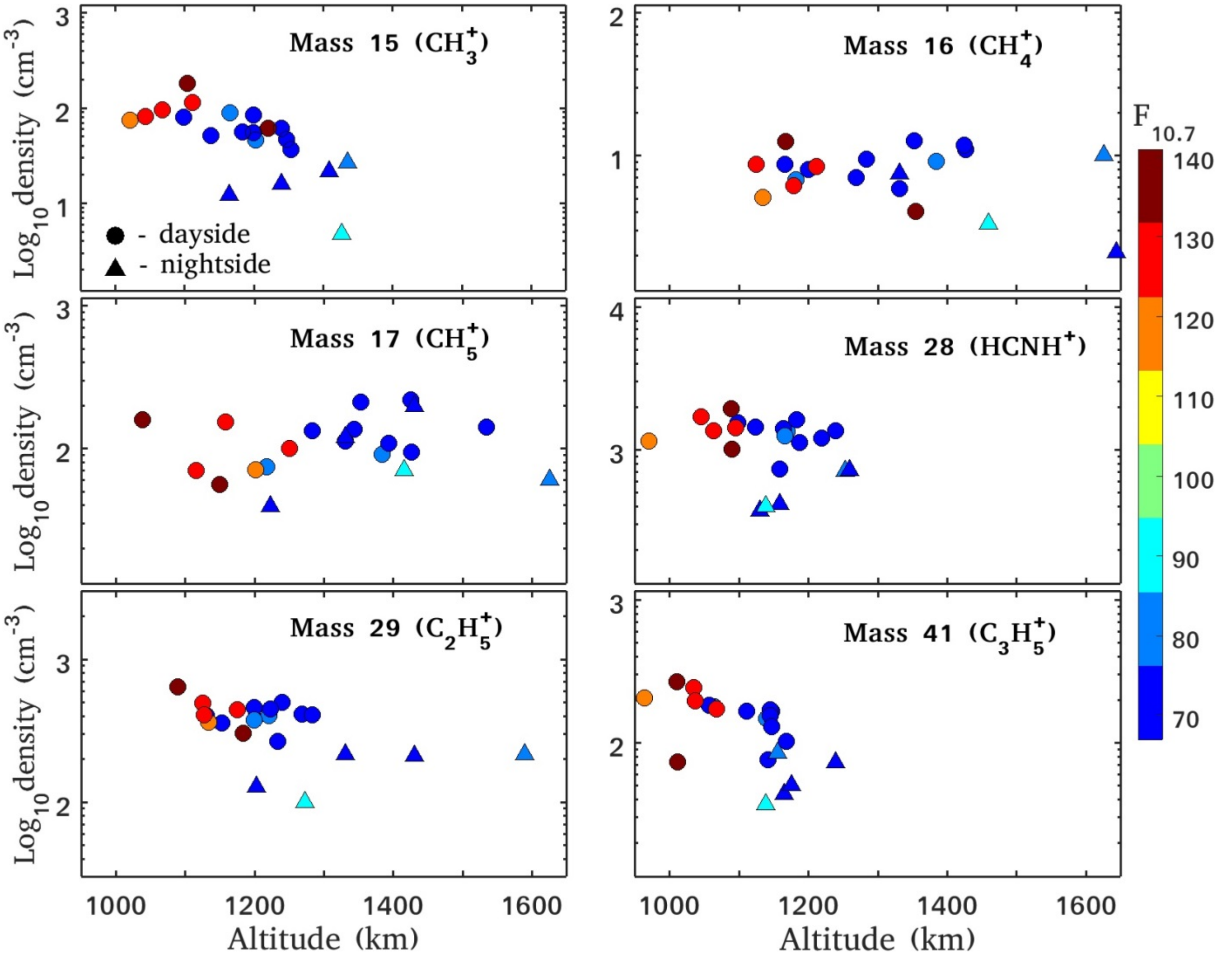

Figure 3.15 - The observed peak ion density of CH_3^+, CH_4^+, CH_5^+, $HCNH^+$, $C_2H_5^+$, and $C_3H_5^+$ corresponding to INMS mass channels 15, 16, 17, 28, 29 and 41 versus altitude. The points are color coded based on the solar $F_{10.7}$ index. The altitudes shown are those altitudes where the ion density profile has a maximum. A total of 21 flybys are included in these scatter plots. Details and description of these flybys appear in Table 3.1 and section 3.2. The error bars due to INMS measurement uncertainty (less than 2%) are not visible in this scale.

First we consider the primary species CH_3^+, which relates directly to N_2^+ production. The peak altitudes are lower for high activity than for low activity, and the peak density values are higher by about 50%, as expected for $F_{10.7}$ values that are about 50% higher. Peak densities of CH_4^+ (a primary species produced directly from methane) are not very different between low and high activity, but note that different solar zenith angles are mixed into this figure. The peak altitudes are lower for higher activity for all ion species, which was also evident in earlier figures. As we show below, this is undoubtedly due to lower neutral densities for the later flybys. For most ion species other than CH_3^+, the peak densities do not show the expected solar activity dependence in Figure 3.15, which is due partly to solar zenith angle effects, as will be considered later.

The most abundant ion species, $HCNH^+$ and $C_2H_5^+$, are linked directly by reactions of CH_3^+ with methane and then with HCN. About 40 percent of $HCNH^+$ is lost to electron dissociative recombination. Distribution of peak altitudes of $HCNH^+$ and $C_2H_5^+$ shows the best correlation with solar activity (or flyby sequence number, since there can be confounding variables) of all species. Specifically, there is higher density at lower altitude with increasing activity. This is illustrated in the mass 28 and 29 panels of Figure 3.15, where all six high solar activity flybys are below 1200 km. Heavy ion species are more abundant lower in the ionosphere; as ion mass increases, the altitude of the peak density decreases. The heaviest ion species, $C_3H_5^+$, tends to reside at lower altitudes as compared to other ions. At high solar activity the peak densities are observed at even lower altitudes, near 1000 km. This is similar to observations of negative heavy ion species at low altitudes (Coates et al., 2011; Wellbrock et al., 2013).

The heavy ion species can have chemical lifetimes lasting long enough to be subject to transport effects and dynamical processes at high altitudes rather than local ionization and chemistry. These ions are produced through ion-neutral chemical reactions and their loss occurs mainly through electron dissociative recombination. The $C_3H_5^+$ profiles also show enhancements at high solar activity near the peak at 1050 km, but at higher altitudes above 1300 km this effect seems to be reversed. At altitudes above 1300 km, T40 measured densities of $HCNH^+$ and $C_3H_5^+$ are higher than for T83 and T86.

Figure 3.16 shows the relative abundance of five ion species versus altitude. The ion species are $HCNH^+$, $C_2H_5^+$, $C_3H_5^+$, CH_5^+, and $C_7H_7^+$ from INMS mass bins 28, 29, 41, 17, and 91, respectively. Data points are color coded by the corresponding average $F_{10.7}$ index. The data show that, generally, the heavy ion species (e.g., $C_7H_7^+$ and $C_3H_5^+$) are detected at lower altitudes compared to the other ion species, which is expected for heavy ions. CH_5^+ is seen at higher altitudes, which is most likely due to the chemical lifetime of this ion species. The data also confirms our previous observation that at higher solar activity, the ion species are observed at lower altitudes.

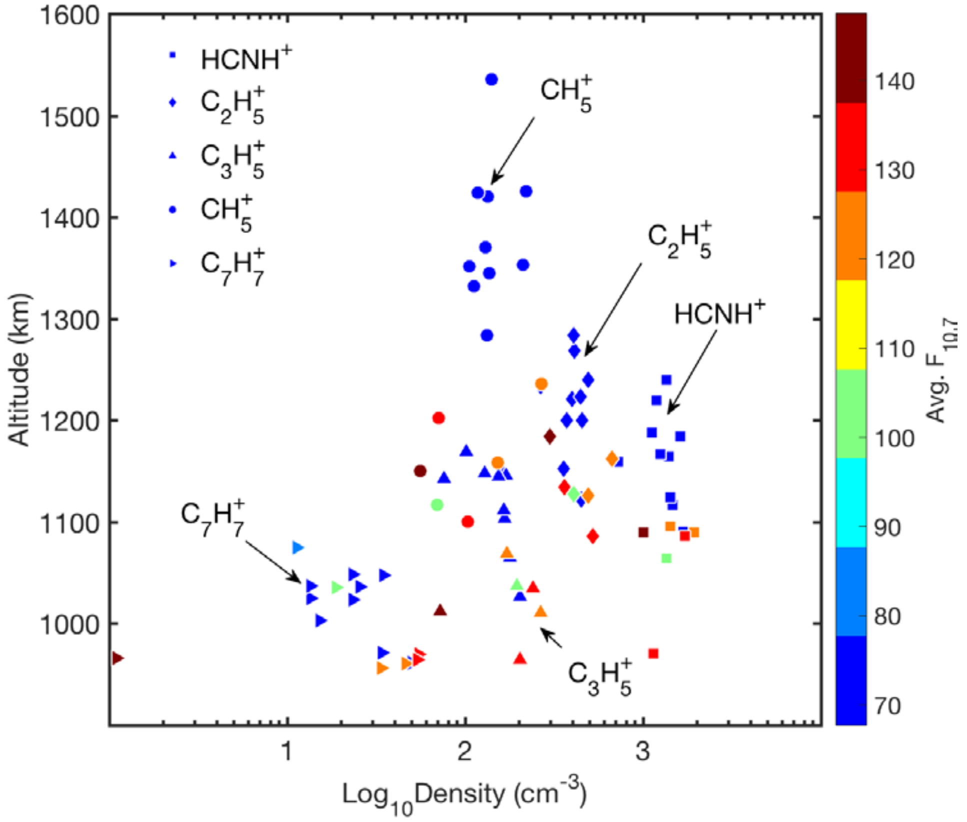

Figure 3.16 - Relative abundance of five ion species versus altitude. The ion species are HCNH$^+$, $C_2H_5^+$, $C_3H_5^+$, CH_5^+, and $C_7H_7^+$ from INMS mass bins 28, 29, 41, 17, and 91, respectively. Data points are color coded by the corresponding average $F_{10.7}$ index as shown on the colorbar.

The lowering for later flybys of the peak altitudes of almost all ion species (and the total ion density) evident in several figures appears to indicate that the thermospheric neutral density has decreased for the later flybys. This agrees with INMS neutral density measurements shown earlier (Figure 3.5). At Earth, the ionospheric level rises at high solar activity mainly due to increased scale height and thermal expansion. At Titan, however, the ionospheric level is decreasing at high solar activity. This effect can be illustrated by plotting ion densities versus measured N_2 density rather than altitude (Figure 3.17), indicating that overall decrease in ionospheric altitudes at high solar activity is a consequence of a less extended neutral atmosphere.

Figure 3.17 shows the measured ion densities as a function of nitrogen abundance for 3 major ions, CH_5^+, $HCNH^+$, and $C_3H_5^+$, and the total ion densities. Flybys that include both ion and neutral measurements are included in this figure and are colored by the $F_{10.7}$ index. The results show enhancements in ion densities for flyby T86, especially at altitudes near the peak. This figure shows that the peak of the ionosphere is at roughly the same nitrogen abundance level for different solar activity levels.

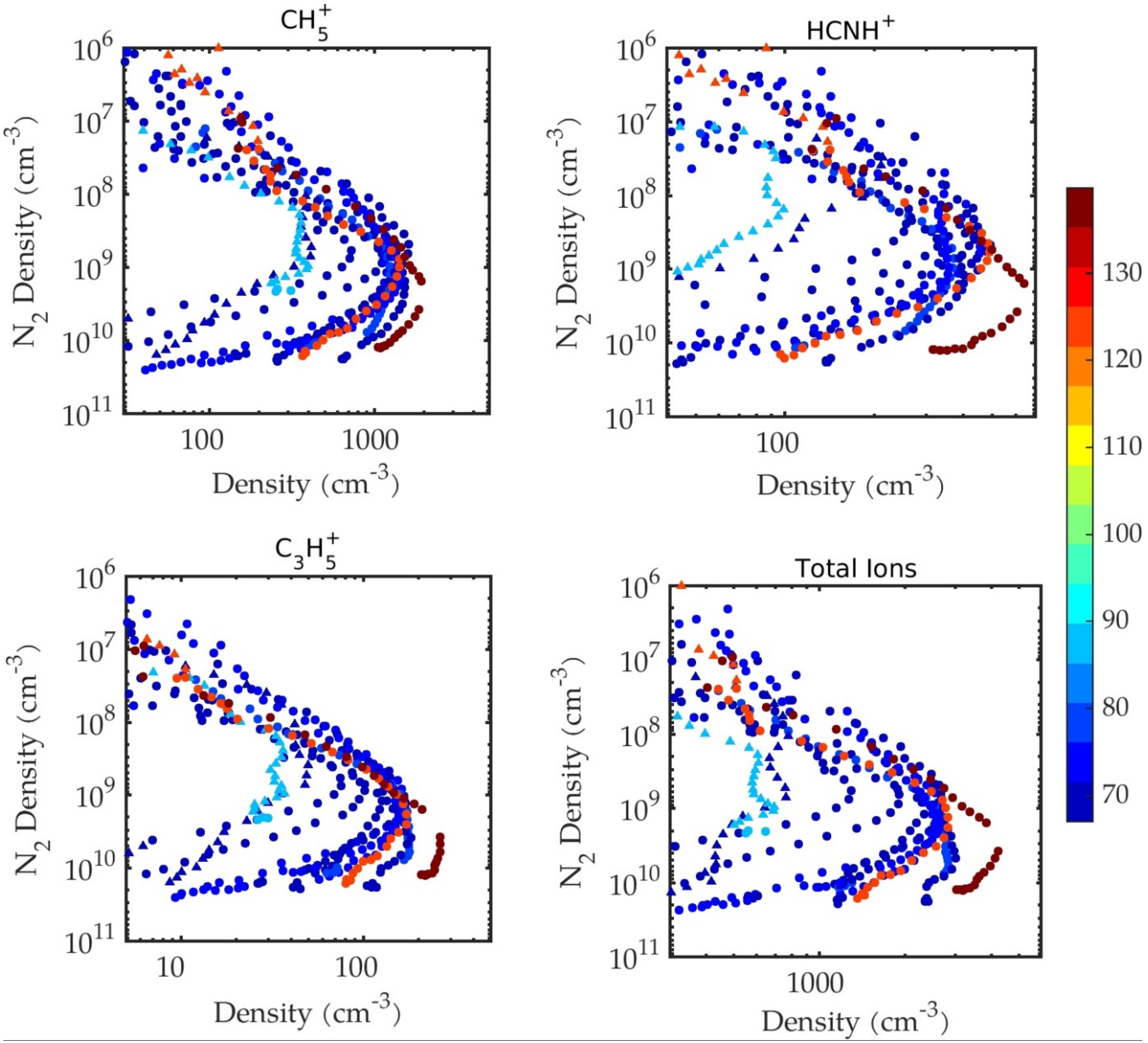

Figure 3.17 - INMS ion density profiles versus nitrogen abundance for major ions CH_5^+, $HCNH^+$, and $C_3H_5^+$, and total ions for all flybys with both ion and neutral measurements. Points are colored by $F_{10.7}$ index shown on the right colorbar and nightside observations are shown with triangles. The INMS counting statistics error bars are not visible in this scale as they are very small. The figure shows that the peak of the ionosphere is positioned at about the same level of nitrogen abundance; however solar zenith angles vary for different flybys.

3.5.2 Solar Zenith Angle Effects

In this section I continue to consider the role of solar zenith angle. Figure 3.18 shows the distribution of the peak density in SZA for the same ion species as in Figure 3.15. The variations with SZA and activity are not clear, with the possible exception of CH_3^+, which shows the expected variations (i.e., higher density at lower SZA and higher activity). The peak densities of CH_3^+, CH_4^+, $HCNH^+$ and $C_3H_5^+$ appear insensitive to SZA out to about 95°, although there is a modest decrease. The CH_5^+ density actually increases with SZA. However, the INMS measured densities for the T48 flyby are noticeably higher than other similar flybys. The high densities of light ions can be attributed to the low solar zenith angle during this flyby. Plots of peak density distribution versus SZA in Figure 3.18, particularly for CH_3^+, CH_4^+, CH_5^+ and $HCNH^+$, show that the density modulation due to solar cycle activity is much weaker than the effect of solar zenith angle. In fact, based on Figure 3.18 alone, solar cycle variation appears weak, which may reflect the relatively modest variation of the solar irradiance for the current solar cycle.

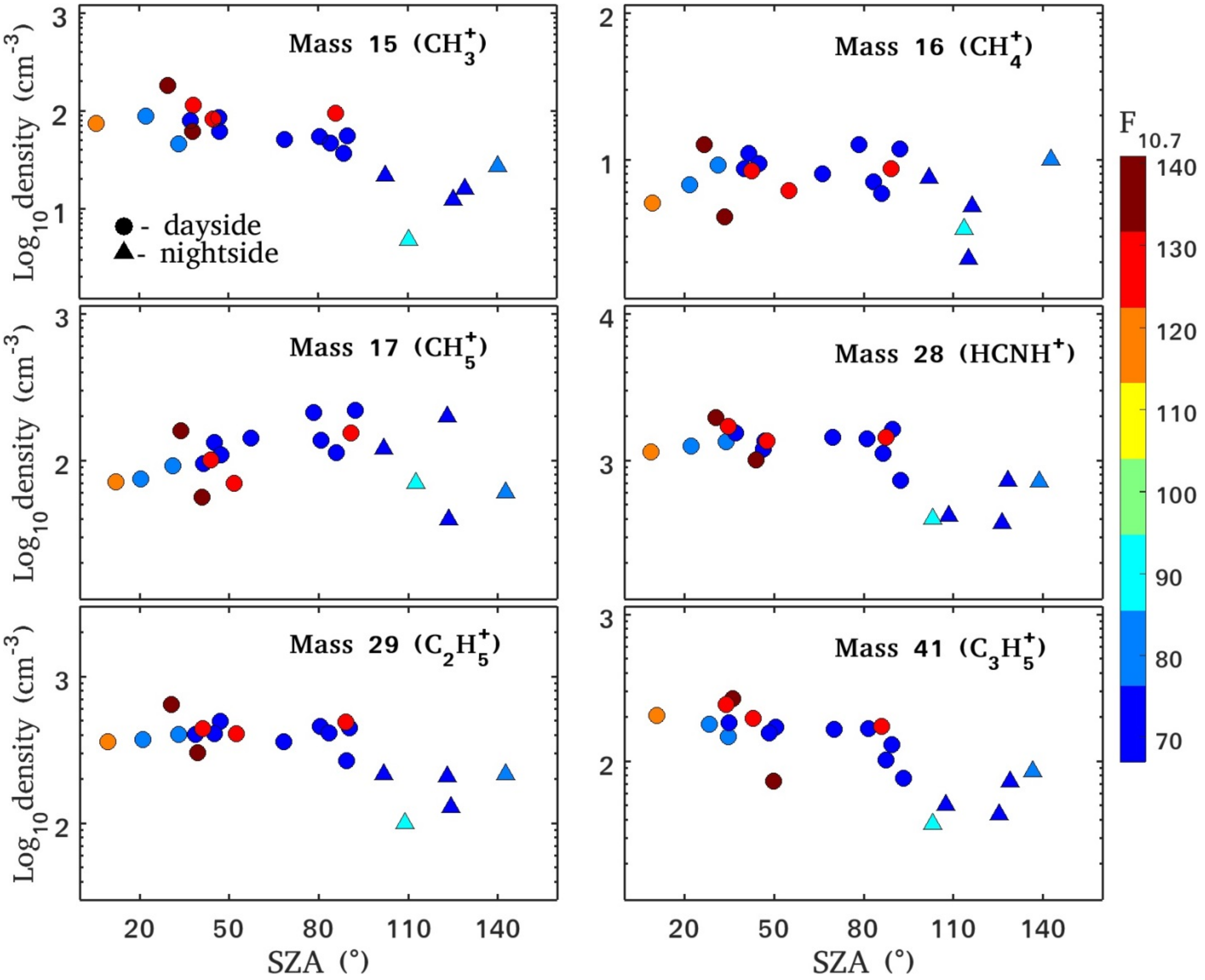

Figure 3.18 - Maximum observed ion densities of CH_3^+, CH_4^+, CH_5^+, $HCNH^+$, $C_2H_5^+$, and $C_3H_5^+$ ion species versus solar zenith angle. The data points are color coded based on the solar $F_{10.7}$ index. The dayside and nightside flybys are shown with circles and triangles, respectively. The heavy ions show less variation with changing SZA. The lower measured densities on the nightside are evident for both heavy ions and light ions. The error bars due to INMS measurement uncertainty (less than 2%) are not visible in this scale.

In Figure 3.18, the drop in the $HCNH^+$ density from day to night is about 65%, whereas in the $C_3H_5^+$ case, density decreases by about 75% over the same period and for the same number of flybys. We performed a data analysis technique (Edberg et al., 2015b) on the INMS ion densities, in an attempt (which was only partially successful) to de-trend the data and further isolate the solar activity effects. To appropriately fit the data, the density profiles are first shifted in altitude so maximum density at each flyby is at the same altitude level of 1000 km. Next, the data points are binned in altitude and a function in the form of equation 3.2 is fit to the ion densities at each altitude level:

$$F(z) = a_z \times \cos(b_z \times sza) \qquad 3.2$$

In this equation a_z is in units of (cm^3 degree)$^{-1}$ and b_z is a scaling factor. We considered an altitude range between 975 to 1700 km, with 75 km intervals. Using finer altitude resolution did not improve the fitting process. In the next step, ion densities are corrected for SZA according to:

$$n_{i_{SZA}}(z) = \frac{n_{i_{initial}}(z)}{\cos(b_z \times sza)} \qquad 3.3$$

In this equation, $n_{i_{initial}}$ is density of ion species i, sza is solar zenith angle at the time of measurement, b_z is the fitting parameter from equation 3.2 and $n_{i_{SZA}}$ is corrected ion density. The effect of this correction procedure is as if the SZA is at 0°.

Panel (a) Figure 3.19 shows the CH_3^+ densities binned in altitude and plotted versus solar zenith angle. The darker colors correspond to lower altitudes (i.e., higher densities). The fitted curve at each altitude bin is also over-plotted on the data with the same colors. Corrected densities appear in panel (b) where for each altitude bin/color we see fairly comparable ion densities at low and high SZAs. Fitting coefficients, a_z and b_z, for CH_3^+ with 95% confidence uncertainties are presented in panel (c). Average b_z is about 0.6, compared to 0.5 for electrons (Edberg et al., 2015a). Analysis of $HCNH^+$ (not shown) produced slightly different coefficients. These coefficients also show more uncertainty than the relevant coefficient for the electrons. Next, we look at density profiles in altitude before and after applying this technique on the data. Panel (d) shows uncorrected CH_3^+ densities and panel (e) shows the corrected densities after removing the SZA dependence. The points are colored by the solar activity (colorbar), and nightside flybys with SZA>100° are marked with triangles.

Removing the SZA dependence from the data caused densities to appear more bundled together. The solar cycle effect is more obvious. Panels (f) and (g) display the results of the same procedure for $HCNH^+$ profiles. The major difference between corrected profiles of CH_3^+ and $HCNH^+$ is that the $HCNH^+$ densities near the peak of the ionosphere are less dispersed after removing the SZA dependence, for both low and high activity profiles. By contrast, for CH_3^+ this is only the case for low solar activity flybys. High activity flybys are still distinguished from low activity flybys by showing enhanced densities. This is probably due to the fact that light primary ion species such as CH_3^+ are a lot more sensitive to solar flux variations than the heavy ions such as $HCNH^+$.

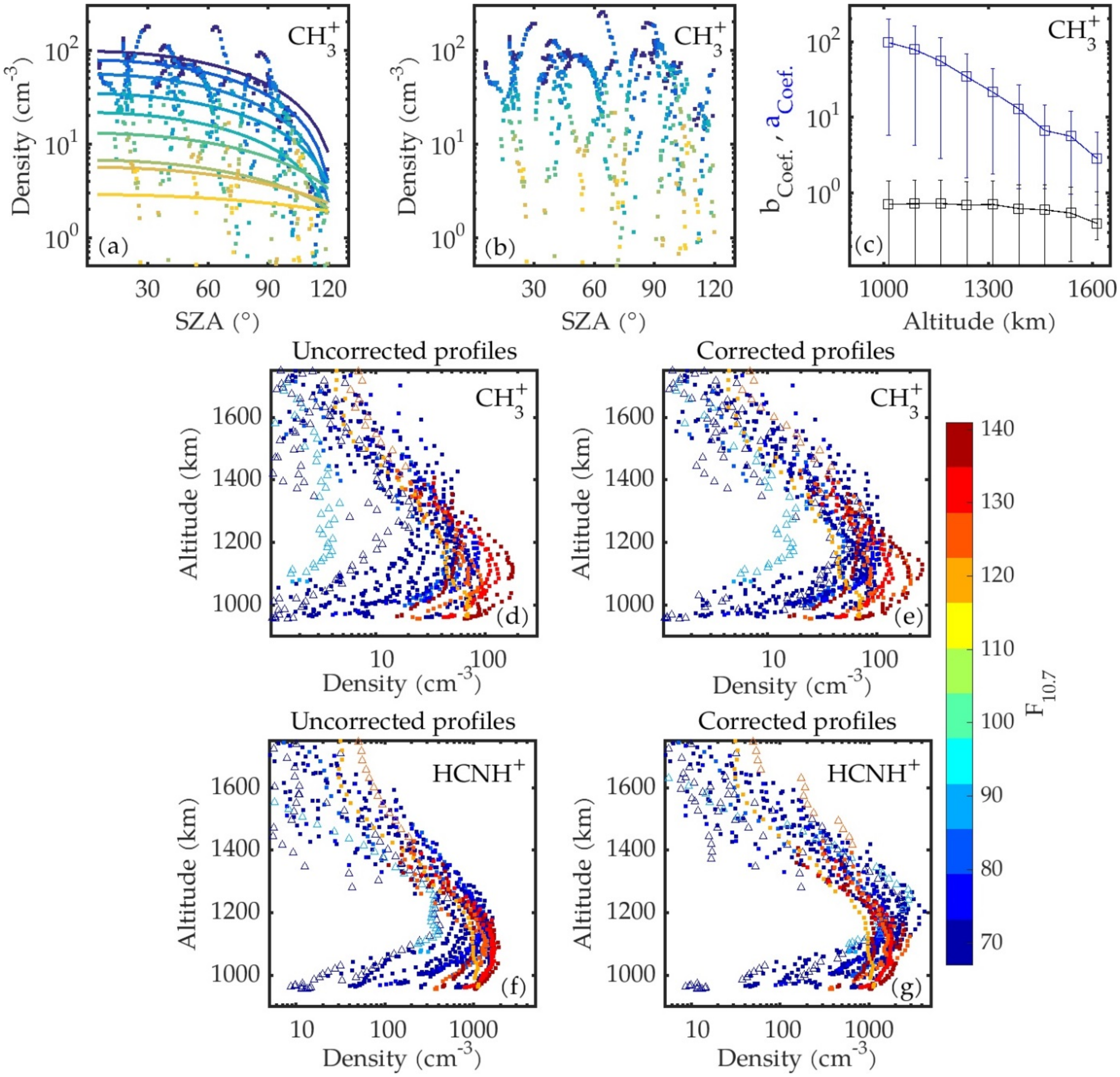

Figure 3.19 - (a) CH_3^+ density versus solar zenith angle color-coded by altitude bins, where darker colors correspond to lower altitudes. Fitting curve at each altitude is over-plotted with the same color. (b) CH_3^+ density versus SZA corrected for SZA effect (see text). (c) The fitting parameters used in equation 3, with 95% confidence level uncertainty bars. (d) CH_3^+ density profiles before removing the SZA effect, Nightside observations (SZA > 100°) are shown with triangles, points and color coded by $F_{10.7}$. (e) CH_3^+ density profiles corrected for SZA effect and color coded by $F_{10.7}$. (f-g). $HCNH^+$ density profiles before and after removing the SZA dependence.

3.5.3 Complete INMS Mass Spectra

Complete INMS ion mass spectra are presented for several altitudes (1000, 1100 and 1250 km) in Figure 3.20. Data segments chosen for this figure come from the outbound parts of the presented flybys and for the dayside. Five flybys are selected from Table 3.1, of which three are at low solar activity (i.e., T17, T39, T40), with the other two at high solar activity (T86 and T95). At each altitude a 30 km bin (±15 km) was adopted and densities were averaged over this range. Statistical uncertainty for most of the data points was small and not visible at this scale. Missing data points are either due to absence of measurement in that altitude range or to very low density measurements. Overall, there are no drastic differences in relative ion abundances across the mass range for the different flybys, and the solar activity effect appears to be greater at 1000 km than at 1250 km. As pointed out for the T5 INMS ion spectra (Cravens et al., 2009), the spectra show that the heavier mass species are relatively more abundant at lower altitudes. For light ions with atomic mass below 20 amu, densities are consistently higher at high solar activity in all three altitudes. For heavy ions (mass/charge greater than 60 Daltons), the increase in the density due to higher solar activity is visible at the lowest altitudes near 1000 km. For the mass spectra of 1000 km panel, the high solar activity flybys (T86 and T95) show higher abundance across the whole mass range.

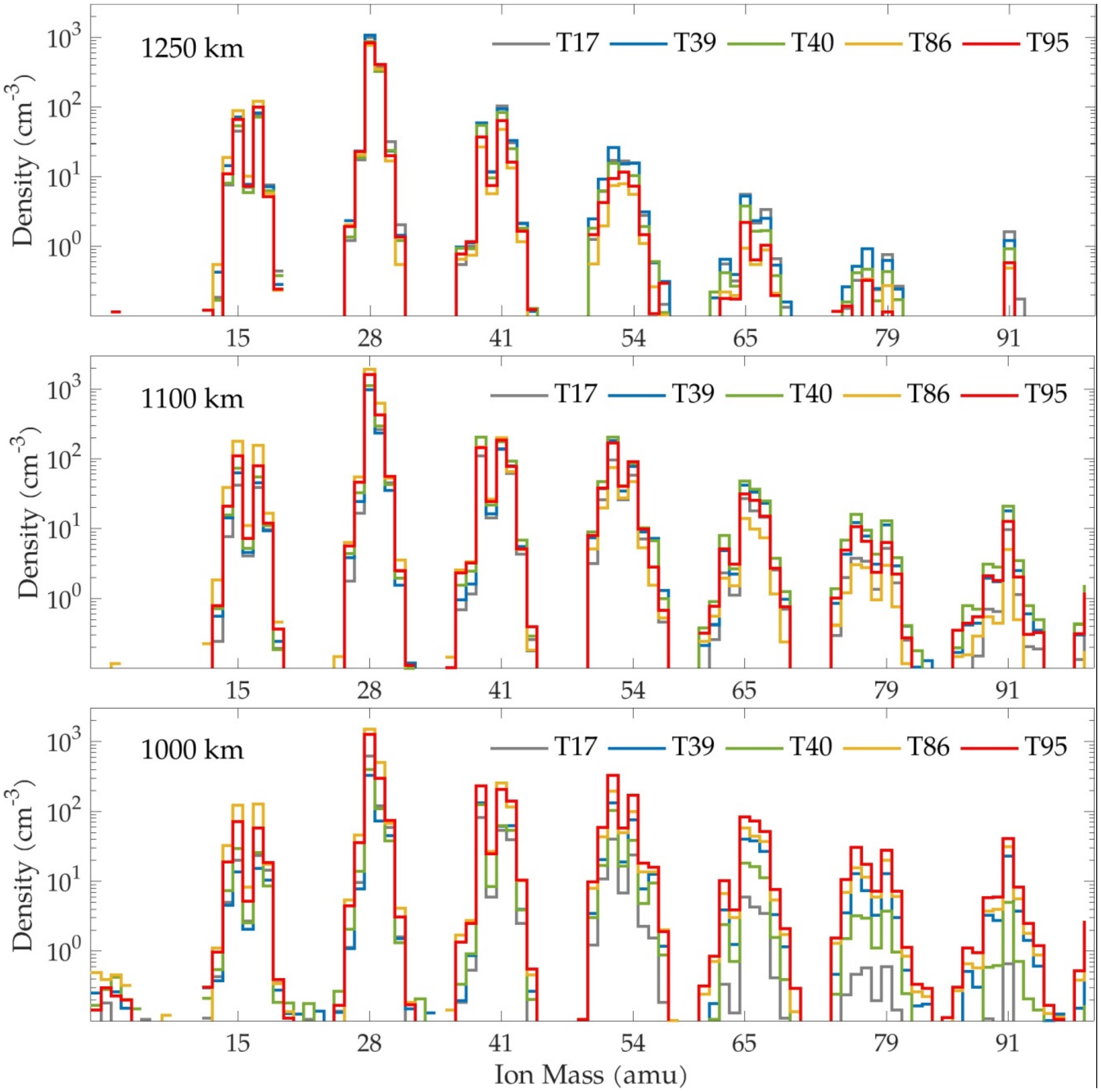

Figure 3.20 - Ion mass spectra measured by INMS at altitudes of 1000km, 1100km and 1250 km. Five dayside flybys, T17 (grey), T39 (blue), T40 (green), T86 (yellow), and T95 (red), are included in the plot. Missing data points at some altitudes are caused either by the density being lower than 0.1 cm^{-3} or by lack of measurement around that altitude. The altitude range is ±15 km. The statistical uncertainty bars were small enough not to be visible for most of the data points and are not shown on the plot to reduce clutter.

3.6 Concluding Remarks

In this chapter, I presented the INMS ion and neutral species measurements of the Titan's ionosphere from multiple Cassini flybys. The total ion density is somewhat enhanced at high solar activity (peak values of ≈ 4000 cm^{-3} versus 3300 cm^{-3} for lower solar zenith angles). The peak observed densities are smaller and are observed at higher altitudes for larger SZAs. Furthermore, the peak altitudes are lower overall for the high activity than for the lower activity and density falls off with altitude as expected up to about 1400 km, above which point more "irregularities" are apparent.

There is a gap in the INMS data from early 2010 to mid-2012, partly because of the absence of close Titan encounters in the Cassini spacecraft trajectory plan. This gap followed the end of the extended Equinox phase of the Cassini mission. During this gap period, one of the important plasma instruments onboard the spacecraft, the Cassini Plasma Spectrometer (CAPS), suffered a series of short circuits and was shut down in early 2012. Since the resumption of low altitude flybys and INMS data flow, the INMS instrument has been detecting lower counts of major neutral species near the peak of the ionosphere, which was then related to contraction of the ionosphere and/or depletion of the underlying neutral atmosphere at higher solar activities. However, there is a possible scenario that could have a dramatic effect on the presented data and interpretations in this chapter. If the instrument has undergone efficiency loss or malfunctioning unknown to the INMS ground team, this could explain the low neutral densities and therefore, would demand further analysis of the results to confirm our interpretations.

Long-term variations of the ionosphere can be studied from time series of the data. Figure 3.21 shows the time series of INMS CH_4 density, the RPWS-LP electron density, the INMS total ion density and their standard deviations at an altitude of 1050±15 km for the time period 2005 to late 2015. Note that the neutral density data is available only up to flyby T86. The 81-day averaged $F_{10.7}$ during this time period is shown in the bottom panel. Yellow triangles on this curve mark the dates of 21 Titan flybys containing ion measurements. T5, T40, T86, and T113 flybys are labeled.

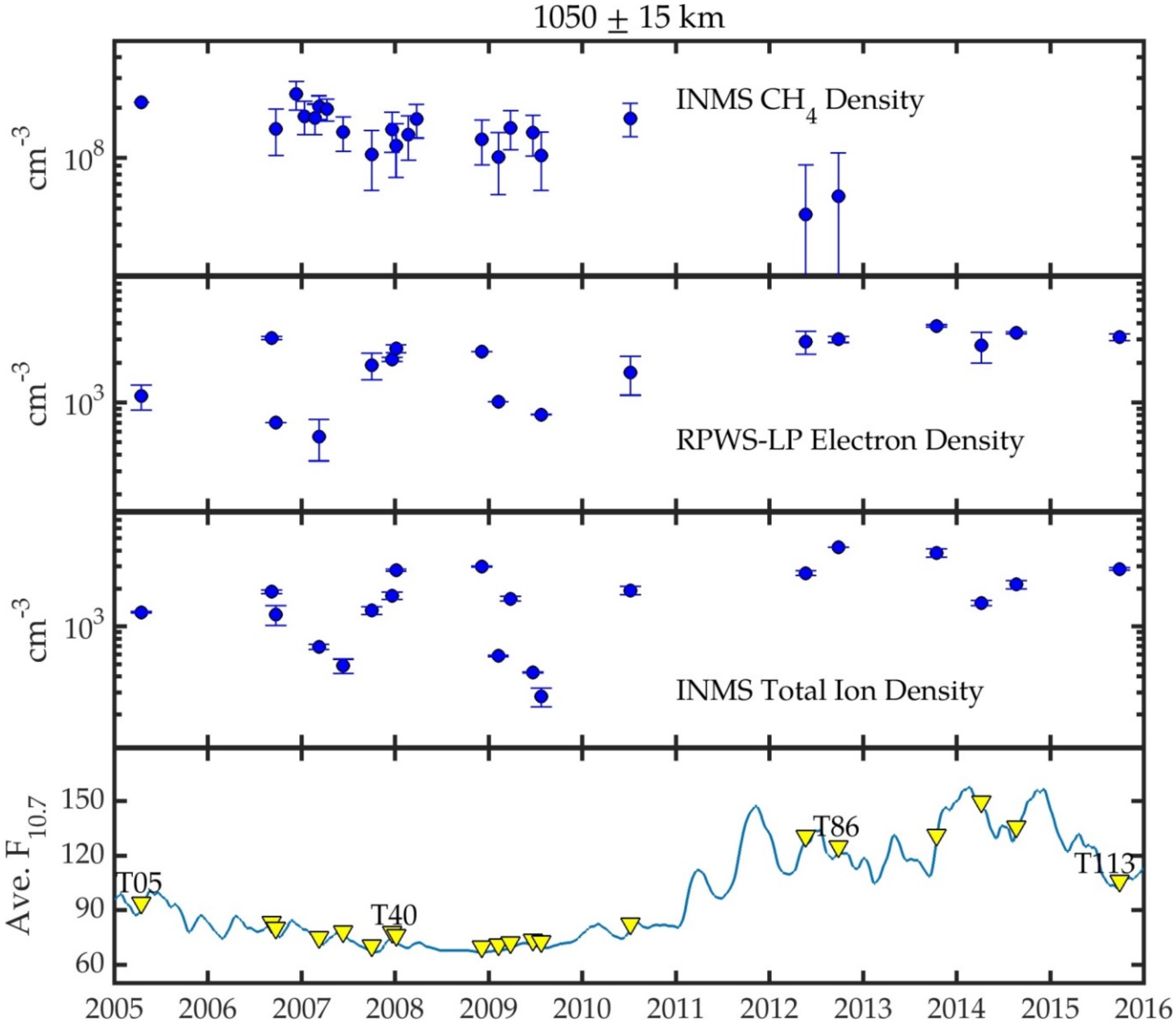

Figure 3.21 - Time series of INMS CH_4 density, RPWS-LP electron density and INMS total ion density at altitudes between 1035 and 1065. The error bars show the counting statistics for each data point. The 81-day averaged $F_{10.7}$ index is shown in the bottom plot where yellow triangles mark the times of the flybys. A few of the flybys are labeled throughout the curve. Rapid variation in total ion density is most likely due to changes in SZA at the time of each flyby. Error bars represent the standard deviation of the samples.

Unfortunately, long-term characteristics of the solar cycle are not readily apparent in the density measurements, so there is a need for more analysis. Densities for high solar activity flybys (i.e., after 2012) do show overall increases for total ion density and electron density, but this is not obvious due to the contribution of other variables and particularly SZA. For example, variation in the total ion density from 2005 to 2010 is due to change in the SZA of the flybys.

Some flybys occurring during low solar activity show densities comparable to flybys at high activity, suggesting that SZA plays a major role in determining peak ion production in the ionosphere.

4 Rosetta Observations of Comet 67P/CG

4.1 General Introduction

The Rosetta spacecraft arrived at comet 67P/Churyumov-Gerasimenko (67P/CG) in August 2014 and accompanied the comet through perihelion at 1.25 Astronomical Units (AU) and into the outbound part of the comet's orbit up to 3.8 AU. Comets have highly elliptical orbits in the solar system. A comet's nucleus is composed of mixtures of frozen volatiles and dust. Sublimation from the surface accounts for loss of cometary species into the space environment (Glassmeier et al., 2007a; Gombosi, 2015). At 3 AU from the Sun, when cometary activity was still low and when the spacecraft orbited the nucleus at radial distances of about 10 – 100 km, the ROSINA – COPS (Rosetta Orbiter Spectrometer for Ion and Neutral Analysis – Comet Pressure Sensor) sensor measured neutral densities of $n_n \approx 10^7$ cm^{-3}. This was consistent with a gas production rate of $Q \approx 10^{26}$ s^{-1}, which is more than 7000 times less than comet Halley's gas production rate during its perihelion passage in 1986 (Balsiger et al., 2007; Bieler et al., 2015).

The driving process in solar wind – comet interaction is the creation of cometary ions and their pickup and assimilation (or partial assimilation) into the solar wind flow. For instance, a study of ion composition and dynamics at comet Halley using Giotto's ion mass spectrometer resulted in observation of significant deflection and slowing of solar wind due to the pickup ion mass-loading process (Balsiger et al., 1986). Pickup ions are created by ionization of relatively slow neutral species, which are then subjected to the Lorentz force associated with the solar wind motional electric field and the interplanetary magnetic field. Photoionization and electron-impact ionization and charge exchange with solar wind protons create cometary photoelectrons and pickup ions. These processes are shown in representative equations, respectively:

$$h\nu + H_2O \rightarrow H_2O^+ + e$$

$$e + H_2O \rightarrow H_2O^+ + e + e \qquad 4.1$$

$$H^+ + H_2O \rightarrow H_2O^+ + H(fast)$$

An electron produced in the first reaction (i.e., a photoelectron) has an energy equal to the photon energy ($h\nu$) minus ionization potential of the neutral species. The charge exchange reaction does not produce an electron but does create a fast neutral H atom. Ionization potential depends on the photoion's final state. The newly-created ions are accelerated by the solar wind motional electric field:

$$\mathbf{E} \approx -\mathbf{u}_{sw} \times \mathbf{B}_{IMF} \qquad 4.2$$

that is about 5×10^{-4} V/m near 3 AU. $\mathbf{u}_{sw}$ is the solar wind velocity and $\mathbf{B}_{IMF}$ is the interplanetary magnetic field (IMF). The ions are also deflected by the magnetic field once they have been accelerated. Pickup ion trajectories start out as cycloidal with a length scale of several ion gyroradii $2\pi r_L$ where the gyroradius is given by: $r_L \approx \frac{u_{sw}}{\Omega} \approx 10^4$ km. The gyrofrequency is $\Omega = \frac{e\mathrm{B}}{m}$.

For an active comet, the pickup process is altered by wave-particle interactions associated with waves generated by unstable cometary ion distribution function. Wave-particle interactions tend to pitch-angle scatter ions and thus further assimilate them into the solar wind flow (Johnstone et al., 1993). During this interaction, momentum conservation will cause the mass loaded solar wind, which initially moves at supersonic speeds, to slow down to subsonic speeds and deflect. Transition of the solar wind from supersonic to subsonic speeds produces a bow shock upstream of the comet (Coates et al., 1991; Coates et al., 1997; Omidi and Winske, 1987).

Consequently, the solar wind magnetic field lines drape around the comet and pile up on the comet's sunward side. For comet Halley, the radial distance of the bow shock was about 30 times greater than the heavy ion gyroradii ($r_L \approx 10^4$ km), but for weaker comets (e.g., comet Giacobini-Zinner) this ratio is smaller and the interaction is less fluid-like (Koenders et al., 2013; Rubin et al., 2014b).

Inside the diamagnetic cavity, ions and neutrals move radially outward and interact with the magnetic field pile up region (Ip and Axford, 1987). Neutral species are unaffected by the enhanced magnetic field while cometary ions are likely to pile up as they approach the region of enhanced magnetic field. Previous studies show the electron-ion recombination has been a major sink for ions in the region just outside the cavity surface (Cravens et al., 1995; Goldstein et al., 1989; Puhl-Quinn and Cravens, 1995). For comet 67P/CG, some of these boundaries and regions may be observed only near perihelion, when the comet is more active and when collisional processes in the neutral coma become more frequent. Characteristics of these boundaries can also be quite different from comet 1P/Halley.

In this chapter I examine plasma observations at comet 67P/CG at different heliocentric and cometocentric distances and present theoretical explanations for the observations. I also discuss new physical processes in the cometary plasma that we learned from the Rosetta spacecraft's extended monitoring of the comet.

Some specific questions I try to answer throughout this chapter are:

1. How does fast moving solar wind flow impact a tenuous cometary atmosphere?
2. What are sources of ions and electrons in the cometary plasma?
3. How does the plasma vary as the comet becomes more active?
4. How do variable solar wind conditions (i.e., density, temperature, flow speed) affect

plasma boundaries?

4.2 Instrument Overview

4.2.1 IES Instrument

The Ion and Electron Sensor (IES) component of the Rosetta Plasma Consortium (RPC) package consists of two top-hat electrostatic analyzers that measure electron and ion counts over a large energy range of 4.3 eV/e up to 18 keV/e and over 2.8π str field-of-view of 360° in azimuth and 90° in elevation (Figure 4.1a). Appendix B includes a table of IES full resolution energy bin structure. The angular resolution for both electron and ion measurements is 5° in elevation, achieved by electrostatically sweeping 16 deflection voltages. There are 16 electron anodes, giving azimuth resolution of 22.5° for electrons. For ions, 9 anodes cover a 45° part of the azimuth in the solar wind direction, giving 5° azimuth resolution for precise solar wind measurements, plus seven anodes that cover the rest of the azimuth, giving 45° resolution in the non-solar wind direction (Figure 4.1b).

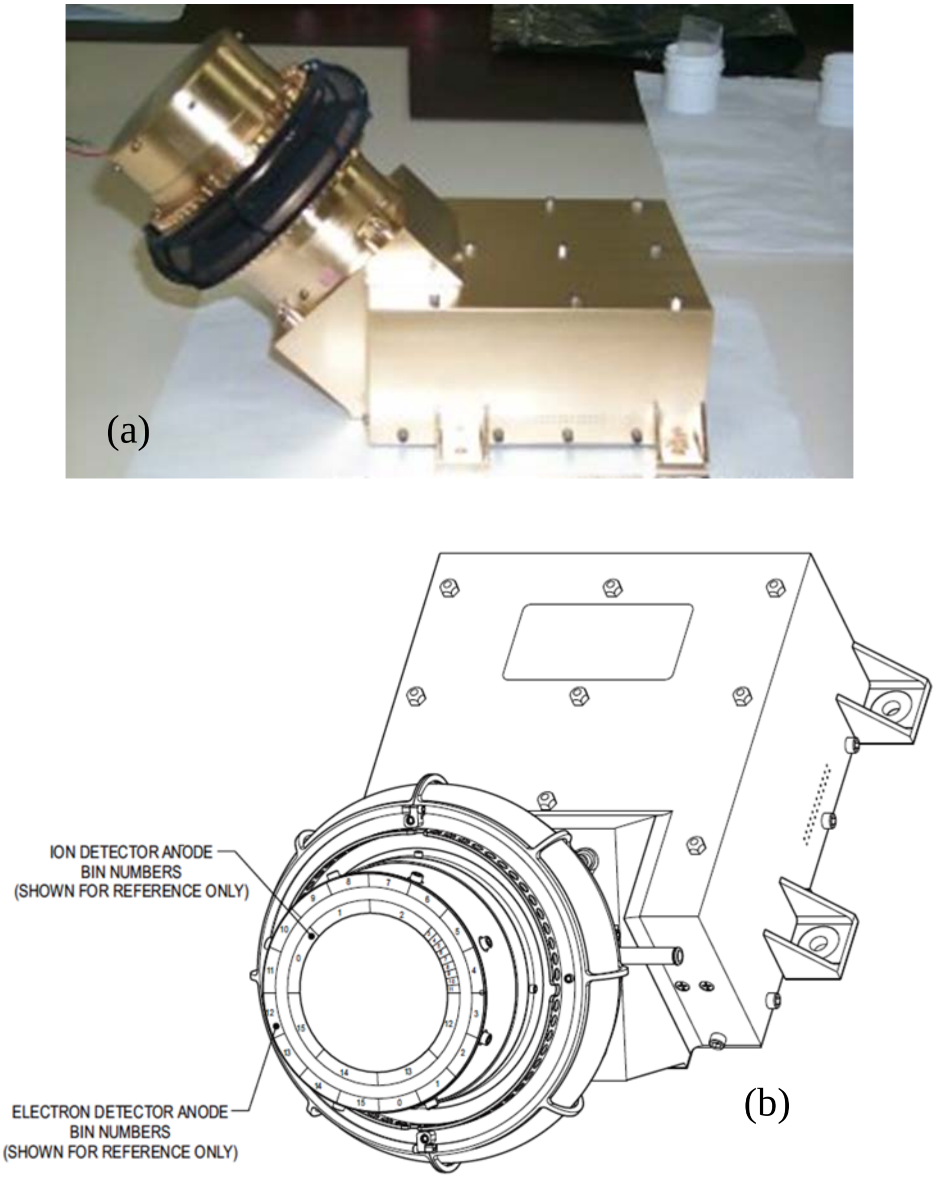

Figure 4.1 - (a) Photo of the IES instrument taken before mounting it on the spacecraft. The IES instrument was developed at the Southwest Research Institute, San Antonio, TX. (b) Schematic of IES anode arrangements for ion and electron detectors. Adapted from Burch et al. (2007).

The spacecraft body and other instruments mounted on the spacecraft block about 25% of the IES field of view. Most of this blockage is in low elevations of the IES field of view. I focus primarily focus on IES electron data from "central" anodes and elevation, for which the instrument response is best known and spacecraft blockages are not an issue.

IES counts are converted to physical fluxes by a conversion factor which takes appropriate solid angles and detector efficiencies into account (Burch et al., 2007). Count rates (dC/dt with units of s^{-1}) for a given direction and energy is given in terms of the differential electron flux by the expression:

$$\frac{dC_{ijk}}{dt} = G_{ij}(E_k)E_kF(\mathrm{n}_{ij}, E_k) \qquad 4.3$$

The instrument directional resolution was discussed above and the indices *i* and *j* denote channels. Energies sampled by IES (E_k) are labeled with index *k*. *F*(n, *E*) is the differential flux (in cm^{-2} s^{-1} eV^{-1} str^{-1}) in the direction given by unit vector n and at energy *E*. The reported geometric factor for IES, $G_{ij}(E_k)$, is 6×10^{-5} cm^2 str eV/eV for each ion pixel (per 5° elevation angle, per 45° azimuth angle) and 3×10^{-5} cm^2 str eV/eV for electrons. Due to non-gyrotropic distribution expected for pickup ions, different IES pixels see different parts of the pickup ion distribution. Assuming a noise level of 2 counts per second per look direction per energy bin, the detectable differential energy flux threshold for IES would be $\sim 2 \times 10^3$ eV/(cm^2 s eV). Due to data downlink constraints, adjacent energy bins and elevation steps are averaged and then transmitted for certain operation modes.

4.2.2 Langmuir Probe (LAP)

The Langmuir Probe instrument (LAP) is a set of two probes than can measure plasma density, electron temperature, and plasma flow velocity (Eriksson et al., 2007). Secondary scientific objectives for LAP include measuring spacecraft potential and electric field measurements up to 8 kHz.

Electron density and temperature are measured by sweeping voltage biased on the probe and measuring currents that the probe collects. For positive voltage potentials electrons dominate the current. Electron temperature and density can be measured from the shape of the I-V curve. At negative potentials, positive ions are collected and these measurements are used to derive average ion drift kinetic energy. Photoelectrons created by sunlight from the probe and other spacecraft surfaces interfere with measuring actual plasma particles in a weak plasma. Therefore, the two probes are mounted on the spacecraft that one of them will always be in the spacecraft structure’s shadow.

Figure 4.2 illustrates the mounting position of these two probes and other RPC suite plasma instruments on the Rosetta spacecraft. Probe 1 (LAP1) is mounted on a 2.24 m long boom, which is shared with the MIP instruments probe explained in the next section. The length of the boom supporting Probe 2 (LAP2) is 1.62 m (1.5 m boom + 12 cm probe length), which is shared with the MAG sensors. LAP probes are five meters apart from one another.

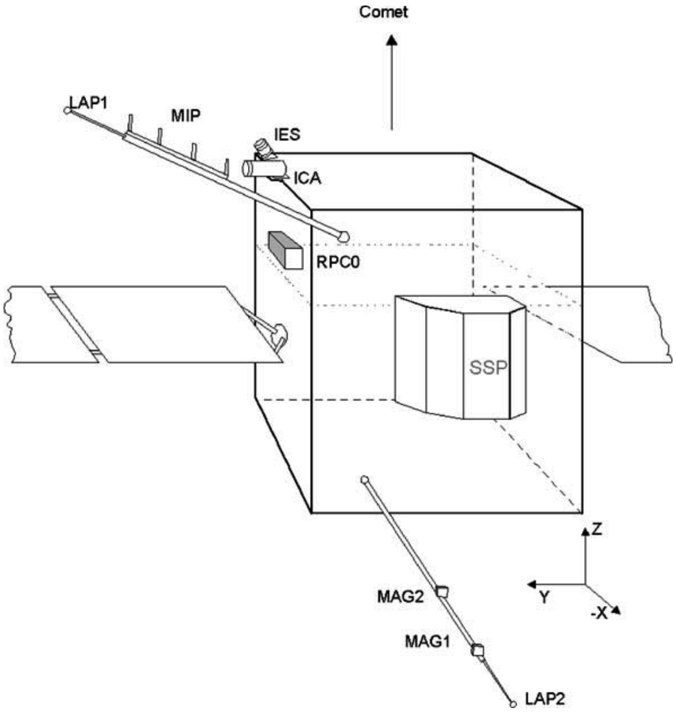

Figure 4.2 - Positions of RPC sensors on the spacecraft body. In this figure, +X direction is towards the Sun and comet direction is marked towards the top of the figure in +Z axis. The length of the supporting boom for LAP1 probe is 2.24 m and 1.62 m for the LAP2. Distance between LAP1 to LAP2 is five meters. Adapted from Eriksson et al. (2007).

4.2.3 Mutual Impedance Probe (MIP)

The RPC-MIP experiment is a mutual impedance probe that retrieves electron densities from the estimated position of the plasma frequency in the MIP complex mutual impedance amplitude and phase spectra (Trotignon et al., 2007). MIP data are available in Short Debye Length (SDL) and Long Debye Length (LDL) modes. Note that LDL mode enables us to estimate electron density in the 30-350 cm^{-3} range. This implies that MIP in the LDL mode is blind to the plasma densities below and above this observational window. By contrast, SDL mode only allows measurements very large densities. Figure 4.2 shows the position of the MIP probes on the spacecraft.

4.2.4 Magnetometer (MAG)

The MAG instrument, composed of two 3-axis fluxgate magnetometers (one inboard and one outboard), both of which are mounted on a 1.5 meter boom with 15 cm separation in between, obtains information about the magnetic field (Glassmeier et al., 2007b). Since the two magnetometers are positioned close to the spacecraft, magnetic field measurements are prone to noise contamination from other instruments and electronic components of the spacecraft. Comparisons of registered signals of the inboard and outboard sensors show that spacecraft noise affected the inboard sensor three times more than the outboard sensor (Richter et al., 2012). Entering magnetic field-free regions allowed the MAG instrument ground team to recalibrate the sensors and produce data that were more reliable.

4.3 Description of the Models

Similarities between the electron transport in Titan’s ionospheric plasma to cometary plasma are essential. In both environments, electrons move and gyrate along the magnetic field line. Hence, my models of the cometary plasma are similar, in principle, to Titan’s ionosphere models discussed in Chapter 2, but are modified for the comet environment. This excludes the photochemical model, however, since this this chapter focuses on electron observations. For the length and time scales that this research considers, the newly created cometary ions can be considered stationary. However, many large scale modeling studies of the comet interaction with solar wind have focused on the ion behavior. We refer to these studies as needed. Figure 4.3 provides an example of such simulations, with a close-up result of the hybrid simulation showing cometary ion densities around the comet in the plane containing the u_{sw} and the motional electron field (Rubin et al., 2014b).

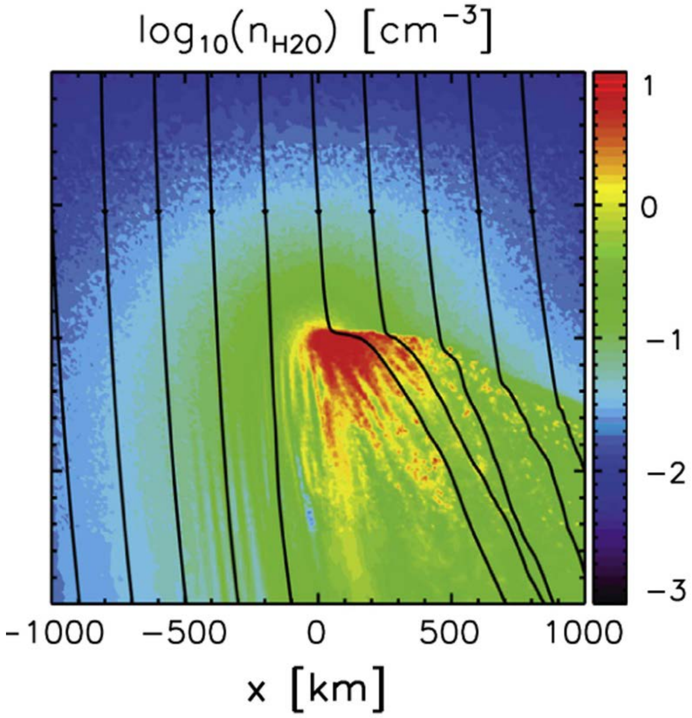

Figure 4.3 - Hybrid model predictions of solar wind interaction with the comet. The Sun is to the left in this simulation and IMF direction is into the page. Colorbar designates water group pickup ion densities in logarithmic scale. Solid black lines indicate electric field direction. Enhanced density region is evident in red colors. Note also the anti-solar deflection of the convection electric field near the nucleus. Adapted from Rubin et al. (2014).

4.3.1 Neutral Coma of Comet 67P/CG

In sections 4.4 and 4.5 we use models to interpret IES data. Such models start with the neutral density. Visual pictures of the comet taken by cameras onboard Rosetta reveal active regions on the comet that create an inhomogeneous environment of dust and possibly neutral gases around the comet. Neutral pressure measurements by the ROSINA-COPS instrument also observed this anisotropy attributed to the complicated shape and illumination pattern on the nucleus combined with the comet’s rotation (Hassig et al., 2015). Previous studies simulated the effect of asymmetric neutral gas distributions and jets in the plasma environment of a comet, and established that the presence of neutral anisotropy around the comet affects interaction of the solar wind with cometary plasma (Jia et al., 2008; Wiehle et al., 2011).

For simplicity, we assume spherical symmetry for neutral density. Although at times, gas production rate is greater in the sunlit northern hemisphere than in the south (Gulkis et al., 2015). At cometocentric distance *r*, total neutral density is given by:

$$n_n(r) = \frac{Q}{4\pi u_n r^2} \tag{4.4}$$

where Q ($\approx 10^{26}$ s^{-1}) is gas production rate of the comet at 3 AU, u_n ($\approx$ 1 km/s) is neutral outflow speed, and *r* is cometocentric distance. The total neutral density from equation 4.4 at $r \approx 30$ km is about 10^7 cm^{-3}. Water was the most abundant species at comet 1P/Halley coma. We assume H_2O accounts for 85% of the total neutral density, while the other 15% is shared between CO_2 (8%) and CO (7%). ROSINA instruments observed considerable variability in the neutral coma, which was associated with the comet's rotation (Hassig et al., 2015). Nonetheless, on average, our neutral profile agrees with the ROSINA observations.

4.3.2 Two-Stream Electron Transport Model

Electrons in the cometary plasma can originate from two sources, which include:

1. The solar wind electrons.
2. Photoelectrons from the ionization of cometary neutral gas.

Solar photons with energies exceeding the ionization potential of the neutral species create ions and photoelectrons. Here, we use the same solar extreme ultraviolet irradiance model for solar minimum conditions as we did in Chapter 2 for Titan. We made adjustments for the comet's heliocentric distance. Photoionization and photoabsorption cross sections for H_2O, CO_2 and CO were used for calculating photoelectron production rate as a function of cometocentric distance and electron energy (Gan and Cravens, 1990). Electron production rates were then used as an input to the two-stream electron transport code that determines steady state electron fluxes as a function of energy and position along the field line.

H_2O, CO_2, and CO cross sections as a function of energy for photoabsorption (Figure 4.4), photoionization (Figure 4.5), electron-impact ionization (Figure 4.6), and elastic scattering (Figure 4.7) processes (Gan, 1991) are presented in the following figures.

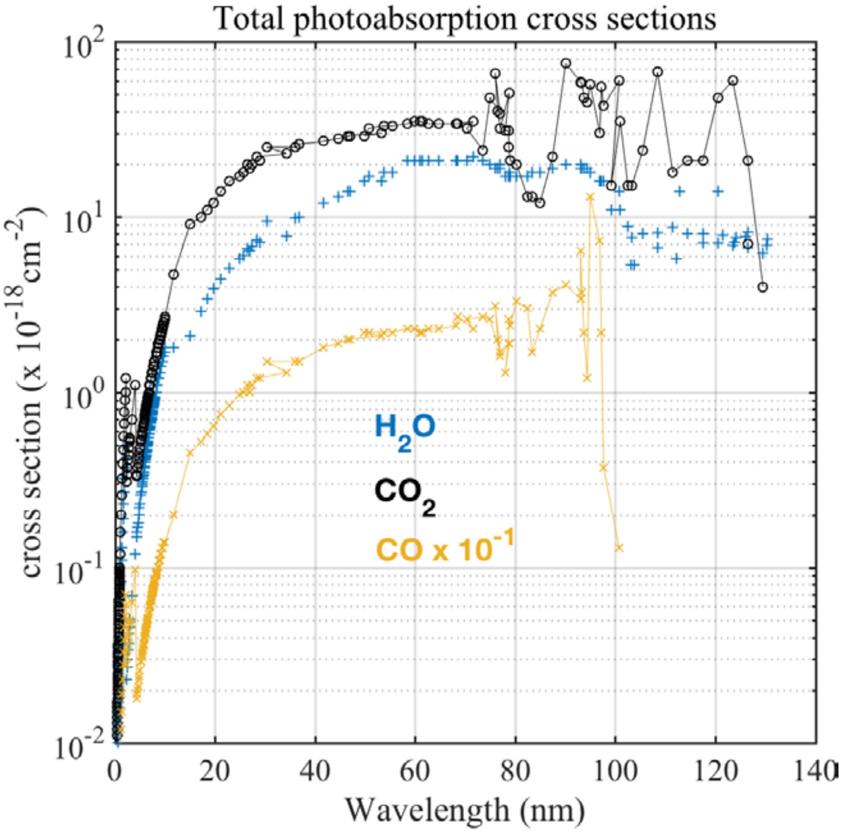

Figure 4.4 – Photoabsorption cross sections as a function of incident photon wavelength (*nm*). H_2O, CO_2, and CO values are presented with blue, black, and yellow colors, respectively. CO cross section values are reduced by a factor of 10 to avoid cluttering the graph. The ordinate is in units of 10^{-18} cm^{-2}.

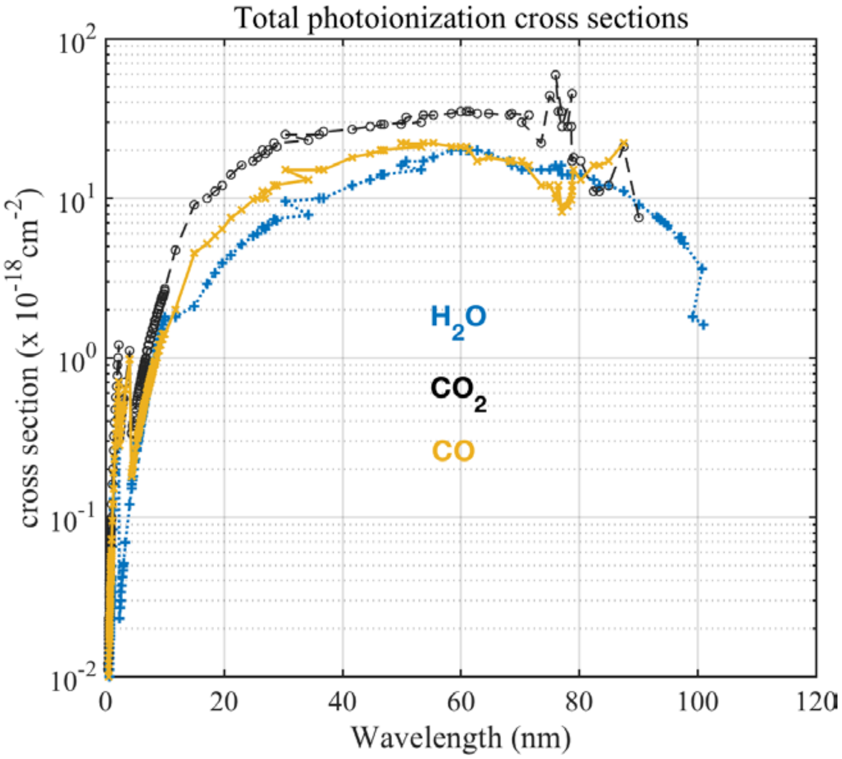

Figure 4.5 - Total photoionization cross sections of H_2O, CO_2, and CO as a function of incident photon wavelength (nm). The ordinate is in units of 10^{-18} cm^{-2}.

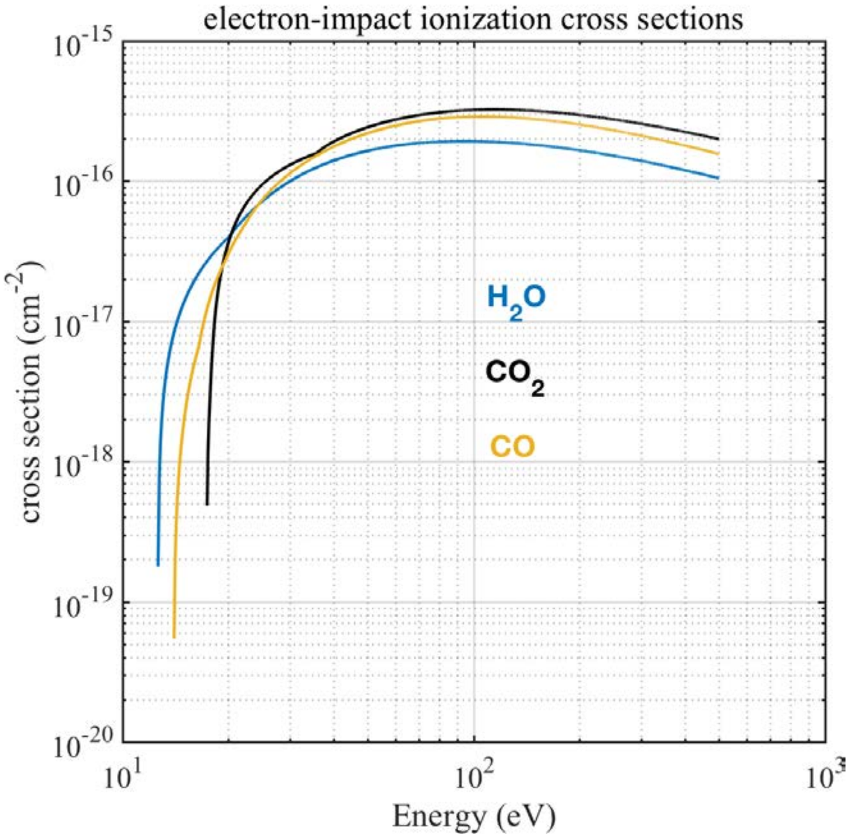

Figure 4.6 - Electron-impact ionization cross sections of H_2O, CO_2, and CO as a function of electron energy (eV).

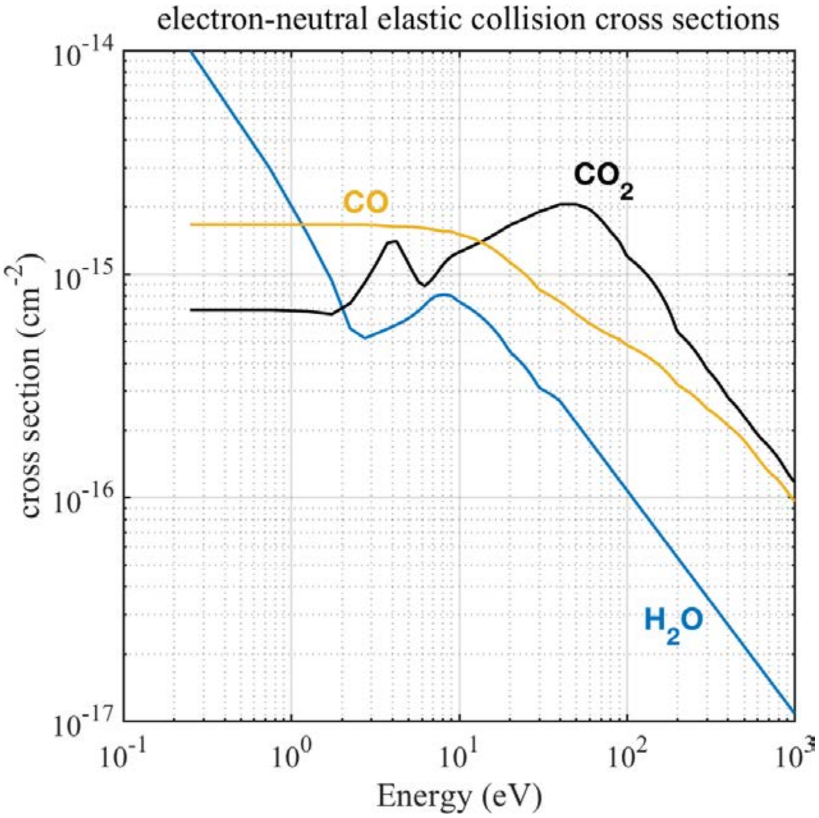

Figure 4.7 - Electron-neutral elastic collision cross sections of H_2O, CO_2, and CO as a function of electron energy (eV). Cross sections for H_2O, CO_2, and CO are presented with blue, black, and yellow lines, respectively.

4.3.3 Ambipolar Electric Field and Quasi-neutrality

No comprehensive model to simulate the effect of ambipolar electric field on the electron distribution function at comets has been published. In this section, I present a simplified treatment of ambipolar electric field effects using the two-stream model.

The generalized Ohm's law (GOL) is a form of the fluid electron momentum equation. This specifies the required electric field to preserve quasi-neutrality conditions in the plasma:

$$\mathbf{E} = -\mathbf{u}_e \times \mathbf{B} - \frac{1}{en_e}\nabla p_e + \eta\mathbf{J} \qquad 4.5$$

Magnetic field is denoted by **B**, electron pressure is $p_e = nk_bT_e$, and **J** is current density. Electron bulk flow velocity, $\mathbf{u}_e$, can be transformed into bulk mass-averaged flow velocity, **u**, plus electron current velocity, which then introduces the Hall term ($\frac{\mathbf{J}\times\mathbf{B}}{en_e}$):

$$\mathbf{E} = -\mathbf{u} \times \mathbf{B} + \frac{1}{en_e}\mathbf{J} \times \mathbf{B} - \frac{1}{en_e}\nabla p_e + \eta\mathbf{J} \qquad 4.6$$

This form of the GOL neglects the inertial terms and the effects of all collision terms are collected into the resistivity, η, in the *Ohmic* term (i.e., the last term).

The component of the electric field along the magnetic field is mainly the ambipolar (or polarization) term: $\mathbf{E}_{pol} = -\frac{1}{n_e e}\nabla p_e$. The component of this field parallel to the magnetic field is given by $\mathbf{E}_{pol} = -\frac{1}{n_e e}\frac{dp_e}{ds}$, where s is distance along the field line. The pressure is the second moment of the electron distribution function and is the average kinetic energy per unit volume in the electron bulk flow frame of reference ($p_e \approx n_e\langle KE\rangle$). Overall electrical potential difference along a magnetic field line between the center of the ion density structure and the outside is roughly the average electron kinetic energy divided by the electron charge: $\Delta V_{pol} \approx \frac{\langle KE\rangle}{e}$. Electrons created within the dense plasma region with energies less than $\sim\Delta V_{pol}$ will be confined (or partially confined) to the vicinity of the nucleus. However, other effects such as $\mathbf{E} \times \mathbf{B}$ drift can remove electrons from this region. External solar wind electrons are accelerated inward (roughly towards the nucleus) by this potential structure and will have their energies enhanced by $\sim e\Delta V_{pol}$. There is no doubt that the motional electric field ($\mathbf{E} = \mathbf{u}_e \times \mathbf{B}$) contribution to **E** from the GOL is altered from its unperturbed solar wind value by interaction with the comet.

Figure 4.8 illustrates our idea of what the plasma environment near the nucleus might look like. Near 3 AU, pickup ions initially move in the direction of the convection electric field and are unaffected by the magnetic field near the nucleus. The ambipolar field is indicated in the schematic. This should partially confine lower energy photoelectrons to the ion density structure. This electron field will accelerate solar wind electrons towards the density enhancement region.

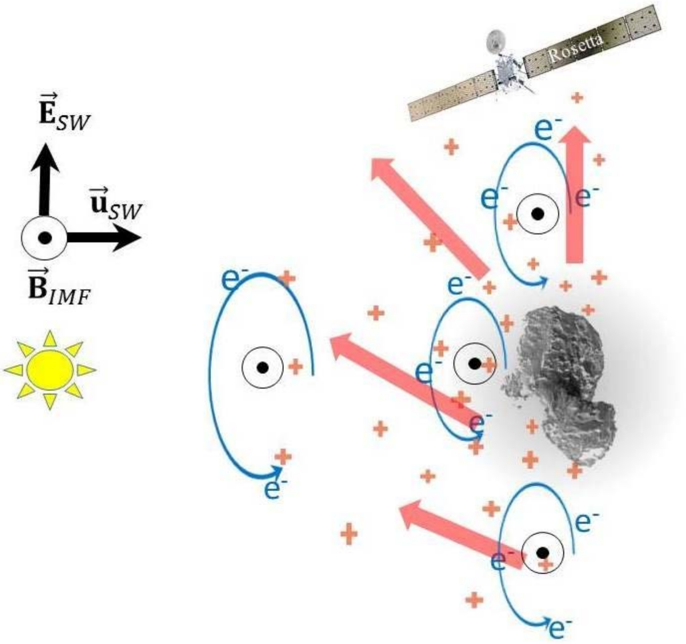

Figure 4.8 - Schematic of plasma and fields. Solar wind electrons and photoelectrons are indicated along with cometary pickup ions. Location of the spacecraft is about 10 km from the nucleus. The electric field, which is a combination of motional electric field and ambipolar field, is also illustrated schematically with red arrows. Magnetic field is assumed to be out of the page.

Sections 4.4.3 and 4.5.3 discuss model results.

4.4 Comet at 3 AU

On August 7, 2014, when Rosetta was at a distance of 100 km from the comet, the ICA instrument started to detect water group ions originating from ionization of the cometary neutral environment (Nilsson et al., 2015). At that time, the outgassing rate of the comet was around 10^{26} s^{-1}. A weak interaction between the solar wind and the cometary neutral coma was predicted for such a production rate (Hansen et al., 2007; Koenders et al., 2015). Later, on September 21, 2014, solar wind protons detected by ICA were found to be deflected from the sunward direction by about 20-30°. This was attributed to conservation of momentum associated with production of cometary pickup ions. ICA observed water group ions with energies up to ~1 keV in a direction opposite to the deflection of the solar wind, as predicted by conservation of momentum.

Measurements of electron densities by LAP and MIP near comet 67P/CG showed values between about 40 and 200 cm^{-3} with an average variation that goes inversely as cometocentric distance r, albeit with large variance due to variations in comet latitude and longitude (Edberg et al., 2015c). There is also good correlation between the electron density and the neutral density measured by ROSINA-COPS (Odelstad et al., 2015).

Trajectories of solar wind protons and alpha particles exhibit modest deflections (several degrees) along with some attenuation (30%) in density due to charge exchange collisions with cometary neutrals (Broiles et al., 2015; Goldstein et al., 2015). The IES and the ICA instruments of RPC both showed deflected protons and pickup cometary ions, with energies ranging from a few eV up to somewhat less than 1 keV, which is much less than the energies expected for fully picked-up ions. The IES has measured occasional pickup ions with energies as high as 17 keV. Interestingly, a beam of H^- ions at solar wind energies (1 keV) was detected by the electron spectrometer and was attributed to two stages of charge exchange (Burch et al., 2015). The proton and pickup ion observations largely confirm predictions made using hybrid and multifluid simulations of the solar wind interaction with the distant comet 67P/CG (Rubin et al., 2014b).

Solar wind interaction with comet 67P/CG at the end of 2014 when it was located near 3 AU, is very different from solar wind interaction with active comets studied previously. Gas production rate was low ($Q \approx 10^{26}$ s^{-1}) and a typical IMF field strength at this heliocentric distance is low ($B \approx 1$ nT). Furthermore, Rosetta was very close to the nucleus ($r \approx 10$- 200 km). Cometary ion gyroradii in the solar wind at 3 AU are about $r_g \approx 3 \times 10^4$ km, more than 1000 times greater than the radius of the nucleus. This means that pickup ions nery near the nucleus are "unmagnetized" (Goldstein et al., 2015; Gulkis et al., 2015; Nilsson et al., 2015). Multifluid and hybrid simulations for this type of interaction have shown that the electric field accelerates cometary ions created near the nucleus. These ions are initially slow-moving such that near-nucleus density ($n_i \approx 10$ - 100 cm^{-3}) is much greater than the solar wind proton density ($n_{sw} \approx 0.5$ cm^{-3}). Table 4.1 summarizes solar wind conditions for 3 AU.

Table 4.1 - Typical Solar Wind Parameters for a Heliocentric Distance of 3 AU

n_{sw} (cm^{-3})	u_{sw} (km/s)	T_{sw} (K)	B_{sw} (nT)	M_{ms}	r_{psw} (km)	r_{PUIsw} (km)
0.5	500	10^5 (≈10 eV)	1	6	10^3	2×10^4

n_{sw}, u_{sw}, T_{esw}, B_{sw}, and M_{ms} are the solar wind density, speed, electron temperature, magnetic field strength, and magnetosonic (i.e., fast mode) Mach number, respectively. r_{psw} (km) and r_{PUIsw} (km) are proton and heavy cometary pickup ion gyroradii, respectively.

The IES instrument started to detect low energy ions in its lowest energy channels in mid-August of 2014, just a few weeks after the spacecraft's arrival at the comet. Figure 4.9 shows example spectrograms from the ion sensor of IES for October 23, 2014, when the comet was at 3.12 AU and the spacecraft was at a distance of 10 km from the comet. The low energy ions observed can be attributed to negative spacecraft potential, which attracted newly born ions to the instrument. Data from the RPC-LAP instrument at 30 km cometocentric distance in early September showed electron fluxes were high enough to start driving the s/c to negative potentials (Odelstad et al., 2015). On October 23, the spacecraft potential was consistently negative, at around -10 to -20 V. Higher energy pickup ions have also been observed starting in September

2014. These ions were thought to have been energized by solar wind motional electric field before they reached the spacecraft.

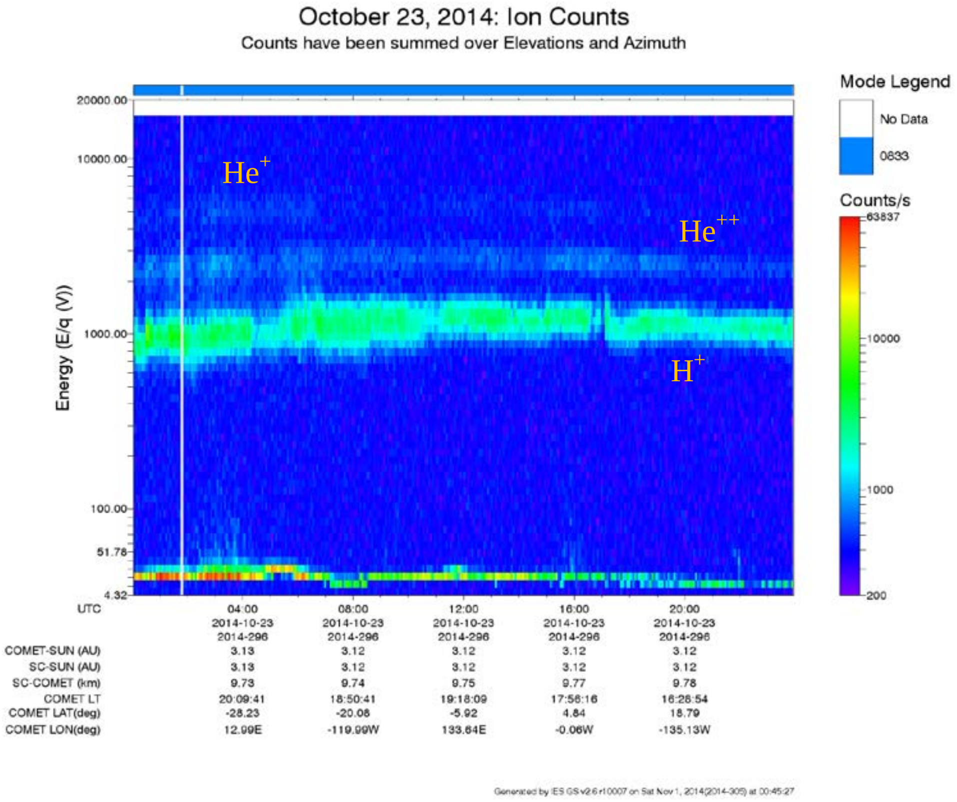

Figure 4.9 - IES ion spectrogram for October 23, 2014. The colorbar shows counts per second per energy bin for the ion sensor. The ordinate shows energy in units of eV and the abscissa is time (heliocentric and cometocentric distances are also shown). Higher energy counts are due to solar wind protons and alpha particles. Low energy counts are thought to be cometary pick-up ions.

Water group ion gyro-radii are very large (~10^5 km) compared to the nucleus size (~4 km) such that newly born pickup ions begin their trajectory parallel to the solar wind motional electric field. This field is approximately 0.5 V/km for typical undisturbed solar wind at 3 AU. Hence, most ions born within about 30 km of the nucleus and reaching the spacecraft should have energies less than roughly 30 eV. Thus, these ions are detectable only in the lowest couple of IES energy bins, except when the spacecraft is negatively charged, which enhances the ion energies.

The most obvious features in the ion spectra are not the pickup ions but rather solar wind protons (H^+) and alpha particles (He^{++}), which are detected at energy/charge channels of ≈ 1000 and ≈ 2000 eV/e, respectively. Some charge-exchanged solar wind alpha particles (producing He^+) are also seen at 4000 eV/e. Solar wind protons were observed to be deflected from the anti-sunward direction by tens of degrees. Alpha particles are deflected by smaller angles because of the acceleration of pickup ions in the opposite direction.

4.4.1 IES Data for Late 2014 and Early 2015- Electron Fluxes

Figure 4.10 shows a color spectrogram of IES electron count rates. When measured near the comet, electron count rates greatly exceed typical solar wind electron count rates and count rates are large over a wide range of energies up to 100 - 200 eV.

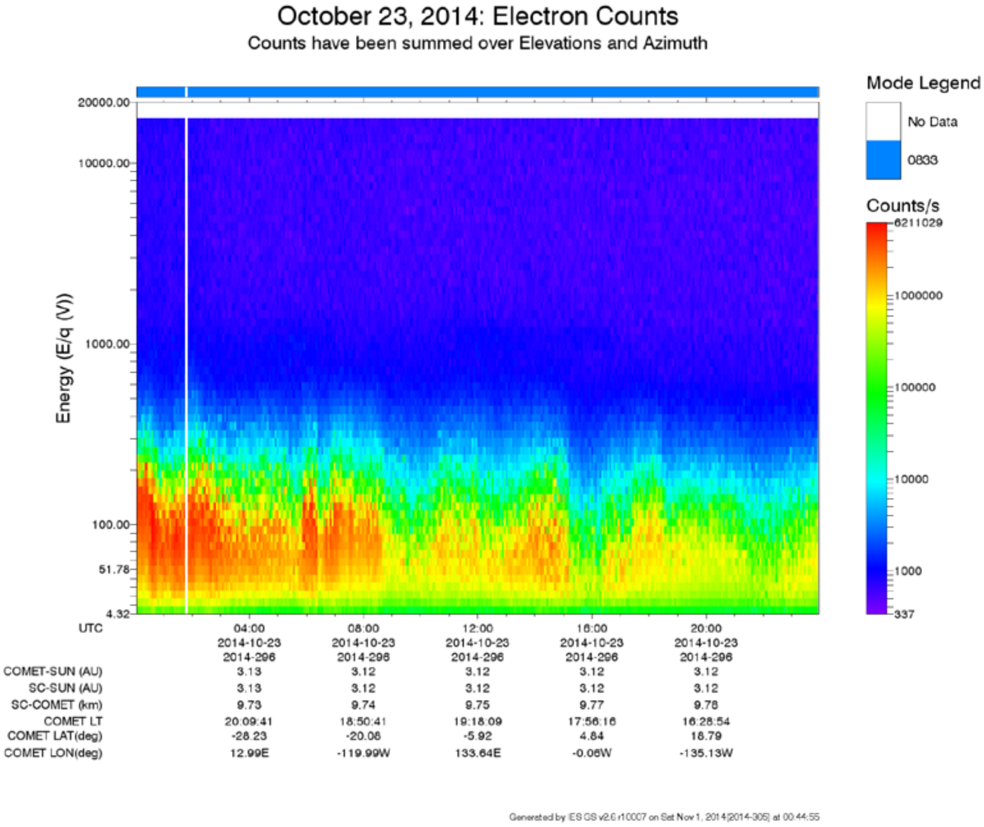

Figure 4.10 - IES color spectrogram showing electron count rates (colorbar) versus energy (vertical axis) and time (horizontal axis). Time variations have been shown to be associated with neutral density measured by the Rosetta ROSINA instrument.

Figure 4.11 shows electron differential particle flux spectra for several days at different heliocentric and cometocentric distances. The spectra are daily averages of the IES measurements. The grey curve in Figure 4.11 shows a solar wind type spectrum from August 1, 2014, when Rosetta arrived in the vicinity of 67P at about 900 km. The comet was at 3.6 AU from the sun with a quite low gas production rate. This spectrum can be fitted with a bi-Maxwellian distribution with two suprathermal electron temperatures, hot and core (fit is not shown). Rosetta approached to closer distances to the comet as low as 9.5 km during October. The black curve in Figure 4.11 is from October 2, where the spacecraft is only 18 km away from the comet's center of mass and well within the coma. This spectrum's composition is mainly surface photoelectrons, photoelectrons from photoionization, and secondary electrons. On October 22, at around 16:30 UTC, a solar wind pressure pulse (identified as a coronal mass ejection or CME), that had merged with a corotating interaction region (CIR) struck the comet and lasted until mid-day of October 23. For simplicity, we refer to this event as the CME event of October 23 throughout the rest of this chapter. The spectrum in purple is measured during this event. A feature in this spectrum at around 1000 eV is particularly noticeable. By the end of October, the spacecraft started to move away from the comet while making measurements at constant orbits (e.g., 10 km, 30 km) for several days. The red curve is from November 5, 2014, when Rosetta was 31 km from the comet. In February 2015, the spacecraft performed a series of maneuvers to make measurements at various distances (more discussion of this event is given below Figure 4.14). In late March 2015, high energy ion counts due to solar wind disappeared from the IES spectrograms, indicating that a substantial amount of plasma is present near the comet to block solar wind from reaching the spacecraft. The spectra in green and blue in Figure 4.11 are from March 23 and June 5, 2015, when the comet was significantly more active.

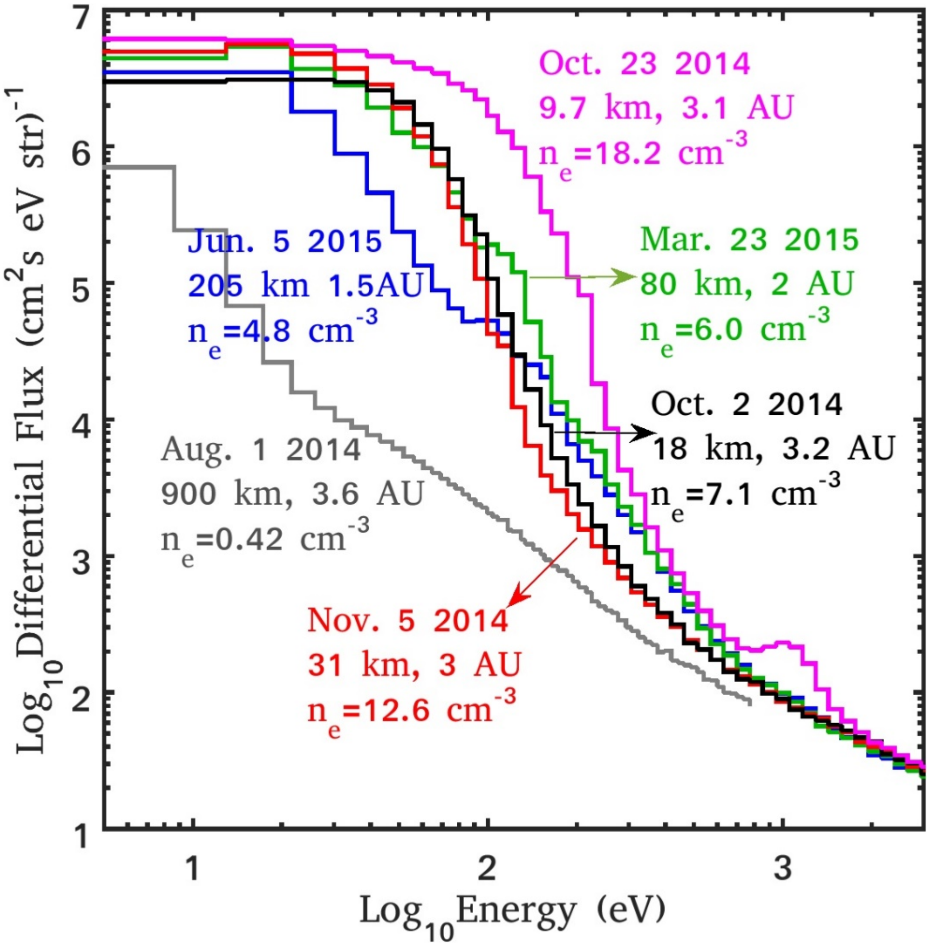

Figure 4.11 - Daily averaged electron differential flux using IES measurements on August 1, 2014 (grey), October 2, 2014 (black), October 23, 2014 (purple), November 5, 2014 (red), March 23, 2015 (green), and June 5, 2015 (blue). The spectrum from August 1, 2014, shows a typical solar wind type electron flux. The October 23, 2014 spectrum was measured during a CME event. The figure indicates distance to the comet in km and distance to the Sun in AU for each spectrum. The other four spectra are typical differential fluxes at the given cometocentric distances.

Differential flux spectra are calculated from the instrument count rates, according to equation 4.6. The IES detection panels record different electron count rates even when the spacecraft is inside a presumably isotropic plasma environment. There are several reasons for this result, including blockage by other spacecraft instruments, IES detection efficiency, and spacecraft potential. The colorbar in Figure 4.12 shows the phase space distribution function amplitude of electrons for individual panels of the IES electron sensor. The top plot is for 100 eV electrons on

September 17, 2014, averaged between 15:00-16:00 UTC. The bottom plot shows the 13 eV electrons measured on October 17, 2014, averaged between 7:00-11:00 UTC. Phase space distribution function for a given energy and direction is obtained through the following expression:

$$f(E,\Omega,r) = \frac{m_e^2}{2E}\frac{d\varphi}{dEd\Omega} \qquad 4.7$$

where $\frac{d\varphi}{dEd\Omega}$ is the differential particle flux similar to the F parameter in equation 4.6, and m_e is the mass of the electron.

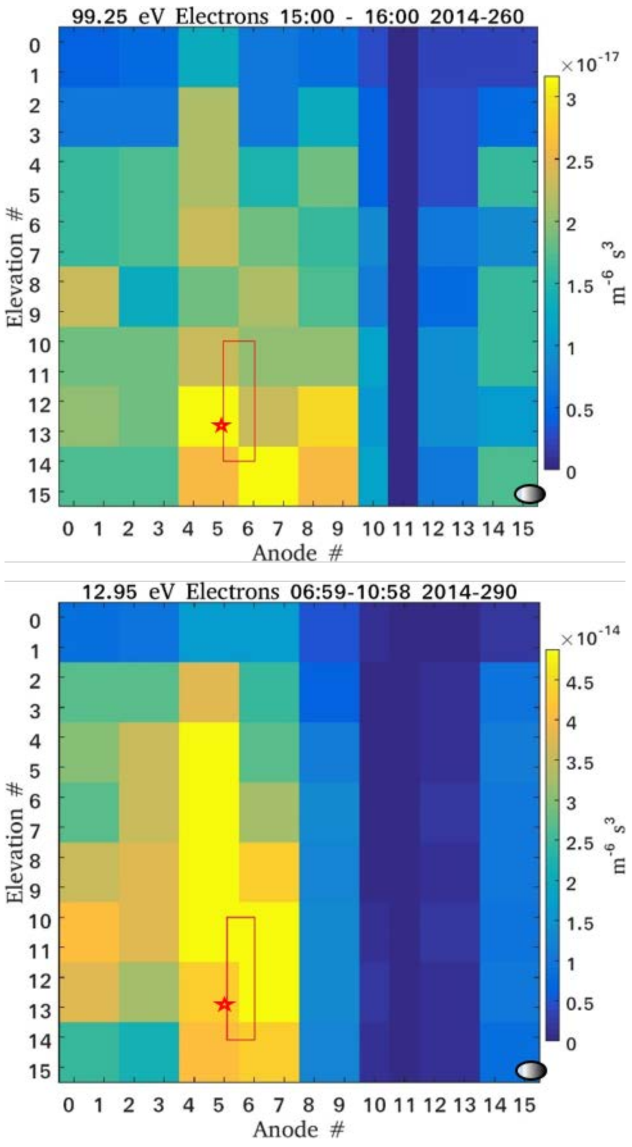

Figure 4.12 - (Top) Phase space distribution function for each IES panel, using corresponding count rates of 100 eV electrons. Data are from September 17, 2014, averaged over 15:00 -16:00 UTC. Colorbar shows amplitude of the phase space distribution function ($m^{-6} s^{3}$) in linear scale. The detection mode on this day combined every two adjacent elevation steps and anodes and energy steps. (Bottom) Phase space distribution function for October 17, 2014, 7:00-11:00 UTC for 13 eV electrons. The IES mode is the same as the top plot. The colorbar shows the amplitude of phase space distribution function ($m^{-6} s^{3}$). Electron counts are mostly seen near anodes 4-7 and elevation steps 10-14. In both plots, positions of the Sun and the comet are shown with a red star and grey oval, respectively.

Electron counts in Figure 4.12 have been averaged for each two adjacent elevation steps and anodes. Counts have also been summed over two adjacent energy bins of the energy sweep. Anodes 4-7 and elevation steps 10-15 clearly show higher yield and are not subject to spacecraft blockage. Therefore, we only used electron counts that are averaged over anodes 5-6 and elevations 10-14 (enclosed with red boxes in Figure 4.12), and assumed an isotropic distribution to calculate flux and density of electrons. In some measurements, it is possible to observe higher counts in panels outside the selected range, but we used the same set of panels for all measurements to expedite the data handling processes.

4.4.2 Multi-Instrument Analysis of the Electron Densities

We obtained suprathermal electron densities and their average energies for the measured spectra by assuming isotropy and by simply integrating such spectra using only the central anodes and elevations. For isotropic plasma in the velocity space, electron density can be calculated by:

$$n_e = 4\pi \int_0^{inf} f(v) v^2 dv \tag{4.8}$$

For isotropic plasma in energy space, one can calculate density with the following expression:

$$n_e = 2\pi\sqrt{2m_e} \int_{4.3\ eV}^{inf} \frac{1}{\sqrt{E}} \left(\frac{d\varphi}{dEd\Omega}\right) dE \tag{4.9}$$

Additionally, average energy of electrons can be calculated by using the following expression:

$$\langle E\rangle = \frac{2\pi\sqrt{2m_e}}{n_e} \int_{4.3\ eV}^{inf} \sqrt{E} \left(\frac{d\varphi}{dEd\Omega}\right) dE \tag{4.10}$$

The integration is carried out over the full range of IES energies starting from the first energy step. This means that electrons with energies lower than a couple of eV (which includes possible cold electron population) will not contribute to our electron densities. The IES energy sweep begins at 4.3 eV. Plus, a negative spacecraft potential will repel even more of the electron population.

Figure 4.13a shows IES electron densities versus distance to the comet from early August 2014 to the end of February 2015. Data points are color coded based on times of measurements. The data only include days where the IES measured continuously in certain detection modes. Figure 4.13b shows the density time series when Rosetta hovered around the comet at about 10 km for a couple of days in October. The IES electron densities (blue dots) are compared with the LAP (green dots) ion densities and the MIP-LDL and SDL electron densities (grey dot and black dots, respectively) for the period between October 16 and October 28, 2014.

Figure 4.13c, on the right axis, shows the average energy of suprathermal electrons calculated from IES data. Typical $\langle E \rangle$ is around 10-30 eV but reached 80 eV on October 23. Time of the CME event is also marked with a vertical dashed line in Figure 4.13b and c. The CME event on October 23, 2014 triggered a very negative spacecraft potential preventing LAP from measuring electron densities on that day. We used MIP electron densities and LAP ion densities instead, for comparison.

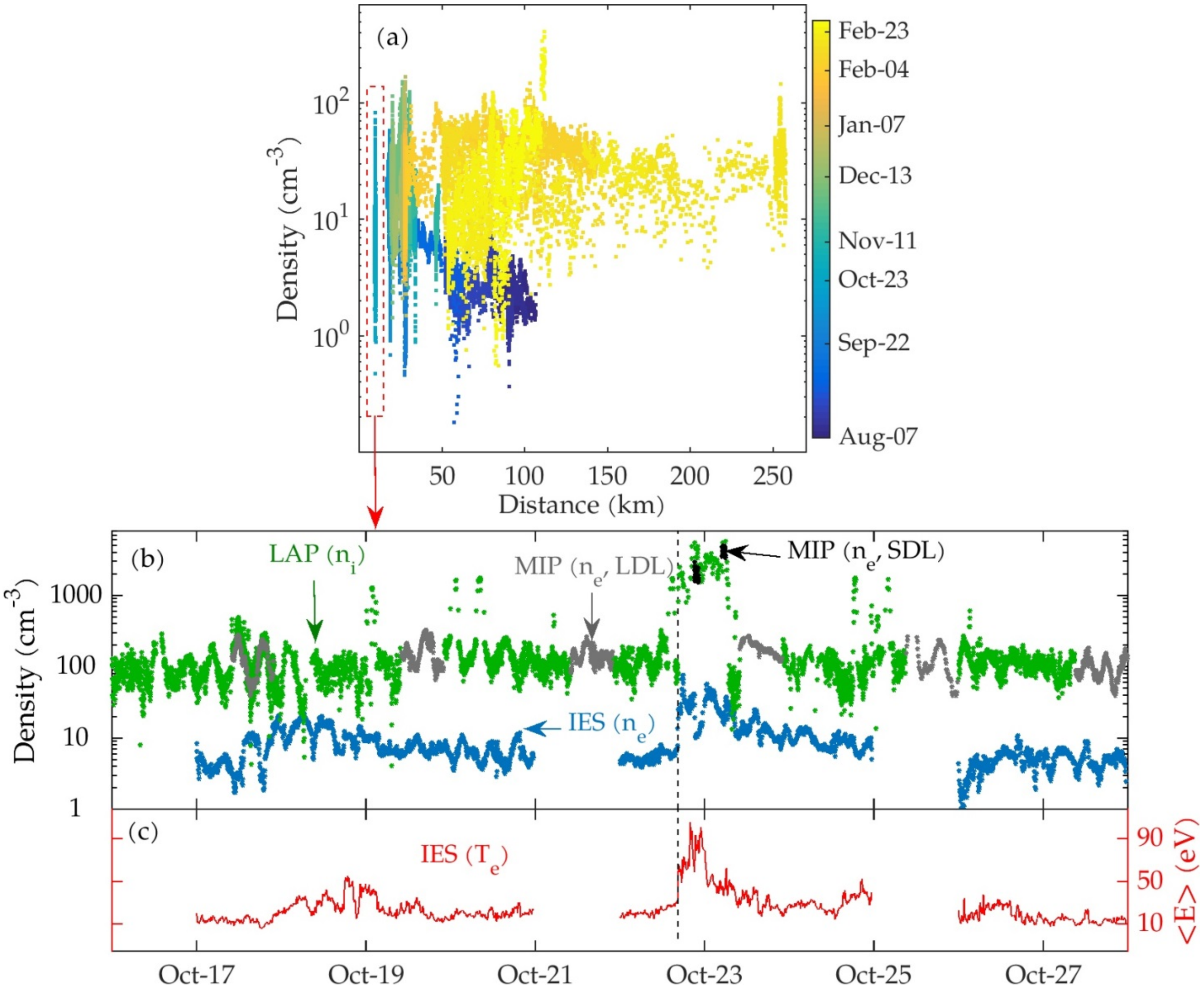

Figure 4.13 - (a) Electron density versus distance to the comet. Data include all days between August 2014 to February 2015, when IES operated continuously on certain modes. Points are color-coded based on times of measurements. The time series for the points near 10 km (indicated by the red rectangle) is shown in panels b and c, which correspond to data between October 16 to October 28, 2014. (b) Time series of IES electron densities (blue dots), LAP ion densities (green dots), and MIP electron densities (grey dots for LDL mode and black dots for SDL mode) are shown. (c) Average suprathermal electron energy from IES data is shown with the red curve with corresponding values on the right axis. The vertical dashed line near October 23 shows onset of enhanced count rate observations due to the CME event.

Figure 4.13a shows IES densities are ≈ 3 - 20 cm^{-3}, where typical solar wind densities at 3 AU are ≈ 0.5 cm^{-3}. Large time variations are evident, with excursions up to about 100 cm^{-3}. The variations appear to be linked with neutral density variations as measured by the ROSINA-COPS sensor (Madanian et al., 2016b). The electron and ion densities measured by LAP and MIP are very comparable and in principle include electrons of all energies. These densities are several times greater than the IES densities that are suprathermal electron densities, due to different detection methods. Evidently, a population of electrons with energies less than ≈ 5 eV exists that IES cannot detect, especially if there is a high spacecraft potential. There seems to be an anti-correlation in density variations between the LAP/MIP and the IES. A dip in the LAP (MIP) ion (electron) densities coincides with an enhancement in the IES data. Given the uncertainties in our methodology, there are a couple of possibilities to explain this anti-correlation. It can be a direct result of bulk plasma flow, or it can be due to the change in the direction of the incoming flow into the IES caused by the spacecraft potential and pointing. Given the correlation between ROSINA-COPS neutral density measurements and LAP (MIP) ion (electron) densities, the anti-correlation between IES and LAP (MIP) ion (electron) densities arguably stems from the fact that at each upsurge of neutral species (i.e., H_2O, CO_2, CO), suprathermal electrons become thermalized through electron-neutral collisions. In addition, secondary and tertiary electrons are produced, which contribute to LAP/MIP measured densities. Suprathermal electron distribution may have solar wind origin or be produced by photoionization; it can also be accelerated inward through various processes such as ambipolar electric field.

The Langmuir probe on Rosetta indicated that the spacecraft (s/c) had an electrical potential relative to the ambient plasma of about $V_{s/c} \approx -5$ V to - 20 V (Edberg et al., 2015c). It is well-known that spacecraft, dust grains, etc., can acquire electrical charge (and thus potential) in space due to several types of charging currents, including ambient plasma electron and ion currents and photocurrents from absorption of solar photons (Hsu et al., 2012). At 3 AU, the cometary nucleus itself should have an electrical potential. Furthermore, spacecraft potential affects comparison of model spectra with IES data, in that instrument cannot detect lower energy (less than the potential) electrons.

In February 2015, a series of maneuvers by Rosetta provided an opportunity to compare IES electron densities with other instruments at short and long cometocentric distances.

In Figure 4.14, the IES electron densities averaged every 5 km are shown with blue squares and LAP electron densities (5 km averaged) are presented with green circles. The LAP data extend to shorter distances than IES as the close approach occurred on February 16. This date is not included in the IES analysis due to poor quality of the IES data. IES electron densities are higher than the LAP measured densities when Rosetta is far from the comet (r > 100 km). This relation tends to reverse as the spacecraft moves closer to the comet.

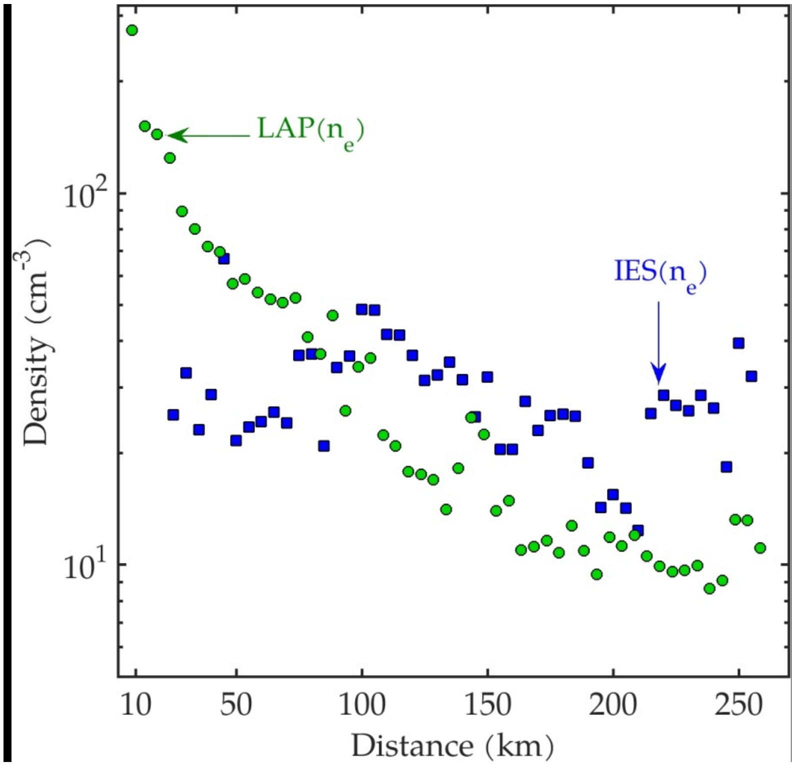

Figure 4.14 - Electron density versus distance to the comet. Data are from February 4-28, 2015. Blue squares represent IES electron densities averaged every 5 km. Green circles represent the LAP 5-km-averaged electron densities are shown with green circles. IES observation on February 16, when Rosetta descended to distances as close as 8.5 km are not included due to poor quality.

Since LAP measures all electrons and IES measures only suprathermal electrons, one would expect that LAP densities would always exceed IES densities. However, at far distances where densities are low, spacecraft potential is positive. In these circumstances, LAP and IES data will also be perturbed by the cloud of spacecraft photoelectrons, particularly for LAP, which measures the integrated flux from all populations. LAP electron density estimates assume that electron temperature can be correctly deduced from the LAP sweeps. Notably, IES densities are calculated only approximately, using just part of the distribution function. A reasonable interpretation of Figure 4.14 is that beyond $r \approx 100$ km the overall electron population is hot and IES observes most of the electron distribution. By contrast, close to the nucleus a cold ($E < 4$ eV) electron population is present and not observed by IES.

4.4.3 Model Cases for Cometary Suprathermal Electrons and Results

Modeling the highly variable electron distribution function near the comet is very difficult. Using models described in section 4.3, we considered several model cases for comet at 3 AU:

1. An electron flux obtained when solar radiation directly photoionizes the surface of the nucleus, sending electrons directly along the magnetic field to the spacecraft. This was carried out by neglecting the coma gas but including photoelectrons produced directly from the surface of the nucleus via photoionization by solar radiation. This procedure would be applicable only for locations where magnetic field lines connect the nucleus to the spacecraft. For this case, we adopted a 5% photoelectron emission efficiency at all photon wavelength/energies and a 5 eV surface work function potential (Weingartner and Draine, 2001).

2. Photoelectrons from photoionization of the coma gas plus solar wind electrons (0.7 cm^{-3} density at 10 eV temperature and 0.005 cm^{-3} at 100 eV), modeling these with the two-stream model for a draped magnetic field but without an ambipolar field.

3. Spectra from the two-stream code with coma photoelectrons plus solar wind electrons, but including a modified boundary condition designed to approximate effects of E_{pol}.

4. Model electron fluxes from the preceding case, but also imposing effects of compression of a fluid parcel near the nucleus, similar to what might take place at an electrostatic shock.

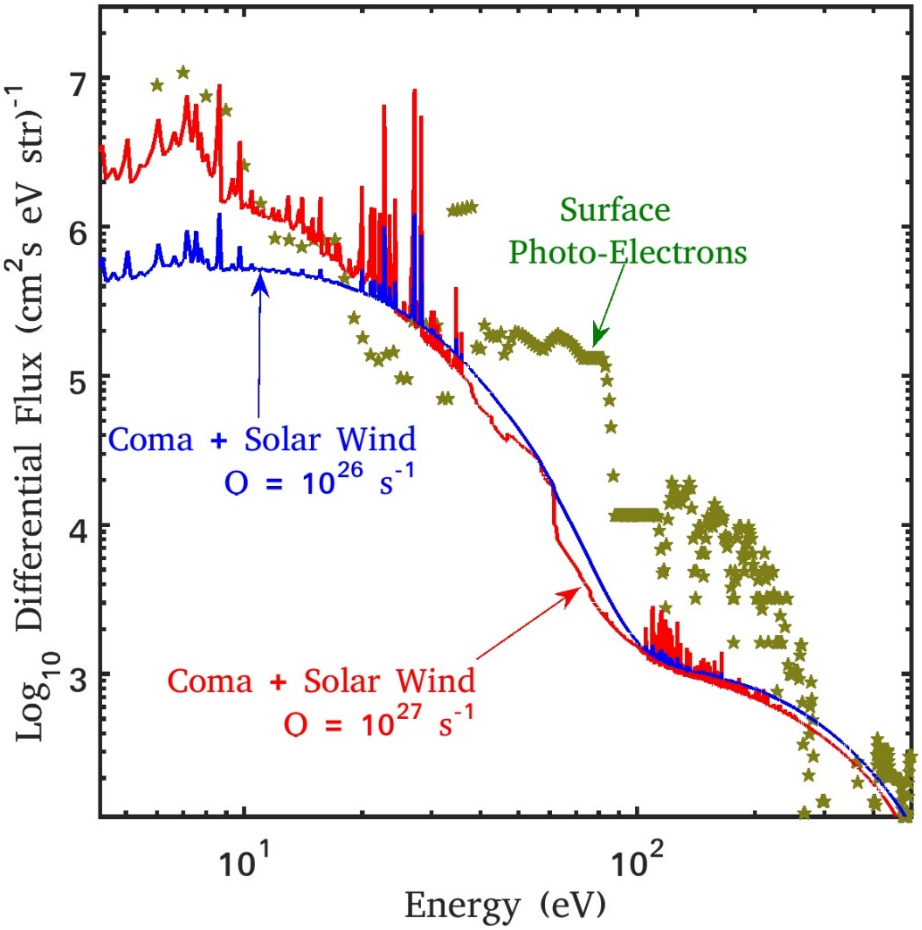

Figure 4.15 - Model spectra for coma photoelectrons plus solar wind electrons at 10 km from the two-stream code for 2 cases: cometary gas production rate of 10^{26} s^{-1} (blue) and 10^{27} s^{-1} (red, possible outburst). A model spectrum for photoelectrons from the surface of the nucleus is also shown as the stars (one for each bin in the solar spectrum model). Photoelectric efficiency at the nucleus is assumed to be 5% for the latter.

Figure 4.15 shows model spectra for a cometocentric distance of 10 km and cases (1) and (2). Lowest fluxes are for coma photoelectrons plus solar wind electrons (case 2) without any additional effects. We adopted two gas production rates: Q=10^{26} s^{-1} at 3 AU, which is typical, and Q=10^{27} s^{-1} to account for a possible extreme outburst. Fluxes associated with nucleus photoelectrons are larger than coma photoelectron fluxes, but these are relevant only for some locations. Detailed structures in the photoelectron energy spectra are due to lines in the solar radiation spectra that produce photoelectrons at specific energies (i.e., photon energy minus ionization potential). For example, photoelectron spectra in planetary ionospheres have characteristic peaks near 27 eV due to absorption of solar He_{II} 30.4 nm photons. Such peaks are evident in Figure 4.15 and Figure 4.16. Putting a boundary potential into the two-stream code (i.e., effects of an ambipolar electric field, section 4.3.3) enhances electron fluxes (case 3), as shown in Figure 4.16.

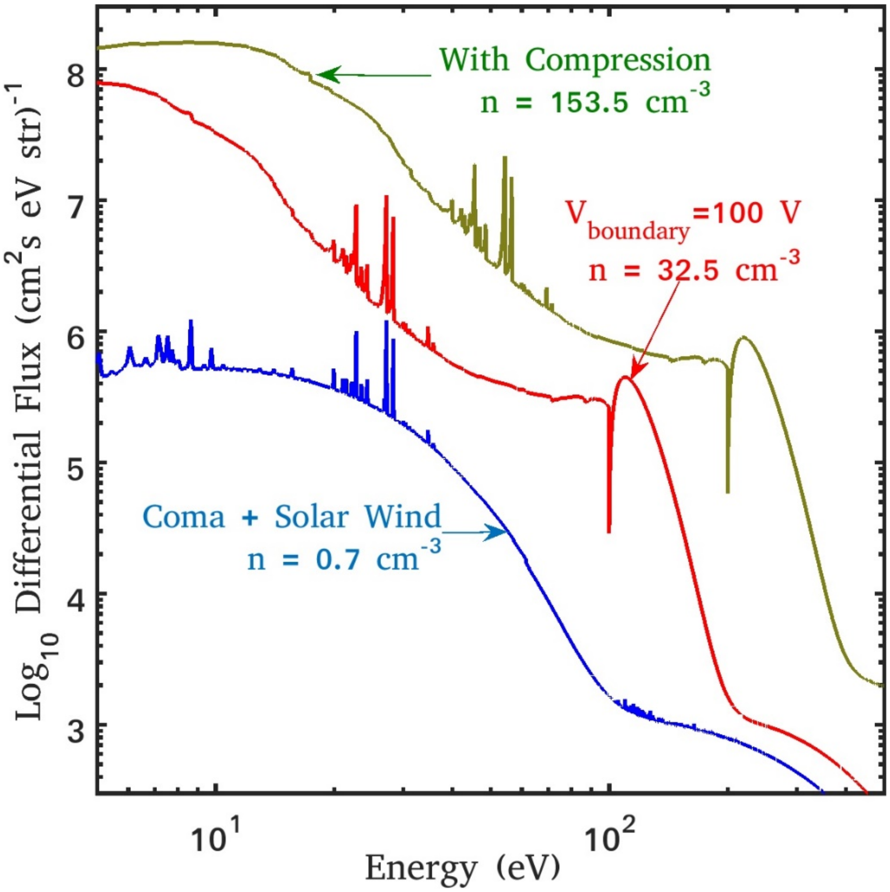

Figure 4.16 - Model coma electron and solar wind electron fluxes at 10 km from the nucleus with ambipolar electric field and/or compression included. The blue curve is the model with no ambipolar potential and no compression. The red curve model includes the ambipolar field (i.e., along the magnetic field), and the green curve also puts in some compression (K=2) as described in the text. Densities shown in the figure are calculated for energies greater than 4.3 eV. Density of the blue spectrum for all energies would be 1.1 cm^{-3}.

For comet 67P/CG near 3 AU, $\Delta V_{pol} \approx 10$ -100 Volts, based on the fact that typical electron energies in Figure 4.10 are 10 - 100 eV. For case (3), effects of the ambipolar/polarization electric field were approximated using a reflecting boundary condition in the two-stream code for energies less than $E_{bound} = e\ \Delta V_{pol}$. We used an accelerated solar wind electron spectrum as the boundary flux for higher energies $E > E_{bound}$. That is, the entire electric field structure in the coma was collapsed into a sharp potential change at the boundary of our model. Several values of E_{bound} were tried; these include E_{bound} = 0 eV, 50 eV, and 100 eV (shows the 100 eV case).

Next, we tried modeling a case (case 4) for which an electron fluid parcel (with its associated frozen-in magnetic field) is slowed down over a distance of the order of the density structure (≈ 100 km or less). Note the magnetic field is not frozen into the ion flow at these length scales, but rather may be frozen into the electron gas. For a decreasing electron bulk flow velocity, the magnetic field should be enhanced due to the $u_e \times B$ term in equation 4.5 plus Faraday's law. In the case of solar wind interaction with comet 67P/CG, multifluid and hybrid simulations affirm that a modest magnetic field increase (i.e., a factor of 2 – 3) is present near the nucleus (Rubin et al., 2014a). This results in an increase of electron perpendicular kinetic energy via the conservation of the first adiabatic invariant, μ:

$$\mu = \frac{\frac{1}{2} m_e v_\perp^2}{B} \qquad 4.11$$

We simply adopt a three-dimensional adiabatic compression of a fluid parcel by a factor of $k \approx 2$ to see how the electron distribution function might be altered. The new electron differential flux relative to uncompressed flux provided by the two-stream code is given by:

$$F'(E') = k \times F(E) \qquad 4.12$$

where new energies are denoted *E'* with *E=E'/k* and *F*(*E*) denotes the original differential electron flux. Figure 4.16 shows this case. The peaks in Figure 4.16 at high energies are due to solar wind electrons accelerated inward by the adopted ambipolar electron potential.

Now we compare some simple model spectra with IES data. Figure 4.17 illustrates 3 omnidirectional electron spectra measured by IES plus one model spectrum (case 4) from Figure 4.16, but with energy resolution reduced to that of the IES instrument for data shown. We also show the model case, but with effects of a -20 V spacecraft potential approximated by shifting each model point down by 20 eV (e.g., the 20 eV point would be moved to 0 eV, etc.). Since detailed photoelectron energy structure was mostly lost when energy resolution was lowered to IES resolution, one does not expect to see individual peaks in the data. The blue spectrum measured when the spacecraft was 900 km from the nucleus is characteristic of a solar wind spectrum for 3 AU ($n_e \approx 0.5$ cm^{-3} and $T_e \approx 10$ eV). The other two IES spectra show fluxes that are 1000 times greater than solar wind fluxes, especially at higher energies, as was discussed earlier. As Figure 4.17 made clear, the electron spectra that IES measured during this time were highly variable, therefore a detailed model-data comparison is not appropriate. Nonetheless, the model does better for September 12 than for October 23, especially for energies above 50 eV. The models illustrate how it is possible to create an electron distribution hotter and denser than the 3 AU solar wind distribution.

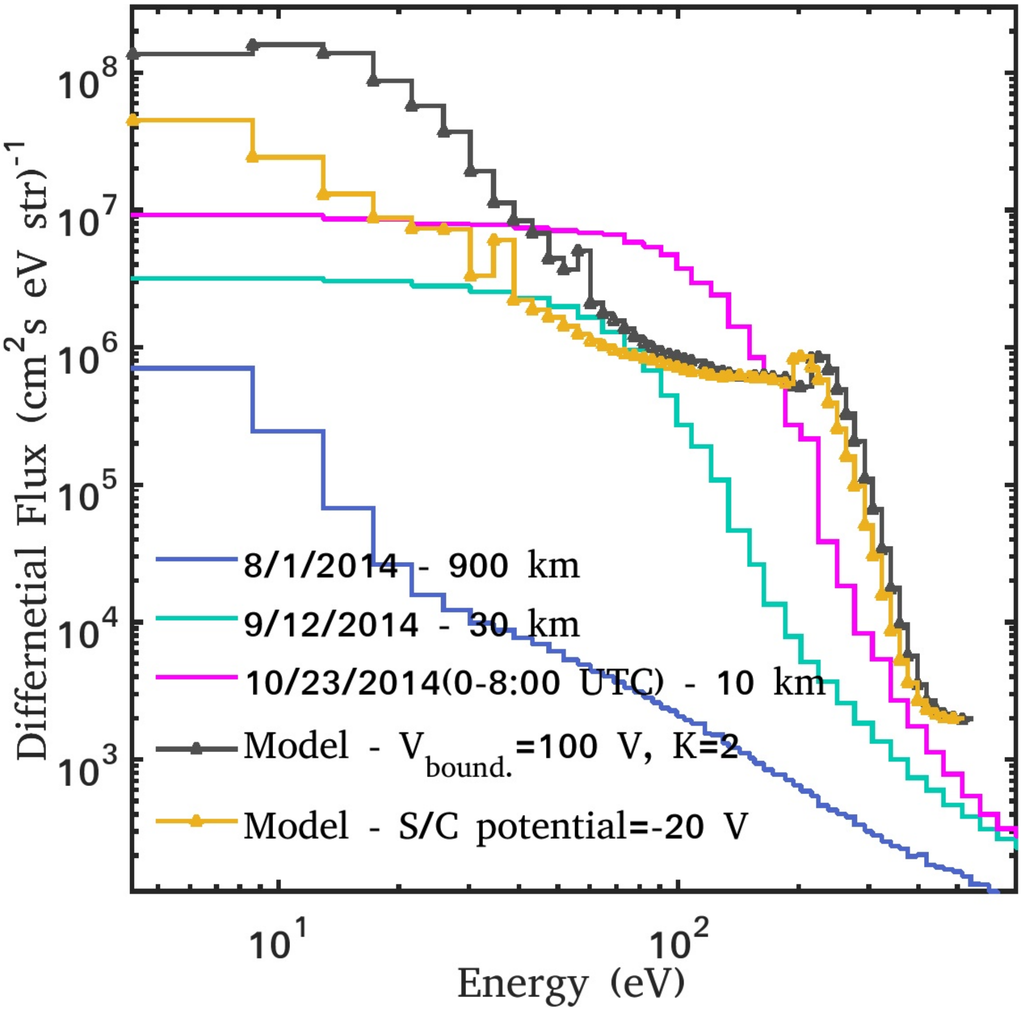

Figure 4.17 - Daily averaged differential electron fluxes versus energy measured by Rosetta RPC-IES at distances of 10 km (red), 30 km (light blue), and 970 km (blue) from the nucleus are shown. The August 1 spectrum appears to be a solar wind electron distribution. The other two spectra near the nucleus show greatly enhanced fluxes. Flux drop-offs are at energies of about 100 - 200 eV. The spectrum on October 23 (00:00-08:00 UTC) is during a CME event. Comet's heliocentric distance for these observations is about 3 AU. Two model spectra are shown for comparison. One is the spectrum for 100 V ambipolar potential plus compression presented in Figure 4.16 (black curve). The other (yellow curve) estimates effects of a - 20 V spacecraft spectrum by shifting the other model spectrum by 20 eV.

Figure 4.18 shows supporting results for the importance of compression. The figure shows 3 IES spectra plus a modified IES spectrum. An interplanetary shock passed the comet between the October 22, 16:30 UT and the October 23, 08:00 UT measurements. The measured electron fluxes were significantly enhanced in this time interval. To see if some extra compression (i.e., via shock-related effects) could help explain this result, we simply took the pre-shock IES spectrum on October 17 and transformed it using equation 4.12 with a compression factor of 2.5. This procedure appears to help explain that compression is somehow influential in observed enhanced electron fluxes. In an independent study, four CME/CIR events between October 2014 and December 2014, including the event discussed here, were analyzed to show that enhancement in densities is due to plasma compression and other possible effects, such as formation of a plasma boundary or tail disconnection events (Edberg et al., 2016).

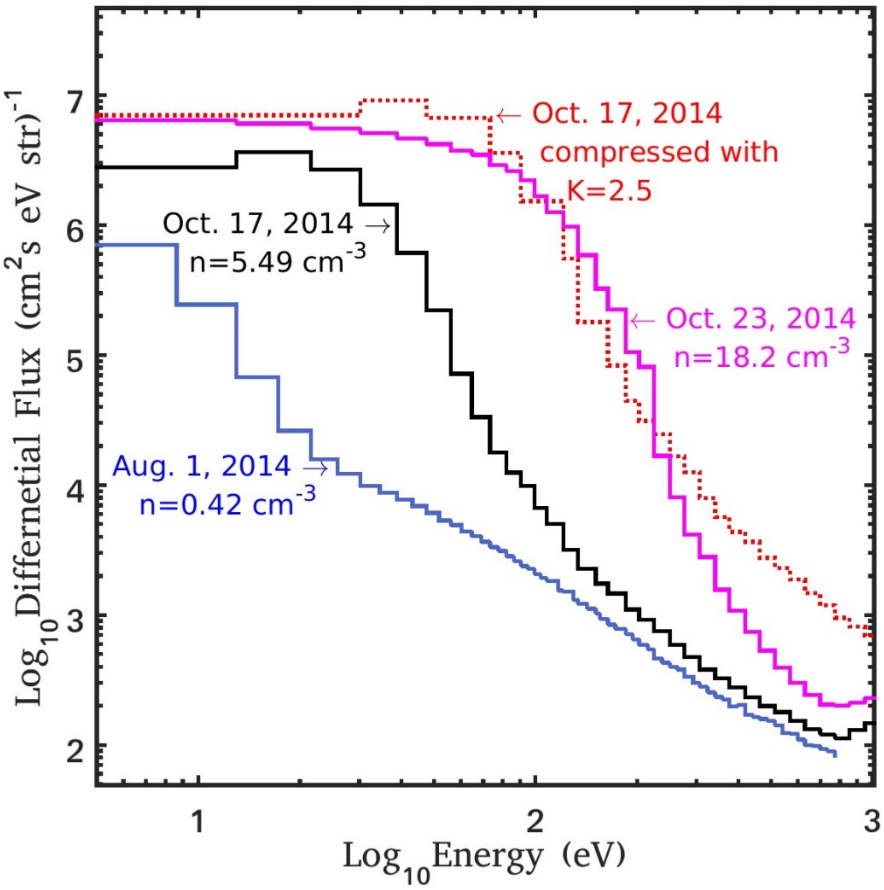

Figure 4.18 - Daily average differential electron fluxes versus energy measured by Rosetta IES at distances of 10 km (magenta and black curves) and 970 km (blue) from the nucleus are shown. The August 1 spectrum appears to be a solar wind electron distribution. An interplanetary shock passed the comet on October 23. The two October 17 spectra differ in that the black curve is just the pre-shock IES daily average spectrum on October 17 while, its enhanced spectrum with a factor of 2.5 compression (as the text describes) is plotted in red dotted line. The compressed spectrum is consistent with extra enhancement associated with shock passage.

4.4.4 Discussion of Plasma and Field Conditions near the Comet

Rosetta measurements have shown that plasma environment near the nucleus of comet 67P/CG at 3 AU is very different from that of active comets, such as Halley in 1986. A standard MHD shock, like that found upstream of the Earth's magnetopause or upstream of a very active comet like Halley, is not present. Creation of a dense plasma (i.e., electrons and ions) cloud near the nucleus with a size-scale much smaller than an ion gyroradius or ion inertial length affects electrons much more than solar wind ions. Newly-created photoions and photoelectrons have low bulk flow velocities with respect to the solar wind (and neutral gas). However, the transition from flowing solar wind electron gas to slow photoelectron gas over some tens of kilometers could be shock-like, but would not be an MHD shock (Cravens, 1997).

Table 4.2 provides estimates of relevant parameters for the cometary environment based on Rosetta data. Solar wind ion scales (10^4 km) far exceed the density structure size-scale, which is about the same as Rosetta's distance from the nucleus (10 - 100 km) during autumn 2014. Note that the photoionization length scale for neutrals is about 10^7 km. Ion inertial length (about 50 – 100 km) is of the order of Rosetta's cometocentric distance. Ions behave kinetically near the nucleus. Ion gyroradii greatly exceed the distance scale (i.e., cometocentric distance *r*) such that single-fluid MHD theory does not apply. The electron gyroradius of about 10 km is somewhat less than the enhancement scale-size (100 km), suggesting that the electrons perhaps can be treated approximately as a fluid. However, this does not mean that the electron distribution function must be Maxwellian, and IES data confirms that the distribution function is not Maxwellian. However, pressure as the second velocity moment of the distribution function ($p_e = n_e <KE>$) should remain a useful dynamical quantity and the generalized Ohm's law (equation 4.6) should be valid, thus ensuring quasi-neutrality.

Table 4.2 - Typical Conditions Near the Nucleus of Comet 67P/CG at 3 AU
(From Rosetta Data and/or Models*)

Cometocentric Distance (r)	30 km (10 - 100 km)
Neutral Density (n_n)	10^7 cm^{-3} (10^6 - 10^8 cm^{-3})
Electron Density ($n_e = n_i$)	20 cm^{-3} (10 - 100 cm^{-3})
Average Electron Energy (kT_{eff})	20 eV (10 - 200 eV)
Peak Magnetic Field (B_{max})	5 nT*
Local Electron Gyroradius (r_{ecom})	5 km*
Charge Exchange Mean Free Path (λ_{mfpcx})	1000 km (10 - 10^4 km)
Electron Neutral Mean Free Path (λ_{mfpen})	10^4 km
Debye Length	5 m
Electron Inertial Length (c/ω_e)	300 m
Ion Inertial Length (c/ω_{pi})	10 km
Solar Wind Electric Field ($E_{sw} \approx u_{sw}B_{sw}$)	5×10^{-4} V/m
Potential Difference :	
Across Inner Coma ($\Delta V \approx rE_{sw}$)	20 Volts (10 - 100 Volts)
Empirical (IES) ΔV	10 - 200 Volts
Cometary Ion Speed ($u_i = \sqrt{\frac{E_{sw}re}{m_i}}$)**	4 km/s (at 50 km)
Average "Thermal" Electron Speed (v_{the})	5000 km/s
Cometary Ion Transport Time ($\tau_{trans} \approx r/u_i$)	20 s (1 - 50 s)
Electron Transport Time ($\tau_{etrans} \approx r / v_{the}$)	10^{-2} s

*E.g., (Rubin et al., 2014b)
**Note $m_i = 18\ m_p$ where m_p is the proton mass.
Possible ranges of parameters are shown in parentheses.

Debye length in the solar wind and/or near the nucleus is only a few meters. Other possibly useful kinetic length scales are the electron and ion inertial lengths of 300 m and 10 km, respectively. Cometary ion speeds due to acceleration by the motional electric field are about 20 km/s, which are much less than solar wind speed or electron thermal velocity.

4.4.5 Electron-Impact Ionization near Comet 67P

Electron-impact ionization of neutrals is another complicating effect in an already complicated scenario. We calculated electron-impact ionization rates by means of simple integration over energy of measured differential electron fluxes (e.g., Figure 4.18) times electron-impact ionization cross sections for H_2O and CO_2 (Cravens et al., 1987; Gan, 1991). The electron-impact ionization rate (or ion production rate) divided by neutral density gives ionization frequency, as listed in Table 4.3. We carried this out for several IES electron spectra (as listed) including two that Figure 4.18 shows. In unperturbed solar wind at 3 AU, far from the nucleus, the electron-impact ionization frequency of water is $I = 1.3 \times 10^{-9}\ s^{-1}$ (for the solar wind electron spectrum shown in Figure 4.18). We obtained values ranging from 1 to $9 \times 10^{-7}\ s^{-1}$ near the nucleus.

Table 4.3 - CO_2 and H_2O electron-impact ionization frequency for IES electron spectra near comet 67P/CG (differential flux spectra are shown in Figure 4.18)

Date	Heliocentric Dist. (AU)	Cometocentric Dist. (km)	I* (CO_2)	I* (H_2O)
8/1/2014	3.6	970	0.019	0.013
10/2/2014	3.3	10	2.9	2.41
10/23/2014	3.1	9.8	9.69	6.6
11/5/2014	3.0	31	2.6	1.95
2/2/2015	2.4	28	2.19	1.57
3/23/2015	2.0	80	2.32	1.69
6/5/2015	1.5	205	0.59	0.44

* Units of *I*: $10^{-7}\ s^{-1}$ - total ion production rate divided by neutral density.

The higher ionization frequencies should have the most effect on solar wind interaction with the comet near the nucleus and at larger heliocentric distances (as Table 4.3 shows), where contribution of photoionization due to solar radiation is less. The overall effect of increased ionization would be to increase local density of cometary ions beyond what photoionization would give and this would enhance the overall interaction. Detailed models of the interaction should include this new ionization. Electron-impact ionization is automatically included in our electron two-stream model.

4.4.6 Interpretation of Time Constants in the Cometary Plasma at 3 AU

An interesting feature of the electron data (e.g., Figure 4.13b and Figure 4.14) is that close to the nucleus (within ~100 km), in addition to a suprathermal population, a cold ($E \leq 4$ eV) thermal electron population exists. At larger cometocentric distances this cold population does not appear to be present, or is very scarce. A cold "ionospheric" electron population was present in the inner coma (i.e., within cometocentric distances of a few thousand km) of comet Halley during its perihelion and was attributed to high electron-neutral cooling rates (Gan and Cravens, 1990; Gombosi et al., 1996). However, the gas production rate of comet 67P near 3 AU was more than 1000 times less than comet Halley's, and perhaps the presence of cold electrons is more surprising. In this section, we estimate some electron time constants and find that existence of a small ($r < 100$ km) region containing cold electrons is indeed reasonable.

The electrons in the cometary environment are initially created as suprathermal electrons – photoelectrons from photoionization by solar EUV and soft x-ray radiation or solar wind electrons that travel into the inner coma. These 5 – 50 eV electrons have speeds of about 1000 km/s or greater and can traverse the ~30 km inner coma in about $\tau_{trans} = \frac{r}{V_e} \approx 0.03\ s$. The electron-neutral collision mean path also far exceeds 30 km. If the electrons were free to travel, initial fluxes and densities would remain relatively unaltered (and suprathermal) as illustrated by the two-stream model results in Figure 4.16, when no ambipolar electric field was included. Another way to show this result is that cooling time associated with electron-neutral collisions, even in the inner coma at 10 – 30 km, greatly exceeds the electron transit time. The electron-water cooling rate for marginally suprathermal electrons of about 1- 5 eV, dominated by rotational and vibrational collisions, is about L ≈ 10^{-8} eV cm^3 s^{-1} (Cravens and Korosmezey, 1986; Schunk and Nagy, 2009), giving a cooling time of $\tau_{en} = \frac{kT_e}{Ln_n} \approx 50\ s$ with kT_e = 5 eV and $n_n \approx 10^7$ cm^{-3} at 30 km and only about 10 s at 10 km. At 100 km, $\tau_{en} \approx 500$ s. In any case, τ_{en} greatly exceeds the transit time. As discussed earlier in this section, however, we know that an ambipolar field that enforces quasi-neutrality must operate to increase the electron density to larger values. In principle, coexistence of slow ions with fast electrons creates an electrical potential that draws electrons into the ion-rich coma so charge quasi-neutrality can be attained.

Residence time of the inner coma plasma is the length scale *r*, divided by the average ion flow speed $u_i \approx 1$ - 10 km/s. This is associated mostly with newborn ions accelerated by the electric field (i.e., motional plus ambipolar). Residence time for ion motion is given by:

$$\tau_{res} = \frac{r}{u_i} \tag{4.13}$$

At 10 to100 km distance, the residence time is about 3 to 30 seconds. Figure 4.3 shows ion densities from global simulations. One can also estimate residence time from a dimensional analysis of the continuity equation ignoring losses:

$$\tau_{res} = \frac{n_e}{P} \tag{4.14}$$

where *P* is ion-electron production rate. *P* can be written as:

$$P = In_n \tag{4.15}$$

$I \approx 10^{-7}$ s^{-1} is the ionization frequency discussed earlier in 4.4.5 and n_n is the neutral density. In the 10 – 30 km region, this gives $\tau_{res} \approx 10 - 100\ s$, which is comparable to the cooling time. In other words, the electron population, starting out superathermal, has time to evolve into a colder population. For $r > 100$ km or so, $n_e \approx 30$ cm^{-3} and $\tau_{res} \approx 300$ s, but the electron neutral cooling time is becoming even larger and electrons will remain suprathermal. Note that electron-ion dissociative recombination time, $\tau_{DR} \approx \frac{1}{\alpha n_e} \approx 10^4\ s$, far exceeds all the time scales discussed above. The dissociative recombination rate coefficient is $\alpha \approx 10^{-7} - 10^{-6}$ cm^3 s^{-1} (Vigren and Galand, 2013).

Another question is whether cold electrons have a Maxwellian distribution function. We know from IES that suprathermal electrons do not. Electron-electron collision frequency is given by (Schunk and Nagy, 2009):

$$\nu_{ee} = 54.5 \frac{n_e}{T_e^{1.5}} \tag{4.16}$$

For very cold electrons (e.g., $E \sim 0.1$ eV or $T_e \approx 10^3$ K) at 10 km, the electron-electron collision frequency is about 0.15 s^{-1}. This corresponds to a time constant of $\tau_{ee} \sim 6\ s$. For somewhat “hotter” cold electrons with E ~ 1 eV ($T_e \sim 10^4$ K), τ_{ee} is around 200 s. This shows that cold electrons can experience at least one Coulomb collision while being constrained by the ambipolar electric field. We can indeed describe the cold electron population near the nucleus ($r < 100$ km) as Maxwellian, or as thermalized.

At comet Halley, thermal electrons “collisionopause” was located at a cometocentric distance of about 1-2 × 10^4 km, within which a cold electron population existed and beyond which electron temperature increased rapidly due to higher electron-neutral cooling times (Gan and

Cravens, 1990). Collisionopause was manifested as a transition boundary in the observed (and modeled) electron densities (Rème, 1991; Reme et al., 1986). Apparently such a transition also exists for comet 67P/CG at 3 AU, but at a distance of only ≈100 km.

Observations also support these claims reasonably well. Interplay between hot and cold electron populations and neutral densities is in fact visible in Figure 4.13b, where there is anti-correlation between IES electron and LAP ion densities. There is also correlation between LAP/MIP peak densities and neutral density variations. Such correlation fits well with the present discussion of the electron-neutral collisional cooling process of hot electrons. The LAP and IES electron densities in Figure 4.14 also suggest the cold electron population becomes significant within 100 km from the comet. At a distance of 50 km, an average density of about 40 cm^{-3} can be estimated for cold thermal electrons and much higher densities at closer distances. It must be noted that the uncertainty of our methodology in calculating the IES electron densities, which can be a factor of 2-3 change in the derived densities, does not obscure the given interpretations, and the relation between the population of thermal and suprathermal electrons remains the same.

4.5 Comet at Perihelion

Much of our understanding of the cometary boundaries emerged from analyzing data from the Giotto spacecraft encounter with comet 1P/Halley on March 14, 1986. The spacecraft entered the diamagnetic cavity at a distance of about 4500 km from the nucleus, where the magnetic field magnitude dropped by 20 nT to almost zero over a distance of 25 km (Neubauer, 1986). For comet 1P/Halley, several studies showed that force balance between magnetic pressure gradient force from the solar wind and ion-neutral drag force in the coma determines stand-off distance of the field-free region (Cravens, 1986; Ip and Axford, 1987; Puhl-Quinn and

Cravens, 1995). This distance is known as the cavity boundary or contact surface. Interaction between unmagnetized outflowing cometary plasma and inflowing magnetized solar wind plasma can be characterized as a tangential discontinuity in which two scale lengths, the Larmor radius of the outflowing ions and the effective distance of the ion-neutral drag force, effectively describe the structure of the discontinuity (Flammer et al., 1991).

In this section, we review plasma environments inside and outside the diamagnetic regions. The interpretation adopted in this section is that these regions were associated with the spacecraft going into and out of a diamagnetic cavity. We will show that IES suprathermal electron differential flux dropped at different energies during the diamagnetic cavity crossing events. We also modeled electron differential fluxes inside and outside the diamagnetic cavity. Figure 4.19 shows an artistic schematic of a possible shape of the diamagnetic cavity boundary around comet 67P/CG. The incident solar wind is from left to right, and the grey shaded area on the right is the region of zero magnetic field (i.e., diamagnetic cavity). Theoretical models have predicted the wavy structure along the boundary, whose most likely cause are plasma instabilities

.

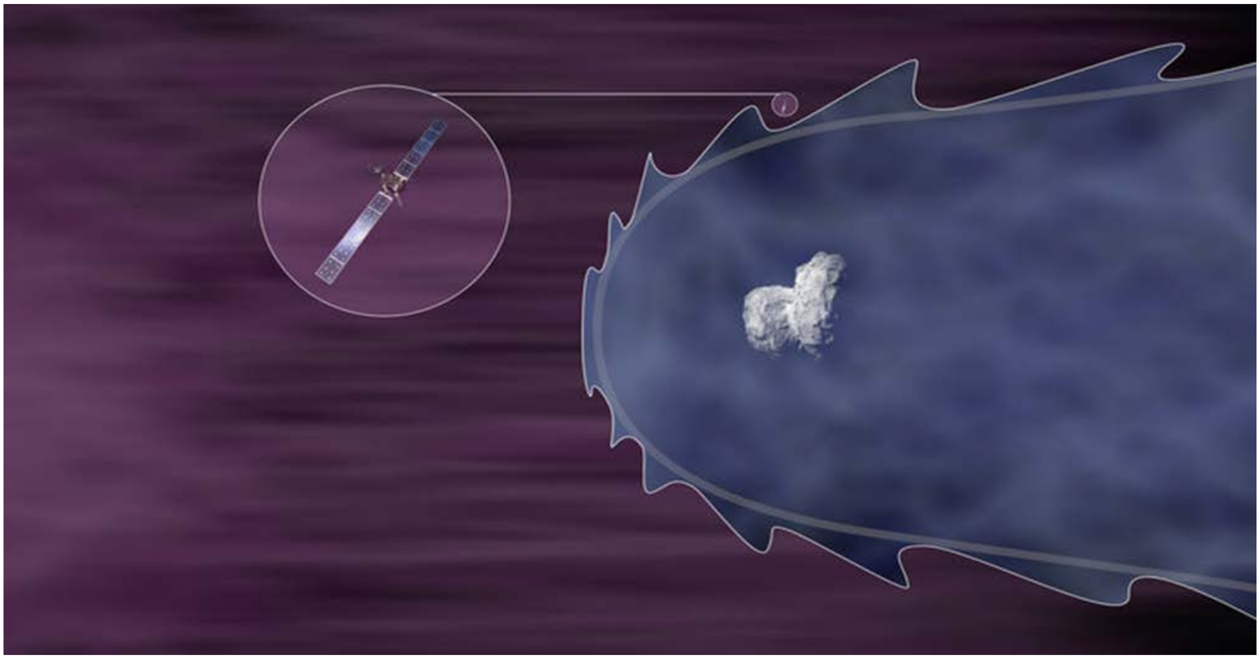

Figure 4.19 - Artistic image of the diamagnetic cavity boundary of comet 67P/CG at perihelion. Solar wind flow is from left to right. The blue shaded area around the comet is the region of zero magnetic field. The zoom out circle shows the Rosetta spacecraft. Photo courtesy: ESA.

Figure 4.20 shows data from IES and MAG instruments between July 25 to August 1, 2015. The top panel shows IES total electron count rates as function of energy (Y-axis) and time (X-axis) are shown in the top panel. The counts have been summed over all elevation and azimuth angles of the IES field of view. The bottom panel of Figure 4.20 shows the three components of the magnetic field in the cometocentric solar equatorial (CSEQ) coordinate system where the +X direction is towards the Sun, the +Z direction is perpendicular to the ecliptic plane, and the +Y completes the right-hand rule. The magnetic field measurement cadence is one second, averaged over one minute, while the IES cycle time is 256 seconds. The shaded areas between dashed lines on July 26 and July 29 mark selected periods with several cavity crossing events, which will be analyzed in more detail in the next section.

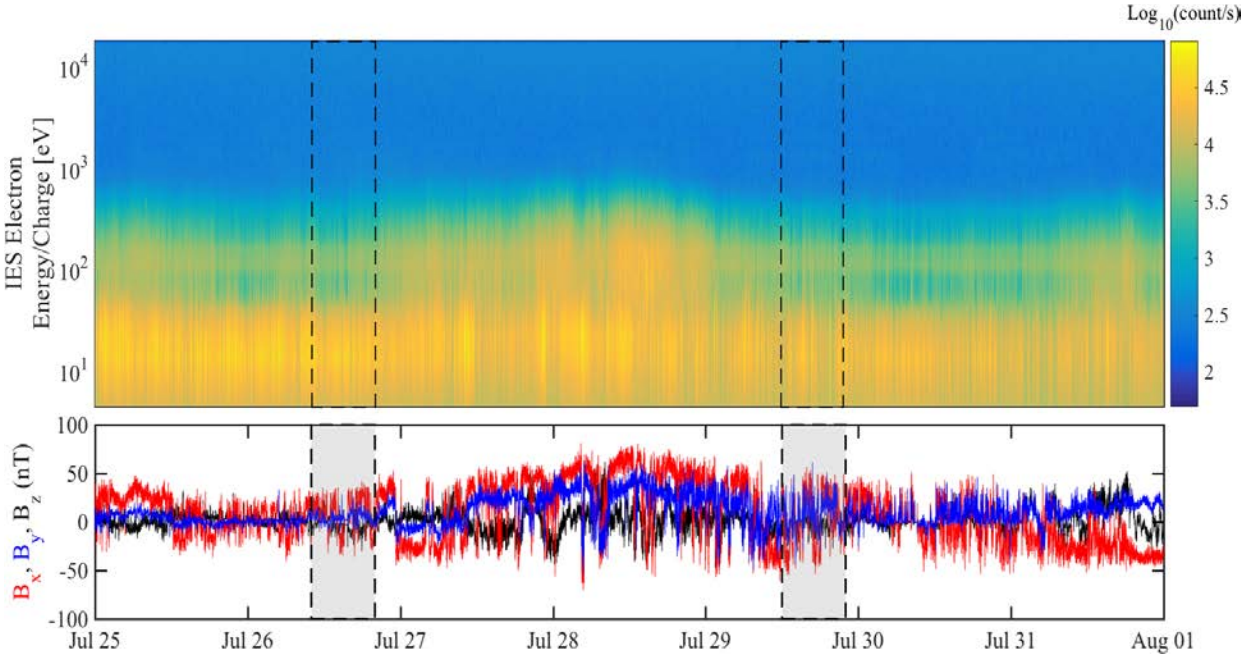

Figure 4.20 - (top) IES measured electron count rate from 2015 July 25 to August 1. The count rates are summed over the full field of view of the IES. (bottom) Three components of the magnetic field measured by MAG in CSEQ coordinate system for the same time period. The shaded areas between dashed lines are the selected time periods when cavity crossing events have been observed. These data will be analyzed in more detail in the paper.

4.5.1 Observation of the Diamagnetic Cavity of Comet 67P/CG

Comet 67P/CG is significantly less active than comet 1P/Halley (between a few hundred to a few thousand times, depending on heliocentric distance) and the meager coma of this comet may not be able to support formation of typical stable cometary boundaries. However, a magnetic pile-up region at comet 67P/CG was observed even before perihelion at 1.5 AU caused by a sudden increase in solar wind dynamic pressure (Volwerk et al., 2016). Nucleus outgassing rate and solar wind dynamic pressure affect location of the ion-neutral collisionopause boundary. This boundary is assumed to be outside the diamagnetic cavity and is characterized by enhanced magnetic field pile-up, reduced electron densities, and accelerated water group ions on the outside edge. On the inside, characteristics are reduced magnetic field pileup, enhanced electron densities, and low energy water group ions (Mandt et al., 2016).

Following extended calibration efforts of magnetic field data, first detection of the diamagnetic cavity at comet 67P/CG was reported near perihelion (Goetz et al., 2016). In July and August 2015, MAG data showed instances of the Rosetta spacecraft crossing a barrier within which magnetic field magnitude plummeted, from about 30 nT to near zero. Two of these events are marked in Figure 4.20.

4.1.1.1 Event on July 26, 2015

For the event on July 26, MAG instrument showed that the spacecraft spent about 25 minutes inside a diamagnetic cavity. This is one of the longest events the spacecraft spent inside the diamagnetic cavity. The longest event occurred on November 20, 2015, lasting about 40 minutes.

Time series of IES measured electron fluxes during the cavity event on July 26 between 10:00:00 to 20:00:00 UTC appears in the top panel of Figure 4.21. IES fluxes of 21, 47, 99, and 202 eV electrons are represented with red, green, blue, and grey lines, respectively. The bottom panel of the figure shows magnetic field magnitude for the same period. The very low, disturbance-free region between the dashed-dotted lines, between 15:20:00 to 15:50:00 UTC, is identified as a magnetic field-free region. The data show a decrease of high energy electron fluxes by about a factor of 2 when magnetic field strength drops, while low energy electrons ($E \leq 21$ eV) show no significant change. The vertical solid lines on this panel mark individual timestamps used for comparing the full electron energy spectra inside and outside the cavity. There are other short instances of near zero field strength such as around 13:20:00 UTC, which are not discussed.

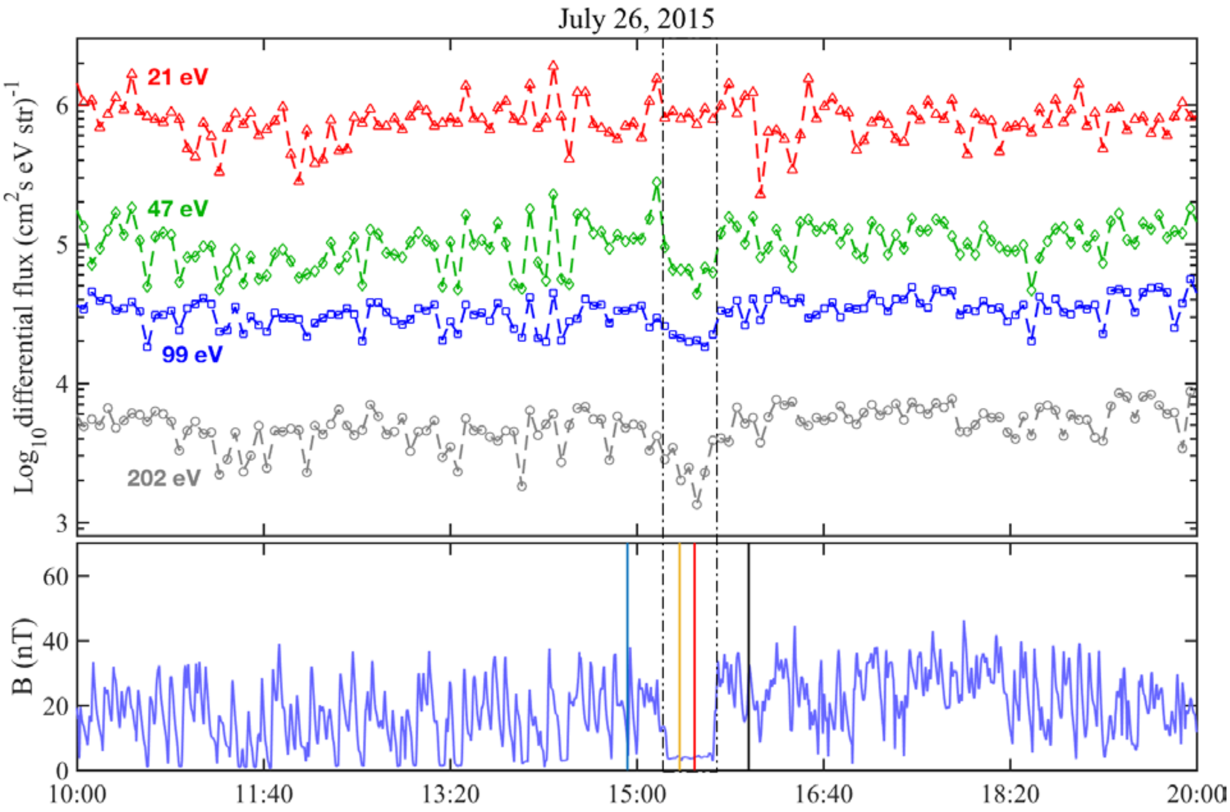

Figure 4.21 – Figure shows IES and MAG data between 10:00:00 to 20:00:00 UTC on 2015 July 26. Top panel shows time series of IES electron fluxes for four different energy channels, 21 eV (red), 47 eV (green), 99 eV (blue), and 202 eV (grey). The bottom panel shows magnitude of the magnetic field measured by MAG for the same period. The two dashed dotted lines show the time when the spacecraft was inside the cavity. Four other solid vertical lines mark timestamps for which Figure 4.22 shows complete energy spectra. Yellow and red lines are timestamps inside the cavity, blue line is a timestamp before entering the cavity, and black timestamp is after exiting the cavity.

Figure 4.22 shows full IES electron energy spectra for these timestamps. Red and yellow curves are electron energy spectra inside the cavity. Blue and purple curves are for outside before and after entering the cavity, respectively. This figure shows that electron fluxes decline at a wider energy range between 40 eV to a couple of hundred eV. This drop is more noticeable for 60-100 eV and 150-200 eV electrons. This signature in IES electron data was used as a search criterion to identify cavity crossing events. A cross comparison of MAG cavity observations with cavity crossing events identified by the IES electron signature has shown very reasonable agreement.

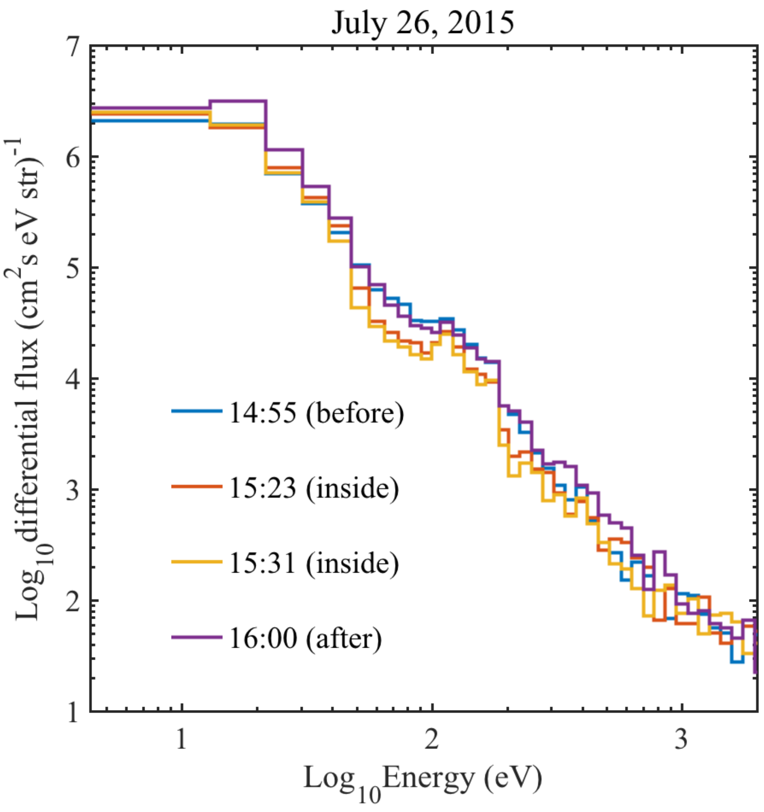

Figure 4.22 – Figure shows the energy spectrum of the IES electron differential flux for four individual timestamps on July 26, 2015. The blue spectrum is from 14:55:00 UTC, where Rosetta has not yet crossed the cavity boundary. The red and yellow spectra are from 15:23:00 and 15:31:00 UTC when Rosetta is considered to be inside the diamagnetic cavity. The spectrum from 16:00:00 UTC (the purple line) shows the measured electron spectrum after the spacecraft left the cavity.

4.1.1.2 Events on July 29, 2015

The event on July 26 is a prolonged period where the spacecraft probed the diamagnetic cavity plasma extensively. The other shorter incidents of magnetic field drop out, such as the events on July 29, could also be considered as a magnetic field-free region because these events, however short, still show common plasma characteristics.

Time series of IES and MAG plasma measurements of cavity crossing events on July 29, between 12:00:00 to 22:00:00 UTC, appear in Figure 4.23. The top panel shows time series of IES electron fluxes and the bottom panel shows magnetic field strength. Dashed lines mark cavity crossing events. Electron fluxes at some specific energies show a considerable drop each time the magnitude of the magnetic field approaches zero and the spacecraft crosses the cavity boundary.

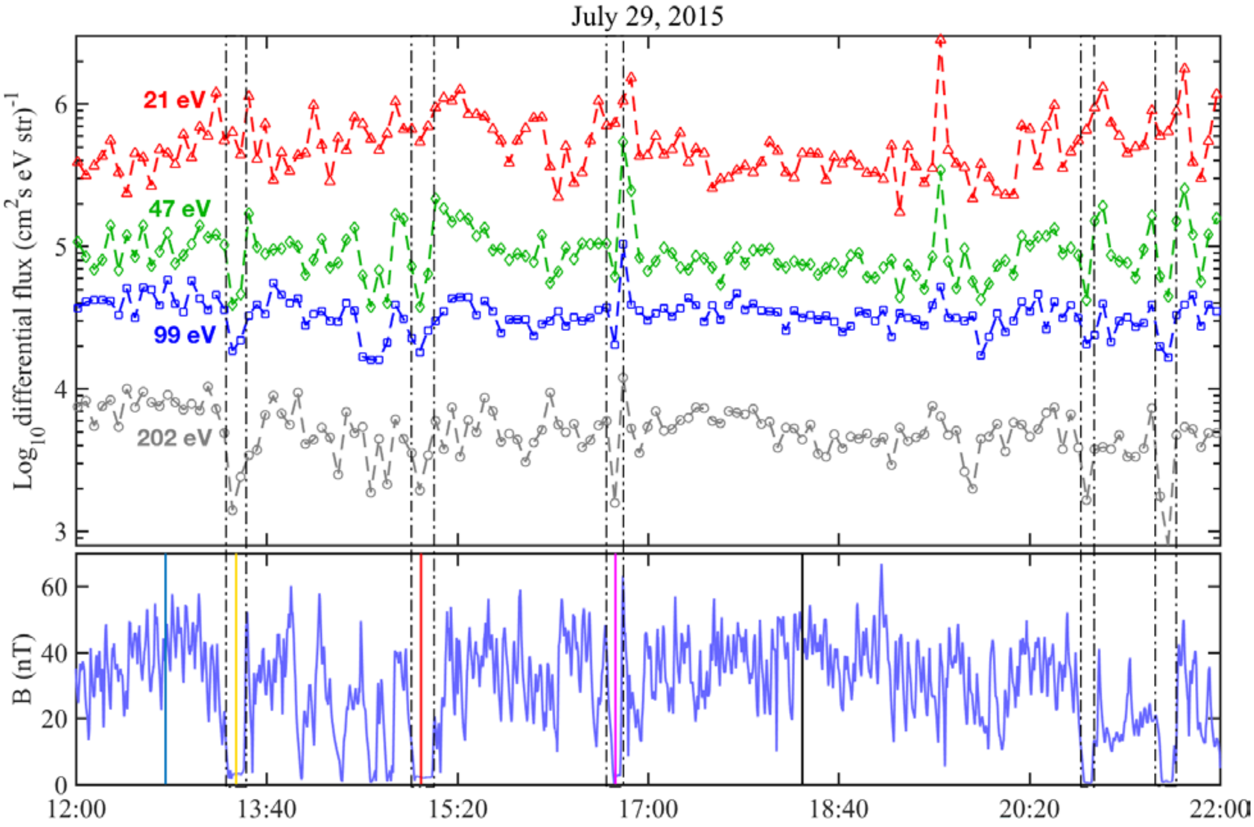

Figure 4.23 - Similar to Figure 22, but for events on July 29, 2015, between 12:00:00 and 22:00:00 UTC. The top panel shows the time series of the IES electron differential flux with energies 21 eV (red), 47 eV (green), 99 eV (blue), and 202 eV (gray). The bottom panel shows the magnitude of the magnetic field measured by MAG for the same period. Dashed rectangles on this panel mark cavity crossing events. The solid lines are drawn at selected timestamps for which Figure 4.24 shows full energy spectra. Blue and black lines are for spectra outside the cavity and yellow, red, and purple lines correspond to spectra inside the cavity.

Figure 4.24 shows the full electron energy spectra for selected timestamps on July 29. There are similarities between electron spectra inside the cavity in this figure and those shown in Figure 4.22 for July 26. The flux of electrons with energy between 40 eV to a few hundred eV has decreased inside the magnetic field dropout regions. For electron energies between 60 – 90 eV and 150 – 200 eV, flux drops are more noticeable.

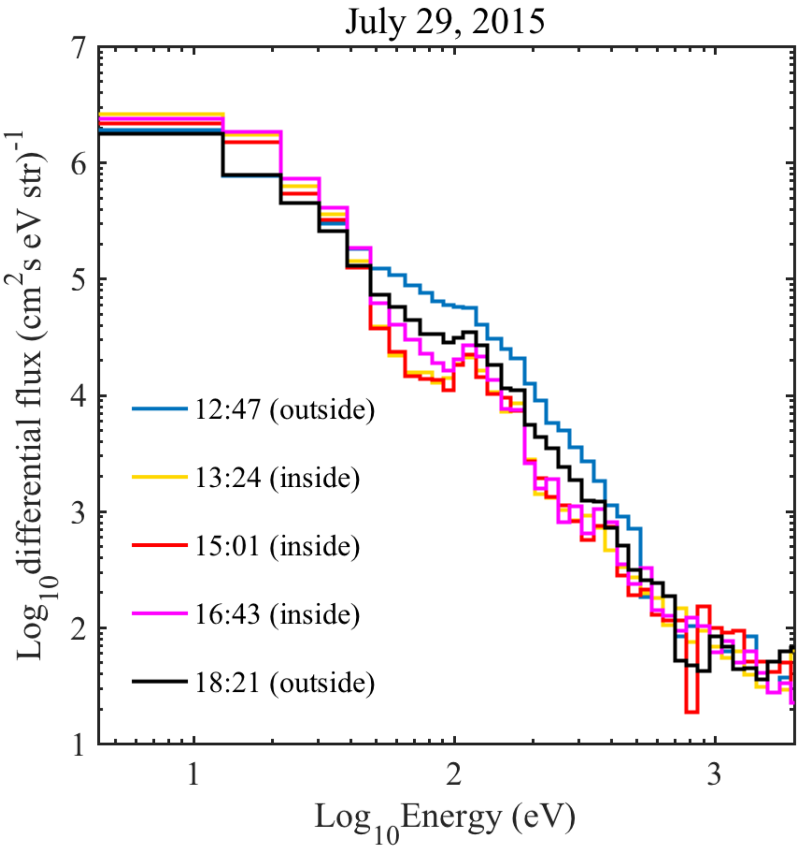

Figure 4.24 - Electron differential flux energy spectra for five individual timestamps on July 29. Blue and black lines show the measured spectra outside of the cavity. Yellow, red, and purple lines correspond to observed spectra in the cavity. The legend includes each timestamp's detail.

IES observations show a modest but consistent drop in electron flux for energies between 40 eV and a few hundred eV at each cavity crossing event. In general, difference in electron flux inside and outside the cavity is not dramatic. A difference of about a factor of 2 is visible for energies between 40 eV and 200 eV. There are larger differences at some specific energy ranges, such as 60-90 eV and 200-250 eV. The fluxes with energies less than ~40 eV either do not change, such as on July 26, or show small increases, as for the July 29 event.

It is important to realize that these observations took place while the spacecraft was escorting the comet and was hovering in the flank region. They differ from comet 1P/Halley's observations, which were made during a transiting flyby. Hence it is unlikely that the spacecraft is moving through the plasma boundaries, but rather the plasma boundaries are expanding and contracting. Spacecraft attitude data help clarify this observation. Figure 4.25 shows time series of positions of the comet (green) and the Sun (red) in IES frame of reference over the entire day of July 29. The top panel shows elevation angles in degree (left) and sweep steps (right). The middle panel shows azimuthal directions of the Sun and the comet, and the bottom panel shows spacecraft distance to the comet on the left axis (black line), and the spacecraft position in comet local time on the right axis (green line). Zero local time corresponds to spacecraft position exactly in between the comet and the Sun.

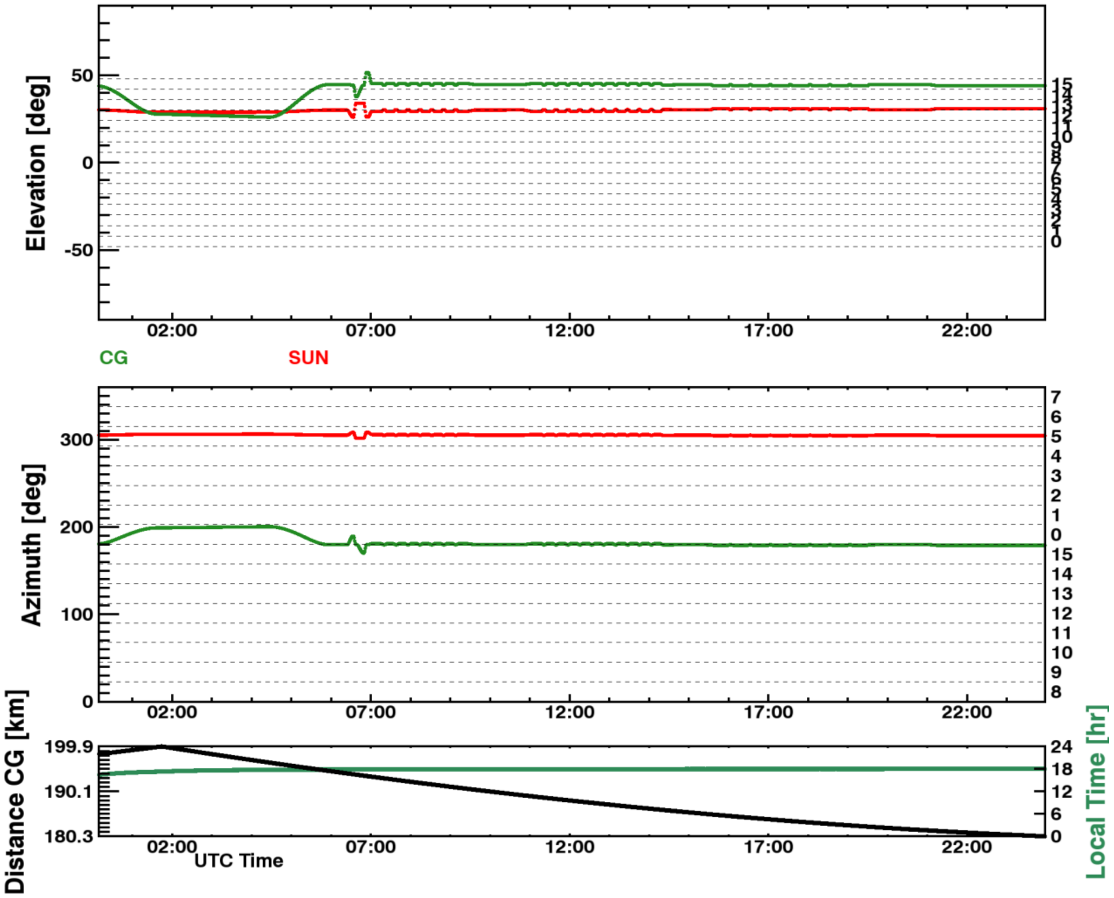

Figure 4.25 – Time series of position of the comet (green) and the Sun (red) in IES frame of reference for July 29, 2015. Elevation directions appear in the top panel. The middle panel shows azimuth angles. The bottom panel shows spacecraft distance to comet (black line / right axis) and spacecraft position in comet local time (green line / left axis).

Spacecraft distance to the comet on this day decreases monotonically by about 20 km. Relative spacecraft position with respect to comet remains the same in the flank region. Spacecraft orientation is also fairly stable; however, Rosetta's plasma instruments recorded multiple cavity crossing events, as was shown in Figure 4.23.

4.5.2 Correlation between Electron Counts and Magnetic Field Strength

We also looked at the correlation between the measured electron counts and the magnitude of the magnetic field for data from July 1 to August 31, 2015. This is the period when the comet is highly active and the cavity boundary is most likely to be present. The scatter plots of Figure 4.26 show count rates of electrons at four different energies versus magnitude of the magnetic field. IES electron counts are summed over all elevations and azimuth angles. Due to difference in measurement cycles, IES and MAG measurement timestamps had to be matched first. Data points are colored based on observation time, specified by the colorbar on the right. The four panels in Figure 4.26 show scatter plots of 13 eV, 99 eV, 151 eV, and 203 eV electrons versus magnetic field strength in nano tesla. The dashed rectangle at the bottom of each plot emphasizes near zero magnetic field strength (below 15 nT) observations, or the counts inside the diamagnetic cavity. Due to uncertainties in MAG measurements and calibration, a range of weak field strengths is selected to represent observations inside and around the cavity boundary instead of an absolute zero field.

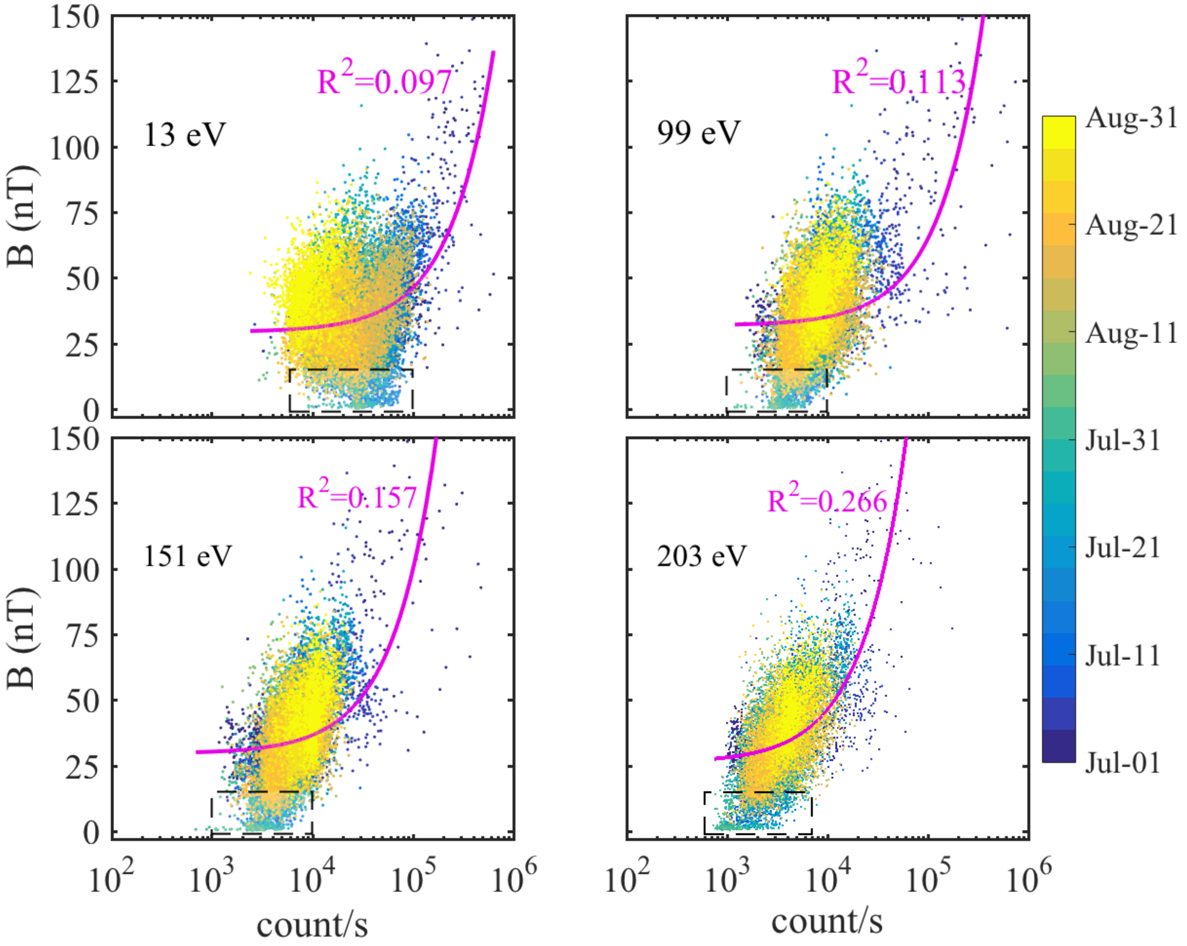

Figure 4.26 – Figures show electron count rates measured by the Rosetta RPC-IES sensor versus magnitude of the magnetic field, for electron energies of 13, 99, 151, and 203 eV. Data points are color coded based on dates of the observations from July 1 to August 31, 2015. The colorbar shows corresponding times. The purple line on each plot shows linear fit on the data with R^2 goodness-of-fit shown next to each curve. Dashed rectangles at the bottom of each plot mark observations inside the diamagnetic cavity, which correspond to the lowest values of magnetic field magnitude.

We applied a linear fit on count rate data in each panel of Figure 4.26 (purple lines), to check for linear correlation between magnetic field strength and electron counts. R^2 coefficient (goodness-of-fit) is shown on each panel. No apparent linear correlation is visible in the fitted curves. However, we made several other observations:

- At high magnetic field strengths more electron count variations are observed and there are fewer variations when the spacecraft is in the cavity. For instance, in 13 eV electrons, count rates of about 30,000 s^{-1} are observed when the magnetic field magnitude is close to the minimum. By contrast, in channel 151 eV, count rate at minimum magnetic field strength is about 2000-3000 s^{-1}.

- Inside the cavity count rates have a narrow range, while outside the cavity the electron count rates have a wider range of values.
- For low energy electrons, count rate inside the cavity is not necessarily the minimum value, but for high energy electrons the minimum count rates occur at lowest magnetic field strengths, or when Rosetta is inside the diamagnetic cavity.

4.5.3 Modeling the Electron Flux near Possible Cavity Boundary of Comet 67P/CG

There have been several modeling attempts to estimate the position of the diamagnetic cavity and other cometary boundaries around comet 67P/CG (Koenders et al., 2013; Koenders et al., 2015; Richter et al., 2015; Rubin et al., 2012; Rubin et al., 2014b). Hybrid models show cometocentric distance of the diamagnetic cavity's boundary in the sun-comet direction at less than 50 km. The cavity crossing events that we discussed in sections 4.1.1.1 and 4.1.1.2 were observed at 170-200 km. Notably, models used gas production rates assumed pre-encounter which appeared to be much lower than the measured values by ROSINA-COPS (Hansen, 2016). Additionally, modeled boundary distances take scaling factor of ~3/2 near terminator plane regions. Modeled bow shock boundary was also estimated to be near 2000 km from the comet, which is much less than the solar wind ion gyroradius. Perhaps this is why plasma boundaries of comet 67P/CG do not resemble cometary plasma of other previously visited comets. Magnetohydrodynamic (MHD) models have shortcomings in simulating the cometary plasma too. However, improved multifluid MHD models are able to simulate draping of the magnetic field lines and ion gyrations near the comet, that agree with hybrid model results. These models predicted plasma instabilities (such as those discussed in Figure 4.19) occur because of asymmetric outgassing from the nucleus or because of sudden drop in the solar wind dynamic pressure.

In this section, we use our two-stream kinetic model to model electron energy distribution around the diamagnetic cavity of comet 67P/CG. For these model results, note that we neglected any surface photoelectrons that might be produced.

For the first model case, we simulated electron differential flux from pure photoionization of the neutral coma with no solar wind electrons (gray curve in Figure 4.27). For comparison, two IES electron flux spectra from inside (dashed magenta curve) and outside (dashed black curve) the diamagnetic cavity from the July 26 event are included in the figure. Note that the energy resolution of the model results is much higher than IES energy resolution. For easier comparison, however, model results have been sorted into an energy bin structure similar to that of the IES instrument. Visible peaks in the spectra around 30 eV and 100 eV correspond to features in the solar irradiance spectrum. The nucleus outgassing rate for all model runs was selected at $Q = 5 \times 10^{27}\ s^{-1}$ and distance to the comet nucleus is around 150 km at a heliocentric distance of 1.25 AU. Table 4.4 provides more details of the model parameters. These values are comparable to the Rosetta measurements during cavity crossing events in late July.

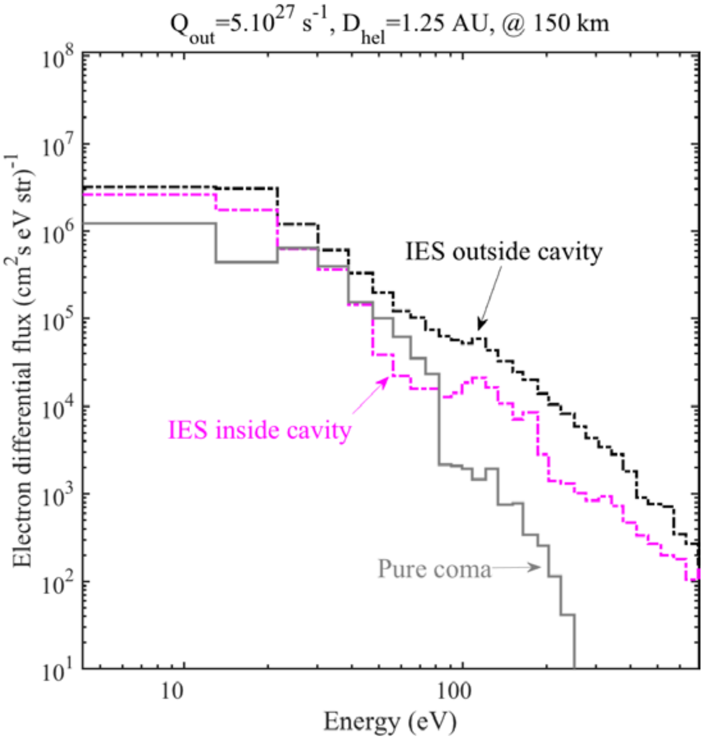

Figure 4.27 - Model spectra for differential flux of electrons for pure coma photoelectrons (gray). For comparison, figure shows two IES electron spectra from July 26, 2015, one for inside the diamagnetic cavity (the dashed magenta curve) and one for completely outside the cavity (the dashed black curve) are shown for comparison. The nucleus gas production rate is 5×10^{27} s^{-1}. The cometocentric distance is 150 km and the heliocentric distance is 1.25 AU. More details of the model parameters appear in Table 4.4.

Table 4.4 - Model parameters for electron flux near diamagnetic cavity boundary of comet 67P/CG at 1.25 AU.

Photoionization

Solar flux irradiance $F_{10.7}$:	118 sfu
Heliocentric distance:	1.25 AU
Model subsolar point:	150 km
Nucleus outgassing rate:	5×10^{27} s^{-1}
Neutral density profile:	$n(r) = \frac{Q}{4\pi r^2 u_n}$
Outflow velocity:	$u_n = 1$ km/s

Solar wind boundary flux parameters (at 1 AU)

Regular solar wind:

n_{core} :	7.0 cm^{-3}
T_{core} :	5 eV (~ $6x10^4$ K)
n_{halo} :	0.2 cm^{-3}
T_{halo} :	100 eV (~10^6 K)

Weak (attenuated) solar wind:

n_{core} :	1.0 cm^{-3}
T_{core} :	5 eV (~ $6x10^4$ K)
n_{halo} :	0.01 cm^{-3}
T_{halo} :	100 eV (~10^6 K)

For the second model case, solar wind electrons were injected as a boundary condition in the model in the form of a bi-Maxwellian distribution. Figure 4.28 shows two separate conditions with solar wind electrons that are over plotted on the previous figure. The red curve is for a weak (low density) solar wind, which represents an attenuated solar wind flux that would be observable inside the cometary bow shock but still outside the diamagnetic cavity. The blue curve is for a regular solar wind electron density which would correspond to the electron environment completely outside of the diamagnetic cavity. Table 4.4 provides densities and temperatures of the solar wind core and halo populations used at the model boundary.

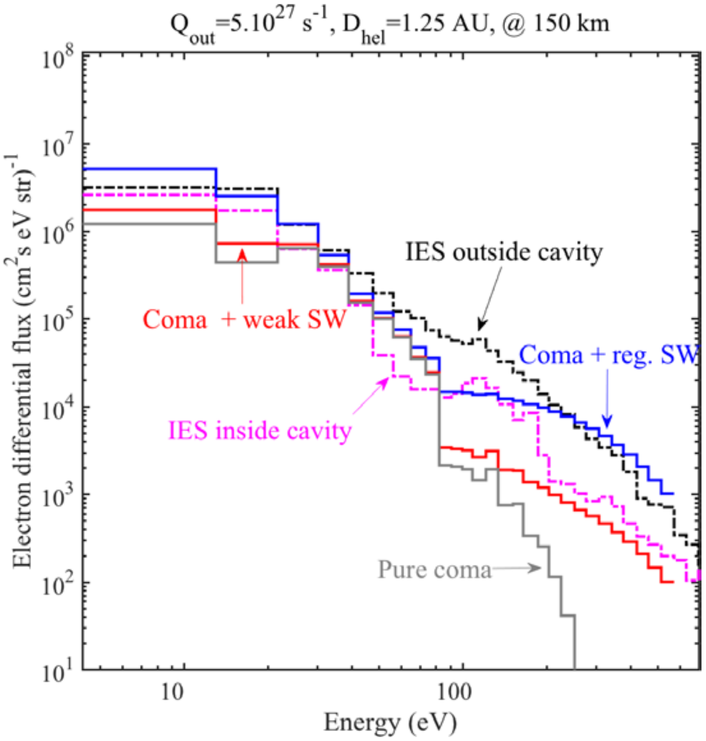

Figure 4.28 – Blue curve shows modeled electron spectra near the cavity boundary with coma photoelectrons and regular solar wind boundary flux. Results are over plotted on Figure 4.27. Red curve shows coma photoelectrons and attenuated (weak) solar wind boundary flux.

To simulate buildup of electrons inside the diamagnetic cavity for the next model case, we constrained motion of electrons by trapping all coma photoelectrons in the region by a reflecting boundary condition, so that the photoelectrons would remain within about 150 km from the nucleus and interact with the neutral coma. We set the solar wind boundary flux to zero for this case. The result of this case is shown with the green curve. Green curve in Figure 4.29 shows this case, which is over plotted on Figure 4.28 to include previous cases for better comparisons.

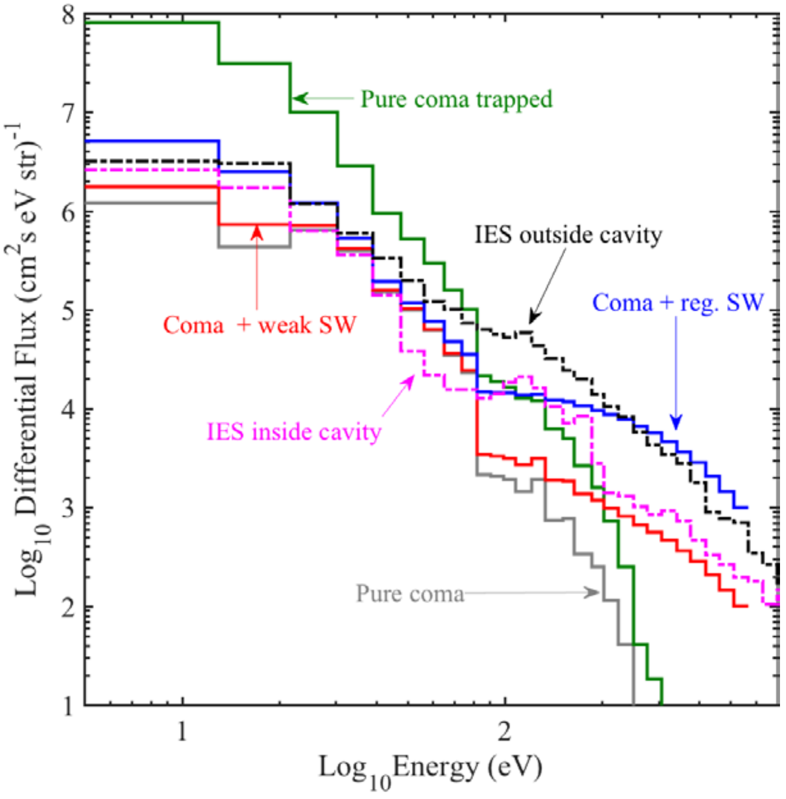

Figure 4.29 – Green curve shows trapped coma photoelectrons with reflecting boundary condition and no solar wind flux, over plotted on Figure 4.28.

4.5.4 Interpretation and Location of the Cavity Boundary

At comet 1P/Halley, thermal pressure of the cometary plasma was insufficient to balance solar wind pressure (i.e., not a Venus-like ionospheric balance). Instead, force balance between the ion-neutral drag force and the magnetic pressure determines position of the cavity boundary (Cravens, 1986; Ip and Axford, 1987). The simple one-dimensional (i.e., along the radius) model by Cravens (1986) reasonably simulated the magnetic field's structure near the cavity boundary at comet 1P/Halley. In that model, a magnetic field pile-up region was assumed to exist upstream from the diamagnetic cavity. In this section we estimate the diamagnetic cavity distance around comet 67P/CG using a similar approach, but with different assumptions.

Water group ions, specifically H_3O^+, are the most abundant ion species in the coma of an active comet (Nilsson et al., 2015). The H_3O^+ is produced through fast reaction of H_2O^+ with water molecules (Korosmezey et al., 1987):

$$H_2O^+ + H_2O \rightarrow H_3O^+ + OH \quad , k_{in} = 1.1 \times 10^{-9} \qquad 4.17$$

where k_{in} is the ion-neutral collision rate. H_3O^+ is consumed by electron dissociative recombination (Damas and Mendis, 1992; Goldstein et al., 1989). The structure of the magnetic field as a function of distance and outgassing rate can be calculated from:

$$\mathrm{B(r)} = \mathrm{B_0}\sqrt{1 - \left(\frac{\mathrm{r_{cs}}}{\mathrm{r}}\right)^2} \qquad 4.18$$

where r is the distance to the comet, r_{cs} is the boundary or stand-off distance, and B_0 is maximum magnitude of the stagnant magnetic field upstream of the comet. B_0 is an independent parameter and can be considered a proxy for solar wind dynamic pressure (Cravens, 1989). Stand-off distance of the cavity boundary is highly sensitive to outgassing rate from the nucleus and the maximum stagnant magnetic field. At a distance of $\mathrm{r} = \mathrm{r_{cs}}$, magnitude of the magnetic field is zero and $\mathrm{r_{cs}}$ can be found from (Madanian et al., 2016a):

$$r_{cs} = 7.08 \times 10^{-18}\ \frac{Q^{\frac{3}{4}}}{B_0}\ [\mathrm{cm}] \qquad 4.19$$

In this equation, B_0 is in units of Gauss, and Q is the nucleus outgassing rate in s^{-1}.

Equation 4.19 can be used to calculate the position of the cavity boundary based on Rosetta measurements of outgassing rate and magnetic field from July 20 to August 10, 2015. Neutral outgassing rates are from ROSINA-COPS measurement. We found the B_0 values by searching for local maxima (peaks) in the magnetic field data according to these criteria:

1. Peak values must be greater than 30 nT.
2. Minimum prominence is 20 nT.
3. Minimum time between two adjacent peaks is one minute.

Corresponding (or closest available) outgassing rates and magnetic field magnitudes at the peak points are then used for estimating the cavity boundary.

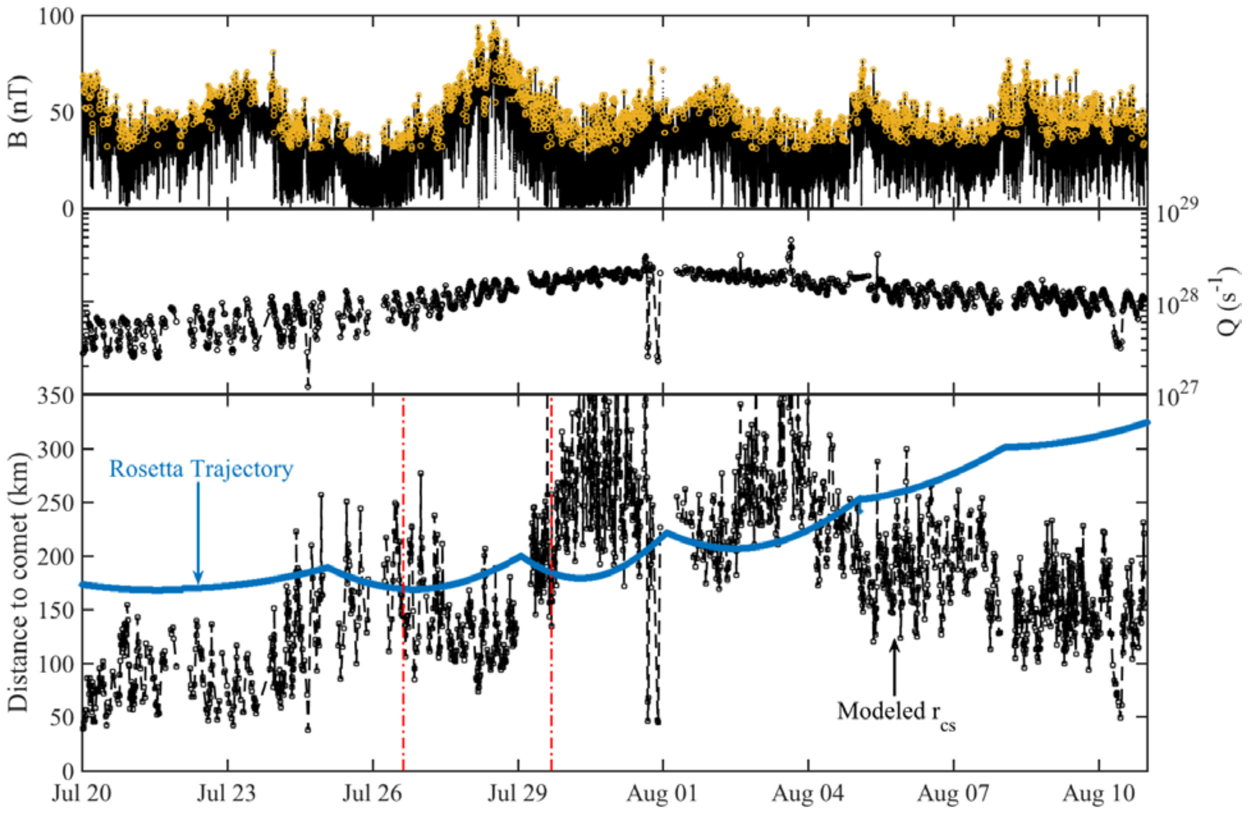

Figure 4.30 - Top panel shows magnitude of the magnetic field in black. Yellow circles represent local maxima in the magnetic field. The middle panel shows the neutral outgassing rate measured by ROSINA-COPS. The third panel shows the Rosetta's distance to the comet (blue curve) and the modeled cavity boundary distances black. The two red vertical lines on this panel mark timestamps of two observed cavity crossing events that we considered earlier.

Results of this simple approach appear in Figure 4.30. The figure's top panel shows the magnetic field magnitude in nT in black. Local peak points in the magnetic field are indicated with yellow circles. The middle panel is the nucleus outgassing rate. The sinusoidal changes on this curve correspond to the 12 hour rotational period of the comet and the northern lobe having an outgassing rate higher than that of the southern lobe. The bottom panel shows the Rosetta spacecraft trajectory (blue line) and modeled cavity boundary distances (r_{cs}). The two vertical dashed lines in red designate two cavity crossing events on July 26 and July 29, 2015, that we reviewed in previous sections.

Estimated r_{cs} agree reasonably well with observed distances of the two cavity crossing events on July 26 and July 29, which were at about 170 km from the nucleus. Some estimates in Figure 4.30 indicate that the spacecraft should have been inside the diamagnetic cavity on July 30 or August 3. A closer look at MAG data for these dates shows that on July 30, magnetic field strength dropped to the lowest values in few instances. But on August 3, while our model predicted that Rosetta should be in the cavity the magnetic field showed no reduction. Therefore, discrepancies may be present because this model provides only a rough estimate of the cavity boundary, and because many plasma complexities were not taken into account. Outgassing rates and magnetic field measurements can also be highly error prone. For instance, outgassing rate is only an approximation of the total production rate and is deduced from a single point measurement at the location of Rosetta.

5 Conclusion

In this dissertation, different aspects of the interaction of two non-magnetized objects in the solar system, Titan and comet 67P/CG, with their external plasma environment were explored. Both model and observations were emphasized, and comparisons were made. Each object shows specific measurable properties in response to modulations of external effects.

5.1 Titan

5.1.1 Physics Learned and New Findings

The state of Titan's highly complex ionosphere is affected by several factors including ionization rate, background neutral atmosphere, relative abundance of minor neutral species, and ionospheric dynamics. In this dissertation changes to the ionosphere due to solar magnetic activity cycle have been investigated. The effects of ion transport in the ionosphere and the significance of the ion-neutral chemistry have also been discussed.

The photoionization of major neutral species by the solar photon flux is the main source of ionization in the dayside ionosphere. The chemical reactions between photoions and neutral species, minor neutral species in particular, result in production of the heavier and more complex ion species. Cassini INMS ion densities and RPWS-LP electron density measurements for 21 Titan flybys and neutral density measurements for 33 flybys were presented. The variation of ionospheric densities due to the changing solar radiation fluxes over parts of solar cycles 23/24 and due to solar zenith angle was considered. The effects were particularly clear for primary ion species which relate to ion production rates. The correlations for other ion species were not so obvious. Several variables including solar zenith angle, spacecraft pointing, seasonal changes, heliocentric distance, and flyby geometry increase the uncertainty of the results (Madanian et al., 2016c).

In particular, the following has been reported in this work:

1. The densities of primary ion species, e.g., CH_3^+, best display the effects of the solar activity cycle. The peak CH_3^+ density appears at higher altitudes as the solar zenith angle (SZA) increases. This is particularly visible for low solar activity. The density peaks for high activity profiles, however, remain at about the same altitude. Removing SZA dependence from CH_3^+ data resulted in less dispersed densities near the peak of the ionosphere while high solar activity observations still showed noticeable enhancements. The same treatment on $HCNH^+$ also reduced the scatter for high and low solar activity data.

2. N_2^+ production rates were calculated for four individual flybys using the methods of *Richard et al.* (2015) but using updated INMS calibration factors. The empirical rates are based on measured CH_3^+ and CH_4 densities. The primary ion production rates, both modeled and empirical, exhibit enhancements with increased solar activity. The altitude of maximum production rate in the rate profiles also decreases for high solar activity. This decrease can be explained by the fact that the production rates are proportional to the density of thermospheric methane, which later flybys have measured to be low.

3. The distribution of peak ion density versus SZA on the dayside shows smaller variations for the heavier ion species than the light/primary ion species. The heavier ion species are produced later in the chemistry chain, and their densities will also be affected by the total electron density through recombination and by variations in minor neutral species.

4. Measured ion densities are affected both by solar activity and by SZA. The effect of solar zenith angle, however, overshadows the solar cycle effect, and comparison of high and low

solar activity could not be made between observations for solar zenith angles that are too different. The T83 flyby is one of the cases considered for high solar activity. The solar zenith angle at closest approach is around 70 degrees, and the ion densities measured during this flyby are lower in comparison with other flybys at high activity periods.

5. Altitude of the peak ion density for all major ions is lower for later flybys (after T80), when solar activity was higher. The neutral density profiles and SZA strongly affect the altitude of the peak ionospheric densities. The altitude of the ionospheric peak drops when the neutral densities for higher solar activity are lower at a given altitude. The depletion of methane abundance at higher solar activity can be related to photodestruction of this molecule by solar radiation (Westlake et al., 2011; Westlake et al., 2014).

6. Comparing the Cassini data of 2015, gathered immediately after solar maximum, to 2008 data near the solar minimum, shows a drop in the altitude of the ionospheric peak and the background neutral atmosphere. Whether this depletion of neutral species at ionospheric layers is due to solar activity (i.e., enhanced photodestruction of methane) or instrumental effect requires more investigations.

5.1.2 Future and Suggested Work for Titan

The present work and previous studies indicate that there are discrepancies between the Cassini INMS in-situ measurement of the ionospheric densities and the photochemical models of Titan’s ionosphere. The ionospheric models tend to overestimate the densities of ion species, particularly the most abundant ion species, $HNCH^+$. A more comprehensive analysis is required to investigate the current chemistry models and to validate the estimated reaction rates. These estimates have sometimes been made by modelers to achieve photochemical equilibrium for specific ion species. Laboratory measurements under simulated environmental conditions or quantum mechanical calculations of the rate constants can significantly lower the uncertainty and perhaps increase the effectiveness of these reactions in the models.

A major loss term for $HCNH^+$ and many other heavy ion species is dissociative electron recombination, which depends on the electron density and temperature. As pointed out by Galand et al. (2014), the electron recombination rate coefficients for many heavy ions are evidently not well known, and the key loss processes for electrons may still be missing in the models. Further investigation on the relation between rate coefficients and electron temperature, ion mass, and so forth, is essential for a better understanding of Titan's ionosphere and for improving the models.

Mixing ratios of minor neutral species directly affects the ionospheric densities. $HCNH^+$, for instance, is mainly produced through reactions of CH_5^+ and $C_2H_5^+$ ions with HCN. A main loss channel for $HCNH^+$ is its reaction with ammonia, NH_3. Currently both HCN and NH_3 density profiles are estimated by ion-neutral chemistry models. A few studies have utilized INMS in-situ measurements to derive HCN abundance at select altitudes and for a limited number of flybys (Cui et al., 2016). However, further research can be done using INMS data to provide more accurate estimates of NH_3 and HCN densities, which distinctly impact $HCNH^+$ densities. One complicating issue with deriving the NH_3 densities is that it is seen as an adsorbed contaminant of the INMS antechamber at mass channel 17. This channel also sees isotopes of methane, $^{13}CH_4$, abundant at low altitude. One way to approach this problem is by measuring the $^{12}CH_4/^{13}CH_4$ isotopes ratio during the inbound and assuming the same altitude dependence of that ratio in the outbound. Given this ratio, a function can be fit on the decaying signal of the outbound data well after the closest approach, which mainly comes from the desorbed gases exposed to vacuum, and the contribution of the NH_3 signal can be calculated (also see discussion by Magee et al. (2009)). It is also possible that the observed NH_3 signal is from the spent hydrazine in the thruster exhaust. But the INMS data of mass 17 signal does not show obvious disruptions during thruster firings.

Furthermore, the ion transport model described in chapter 2 was an initial attempt to study effects of ionospheric transport on the photochemical equilibrium densities. I showed that one dimensional ionospheric transport can have a significant effect in altitudes above 1400 km. A more realistic transport regime with radial, zonal, and azimuthal components and full ion chemistry can result in much different impacts on the ion densities, even at lower ionospheric altitudes.

5.2 Comet 67P/CG

The second part of this dissertation focused on investigating the plasma environment around comet 67P/CG, which was the target of the Rosetta mission. I investigated the behavior of electrons near the nucleus of comet 67P/CG using Rosetta RPC-IES data plus model calculations.

5.2.1 Physics Learned and New Findings

5.2.1.1 Comet at 3 AU

The Rosetta IES experiment revealed the presence of greatly enhanced electron fluxes and densities near the nucleus, confirmed by the density measurements of the LAP and MIP instruments. Our modeling efforts demonstrated that the observed electrons are a combination of compressed solar wind electrons plus photoelectrons due to the photoionization of the comet’s surface and the coma gas by solar radiation. The electron density and flux enhancements that were observed are evidently associated with an ion density enhancement consisting of slowly moving pickup ions created by the ionization of neutrals. Such a density enhancement was predicted by pre-encounter simulations. I also conclude that unperturbed photoelectron fluxes or solar wind electron fluxes at some energies are too low to match measured fluxes. Each photoion (i.e., pickup ion) created comes with a photoelectron, but the electron fluxes (and densities) associated with the photoelectrons in the two-stream model are not sufficient to explain the IES data in the range of 5-200 eV, while the lower energy electrons are much higher than the observations. The ions move slowly so that their density builds up, whereas the electrons quickly escape from the vicinity of the nucleus, unless they are prevented by electric fields or collisions. Three processes must be operating near the nucleus:

1. Collisional cooling of suprathermal electrons through electron-neutral collisions.
2. Confinement of the electrons near the nucleus by an ambipolar electric field.
3. Enhancement of the fluxes due to compression of the electron gas near the nucleus.

We also showed that at 3 AU within 100 km from the nucleus, cooling of suprathermal electrons through electron-neutral collisions becomes significant, and a population of cold thermal electrons begins to build up, which is also confined by the ambipolar electric field.

Compression due to deceleration, confinement by an ambipolar field, and addition of electrons by photoionization, all evidently play a role in determining the electron distribution function (i.e., electron spectrum), but our models put these effects in sequentially and simplistically rather than simultaneously. Nonetheless, the model results and the IES electron data agree in many respects, indicating that we have probably identified key processes in the near-nucleus solar wind comet interaction at 3 AU.

5.2.1.2 Comet at Perihelion

Rosetta spacecraft observations of comet 67P/CG near perihelion were also analyzed. The suprathermal electron fluxes inside the diamagnetic cavity are moderately lower than outside. The flux of electrons with energies between 40 eV to a couple of hundred eV shows a decrease inside the cavity, with more noticeable drops at energies around 60-100 eV and 150-250 eV.

A possible reason for the lower electron fluxes in the cavity could be that solar wind suprathermal electrons are, somehow, obstructed from reaching inside the diamagnetic cavity. More specifically, the diamagnetic cavity is partially shielded from attenuated suprathermal solar wind electrons. Another possible explanation is that a lower solar wind dynamic pressure is required to have a diamagnetic cavity, and a lower solar wind dynamic pressure means lower suprathermal electron fluxes. It should be noted that when the spacecraft is outside the cavity, higher fluxes are observed at higher magnetic field magnitudes. This is an indication that for a high magnetic field strength, there is a high solar wind dynamic pressure, which then correlates with high solar wind electron flux and density.

A comparison of the modeled spectra with the IES measurements suggests that inside the cavity, coma photoelectrons (model case 1) are not sufficient to explain the IES data, and either a trapping mechanism and/or solar wind electrons are needed. At an energy range between 40 to 90 eV, the IES electron flux is lower than what model case 2 predicts, suggesting that there are obstacles for external (i.e., solar wind) electrons with those energies to reach inside the cavity boundary, in agreement with our earlier speculation.

Furthermore, multiple diamagnetic cavity crossing events seen in the data can be attributed to the very dynamic solar wind conditions and the fact that during perihelion passage, the spacecraft distance to the comet was about and beyond 150 km. This puts the spacecraft far outside the predicted diamagnetic cavity boundary (Koenders et al., 2015). The most likely explanation for this moving/transient boundary is the existence of Kelvin-Helmholtz instabilities propagating tail-ward along the cavity surface. The transient nature of these events, however, makes it difficult to compare the observations at comet 67P/CG with other comets such as 1P/Halley.

5.2.2 Future and Suggested Work

Further cometary research opportunities immediately present themselves from this research. Additional multi-instrument analyses of the plasma are required for dayside and nightside excursions when Rosetta maneuvered far away from the comet. The dayside excursion in September – October 2015 provides an opportunity to observe and study the possible effects of a bow shock upstream of the comet.

From Figure 4.17, something is probably still missing from the model for some cases (wave-particle heating perhaps). The underestimation of the electron population in the model spectrum at some energies may also be due to the use of a solar minimum radiation flux. Using a flux for higher solar activity would increase the electron densities and can bring the model results closer to the IES observation.

The effects of the ambipolar electric field and plasma compression on the electrons were only approximated in this work. A more detailed model of electron transport able to incorporate and simulate the changes in magnetic field and parallel component of the electric field is in demand. Preliminary work is also underway to utilize a Monte-Carlo transport scheme in the cometary plasma.

Nature of the comet 67P/CG diamagnetic cavity is not well understood yet. Estimates of the cavity boundary in Figure 4.30 are based on a Halley-type cavity, which might not be entirely correct. Even though the model gave reasonably accurate predictions of stand-off boundary distances for some periods, it contradicts observations in other times. For instance, between July 29 and August 4 our model predicted that Rosetta should be inside the diamagnetic cavity region. Yet, as pointed out earlier, observations show that the spacecraft was outside the diamagnetic region during that period. The plasma environment of comet 67P/CG is highly complex and a classic Halley-type diamagnetic cavity formalism cannot always explain the diamagnetic regions.

Possible electron cooling processes can contribute to the lower flux of electrons at certain energies inside the diamagnetic cavity. Wave-particle interactions and plasma instabilities in the region near the cavity boundary are also important characteristics of such environments that require additional research.

References

Anicich, V.G., 2003. An Index of the Literature for Bimolecular Gas Phase Cation-Molecule Reaction Kinetics. In: C.I.o.T. Jet Propul. Lab. (Editor). NASA, Pasadena, CA, pp. 1–28, 53–262, 668–701.

Balsiger, H., Altwegg, K., Bochsler, P., Eberhardt, P., Fischer, J., Graf, S., Jackel, A., Kopp, E., Langer, U., Mildner, M., Muller, J., Riesen, T., Rubin, M., Scherer, S., Wurz, P., Wuthrich, S., Arijs, E., Delanoye, S., De Keyser, J., Neefs, E., Nevejans, D., Reme, H., Aoustin, C., Mazelle, C., Medale, J.L., Sauvaud, J.A., Berthelier, J.J., Bertaux, J.L., Duvet, L., Illiano, J.M., Fuselier, S.A., Ghielmetti, A.G., Magoncelli, T., Shelley, E.G., Korth, A., Heerlein, K., Lauche, H., Livi, S., Loose, A., Mall, U., Wilken, B., Gliem, F., Fiethe, B., Gombosi, T.I., Block, B., Carignan, G.R., Fisk, L.A., Waite, J.H., Young, D.T. and Wollnik, H., 2007. Rosina - Rosetta orbiter spectrometer for ion and neutral analysis. Space Science Reviews, 128(1-4): 745-801.

Balsiger, H., Altwegg, K., Buhler, F., Geiss, J., Ghielmetti, A.G., Goldstein, B.E., Goldstein, R., Huntress, W.T., Ip, W.H., Lazarus, A.J., Meier, A., Neugebauer, M., Rettenmund, U., Rosenbauer, H., Schwenn, R., Sharp, R.D., Shelley, E.G., Ungstrup, E. and Young, D.T., 1986. Ion Composition and Dynamics at Comet Halley. Nature, 321(6067): 330-334.

Bell, J.M., Bougher, S.W., Waite, J.H., Ridley, A.J., Magee, B.A., Mandt, K.E., Westlake, J., DeJong, A.D., Bar-Nun, A., Jacovi, R., Toth, G. and De La Haye, V., 2010. Simulating the one-dimensional structure of Titan's upper atmosphere: 1. Formulation of the Titan Global Ionosphere-Thermosphere Model and benchmark simulations. Journal of Geophysical Research-Planets, 115.

Bertucci, C.L., 2009. Characteristics and variability of Titan's magnetic environment. Philos Trans A Math Phys Eng Sci, 367(1889): 789-98.

Bieler, A., Altwegg, K., Balsiger, H., Berthelier, J.J., Calmonte, U., Combi, M., De Keyser, J., Fiethe, B., Fougere, N., Fuselier, S., Gasc, S., Gombosi, T., Hansen, K., Hassig, M., Huang, Z.G., Jackel, A., Ha, X.Z., Le Roy, L., Mall, U.A., Reme, H., Rubin, M., Tenishev, V., Toth, G., Tzou, C.Y. and Wurz, P., 2015. Comparison of 3D kinetic and hydrodynamic models to ROSINA-COPS measurements of the neutral coma of 67P/Churyumov-Gerasimenko. Astronomy & Astrophysics, 583: A7.

Bird, M.K., Dutta-Roy, R., Asmar, S.W. and Rebold, T.A., 1997. Detection of Titan's ionosphere from Voyager 1 radio occultation observations. Icarus, 130(2): 426-436.

Broiles, T.W., Burch, J.L., Clark, G., Koenders, C., Behar, E., Goldstein, R., Fuselier, S.A., Mandt, K.E., Mokashi, P. and Samara, M., 2015. Rosetta observations of solar wind interaction with the comet 67P/Churyumov-Gerasimenko. Astronomy & Astrophysics, 583: A21.

Broiles, T.W., Livadiotis, G., Burch, J.L., Chae, K., Clark, G., Cravens, T.E., Davidson, R., Eriksson, A., Frahm, R.A., Fuselier, S.A., Goldstein, J., Goldstein, R., Henri, P., Madanian, H., Mandt, K., Mokashi, P., Pollock, C., Rahmati, A., Samara, M. and Schwartz, S.J., 2016. Characterizing cometary electrons with kappa distributions. Journal of Geophysical Research-Space Physics, 121(8): 7407-7422.

Burch, J.L., Goldstein, R., Cravens, T.E., Gibson, W.C., Lundin, R.N., Pollock, C.J., Winningham, J.D. and Young, D.T., 2007. RPC-IES: The ion and electron sensor of the Rosetta Plasma Consortium. Space Science Reviews, 128(1-4): 697-712.

Burch, J.L., Gombosi, T.I., Clark, G., Mokashi, P. and Goldstein, R., 2015. Observation of charged nanograins at comet 67P/Churyumov-Gerasimenko. Geophysical Research Letters, 42(16): 6575-6581.

Carr, C., Cupido, E., Lee, C.G.Y., Balogh, A., Beek, T., Burch, J.L., Dunford, C.N., Eriksson, A.I., Gill, R., Glassmeier, K.H., Goldstein, R., Lagoutte, D., Lundin, R., Lundin, K., Lybekk, B., Michau, J.L., Musmann, G., Nilsson, H., Pollock, C., Richter, I. and Trotignon, J.G., 2007. RPC: The Rosetta Plasma Consortium. Space Science Reviews, 128(1-4): 629-647.

Chamberlin, P.C., Woods, T.N. and Eparvier, F.G., 2007. Flare Irradiance Spectral Model (FISM): Daily component algorithms and results. Space Weather, 5(7): n/a-n/a.

Cicerone, R.J., Swartz, W.E., Stolarski, R.S., Nagy, A.F. and Nisbet, J.S., 1973. Thermalization and Transport of Photoelectrons: A Comparison of Theoretical Approaches. Journal of Geophysical Research, 78(28): 6709-6728.

Coates, A.J., 2009. Interaction of Titan's ionosphere with Saturn's magnetosphere. Philos Trans A Math Phys Eng Sci, 367(1889): 773-88.

Coates, A.J., Crary, F.J., Lewis, G.R., Young, D.T., Waite, J.H. and Sittler, E.C., 2007. Discovery of heavy negative ions in Titan's ionosphere. Geophysical Research Letters, 34(22).

Coates, A.J., Johnstone, A.D. and Kessel, R.L., 1991. Plasma parameters near the comet Halley bow shock.

Coates, A.J., Mazelle, C. and Neubauer, F.M., 1997. Bow shock analysis at comets Halley and Grigg-Skjellerup. Journal of Geophysical Research-Space Physics, 102(A4): 7105-7113.

Coates, A.J., Wahlund, J.E., Agren, K., Edberg, N., Cui, J., Wellbrock, A. and Szego, K., 2011. Recent Results from Titan's Ionosphere. Space Science Reviews, 162(1-4): 85-111.

Coustenis, A., Bampasidis, G., Achterberg, R.K., Lavvas, P., Jennings, D.E., Nixon, C.A., Teanby, N.A., Vinatier, S., Flasar, F.M., Carlson, R.C., Orton, G., Romani, P.N., Guandique, E.A. and Stamogiorgos, S., 2013. Evolution of the Stratospheric Temperature and Chemical Composition over One Titanian Year. Astrophysical Journal, 779(2): 177.

Coustenis, A., Salama, A., Lellouch, E., Encrenaz, Th., Bjoraker, G., Samuelson, R. E., de Graauw, Th., Feuchtgruber, H., Kessler, M. F., 1998. Evidence for water vapor in Titan’s atmosphere from ISO/SWS data. Astronomy & Astrophysics, 336: L85-L89.

Cravens, T.E., 1986. The Physics of the Cometary Contact Surface. In: B. Battrick, E.J. Rolfe and R. Reinhard (Editors), 20th ESLAB Symp. the Exploration of Halley’s Comet. Eur. Space Agency Spec. Publ.

Cravens, T.E., 1989. A Magnetohydrodynamical Model of the Inner Coma of Comet Halley. Journal of Geophysical Research-Space Physics, 94(A11): 15025-15040.

Cravens, T.E., 1997. Physics of Solar System Plasmas. Cambridge University Press.

Cravens, T.E. and Gombosi, T.I., 2004. Cometary magnetospheres: a tutorial. Comparative Magnetospheres, 33(11): 1968-1976.

Cravens, T.E. and Korosmezey, A., 1986. Vibrational and rotational cooling of electrons by water vapor. **Planetary and Space Science**, 34: 961-970.

Cravens, T.E., Kozyra, J.U., Nagy, A.F., Gombosi, T.I. and Kurtz, M., 1987. Electron-Impact Ionization in the Vicinity of Comets. Journal of Geophysical Research-Space Physics, 92(A7): 7341-7353.

Cravens, T.E., Lindgren, C.J. and Puhl-Quinn, P., 1995. The comet Halley Diamagnetic Cavity Boundary. advances in Space Research, 16(4).

Cravens, T.E., Richard, M., Ma, Y.J., Bertucci, C., Luhmann, J.G., Ledvina, S., Robertson, I.P., Wahlund, J.E., Agren, K., Cui, J., Muller-Wodarg, I., Waite, J.H., Dougherty, M., Bell, J. and Ulusen, D., 2010. Dynamical and magnetic field time constants for Titan's ionosphere: Empirical estimates and comparisons with Venus. Journal of Geophysical Research-Space Physics, 115.

Cravens, T.E., Robertson, I.P., Clark, J., Wahlund, J.E., Waite, J.H., Ledvina, S.A., Niemann, H.B., Yelle, R.V., Kasprzak, W.T., Luhmann, J.G., McNutt, R.L., Ip, W.H., De La Haye, V., Muller-Wodarg, I., Young, D.T. and Coates, A.J., 2005. Titan's ionosphere: Model comparisons with Cassini Ta Data. Geophysical Research Letters, 32(12): n/a-n/a.

Cravens, T.E., Robertson, I.P., Waite, J.H., Yelle, R.V., Kasprzak, W.T., Keller, C.N., Ledvina, S.A., Niemann, H.B., Luhmann, J.G., McNutt, R.L., Ip, W.H., De La Haye, V., Mueller-Wodarg, I., Wahlund, J.E., Anicich, V.G. and Vuitton, V., 2006. Composition of titan's ionosphere. Geophysical Research Letters, 33(7).

Cravens, T.E., Yelle, R.V., Wahlund, J.E., Shemansky, D.E. and Nagy, A.F., 2009. Composition and structure of the ionosphere and thermosphere. In: R.H. Brown, J.P. Lebreton and J.H. Waite (Editors), Titan From Cassini-Huygens. Springer, New York, pp. 259-295.

Cui, J., Cao, Y.T., Lavvas, P.P. and Koskinen, T.T., 2016. The Variability of Hcn in Titan's Upper Atmosphere as Implied by the Cassini Ion-Neutral Mass Spectrometer Measurements. Astrophysical Journal Letters, 826(1): L5.

Cui, J., Galand, M., Yelle, R.V., Wahlund, J.E., Ågren, K., Waite, J.H. and Dougherty, M.K., 2010. Ion transport in Titan's upper atmosphere. Journal of Geophysical Research: Space Physics, 115(A6): n/a-n/a.

Cui, J., Yelle, R.V., Strobel, D.F., Müller-Wodarg, I.C.F., Snowden, D.S., Koskinen, T.T. and Galand, M., 2012. The CH4structure in Titan's upper atmosphere revisited. Journal of Geophysical Research: Planets, 117(E11): n/a-n/a.

Cui, J., Yelle, R.V., Vuitton, V., Waite, J.H., Kasprzak, W.T., Gell, D.A., Niemann, H.B., Muller-Wodarg, I.C.F., Borggren, N., Fletcher, G.G., Patrick, E.L., Raaen, E. and Magee, B.A., 2009. Analysis of Titan's neutral upper atmosphere from Cassini Ion Neutral Mass Spectrometer measurements. Icarus, 200(2): 581-615.

Damas, M.C. and Mendis, D.A., 1992. A three-dimensional axisymmetric photochemical flow model of the cometary 'inner' shock layer. The Astrophysical Journal, 396: 704.

Edberg, N.J.T., Andrews, D.J., Bertucci, C., Gurnett, D.A., Holmberg, M.K.G., Jackman, C.M., Kurth, W.S., Menietti, J.D., Opgenoorth, H.J., Shebanits, O., Vigren, E. and Wahlund, J.E., 2015a. Effects of Saturn's magnetospheric dynamics on Titan's ionosphere. Journal of Geophysical Research-Space Physics, 120(10): 8884-8898.

Edberg, N.J.T., Andrews, D.J., Bertucci, C., Gurnett, D.A., Holmberg, M.K.G., Jackman, C.M., Kurth, W.S., Menietti, J.D., Opgenoorth, H.J., Shebanits, O., Vigren, E. and Wahlund, J.E., 2015b. Effects of Saturn's magnetospheric dynamics on Titan's ionosphere. Journal of Geophysical Research: Space Physics, 120(10): 8884-8898.

Edberg, N.J.T., Eriksson, A.I., Odelstad, E., Henri, P., Lebreton, J.P., Gasc, S., Rubin, M., Andre, M., Gill, R., Johansson, E.P.G., Johansson, F., Vigren, E., Wahlund, J.E., Carr, C.M., Cupido, E., Glassmeier, K.H., Goldstein, R., Koenders, C., Mandt, K., Nemeth, Z., Nilsson, H., Richter, I., Wieser, G.S., Szego, K. and Volwerk, M., 2015c. Spatial distribution of low-energy plasma around comet 67P/CG from Rosetta measurements. Geophysical Research Letters, 42(11): 4263-4269.

Edberg, N.J.T., Eriksson, A.I., Odelstad, E., Vigren, E., Andrews, D.J., Johansson, F., Burch, J.L., Carr, C.M., Cupido, E., Glassmeier, K.H., Goldstein, R., Halekas, J.S., Henri, P., Koenders, C., Mandt, K., Mokashi, P., Nemeth, Z., Nilsson, H., Ramstad, R., Richter, I. and Wieser, G.S., 2016. Solar wind interaction with comet 67P: Impacts of corotating interaction regions. Journal of Geophysical Research: Space Physics, 121(2): 949-965.

Eriksson, A.I., Bostrom, R., Gill, R., Ahlen, L., Jansson, S.E., Wahlund, J.E., Andre, M., Malkki, A., Holtet, J.A., Lybekk, B., Pedersen, A. and Blomberg, L.G., 2007. RPC-LAP: The Rosetta Langmuir probe instrument. Space Science Reviews, 128(1-4): 729-744.

Eviatar, A. and Goldstein, B.E., 1988. A Unidimensional Model of Comet Ionosphere Structure. Journal of Geophysical Research-Space Physics, 93(A3): 1759-1765.

Flammer, K.R., Omidi, N. and Quest, K.B., 1991. The Structure of a Tangential Discontinuity - Application to the Cometary Ionopause. Geophysical Research Letters, 18(3): 369-372.

Fontenla, J.M., Harder, J., Livingston, W., Snow, M. and Woods, T., 2011. High-resolution solar spectral irradiance from extreme ultraviolet to far infrared. Journal of Geophysical Research-Atmospheres, 116.

Fontenla, J.M., Landi, E., Snow, M. and Woods, T., 2014. Far- and Extreme-UV Solar Spectral Irradiance and Radiance from Simplified Atmospheric Physical Models. Solar Physics, 289(2): 515-544.

Galand, M., Coates, A., Cravens, T. and Wahlund, J.-E., 2014. Titan’s ionosphere. In: I.C.F. Mueller-Wodarg (Editor), Titan: Interior, Surface, Atmosphere, and Space Environment. Cambridge Univ. Press, New York, pp. 378-418.

Gallagher, J.W., Brion, C.E., Samson, J.A.R. and Langhoff, P.W., 1988. Absolute cross sections for molecular photoabsorption, partial photoionization, and ionic photo fragmentation processes. J. Phys. Chem. Ref. Data, 17(9).

Gan, L., 1991. ELECTRON DISTRIBUTIONAND SOLAR WIND INTERACTION WITH NONMAGNETIZED PLANETS, University of Michigan.

Gan, L. and Cravens, T.E., 1990. Electron Energetics in the Inner Coma of Comet Halley. Journal of Geophysical Research-Space Physics, 95(A5): 6285-6303.

Gan, L., Keller, C.N. and Cravens, T.E., 1992. Electrons in the ionosphere of Titan. Journal of Geophysical Research, 97: 2136–12151.

Glassmeier, K.H., Boehnhardt, H., Koschny, D., Kuhrt, E. and Richter, I., 2007a. The ROSETTA Mission: Flying towards the origin of the solar system. Space Science Reviews, 128(1-4): 1-21.

Glassmeier, K.H., Richter, I., Diedrich, A., Musmann, G., Auster, U., Motschmann, U., Balogh, A., Carr, C., Cupido, E., Coates, A., Rother, M., Schwingenschuh, K., Szego, K. and Tsurutani, B., 2007b. RPC-MAG - The fluxgate magnetometer in the ROSETTA plasma consortium. Space Science Reviews, 128(1-4): 649-670.

Goetz, C., Koenders, C., Richter, I., Altwegg, K., Burch, J., Carr, C., Cupido, E., Eriksson, A., Guttler, C., Henri, P., Mokashi, P., Nemeth, Z., Nilsson, H., Rubin, M., Sierks, H., Tsurutani, B., Vallat, C., Volwerk, M. and Glassmeier, K.H., 2016. First detection of a diamagnetic cavity at comet 67P/Churyumov-Gerasimenko. Astronomy & Astrophysics, 588: A24.

Goldstein, B.E., Altwegg, K., Balsiger, H., Fuselier, S.A., Ip, W.H., Meier, A., Neugebauer, M., Rosenbauer, H. and Schwenn, R., 1989. Observations of a shock and a recombination layer at the contact surface of comet Halley. Journal of Geophysical Research, 94(A12): 17251.

Goldstein, R., Burch, J.L., Mokashi, P., Broiles, T., Mandt, K., Hanley, J., Cravens, T., Rahmati, A., Samara, M., Clark, G., Hassig, M. and Webster, J.M., 2015. The Rosetta Ion and Electron Sensor (IES) measurement of the development of pickup ions from comet 67P/Churyumov-Gerasimenko. Geophysical Research Letters, 42(9): 3093-3099.

Gombosi, T.I., 2015. Physics of cometary magnetospheres. In: A. Keiling, C.M. Jackman and P.A. Delamere (Editors), Magnetotails in the Solar System. John Wiley.

Gombosi, T.I., De Zeeuw, D.L., Häberli, R.M. and Powell, K.G., 1996. hree dimensional multiscale MHD model of cometary plasma environment. journal of Geophysical Research, 101(A7): 15233–15253.

Gulkis, S., Allen, M., von Allmen, P., Beaudin, G., Biver, N., Bockelee-Morvan, D., Choukroun, M., Crovisier, J., Davidsson, B.J., Encrenaz, P., Encrenaz, T., Frerking, M., Hartogh, P., Hofstadter, M., Ip, W.H., Janssen, M., Jarchow, C., Keihm, S., Lee, S., Lellouch, E., Leyrat, C., Rezac, L., Schloerb, F.P. and Spilker, T., 2015. Cometary science. Subsurface properties and early activity of comet 67P/Churyumov-Gerasimenko. Science, 347(6220): aaa0709.

Gurnett, D.A., Kurth, W.S., Kirchner, D.L., Hospodarsky, G.B., Averkamp, T.F., Zarka, P., Lecacheux, A., Manning, R., Roux, A., Canu, P. and others, 2004. The Cassini radio and plasma wave investigation, The Cassini-Huygens Mission. Springer, pp. 395–463.

Hansen, K.C., 2016. Evolution of water production of 67P/Churyumov-Gerasimenko: An empirical model and a multi-instrument study. Monthly Notices of the Royal Astronomical Society.

Hansen, K.C., Bagdonat, T., Motschmann, U., Alexander, C., Combi, M.R., Cravens, T.E., Gombosi, T.I., Jia, Y.D. and Robertson, I.P., 2007. The plasma environment of comet 67P/Churyumov-Gerasimenko throughout the Rosetta main mission. Space Science Reviews, 128(1-4): 133-166.

Hassig, M., Altwegg, K., Balsiger, H., Bar-Nun, A., Berthelier, J.J., Bieler, A., Bochsler, P., Briois, C., Calmonte, U., Combi, M., De Keyser, J., Eberhardt, P., Fiethe, B., Fuselier, S.A., Galand, M., Gasc, S., Gombosi, T.I., Hansen, K.C., Jackel, A., Keller, H.U., Kopp, E., Korth, A., Kuhrt, E., Le Roy, L., Mall, U., Marty, B., Mousis, O., Neefs, E., Owen, T., Reme, H., Rubin, M., Semon, T., Tornow, C., Tzou, C.Y., Waite, J.H. and Wurz, P., 2015. Cometary science. Time variability and heterogeneity in the coma of 67P/Churyumov-Gerasimenko. Science, 347(6220): aaa0276.

Hinteregger, H.E., Fukui, K. and Gilson, B.R., 1981. Observational, Reference and Model Data on Solar Euv, from Measurements on Ae-E. Geophysical Research Letters, 8(11): 1147-1150.

Hsu, H.W., Horányi, M., Kempf, S. and Grün, E., 2012. Spacecraft charging near Enceladus. Geophysical Research Letters, 39(6): n/a-n/a.

Ip, W.-H. and Axford, W.I., 1987. The formation of a magnetic-field-free cavity at Comet Halley. Nature, 325.

Jia, Y., Combi, M., Hansen, K., Gombosi, T., Crary, F. and Young, D., 2008. A 3-D global MHD model for the effect of neutral jets during the Deep Space 1 Comet 19P/Borrelly flyby. Icarus, 196(1): 249-257.

Johnstone, A.D., Coates, A.J., Huddleston, D.E., Jockers, K., Wilken, B. and Borg, H., 1993. Observations of the solar wind and cometary ions in the encounter between Giotto and Comet Grigg-Skjellerup. Astronomy & Astrophysics, 273.

Keller, C.N., Anicich, V.G. and Cravens, T.E., 1998. Model of Titan's ionosphere with detailed hydrocarbon ion chemistry. Planetary and Space Science, 46(9-10): 1157-1174.

Keller, C.N., Cravens, T.E. and Gan, L., 1992. A Model of the Ionosphere of Titan. Journal of Geophysical Research-Space Physics, 97(A8): 12117-12135.

Kliore, A.J., Nagy, A.F., Marouf, E.A., French, R.G., Flasar, F.M., Rappaport, N.J., Anabttawi, A., Asmar, S.W., Kahann, D.S., Barbinis, E., Goltz, G.L., Fleischman, D.U. and Rochblatt, D.J., 2008. First results from the Cassini radio occultations of the Titan ionosphere. Journal of Geophysical Research-Space Physics, 113(A9).

Koenders, C., Glassmeier, K.H., Richter, I., Motschmann, U. and Rubin, M., 2013. Revisiting cometary bow shock positions. Planetary and Space Science, 87: 85-95.

Koenders, C., Glassmeier, K.H., Richter, I., Ranocha, H. and Motschmann, U., 2015. Dynamical features and spatial structures of the plasma interaction region of 67P/Churyumov-Gerasimenko and the solar wind. Planetary and Space Science, 105: 101-116.

Korosmezey, A., Cravens, T.E., Gombosi, T.I., Nagy, A.F., Mendis, D.A., Szego, K., Gribov, B.E., Sagdeev, R.Z., Shapiro, V.D. and Shevchenko, V.I., 1987. A New Model of Cometary Ionospheres. Journal of Geophysical Research-Space Physics, 92(A7): 7331-7340.

Krasnopolsky, V.A., 2009. A photochemical model of Titan's atmosphere and ionosphere. Icarus, 201(1): 226-256.

Krasnopolsky, V.A., 2014. Chemical composition of Titan's atmosphere and ionosphere: Observations and the photochemical model. Icarus, 236: 83-91.

Lean, J.L., Warren, H.P., Mariska, J.T. and Bishop, J., 2003. A new model of solar EUV irradiance variability - 2. Comparisons with empirical models and observations and implications for space weather. Journal of Geophysical Research-Space Physics, 108(A2).

Ledvina, S.A. and Cravens, T.E., 1998. A 3-D MHD model of plasma flow around Titan. Planetary and Space Science, 46.

Luhmann, J.G., Ulusen, D., Ledvina, S.A., Mandt, K., Magee, B., Waite, J.H., Westlake, J., Cravens, T.E., Robertson, I., Edberg, N., Agren, K., Wahlund, J.E., Ma, Y.J., Wei, H., Russell, C.T. and Dougherty, M.K., 2012. Investigating magnetospheric interaction effects on Titan's ionosphere with the Cassini orbiter Ion Neutral Mass Spectrometer, Langmuir Probe and magnetometer observations during targeted flybys. Icarus, 219(2): 534-555.

Ma, Y.J., Nagy, A.F., Cravens, T.E., Sokolov, I.V., Clark, J. and Hansen, K.C., 2004. 3-D global MHD model prediction for the first close flyby of Titan by Cassini. Geophysical Research Letters, 31(22).

Ma, Y.J., Nagy, A.F., Cravens, T.E., Sokolov, I.V., Hansen, K.C., Wahlund, J.E., Crary, F.J., Coates, A.J. and Dougherty, M.K., 2006. Comparisons between MHD model calculations and observations of Cassini flybys of Titan. Journal of Geophysical Research-Space Physics, 111(A5).

Madanian, H., Cravens, T.E., Burch, J., Goldstein, R., Rubin, M., Nemeth, Z., Goetz, C., Koenders, C. and Altwegg, K., 2016a. Plasma Environment around Comet 67p/Churyumov–Gerasimenko at Perihelion: Model Comparison with Rosetta Data. The Astronomical Journal, 153(1): 30.

Madanian, H., Cravens, T.E., Rahmati, A., Goldstein, R., Burch, J., Eriksson, A.I., Edberg, N.J.T., Henri, P., Mandt, K., Clark, G., Rubin, M., Broiles, T. and Reedy, N.L., 2016b.

Suprathermal electrons near the nucleus of comet 67P/Churyumov-Gerasimenko at 3 AU: Model comparisons with Rosetta data. Journal of Geophysical Research: Space Physics, 121(6): 5815-5836.

Madanian, H., Cravens, T.E., Richard, M.S., Waite, J.H., Edberg, N.J.T., Westlake, J.H. and Wahlund, J.E., 2016c. Solar cycle variations in ion composition in the dayside ionosphere of Titan. Journal of Geophysical Research: Space Physics, 121(8): 8013-8037.

Magee, B.A., Waite, J.H., Mandt, K.E., Westlake, J., Bell, J. and Gell, D.A., 2009. INMS-derived composition of Titan's upper atmosphere: Analysis methods and model comparison. Planetary and Space Science, 57(14-15): 1895-1916.

Mandt, K.E., Eriksson, A., Edberg, N.J.T., Koenders, C., Broiles, T., Fuselier, S.A., Henri, P., Nemeth, Z., Alho, M., Biver, N., Beth, A., Burch, J., Carr, C., Chae, K., Coates, A.J., Cupido, E., Galand, M., Glassmeier, K.H., Goetz, C., Goldstein, R., Hansen, K.C., Haiducek, J., Kallio, E., Lebreton, J.P., Luspay-Kuti, A., Mokashi, P., Nilsson, H., Opitz, A., Richter, I., Samara, M., Szego, K., Tzou, C.Y., Volwerk, M., Simon Wedlund, C. and Stenberg Wieser, G., 2016. RPC observation of the development and evolution of plasma interaction boundaries at 67P/Churyumov-Gerasimenko. Monthly Notices of the Royal Astronomical Society, 462(Suppl 1): S9-S22.

Mandt, K.E., Gell, D.A., Perry, M., Hunter Waite, J., Crary, F.A., Young, D., Magee, B.A., Westlake, J.H., Cravens, T., Kasprzak, W., Miller, G., Wahlund, J.-E., Ågren, K., Edberg, N.J.T., Heays, A.N., Lewis, B.R., Gibson, S.T., de la Haye, V. and Liang, M.-C., 2012. Ion densities and composition of Titan's upper atmosphere derived from the Cassini Ion Neutral Mass Spectrometer: Analysis methods and comparison of measured ion densities to photochemical model simulations. Journal of Geophysical Research: Planets, 117(E10): n/a-n/a.

McEwan, M.J. and Anicich, V.G., 2007. Titan's ion chemistry: a laboratory perspective. Mass Spectrom Rev, 26(2): 281-319.

Muller-Wodarg, I.C.F., Yelle, R.V., Cui, J. and Waite, J.H., 2008. Horizontal structures and dynamics of Titan's thermosphere. Journal of Geophysical Research-Planets, 113(E10).

Muller-Wodarg, I.C.F., Yelle, R.V., Mendillo, M.J. and Aylward, A.D., 2003. On the global distribution of neutral gases in Titan's upper atmosphere and its effect on the thermal structure. Journal of Geophysical Research-Space Physics, 108(A12).

Neubauer, F.M., 1986. First results from the Giotto magnetometer experiment at comet Halley. Nature, 321.

Neubauer, F.M., Gurnett, D.A., Scudder, J.D. and Hartle, R.E., 1984. Titan’s magnetospheric interaction. In: T. Gehrels and M.S. Matthew (Editors), Saturn. University of Arizona Press, Tuscon, pp. 760.

Neugebauer, M., 1987. The pickup of cometary protons by the solar wind. Astronomy & Astrophysics, 187: 21-24.

Nicholson, D.R., 1983. Introduction to Plasma Theory. John Wiley & Sons.

Nilsson, H., Stenberg Wieser, G., Behar, E., Wedlund, C.S., Gunell, H., Yamauchi, M., Lundin, R., Barabash, S., Wieser, M., Carr, C., Cupido, E., Burch, J.L., Fedorov, A., Sauvaud, J.A., Koskinen, H., Kallio, E., Lebreton, J.P., Eriksson, A., Edberg, N., Goldstein, R., Henri, P., Koenders, C., Mokashi, P., Nemeth, Z., Richter, I., Szego, K., Volwerk, M., Vallat, C. and Rubin, M., 2015. Cometary science. Birth of a comet magnetosphere: a spring of water ions. Science, 347(6220): aaa0571.

Odelstad, E., Eriksson, A.I., Edberg, N.J.T., Johansson, F., Vigren, E., Andre, M., Tzou, C.Y., Carr, C. and Cupido, E., 2015. Evolution of the plasma environment of comet 67P from spacecraft potential measurements by the Rosetta Langmuir probe instrument. Geophysical Research Letters, 42(23): 10,126-10,134.

Omidi, N. and Winske, D., 1987. A Kinetic-Study of Solar-Wind Mass Loading and Cometary Bow Shocks. Journal of Geophysical Research-Space Physics, 92(A12): 13409-13426.

Press, W.H., Teukolsky, S.A., Vetterling, W.T. and Flannery, B.P., 2007. Numerical Recipes: The Art of Scientific Computing.

Puhl-Quinn, P. and Cravens, T.E., 1995. One-dimensional hybrid simulations of the diamagnetic cavity boundary region of comet Halley. Journal of Geophysical Research, 100(A11): 21631-21644.

Rème, H., 1991. Cometary plasma observations between the shock and the contact surface. In: A.D. Johnstone (Editor), Cometary Plasma Processes. AGU Geophysical Monograph Series, pp. 87–105.

Reme, H., Sauvaud, J.A., Duston, C., Cotin, F., Cros, A., Anderson, K.A., Carlson, C.W., Curtis, D.W., Lin, R.P., Mendis, D.A., Korth, A. and Richter, A.K., 1986. Comet Halley Solar-Wind Interaction from Electron Measurements Aboard Giotto. Nature, 321(6067): 349-352.

Richard, M.S., 2013. PLASMA INTERACTIONS IN TITAN'S IONOSPHERE, University of Kansas, Lawrence, KS, 516 pp.

Richard, M.S., Cravens, T.E., Wylie, C., Webb, D., Chediak, Q., Mandt, K., Waite, J.H., Rymer, A., Bertucci, C., Wellbrock, A., Windsor, A. and Coates, A.J., 2015a. An empirical approach to modeling ion production rates in Titan's ionosphere II: Ion production rates on the nightside. Journal of Geophysical Research-Space Physics, 120(2): 1281-1298.

Richard, M.S., Cravens, T.E., Wylie, C., Webb, D., Chediak, Q., Perryman, R., Mandt, K., Westlake, J., Waite, J.H., Robertson, I., Magee, B.A. and Edberg, N.J.T., 2015b. An empirical approach to modeling ion production rates in Titan's ionosphere I: Ion production rates on the dayside and globally. Journal of Geophysical Research-Space Physics, 120(2): 1264-1280.

Richards, P.G., Fennelly, J.A. and Torr, D.G., 1994. EUVAC: A Solar EUV flux model for aeronomic calculations.

Richter, I., Auster, H.U., Glassmeier, K.H., Koenders, C., Carr, C.M., Motschmann, U., Muller, J. and McKenna-Lawlor, S., 2012. Magnetic field measurements during the ROSETTA flyby at asteroid (21)Lutetia. Planetary and Space Science, 66(1): 155-164.

Richter, I., Koenders, C., Auster, H.U., Fruhauff, D., Gotz, C., Heinisch, P., Perschke, C., Motschmann, U., Stoll, B., Altwegg, K., Burch, J., Carr, C., Cupido, E., Eriksson, A., Henri, P., Goldstein, R., Lebreton, J.P., Mokashi, P., Nemeth, Z., Nilsson, H., Rubin, M., Szego, K., Tsurutani, B.T., Vallat, C., Volwerk, M. and Glassmeier, K.H., 2015. Observation of a new type of low-frequency waves at comet 67P/Churyumov-Gerasimenko. Annales Geophysicae, 33(8): 1031-1036.

Robertson, I.P., Cravens, T.E., Waite, J.H., Yelle, R.V., Vuitton, V., Coates, A.J., Wahlund, J.E., Agren, K., Mandt, K., Magee, B., Richard, M.S. and Fattig, E., 2009. Structure of Titan's ionosphere: Model comparisons with Cassini data. Planetary and Space Science, 57(14-15): 1834-1846.

Rubin, M., Combi, M.R., Daldorff, L.K.S., Gombosi, T.I., Hansen, K.C., Shou, Y., Tenishev, V.M., Toth, G., van der Holst, B. and Altwegg, K., 2014a. Comet 1p/Halley Multifluid Mhd Model for the Giotto Fly-By. Astrophysical Journal, 781(2): 86.

Rubin, M., Hansen, K.C., Combi, M.R., Daldorff, L.K.S., Gombosi, T.I. and Tenishev, V.M., 2012. Kelvin-Helmholtz instabilities at the magnetic cavity boundary of comet 67P/Churyumov-Gerasimenko. Journal of Geophysical Research: Space Physics, 117(A6): n/a-n/a.

Rubin, M., Koenders, C., Altwegg, K., Combi, M.R., Glassmeier, K.H., Gombosi, T.I., Hansen, K.C., Motschmann, U., Richter, I., Tenishev, V.M. and Toth, G., 2014b. Plasma environment of a weak comet - Predictions for Comet 67P/Churyumov-Gerasimenko from multifluid-MHD and Hybrid models. Icarus, 242: 38-49.

Rymer, A.M., Smith, H.T., Wellbrock, A., Coates, A.J. and Young, D.T., 2009. Discrete classification and electron energy spectra of Titan's varied magnetospheric environment. Geophysical Research Letters, 36(15): n/a-n/a.

Sagnières, L.B.M., Galand, M., Cui, J., Lavvas, P.P., Vigren, E., Vuitton, V., Yelle, R.V., Wellbrock, A. and Coates, A.J., 2015. Influence of local ionization on ionospheric densities in Titan's upper atmosphere. Journal of Geophysical Research: Space Physics, 120(7): 5899-5921.

Schunk, R.W. and Nagy, A.F., 2009. Ionospheres. Cambridge Univ. Press, Cambridge, UK.

Solomon, S.C., Qian, L. and Burns, A.G., 2013. The anomalous ionosphere between solar cycles 23 and 24. Journal of Geophysical Research: Space Physics, 118(10): 6524-6535.

Teolis, B.D., Niemann, H.B., Waite, J.H., Gell, D.A., Perryman, R.S., Kasprzak, W.T., Mandt, K.E., Yelle, R.V., Lee, A.Y., Pelletier, F.J., Miller, G.P., Young, D.T., Bell, J.M., Magee, B.A., Patrick, E.L., Grimes, J., Fletcher, G.G. and Vuitton, V., 2015. A Revised Sensitivity Model for Cassini INMS: Results at Titan. Space Science Reviews, 190(1-4): 47-84.

Tobiska, W.K., 2007. SOLAR2000 v2.30 and SOLARFLARE v1.01: New capabilities for space system operations. American Institute of Aeronautics and Astronautics, Inc.

Toublanc, D., Parisot, J.P., Brillet, J., Gautier, D., Raulin, F. and McKay, C.P., 1995. Photochemical modeling of Titan's atmosphere. Icarus, 113(1): 2-26.

Trotignon, J.G., Michau, J.L., Lagoutte, D., Chabassiere, M., Chalumeau, G., Colin, F., Decreau, P.M.E., Geiswiller, J., Gille, P., Grard, R., Hachemi, T., Hamelin, M., Eriksson, A., Laakso, H., Lebreton, J.P., Mazelle, C., Randriamboarison, O., Schmidt, W., Smit, A., Telljohann, U. and Zamora, P., 2007. RPC-MIP: The mutual impedance probe of the Rosetta Plasma Consortium. Space Science Reviews, 128(1-4): 713-728.

Vigren, E. and Galand, M., 2013. Predictions of Ion Production Rates and Ion Number Densities within the Diamagnetic Cavity of Comet 67p/Churyumov-Gerasimenko at Perihelion. Astrophysical Journal, 772(1): 33.

Volwerk, M., Richter, I., Tsurutani, B., Gotz, C., Altwegg, K., Broiles, T., Burch, J., Carr, C., Cupido, E., Delva, M., Dosa, M., Edberg, N.J.T., Eriksson, A., Henri, P., Koenders, C., Lebreton, J.P., Mandt, K.E., Nilsson, H., Opitz, A., Rubin, M., Schwingenschuh, K., Wieser, G.S., Szego, K., Vallat, C., Vallieres, X. and Glassmeier, K.H., 2016. Mass-loading, pile-up, and mirror-mode waves at comet 67P/Churyumov-Gerasimenko. Annales Geophysicae, 34(1): 1-15.

Vuitton, V., Yelle, R.V. and Anicich, V.G., 2006. The nitrogen chemistry of Titan's upper atmosphere revealed. Astrophysical Journal, 647(2): L175-L178.

Vuitton, V., Yelle, R.V. and McEwan, M.J., 2007. Ion chemistry and N-containing molecules in Titan's upper atmosphere. Icarus, 191(2): 722-742.

Wahlund, J.E., Bostrom, R., Gustafsson, G., Gurnett, D.A., Kurth, W.S., Pedersen, A., Averkamp, T.F., Hospodarsky, G.B., Persoon, A.M., Canu, P., Neubauer, F.M., Dougherty, M.K., Eriksson, A.I., Morooka, M.W., Gill, R., Andre, M., Eliasson, L. and Muller-Wodarg, I., 2005. Cassini measurements of cold plasma in the ionosphere of Titan. Science, 308(5724): 986-9.

Waite, J.H., Jr., Niemann, H., Yelle, R.V., Kasprzak, W.T., Cravens, T.E., Luhmann, J.G., McNutt, R.L., Ip, W.H., Gell, D., De La Haye, V., Muller-Wordag, I., Magee, B., Borggren, N., Ledvina, S., Fletcher, G., Walter, E., Miller, R., Scherer, S., Thorpe, R., Xu, J., Block, B. and Arnett, K., 2005. Ion neutral mass spectrometer results from the first flyby of Titan. Science, 308(5724): 982-6.

Waite, J.H., Jr., Young, D.T., Cravens, T.E., Coates, A.J., Crary, F.J., Magee, B. and Westlake, J., 2007. The process of tholin formation in Titan's upper atmosphere. Science, 316(5826): 870-5.

Waite, J.H., Lewis, W.S., Kasprzak, W.T., Anicich, V.G., Block, B.P., Cravens, T.E., Fletcher, G.G., Ip, W.-H., Luhmann, J.G., McNutt, R.L. and others, 2004. The Cassini ion and neutral mass spectrometer (INMS) investigation, The Cassini-Huygens Mission. Springer, pp. 113–231.

Weingartner, J.C. and Draine, B.T., 2001. Photoelectric emission from interstellar dust: Grain charging and gas heating. Astrophysical Journal Supplement Series, 134(2): 263-281.

Wellbrock, A., Coates, A.J., Jones, G.H., Lewis, G.R. and Waite, J.H., 2013. Cassini CAPS-ELS observations of negative ions in Titan's ionosphere: Trends of density with altitude. Geophysical Research Letters, 40(17): 4481-4485.

Westlake, J.H., Bell, J.M., Waite, J.H., Johnson, R.E., Luhmann, J.G., Mandt, K.E., Magee, B.A. and Rymer, A.M., 2011. Titan's thermospheric response to various plasma environments. Journal of Geophysical Research: Space Physics, 116(A3).

Westlake, J.H., Waite, J.H., Bell, J.M. and Perryman, R., 2014. Observed decline in Titan's thermospheric methane due to solar cycle drivers. Journal of Geophysical Research: Space Physics, 119(10): 8586-8599.

Westlake, J.H., Waite, J.H., Mandt, K.E., Carrasco, N., Bell, J.M., Magee, B.A. and Wahlund, J.E., 2012. Titan's ionospheric composition and structure: Photochemical modeling of Cassini INMS data. Journal of Geophysical Research: Planets, 117(E1): n/a-n/a.

Wiehle, S., Motschmann, U., Gortsas, N., Glassmeier, K.H., Muller, J. and Koenders, C., 2011. Simulation of cometary jets in interaction with the solar wind. Advances in Space Research, 48(6): 1108-1113.

Yung, Y.L., Allen, M. and Pinto, J.P., 1984. Photochemistry of the Atmosphere of Titan - Comparison between Model and Observations. Astrophysical Journal Supplement Series, 55(3): 465-506.

Appendix A Ionospheric Chemistry

In this appendix section the ion-neutral reaction rate constants and electron dissociative recombination parameters used in the photochemical model described in Chapter 2 are provided. Table A.1 contains the ion-neutral reaction rate constants for 1155 reactions. Table A.2 shows the electron dissociative recombination rate constants, α, and the temperature dependence parameter, β (see equation 2.16). These tables are built upon previous modeling efforts (Cravens et al., 2006; Keller et al., 1998; Richard, 2013; Robertson et al., 2009).

A.1 Ion-Neutral Chemistry

Table A.1 – Ion-neutral reaction rate constants.

Ion	+	Neutral	→	Ion product	Rate Constant (cm^3 s^{-1})
N2+	+	CH4	→	CH3+	1.040E-09
N2+	+	CH4	→	CH2+	1.030E-10
N2+	+	H2	→	HN2+	2.000E-09
N2+	+	N	→	N+	1.000E-11
N2+	+	NH	→	HN+	6.500E-10
N2+	+	C2H2	→	HN2+	2.400E-10
N2+	+	C2H2	→	CHN+	1.200E-11
N2+	+	C2H2	→	C2H2+	1.480E-10
N2+	+	C2H4	→	HN2+	1.300E-10
N2+	+	C2H4	→	CHN+	1.300E-10
N2+	+	C2H4	→	CH2N+	1.300E-10
N2+	+	C2H4	→	C2H3+	6.500E-10
N2+	+	C2H4	→	C2H2+	2.600E-10
N2+	+	HCN	→	CHN+	3.900E-10
N2+	+	C2H6	→	CH2N+	1.300E-10
N2+	+	C2H6	→	C2H6+	1.300E-10
N2+	+	C2H6	→	C2H5+	2.160E-10
N2+	+	C2H6	→	C2H4+	4.320E-10
N2+	+	C2H6	→	C2H3+	5.040E-10
N2+	+	C2H6	→	C2H2+	2.880E-10
N2+	+	HC3N	→	HN2+	1.050E-09
N2+	+	HC3N	→	C3HN+	3.500E-09

N2+	+	H2O	→	HN2+	5.040E-10
N2+	+	H2O	→	H2O+	1.900E-09
N2+	+	CO	→	CO+	7.300E-11
N2+	+	C2N2	→	C2N2+	9.300E-10
N2+	+	NH3	→	NH4+	1.950E-09
N2+	+	NH3	→	NH3+	1.900E-09
N2+	+	O	→	NO+	1.300E-10
N2+	+	CH3CN	→	CH3CN+	3.150E-10
N2+	+	CH3CN	→	CH2CN+	1.370E-09
N2+	+	CH3CN	→	C2HN+	4.200E-10
N2+	+	C2H5CN	→	CH3+	6.800E-10
N2+	+	C2H5CN	→	C2H2+	5.100E-10
N2+	+	C2H5CN	→	C2H3CNH+	2.210E-09
N2+	+	CH3NH2	→	CH2NH2+	8.800E-10
N2+	+	CH3NH2	→	CH3NH2+	7.200E-11
N+	+	CH4	→	CH4+	5.750E-11
N+	+	CH4	→	CH3+	5.750E-10
N+	+	CH4	→	CHN+	4.140E-10
N+	+	CH4	→	CH2N+	4.140E-10
N+	+	H2	→	HN+	1.000E-09
N+	+	NH	→	N2+	3.700E-10
N+	+	NH	→	HN+	3.700E-10
N+	+	C2H2	→	C2H2+	1.050E-09
N+	+	C2H2	→	CNC+	2.250E-10
N+	+	C2H2	→	C2HN+	2.250E-10
N+	+	C2H4	→	CHN+	1.500E-10
N+	+	C2H4	→	CH2N+	2.250E-10
N+	+	C2H4	→	C2H4+	5.250E-10
N+	+	C2H4	→	C2H3+	3.750E-10
N+	+	C2H4	→	C2H2+	1.500E-10
N+	+	C2H4	→	C2HN+	7.500E-11
N+	+	HCN	→	CH+	1.300E-09
N+	+	HCN	→	CHN+	2.410E-09
N+	+	C2H6	→	CH2N+	1.300E-10
N+	+	C2H6	→	C2H5+	1.300E-10
N+	+	C2H6	→	C2H4+	7.150E-10
N+	+	C2H6	→	C2H3+	3.250E-10
N+	+	HC3N	→	C3H+	1.600E-09
N+	+	HC3N	→	C3HN+	2.650E-09
N+	+	H2O	→	H2O+	2.700E-09
N+	+	CO	→	C+	5.600E-13
N+	+	CO	→	NO+	6.160E-12
N+	+	CO	→	CO+	4.930E-11

N+	+	C2N2	→	C2H2+	3.400E-10
N+	+	C2N2	→	CNC+	1.360E-09
N+	+	C2N2	→	C2N2+	1.400E-09
N+	+	NH3	→	NH4+	2.400E-09
N+	+	NH3	→	NH2+	2.160E-10
N+	+	CH3CN	→	CH3CN+	5.000E-10
N+	+	C2H5CN	→	N2+	2.310E-09
N+	+	C2H5CN	→	lC3H3+	4.200E-10
N+	+	C2H5CN	→	cC3H3+	4.200E-10
N+	+	C2H5CN	→	C2H3CNH+	1.050E-09
N+	+	CH3NH2	→	CH2NH2+	9.800E-10
CH5+	+	NH	→	NH2+	7.100E-10
CH5+	+	C2H2	→	C2H3+	1.480E-09
CH5+	+	C2H4	→	C2H5+	1.000E-09
CH5+	+	HCN	→	CH2N+	2.700E-09
CH5+	+	C2H6	→	C2H5+	2.030E-10
CH5+	+	C2H6	→	C2H7+	1.150E-09
CH5+	+	H	→	CH4+	1.500E-10
CH5+	+	HC3N	→	C3H2N+	4.500E-09
CH5+	+	H2O	→	H3O+	3.700E-09
CH5+	+	CO	→	HCO+	9.900E-10
CH5+	+	NH3	→	NH4+	2.500E-09
CH5+	+	O	→	H3CO+	4.400E-12
CH5+	+	CH2NH	→	CH2NH2+	2.090E-09
CH5+	+	CH3CN	→	CH3CNH+	4.900E-09
CH5+	+	CH3NH2	→	CH2NH2+	1.000E-09
CH5+	+	C6H6	→	C6H7+	2.000E-09
CH4+	+	CH4	→	CH5+	1.140E-09
CH4+	+	H2	→	CH5+	3.500E-11
CH4+	+	C2H2	→	C2H3+	1.120E-09
CH4+	+	C2H2	→	C2H2+	1.440E-09
CH4+	+	C2H2	→	lC3H3+	1.630E-10
CH4+	+	C2H2	→	cC3H3+	1.510E-10
CH4+	+	C2H4	→	C2H5+	4.230E-10
CH4+	+	C2H4	→	C2H4+	1.380E-09
CH4+	+	C2H4	→	cC3H3+	6.000E-11
CH4+	+	HCN	→	CH2N+	3.230E-09
CH4+	+	HCN	→	CH3CNH+	6.600E-11
CH4+	+	C2H6	→	C2H4+	1.910E-09
CH4+	+	HC3N	→	C3H2N+	2.500E-09
CH4+	+	H2O	→	H3O+	2.500E-09
CH4+	+	CO	→	HCO+	1.040E-09
CH4+	+	NH3	→	NH4+	1.150E-09

CH4+	+	NH3	→	NH3+	1.650E-09
CH4+	+	CH3CN	→	CH3CNH+	3.900E-09
CH4+	+	C2H3CN	→	C3HN+	5.000E-11
CH4+	+	C2H3CN	→	C3H2N+	3.500E-11
CH4+	+	C2H3CN	→	C2H3CN+	3.500E-10
CH4+	+	CH3NH2	→	CH2NH2+	8.800E-10
CH4+	+	CH3NH2	→	CH3NH2+	1.320E-09
CH3+	+	CH4	→	C2H5+	1.100E-09
CH3+	+	H2	→	CH5+	5.000E-13
CH3+	+	N	→	CHN+	3.350E-11
CH3+	+	N	→	CH2N+	3.350E-11
CH3+	+	NH	→	CH2N+	7.400E-10
CH3+	+	C2H2	→	lC3H3+	5.750E-10
CH3+	+	C2H2	→	cC3H3+	5.750E-10
CH3+	+	C2H4	→	C2H5+	2.600E-10
CH3+	+	C2H4	→	C2H4+	1.700E-09
CH3+	+	C2H4	→	C2H3+	4.880E-10
CH3+	+	C2H4	→	lC3H3+	4.240E-11
CH3+	+	C2H4	→	C3H5+	6.000E-11
CH3+	+	C2H4	→	cC3H3+	4.600E-11
CH3+	+	HCN	→	CH3CNH+	2.000E-10
CH3+	+	C2H6	→	C2H5+	1.480E-09
CH3+	+	C2H6	→	C3H5+	1.570E-10
CH3+	+	C2H6	→	cC3H3+	1.570E-10
CH3+	+	C2H6	→	C3H7+	1.040E-10
CH3+	+	HC3N	→	cC3H3+	2.110E-09
CH3+	+	HC3N	→	C4H3NH+	2.190E-09
CH3+	+	C3H4	→	C2H5+	1.240E-09
CH3+	+	C3H4	→	C2H3+	2.850E-10
CH3+	+	C3H4	→	lC3H3+	1.430E-10
CH3+	+	C3H4	→	cC3H3+	1.430E-10
CH3+	+	C3H4	→	C4H5+	1.900E-10
CH3+	+	C4H2	→	lC3H3+	1.170E-09
CH3+	+	C4H2	→	cC3H3+	1.270E-09
CH3+	+	C4H2	→	C5H3+	1.300E-10
CH3+	+	C2N2	→	C3H3N2+	8.000E-12
CH3+	+	C2N2	→	CH2CN+	7.200E-11
CH3+	+	C3H2	→	C4H3+	2.700E-09
CH3+	+	NH3	→	NH4+	3.040E-10
CH3+	+	NH3	→	CH2NH2+	1.300E-09
CH3+	+	O	→	HCO+	4.000E-10
CH3+	+	CH3CN	→	CH2N+	1.040E-09
CH3+	+	CH3CN	→	C2H5+	6.660E-10

CH3+	+	CH3CN	→	CH3CNH+	1.100E-09
CH3+	+	CH3CN	→	C2H5CNH+	9.000E-11
CH3+	+	CH3CN	→	CH3NH3+	9.000E-11
CH3+	+	C2H3CN	→	CH3CNH+	4.300E-09
CH3+	+	C2H3CN	→	C2H3CNH+	2.600E-10
CH3+	+	CH3NH2	→	CH2NH2+	1.440E-09
CH3+	+	CH3NH2	→	CH3NH2+	1.760E-09
CH3+	+	C6H2	→	C7H3+	1.200E-09
CH3+	+	C8H2	→	C9H3+	1.200E-09
CH3+	+	C5H5N	→	C5H5N+	6.590E-10
CH3+	+	C5H5N	→	C5H6N+	2.830E-10
CH3+	+	C5H5N	→	C5H4N+	6.280E-10
CH3+	+	C5H5N	→	CH3C5H5N+	1.570E-09
CH2+	+	CH4	→	C2H5+	3.900E-10
CH2+	+	CH4	→	C2H4+	9.100E-10
CH2+	+	H2	→	CH3+	1.100E-09
CH2+	+	N	→	CN+	1.100E-10
CH2+	+	N	→	CHN+	1.100E-10
CH2+	+	NH	→	CH2N+	7.500E-10
CH2+	+	C2H2	→	cC3H3+	2.500E-09
CH2+	+	HCN	→	CH2CN+	1.800E-09
CH2+	+	HC3N	→	C3H2N+	4.100E-09
CH2+	+	H2O	→	H3CO+	2.050E-09
CH2+	+	NH3	→	NH4+	1.260E-09
CH2+	+	O	→	HCO+	7.500E-10
CH2+	+	C2H3CN	→	C2H3CN+	2.300E-09
CH2+	+	CH3NH2	→	CH2NH2+	1.150E-09
CH2+	+	CH3NH2	→	CH3NH2+	7.700E-10
CH+	+	CH4	→	C2H4+	6.500E-11
CH+	+	CH4	→	C2H3+	1.090E-09
CH+	+	CH4	→	C2H2+	1.430E-10
CH+	+	H2	→	CH2+	1.200E-09
CH+	+	N	→	CN+	1.900E-10
CH+	+	NH	→	CN+	7.600E-10
CH+	+	C2H2	→	C3H2+	2.400E-09
CH+	+	HCN	→	CH2N+	2.100E-09
CH+	+	HCN	→	CNC+	4.200E-10
CH+	+	HCN	→	C2HN+	2.800E-10
CH+	+	H	→	C+	7.500E-10
CH+	+	H2O	→	H3O+	1.450E-09
CH+	+	H2O	→	HCO+	1.450E-09
CH+	+	CO	→	HCO+	7.000E-12
CH+	+	NH3	→	NH4+	4.050E-10

CH+	+	NH3	→	NH3+	4.590E-10
CH+	+	O	→	CO+	3.500E-10
C+	+	CH4	→	C2H3+	9.360E-10
C+	+	CH4	→	C2H2+	3.640E-10
C+	+	H2	→	CH+	1.200E-16
C+	+	NH	→	CN+	7.800E-10
C+	+	C2H2	→	C3H+	2.630E-09
C+	+	C2H4	→	C2H4+	2.250E-10
C+	+	C2H4	→	C2H3+	1.200E-10
C+	+	C2H4	→	lC3H3+	6.300E-10
C+	+	C2H4	→	cC3H3+	1.020E-09
C+	+	C2H4	→	C3H+	7.500E-11
C+	+	C2H4	→	C3H2+	4.350E-10
C+	+	HCN	→	CNC+	2.950E-09
C+	+	C2H6	→	C2H5+	2.310E-10
C+	+	C2H6	→	C2H4+	1.160E-10
C+	+	C2H6	→	C2H3+	4.950E-10
C+	+	C2H6	→	C2H2+	8.250E-11
C+	+	C2H6	→	cC3H3+	7.100E-10
C+	+	C2H6	→	C3H2+	1.650E-11
C+	+	HC3N	→	C3H+	3.850E-09
C+	+	HC3N	→	CNC+	1.100E-10
C+	+	HC3N	→	C4N+	1.270E-09
C+	+	HC3N	→	C3+	2.750E-10
C+	+	HC3N	→	C4H+	1.400E-09
C+	+	C3H4	→	C2H3+	1.900E-10
C+	+	C3H4	→	C2H2+	1.900E-10
C+	+	C3H4	→	lC3H3+	3.800E-10
C+	+	C3H4	→	C3H5+	5.700E-10
C+	+	C3H4	→	C4H2+	5.700E-10
C+	+	H2O	→	H2O+	2.400E-10
C+	+	H2O	→	HCO+	2.160E-09
C+	+	C3H8	→	C2H3+	6.300E-10
C+	+	C3H8	→	cC3H3+	3.600E-10
C+	+	C3H8	→	C3H7+	5.400E-10
C+	+	C3H8	→	C4H5+	9.000E-11
C+	+	C4H2	→	C3H+	1.450E-10
C+	+	C4H2	→	C4H2+	1.310E-09
C+	+	C3H6	→	C2H3+	6.000E-10
C+	+	C3H6	→	C2H2+	3.000E-10
C+	+	C3H6	→	lC3H3+	1.500E-10
C+	+	C3H6	→	C3H5+	4.000E-10
C+	+	C3H6	→	cC3H3+	1.500E-10

C+	+	C3H6	→	C3H6+	2.000E-10
C+	+	C3H6	→	C4H3+	2.000E-10
C+	+	C2N2	→	CNC+	1.900E-09
C+	+	C3H2	→	C4H+	1.000E-09
C+	+	NH3	→	NH3+	5.060E-10
C+	+	O	→	CO+	2.500E-18
C+	+	C6H2	→	C7H+	1.200E-09
C+	+	C7H4	→	C7H3+	7.500E-10
C+	+	C8H2	→	C9+	1.200E-09
C+	+	C8H2	→	C9H+	1.200E-09
C+	+	C4H3N	→	C4H3+	5.000E-09
C+	+	C6H3N	→	C6H3+	5.000E-09
H3+	+	N2	→	HN2+	1.860E-09
H3+	+	CH4	→	CH5+	2.400E-09
H3+	+	NH	→	NH2+	1.300E-09
H3+	+	C2H2	→	C2H3+	3.200E-09
H3+	+	C2H4	→	C2H5+	8.700E-10
H3+	+	C2H4	→	C2H3+	2.030E-09
H3+	+	HCN	→	CH2N+	7.500E-09
H3+	+	C2H6	→	C2H5+	2.900E-09
H3+	+	HC3N	→	C3H2N+	9.800E-09
H3+	+	C3H4	→	C2H3+	9.000E-10
H3+	+	C3H4	→	C3H5+	2.100E-09
H3+	+	H2O	→	H3O+	5.300E-09
H3+	+	C4H2	→	C4H3+	2.600E-09
H3+	+	CO	→	HCO+	1.740E-09
H3+	+	C3H6	→	C2H3+	9.300E-10
H3+	+	C3H6	→	C3H5+	2.170E-09
H3+	+	C2N2	→	HC2N2+	2.800E-09
H3+	+	NH3	→	NH4+	4.390E-09
H3+	+	CH3CN	→	CH3CNH+	8.900E-09
H3+	+	C2H3CN	→	C4H3NH+	9.000E-09
H3+	+	C2H5CN	→	C2H5CNH+	8.900E-09
H3+	+	C6H2	→	C6H3+	2.000E-09
H3+	+	C7H4	→	C7H5+	2.500E-09
H3+	+	C8H2	→	C8H3+	2.000E-09
H2+	+	N2	→	HN2+	2.000E-09
H2+	+	CH4	→	CH5+	1.140E-10
H2+	+	CH4	→	CH4+	1.410E-09
H2+	+	CH4	→	CH3+	2.280E-09
H2+	+	H2	→	H3+	2.000E-09
H2+	+	N	→	HN+	1.900E-09
H2+	+	NH	→	HN+	7.600E-10

H2+	+	C2H2	→	C2H3+	4.770E-10
H2+	+	C2H2	→	C2H2+	4.820E-09
H2+	+	C2H4	→	C2H4+	2.210E-09
H2+	+	C2H4	→	C2H3+	1.810E-09
H2+	+	C2H4	→	C2H2+	8.820E-10
H2+	+	C2H6	→	C2H6+	2.940E-10
H2+	+	C2H6	→	C2H5+	1.370E-09
H2+	+	C2H6	→	C2H4+	2.350E-09
H2+	+	C2H6	→	C2H3+	6.860E-10
H2+	+	C2H6	→	C2H2+	1.960E-10
H2+	+	H	→	H+	6.400E-10
H2+	+	H2O	→	H3O+	3.430E-09
H2+	+	H2O	→	H2O+	3.870E-09
H2+	+	CO	→	CO+	6.440E-10
H2+	+	CO	→	HCO+	2.900E-09
H2+	+	NH3	→	NH3+	5.700E-09
H+	+	CH4	→	CH4+	7.470E-10
H+	+	CH4	→	CH3+	3.400E-09
H+	+	H2	→	H3+	1.300E-16
H+	+	NH	→	HN+	2.100E-09
H+	+	C2H2	→	C2H2+	5.400E-10
H+	+	C2H4	→	C2H4+	9.800E-10
H+	+	C2H4	→	C2H3+	2.940E-09
H+	+	C2H4	→	C2H2+	9.800E-10
H+	+	HCN	→	CHN+	1.100E-08
H+	+	C2H6	→	CH3+	2.450E-10
H+	+	C2H6	→	C2H5+	2.450E-10
H+	+	C2H6	→	C2H4+	1.470E-09
H+	+	C2H6	→	C2H3+	2.940E-09
H+	+	HC3N	→	C3HN+	4.000E-09
H+	+	H2O	→	H2O+	6.900E-09
H+	+	C4H2	→	C4H2+	2.000E-09
H+	+	C4H2	→	C4H+	2.000E-09
H+	+	NH3	→	NH3+	3.700E-09
H+	+	CH2NH	→	NH2+	1.000E-09
H+	+	CH3CN	→	CH3+	3.000E-09
H+	+	CH3CN	→	CH3CN+	8.400E-09
H+	+	CH3CN	→	CH2CN+	6.000E-10
H+	+	C7H4	→	C7H3+	2.000E-09
H+	+	C7H4	→	C7H4+	2.000E-09
H+	+	HC5N	→	HC5N+	4.000E-09
HN+	+	N2	→	HN2+	6.500E-10
HN+	+	CH4	→	CH5+	9.600E-11

HN+	+	CH4	→	CH2N+	6.720E-10
HN+	+	CH4	→	NH2+	1.920E-10
HN+	+	H2	→	H3+	1.850E-10
HN+	+	H2	→	NH2+	1.050E-09
HN+	+	NH	→	NH2+	1.000E-09
HN+	+	C2H4	→	CH2N+	3.000E-10
HN+	+	C2H4	→	C2H4+	3.750E-10
HN+	+	C2H4	→	C2H3+	3.750E-10
HN+	+	C2H4	→	C2H2+	1.500E-10
HN+	+	C2H4	→	CH3CN+	1.500E-10
HN+	+	H2O	→	H3O+	1.050E-09
HN+	+	H2O	→	H2O+	1.050E-09
HN+	+	H2O	→	NH3+	1.750E-10
HN+	+	H2O	→	NH2+	8.750E-10
HN+	+	CO	→	OCN+	5.390E-10
HN+	+	CO	→	HCO+	4.410E-10
HN+	+	NH3	→	NH4+	6.000E-10
HN+	+	NH3	→	NH3+	1.800E-09
N2+	+	CH4	→	HN2+	0.000E+00
HN2+	+	N2	→	H3+	5.100E-18
HN2+	+	CH4	→	CH5+	8.900E-10
HN2+	+	H2	→	H3+	5.100E-18
HN2+	+	NH	→	NH2+	6.400E-10
HN2+	+	C2H2	→	C2H3+	1.400E-09
HN2+	+	HCN	→	CH2N+	3.200E-09
HN2+	+	C2H6	→	CH5+	1.130E-09
HN2+	+	C2H6	→	C2H5+	1.130E-09
HN2+	+	C2H6	→	C2H7+	1.690E-10
HN2+	+	HC3N	→	C3H2N+	4.200E-09
HN2+	+	C3H4	→	lC3H3+	7.500E-10
HN2+	+	C3H4	→	cC3H3+	7.500E-10
HN2+	+	H2O	→	H3O+	2.600E-09
HN2+	+	C4H2	→	C4H3+	1.100E-09
HN2+	+	CO	→	HCO+	8.800E-10
HN2+	+	C2N2	→	HC2N2+	1.200E-09
HN2+	+	NH3	→	NH4+	2.300E-09
HN2+	+	CH3CN	→	CH3CNH+	4.100E-09
HN2+	+	C2H3CN	→	C2H3CNH+	1.500E-09
HN2+	+	C2H4	→	C2H5+	1.000E-09
HN2+	+	C3H4	→	C3H5+	1.500E-09
CN+	+	CH4	→	CH4+	1.500E-10
CN+	+	CH4	→	CH3+	5.000E-10
CN+	+	CH4	→	CHN+	1.500E-10

CN+	+	CH4	→	CH2N+	1.000E-10
CN+	+	CH4	→	CH2CN+	1.000E-10
CN+	+	H2	→	CHN+	1.600E-09
CN+	+	N	→	N2+	6.100E-10
CN+	+	C2H2	→	C2H2+	8.000E-10
CN+	+	C2H2	→	C3HN+	2.000E-10
CN+	+	C2H4	→	CHN+	3.250E-10
CN+	+	C2H4	→	C2H4+	9.100E-10
CN+	+	C2H4	→	C3H2N+	6.500E-11
CN+	+	HCN	→	CHN+	2.240E-09
CN+	+	HCN	→	C2N2+	4.590E-10
CN+	+	C2H6	→	C2H5+	3.800E-10
CN+	+	C2H6	→	C2H4+	1.240E-09
CN+	+	C2H6	→	C2H3+	2.850E-10
CN+	+	H	→	H+	6.400E-10
CN+	+	HC3N	→	C3HN+	3.680E-09
CN+	+	H2O	→	CHN+	1.600E-09
CN+	+	H2O	→	CH2N+	4.800E-10
CN+	+	H2O	→	H2O+	3.200E-10
CN+	+	H2O	→	HNCO+	6.400E-10
CN+	+	H2O	→	HCO+	1.600E-10
CN+	+	C4H2	→	C4H2+	7.280E-10
CN+	+	C4H2	→	HC5N+	2.430E-10
CN+	+	CO	→	CO+	4.400E-10
CN+	+	C2N2	→	CNC+	5.250E-11
CN+	+	C2N2	→	C2N2+	1.630E-09
CN+	+	CH3CN	→	CH3+	6.800E-10
CN+	+	CH3CN	→	C2H3+	3.400E-10
CN+	+	CH3CN	→	CH3CN+	1.700E-09
CN+	+	CH3CN	→	CH2CN+	6.800E-10
CHN+	+	CH4	→	CH2N+	1.140E-09
CHN+	+	CH4	→	C2H3+	1.270E-10
CHN+	+	H2	→	CH2N+	8.800E-10
CHN+	+	N	→	CH+	2.200E-10
CHN+	+	NH	→	NH2+	6.500E-10
CHN+	+	C2H2	→	C2H4+	1.150E-09
CHN+	+	C2H2	→	C2H3+	2.030E-10
CHN+	+	C2H2	→	C2H2+	6.000E-10
CHN+	+	C2H2	→	C3H2N+	9.000E-10
CHN+	+	HCN	→	CH2N+	1.450E-09
CHN+	+	H	→	H+	3.700E-11
CHN+	+	HC3N	→	C3HN+	2.390E-09
CHN+	+	HC3N	→	C3H2N+	2.210E-09

CHN+	+	H2O	→	CH2N+	1.800E-10
CHN+	+	H2O	→	H3O+	1.800E-09
CHN+	+	H2O	→	H2O+	1.800E-09
CHN+	+	CO	→	HCO+	1.380E-10
CHN+	+	NH3	→	NH3+	1.680E-09
CHN+	+	CH3CN	→	CH3CNH+	1.900E-09
HCNH+	+	C2H4	→	C2H5CNH+	2.000E-11
CH2N+	+	HC3N	→	C3H2N+	3.400E-09
CH2N+	+	H2O	→	H3O+	8.800E-13
CH2N+	+	C4H2	→	C4H3+	1.800E-09
CH2N+	+	NH3	→	NH4+	2.300E-09
CH2N+	+	CH2NH	→	CH2NH2+	2.700E-09
CH2N+	+	CH3CN	→	CH3CNH+	3.800E-09
CH2N+	+	C2H3CN	→	C2H3CNH+	4.500E-09
CH2N+	+	C2H5CN	→	C2H5CNH+	4.200E-09
CH2N+	+	C6H6	→	C6H7+	1.100E-09
CH2N+	+	C6H6	→	CH3NH3+	2.000E-09
CH2N+	+	C6H2	→	C6H3+	3.000E-09
CH2N+	+	C7H4	→	C7H5+	3.000E-09
CH2N+	+	C7H8	→	C7H9+	3.000E-09
CH2N+	+	C8H2	→	C8H3+	3.000E-09
CH2N+	+	C4H3N	→	C4H3NH+	3.000E-09
CH2N+	+	HC5N	→	HC5NH+	3.000E-09
CH2N+	+	C5H5N	→	C5H5N+	3.000E-09
CH2N+	+	C6H3N	→	C6H3NH+	3.000E-09
CH2N+	+	C6H7N	→	C7H7NH+	3.000E-09
HCNH+	+	H2	→	CH2NH2+	1.000E-12
HCNH+	+	C2H2	→	C3H2N+	5.000E-10
HCNH+	+	C2H4	→	C2H3CNH+	5.000E-11
C2H6+	+	C2H2	→	C2H5+	2.470E-10
C2H6+	+	C2H2	→	C3H5+	9.100E-10
C2H6+	+	C2H2	→	C4H7+	1.430E-10
C2H6+	+	C2H4	→	C2H4+	1.150E-09
C2H6+	+	HCN	→	CH2N+	1.140E-09
C2H6+	+	HCN	→	C2H5CNH+	6.000E-11
C2H6+	+	H	→	C2H5+	1.000E-10
C2H6+	+	H2O	→	H3O+	2.950E-09
C2H6+	+	NH3	→	NH4+	1.610E-09
C2H6+	+	NH3	→	NH3+	6.240E-10
C2H5+	+	CH4	→	C3H7+	9.000E-14
C2H5+	+	C2H2	→	lC3H3+	6.840E-11
C2H5+	+	C2H2	→	cC3H3+	6.840E-11
C2H5+	+	C2H2	→	C4H5+	1.220E-10

C2H5+	+	C2H4	→	C3H5+	3.550E-10
C2H5+	+	HCN	→	CH2N+	2.700E-09
C2H5+	+	C2H6	→	C3H7+	5.460E-12
C2H5+	+	H	→	C2H4+	1.000E-11
C2H5+	+	HC3N	→	C3H2N+	3.550E-10
C2H5+	+	C3H4	→	C3H5+	1.260E-09
C2H5+	+	C3H4	→	C4H5+	1.400E-10
C2H5+	+	H2O	→	H3O+	1.890E-09
C2H5+	+	H2O	→	HC2N2+	1.200E-09
C2H5+	+	C3H8	→	C3H7+	6.300E-10
C2H5+	+	C4H2	→	C4H3+	3.000E-09
C2H5+	+	C2N2	→	HC2N2+	8.000E-11
C2H5+	+	NH3	→	NH4+	2.100E-09
C2H5+	+	CH2NH	→	CH2NH2+	2.570E-09
C2H5+	+	CH3CN	→	CH3CNH+	3.800E-09
C2H5+	+	C2H3CN	→	C2H3CNH+	3.000E-09
C2H5+	+	C2H5CN	→	C2H5CNH+	4.090E-09
C2H5+	+	C6H6	→	C6H7+	2.600E-09
C2H5+	+	C6H6	→	CH3NH3+	1.520E-09
C2H5+	+	C6H2	→	C6H3+	3.000E-09
C2H5+	+	C7H4	→	C7H5+	3.000E-09
C2H5+	+	C7H8	→	C7H9+	3.000E-09
C2H5+	+	C8H2	→	C8H3+	3.000E-09
C2H5+	+	C4H3N	→	C4H3NH+	3.000E-09
C2H5+	+	HC5N	→	HC5NH+	3.000E-09
C2H5+	+	C5H5N	→	C5H5N+	3.000E-09
C2H5+	+	C6H3N	→	C6H3NH+	3.000E-09
C2H5+	+	C6H7N	→	C7H7NH+	3.000E-09
C2H4+	+	N	→	CH3CN+	3.000E-10
C2H4+	+	C2H2	→	cC3H3+	6.470E-10
C2H4+	+	C2H2	→	C4H5+	1.930E-10
C2H4+	+	C2H4	→	C3H5+	7.030E-10
C2H4+	+	C2H4	→	C3H4+	4.740E-11
C2H4+	+	C2H4	→	C4H7+	4.740E-11
C2H4+	+	C2H6	→	C3H6+	3.610E-13
C2H4+	+	C2H6	→	C3H7+	4.790E-12
C2H4+	+	H	→	C2H3+	3.000E-10
C2H4+	+	HC3N	→	C3H2N+	1.280E-09
C2H4+	+	HC3N	→	C5H4N+	2.250E-10
C2H4+	+	C3H4	→	C3H4+	2.200E-10
C2H4+	+	C3H4	→	C4H5+	3.300E-10
C2H4+	+	C3H4	→	C5H7+	5.500E-10
C2H4+	+	C3H8	→	C3H6+	6.600E-10

C2H4+	+	C3H8	→	C3H7+	5.400E-10
C2H4+	+	C3H6	→	C3H6+	1.170E-10
C2H4+	+	C3H6	→	C4H7+	1.300E-11
C2H4+	+	C3H2	→	C4H3+	1.500E-09
C2H4+	+	NH3	→	NH4+	1.800E-09
C2H4+	+	NH3	→	NH3+	1.800E-09
C2H4+	+	O	→	HCO+	8.400E-11
C2H4+	+	CH3CN	→	CH3CNH+	2.700E-09
C2H4+	+	C2H5CN	→	C2H5CNH+	4.500E-09
C2H4+	+	C6H2	→	C7H3+	5.000E-10
C2H3+	+	CH4	→	C3H5+	1.900E-10
C2H3+	+	N	→	CH2N+	2.400E-11
C2H3+	+	N	→	CH2CN+	2.200E-12
C2H3+	+	N	→	C2HN+	1.980E-11
C2H3+	+	C2H2	→	C2H3+	5.040E-10
C2H3+	+	C2H2	→	C4H3+	2.160E-10
C2H3+	+	C2H4	→	C2H5+	8.200E-10
C2H3+	+	HCN	→	CH2N+	2.300E-09
C2H3+	+	C2H6	→	C2H5+	2.910E-10
C2H3+	+	C2H6	→	C3H5+	2.480E-10
C2H3+	+	C2H6	→	C4H7+	8.060E-11
C2H3+	+	H	→	C2H2+	6.800E-11
C2H3+	+	HC3N	→	C3H2N+	3.800E-09
C2H3+	+	C3H4	→	C3H5+	1.500E-09
C2H3+	+	H2O	→	H3O+	1.100E-09
C2H3+	+	C4H2	→	C4H3+	3.000E-10
C2H3+	+	C4H2	→	C6H3+	3.000E-10
C2H3+	+	C3H6	→	C4H7+	8.700E-10
C2H3+	+	C2N2	→	C3H+	5.500E-10
C2H3+	+	C2N2	→	HC2N2+	1.100E-09
C2H3+	+	C3H2	→	CH3C4H+	8.000E-10
C2H3+	+	NH3	→	NH4+	2.500E-09
C2H3+	+	C2H3CN	→	C2H3CNH+	3.500E-09
C2H3+	+	C6H6	→	C6H7+	1.600E-09
C2H3+	+	C6H2	→	C6H3+	3.000E-10
C2H3+	+	C6H2	→	C8H3+	3.000E-10
C2H2+	+	CH4	→	C3H5+	7.030E-10
C2H2+	+	CH4	→	C3H4+	1.870E-10
C2H2+	+	H2	→	C2H3+	1.000E-11
C2H2+	+	N	→	CH+	2.500E-11
C2H2+	+	N	→	CNC+	7.500E-11
C2H2+	+	N	→	C2HN+	1.500E-10
C2H2+	+	NH	→	CH2CN+	6.500E-10

C2H2+	+	C2H2	→	C4H2+	4.480E-10
C2H2+	+	C2H2	→	C4H3+	9.520E-10
C2H2+	+	C2H4	→	C2H5+	1.240E-10
C2H2+	+	C2H4	→	C2H4+	2.480E-10
C2H2+	+	C2H4	→	C3H5+	7.450E-10
C2H2+	+	C2H4	→	cC3H3+	8.280E-11
C2H2+	+	C2H4	→	C3H4+	1.380E-11
C2H2+	+	C2H4	→	C4H5+	6.900E-11
C2H2+	+	C2H4	→	C4H7+	1.240E-10
C2H2+	+	HCN	→	CH2N+	2.380E-10
C2H2+	+	HCN	→	C3H2N+	1.220E-10
C2H2+	+	C2H6	→	C2H5+	1.240E-10
C2H2+	+	C2H6	→	C2H4+	2.480E-10
C2H2+	+	C2H6	→	C3H5+	7.450E-10
C2H2+	+	C2H6	→	cC3H3+	8.280E-11
C2H2+	+	C2H6	→	C3H4+	1.380E-11
C2H2+	+	C2H6	→	C4H5+	6.900E-11
C2H2+	+	C2H6	→	C4H7+	1.240E-10
C2H2+	+	HC3N	→	C4H2+	3.700E-10
C2H2+	+	HC3N	→	C5H3N+	2.000E-12
C2H2+	+	C3H4	→	C3H5+	7.500E-11
C2H2+	+	C3H4	→	C3H4+	7.500E-10
C2H2+	+	C3H4	→	C5H5+	6.750E-10
C2H2+	+	H2O	→	H3O+	2.200E-10
C2H2+	+	C3H8	→	C3H6+	1.950E-10
C2H2+	+	C3H8	→	C3H7+	6.500E-10
C2H2+	+	C3H8	→	C4H7+	6.500E-11
C2H2+	+	C4H2	→	C4H2+	1.530E-09
C2H2+	+	C4H2	→	C6H3+	1.400E-10
C2H2+	+	C3H6	→	C3H6+	1.300E-09
C2H2+	+	C3H2	→	C5H2+	7.000E-10
C2H2+	+	NH3	→	NH4+	9.610E-10
C2H2+	+	NH3	→	NH3+	2.140E-09
C2H2+	+	O	→	HCO+	8.500E-11
C2H2+	+	CH3CN	→	C3H5+	1.060E-09
C2H2+	+	CH3CN	→	C3H4+	1.060E-09
C2H2+	+	CH3CN	→	CH2NH2+	2.900E-09
C2H2+	+	CH3CN	→	CH3CNH+	8.360E-10
C2H2+	+	C2H3CN	→	C2H3CNH+	6.500E-10
C2H2+	+	C2H5CN	→	C3H5+	3.990E-09
C2H2+	+	C2H5CN	→	C2H5CNH+	2.100E-10
C2H2+	+	CH3NH2	→	CH2NH2+	7.000E-10
C2H2+	+	CH3NH2	→	CH3NH2+	8.000E-10

C2H2+	+	CH3NH2	→	CH3NH3+	1.300E-09
C2H2+	+	C6H2	→	C8H3+	5.000E-10
C2H2+	+	HC5N	→	H3C7N+	2.000E-12
C2H+	+	CH4	→	C2H2+	3.740E-10
C2H+	+	CH4	→	lC3H3+	3.740E-10
C2H+	+	CH4	→	C3H5+	2.200E-10
C2H+	+	CH4	→	cC3H3+	3.740E-10
C2H+	+	CH4	→	C3H4+	1.320E-10
C2H+	+	H2	→	C2H2+	1.240E-09
C2H+	+	N	→	CH+	9.500E-11
C2H+	+	C2H2	→	C4H2+	1.850E-09
C2H+	+	HCN	→	CH2N+	9.450E-10
C2H+	+	HCN	→	C2H2+	5.400E-10
C2H+	+	HCN	→	C3HN+	1.220E-09
C2H+	+	HC3N	→	C3H2N+	1.410E-09
C2H+	+	HC3N	→	C4H2+	4.560E-10
C2H+	+	HC3N	→	HC5N+	1.180E-09
C2H+	+	HC3N	→	C4H+	7.600E-10
C2H+	+	NH3	→	NH4+	5.500E-10
C2H+	+	NH3	→	CH2CN+	5.500E-10
C2H+	+	O	→	HCO+	3.300E-10
lC3H3+	+	N	→	C3HN+	5.800E-11
lC3H3+	+	N	→	C3H2N+	1.300E-10
lC3H3+	+	C2H2	→	cC3H3+	2.000E-10
lC3H3+	+	C2H2	→	C5H3+	1.000E-09
lC3H3+	+	C2H4	→	C5H5+	1.100E-09
lC3H3+	+	HCN	→	C4H3NH+	4.800E-10
lC3H3+	+	H2O	→	H3O+	3.200E-12
lC3H3+	+	C3H8	→	C3H7+	8.040E-10
lC3H3+	+	C3H8	→	C4H7+	3.960E-10
lC3H3+	+	C4H2	→	cC3H3+	3.360E-10
lC3H3+	+	C4H2	→	C5H3+	1.060E-09
lC3H3+	+	C4H2	→	C7H5+	1.000E-13
lC3H3+	+	C3H2	→	C6H3+	1.000E-09
lC3H3+	+	NH3	→	NH4+	1.100E-09
lC3H3+	+	O	→	HCO+	2.000E-10
lC3H3+	+	CH3CN	→	CH3CN+	1.600E-10
lC3H3+	+	C2H5CN	→	CH3C5H5N+	3.000E-10
lC3H3+	+	C6H6	→	C7H7+	7.000E-10
lC3H3+	+	C6H2	→	C9H3+	1.000E-09
C3H5+	+	N	→	C2H4+	1.100E-10
C3H5+	+	N	→	C2H3CN+	1.500E-11
C3H5+	+	C2H2	→	C5H5+	3.800E-10

C3H5+	+	C2H4	→	C5H7+	8.900E-11
C3H5+	+	C2H4	→	C5H9+	5.100E-11
C3H5+	+	HCN	→	C4H5NH+	1.500E-10
C3H5+	+	H	→	C2H3+	9.500E-12
C3H5+	+	H	→	C2H2+	5.000E-13
C3H5+	+	HC3N	→	C3H2N+	3.800E-10
C3H5+	+	C3H4	→	C6H7+	3.500E-10
C3H5+	+	C3H8	→	C3H7+	3.900E-10
C3H5+	+	C3H8	→	C4H7+	2.820E-11
C3H5+	+	C4H2	→	C5H5+	1.500E-10
C3H5+	+	CO	→	C5H5+	3.800E-10
C3H5+	+	C3H6	→	C4H7+	1.000E-09
C3H5+	+	CH2NH	→	CH2NH2+	1.750E-09
C3H5+	+	C2H3CN	→	C2H3CNH+	1.000E-09
C3H5+	+	C2H5CN	→	C2H5CNH+	2.670E-09
C3H5+	+	C6H6	→	C6H7+	1.150E-10
C3H5+	+	C6H6	→	C7H7+	1.040E-09
C3H5+	+	C6H6	→	CH2NH2+	4.750E-10
C3H5+	+	C6H6	→	CH3NH3+	7.600E-10
cC3H3+	+	C4H2	→	C7H5+	1.000E-13
cC3H3+	+	C3H2	→	C6H3+	1.000E-09
cC3H3+	+	NH3	→	NH4+	1.100E-09
cC3H3+	+	C2H5CN	→	CH3C5H5N+	3.000E-10
cC3H3+	+	C6H2	→	C9H3+	1.000E-09
H3O+	+	C2H4	→	C2H5+	2.000E-12
H3O+	+	HCN	→	CH2N+	3.800E-09
H3O+	+	HC3N	→	C3H2N+	3.900E-09
H3O+	+	C3H4	→	C3H5+	1.800E-09
H3O+	+	C4H2	→	C4H3+	1.100E-09
H3O+	+	NH3	→	NH4+	2.200E-09
H3O+	+	CH2NH	→	CH2NH2+	3.000E-09
H3O+	+	CH3CN	→	CH3CNH+	4.500E-09
H3O+	+	C2H5CN	→	C3H5+	4.600E-09
H3O+	+	C6H6	→	CH3NH3+	2.100E-09
H2O+	+	CH4	→	H3O+	1.120E-09
H2O+	+	H2	→	H3O+	7.600E-10
H2O+	+	N	→	NO+	2.800E-11
H2O+	+	C2H2	→	C2H2+	1.900E-09
H2O+	+	C2H4	→	C2H5+	1.500E-09
H2O+	+	C2H4	→	C2H4+	1.500E-09
H2O+	+	HCN	→	CH2N+	1.050E-09
H2O+	+	HCN	→	H3O+	1.050E-09
H2O+	+	C2H6	→	C2H6+	6.400E-11

H2O+	+	C2H6	→	C2H5+	1.600E-11
H2O+	+	C2H6	→	C2H4+	1.920E-10
H2O+	+	C2H6	→	H3O+	1.330E-09
H2O+	+	H	→	H3O+	7.600E-10
H2O+	+	H2O	→	H3O+	1.850E-09
H2O+	+	CO	→	HCO+	4.250E-09
H2O+	+	C2N2	→	HC2N2+	1.000E-09
H2O+	+	NH3	→	NH4+	9.450E-10
H2O+	+	NH3	→	NH3+	2.210E-09
C3H+	+	CH4	→	C2H3+	7.830E-10
C3H+	+	CH4	→	cC3H3+	1.100E-10
C3H+	+	CH4	→	C4H3+	8.700E-11
C3H+	+	H2	→	lC3H3+	1.690E-12
C3H+	+	H2	→	cC3H3+	1.690E-12
C3H+	+	H2	→	C3H2+	5.200E-12
C3H+	+	H2	→	C6H3+	1.350E-11
C3H+	+	N	→	C3HN+	2.700E-11
C3H+	+	C2H2	→	C5H2+	8.400E-10
C3H+	+	C2H4	→	lC3H3+	9.030E-10
C3H+	+	C2H4	→	cC3H3+	9.000E-10
C3H+	+	C2H4	→	C5H3+	4.750E-11
C3H+	+	HCN	→	CH2N+	4.400E-10
C3H+	+	C3H4	→	C4H3+	1.400E-09
C3H+	+	H2O	→	C2H3+	4.500E-10
C3H+	+	H2O	→	HC3O+	2.250E-11
C3H+	+	H2O	→	HCO+	4.500E-10
C3H+	+	C4H2	→	C4H2+	6.000E-11
C3H+	+	C4H2	→	C5H2+	1.020E-09
C3H+	+	NH3	→	NH4+	8.000E-10
C3H+	+	NH3	→	C2H3CN+	1.650E-09
C3H+	+	NH3	→	NH3+	3.200E-10
C3H+	+	CH3CN	→	C2H3+	6.000E-10
C3H+	+	CH3CN	→	C3H2N+	9.900E-10
C3H+	+	CH3CN	→	CH3CNH+	4.500E-10
C3H+	+	CH3CN	→	C5H4N+	9.000E-10
C3H+	+	CH3NH2	→	CH2NH2+	1.900E-09
C3H2+	+	CH4	→	cC3H3+	4.680E-10
C3H2+	+	CH4	→	C4H5+	8.250E-11
C3H2+	+	N	→	CH2N+	6.600E-12
C3H2+	+	N	→	C2H2+	3.740E-11
C3H2+	+	C2H2	→	C5H3+	2.000E-09
C3H2+	+	C2H4	→	lC3H3+	2.750E-10
C3H2+	+	C2H4	→	C3H4+	6.600E-10

C3H2+	+	C2H4	→	C5H3+	2.750E-10
C3H2+	+	C2H4	→	C5H5+	4.400E-10
C3H2+	+	H	→	C3H+	6.000E-11
C3H2+	+	C3H4	→	C5H3+	2.340E-10
C3H2+	+	C3H4	→	C4H2+	1.170E-10
C3H2+	+	C3H4	→	C4H3+	1.560E-10
C3H2+	+	C3H4	→	C6H5+	2.600E-10
C3H2+	+	C3H4	→	C4H4+	5.330E-10
C3H2+	+	H2O	→	C2H4+	4.800E-11
C3H2+	+	C3H8	→	lC3H3+	1.800E-10
C3H2+	+	C3H8	→	cC3H3+	1.800E-10
C3H2+	+	C3H8	→	C3H7+	5.400E-10
C3H2+	+	C3H8	→	C5H7+	1.200E-10
C3H2+	+	C4H2	→	C7H2+	3.000E-10
C3H2+	+	C4H2	→	C7H3+	3.000E-10
C3H2+	+	C3H2	→	C6H3+	1.000E-09
C3H2+	+	NH3	→	C2H3CNH+	1.200E-09
C3H2+	+	O	→	HCO+	2.000E-10
C3H2+	+	C6H2	→	C9H2+	3.000E-10
C3H2+	+	C6H2	→	C9H3+	3.000E-10
C3H4+	+	C2H2	→	C5H5+	4.200E-10
C3H4+	+	C2H4	→	C4H5+	9.130E-11
C3H4+	+	C2H4	→	C5H7+	7.390E-10
C3H4+	+	H	→	cC3H3+	3.000E-11
C3H4+	+	HC3N	→	C3H2N+	1.800E-10
C3H4+	+	C3H4	→	C3H5+	1.980E-10
C3H4+	+	C3H4	→	C5H5+	2.200E-11
C3H4+	+	C3H4	→	C6H7+	7.480E-10
C3H4+	+	C3H4	→	C6H5+	8.800E-11
C3H4+	+	C3H4	→	C4H4+	2.200E-11
C3H4+	+	C4H2	→	C7H5+	1.670E-09
C3H4+	+	C4H2	→	CH3C4H+	1.260E-10
C3H4+	+	O	→	HCO+	2.000E-10
C3H4+	+	C2H5CN	→	C2H5CNH+	3.710E-09
C3H4+	+	C2H5CN	→	CH3C5H5N+	1.950E-10
C3H6+	+	C2H2	→	C4H5+	8.040E-11
C3H6+	+	C2H2	→	C5H7+	5.900E-10
C3H6+	+	C2H4	→	C4H7+	1.800E-27
C3H6+	+	HCN	→	CH3CN+	1.600E-10
C3H6+	+	HCN	→	C4H5NH+	2.400E-10
C3H6+	+	C3H6	→	C3H7+	2.100E-10
C3H6+	+	C3H6	→	C4H7+	2.800E-10
C3H6+	+	C3H6	→	C5H9+	4.200E-10

C3H6+	+	NH3	→	NH4+	3.000E-10
C3H7+	+	H	→	C3H6+	3.700E-11
C4H5+	+	N	→	C4H3NH+	1.000E-10
C4H5+	+	C2H2	→	C6H5+	1.600E-10
C4H5+	+	C2H4	→	C6H7+	7.300E-11
C4H5+	+	C3H4	→	C7H7+	1.500E-10
C4H5+	+	C3H4	→	C6H5+	5.000E-11
C4H5+	+	C4H2	→	C6H5+	1.000E-09
C4H7+	+	C3H4	→	C7H9+	1.500E-10
C4H7+	+	CH3CN	→	CH3CNH+	5.200E-11
C5H3+	+	O	→	HCO+	2.000E-10
C5H5+	+	N	→	C5H3N+	1.000E-10
C5H5+	+	C2H2	→	C7H7+	1.700E-10
C5H5+	+	C2H2	→	C7H5+	1.000E-09
C5H5+	+	C3H4	→	C6H7+	5.600E-10
C5H5+	+	C3H4	→	C8H6P	9.000E-11
C5H5+	+	C3H4	→	C8H8P	7.500E-10
C5H5+	+	C4H2	→	C7H7+	2.200E-10
C5H5+	+	C4H2	→	C7H5+	2.200E-10
C5H5+	+	NH3	→	NH4+	6.500E-10
C5H5+	+	CH2NH	→	CH2NH2+	3.200E-10
C5H5+	+	CH3CN	→	C7H7+	7.330E-11
C5H5+	+	CH3CN	→	C7H5+	7.330E-11
C5H5+	+	CH3CN	→	C9H7+	7.330E-11
C5H5+	+	C6H6	→	CH2NH2+	2.500E-11
C5H5+	+	C6H6	→	CH3NH3+	2.000E-10
C6H7+	+	C3H4	→	C7H7+	9.700E-11
C7H7+	+	CH4	→	C8H5+	3.000E-11
C7H7+	+	C2H2	→	C11H9+	1.000E-09
C7H7+	+	C2H2	→	C9H8P	5.000E-10
C7H7+	+	C2H2	→	C9H9P	1.000E-10
C7H7+	+	C2H2	→	C11H8P	1.000E-09
C7H7+	+	C2H4	→	C9H8P	5.000E-10
C7H7+	+	C2H4	→	C9H9P	5.000E-10
C7H7+	+	C2H4	→	C8H5+	2.000E-10
C7H7+	+	C2H6	→	C8H8P	2.000E-10
C7H7+	+	C3H4	→	C10H9+	5.000E-10
C7H7+	+	C3H4	→	C8H8P	5.600E-10
C7H7+	+	C3H4	→	C10H10P	5.000E-10
C7H7+	+	C4H2	→	C11H9+	1.000E-09
C7H7+	+	C4H2	→	C11H9N+	1.000E-09
C7H7+	+	CH2NH	→	CH2NH2+	3.400E-11
C7H7+	+	C6H6	→	CH3NH2+	1.800E-12

C7H7+	+	C6H6	→	CH3NH3+	1.620E-11
C3HN+	+	CH4	→	C3H5+	2.280E-10
C3HN+	+	CH4	→	C3H4+	8.300E-11
C3HN+	+	CH4	→	C3H2N+	2.910E-10
C3HN+	+	CH4	→	CH3CN+	2.280E-10
C3HN+	+	H2	→	C2H2+	1.650E-12
C3HN+	+	H2	→	C3H2N+	2.800E-12
C3HN+	+	N	→	C3H+	9.600E-11
C3HN+	+	N	→	CNC+	1.440E-10
C3HN+	+	C2H2	→	C2H4+	1.280E-10
C3HN+	+	C2H2	→	C2H2+	1.280E-10
C3HN+	+	C2H2	→	C4H2+	5.120E-10
C3HN+	+	C2H4	→	C2H4+	5.360E-10
C3HN+	+	C2H4	→	C3H2N+	1.340E-10
C3HN+	+	HCN	→	CH2N+	3.900E-10
C3HN+	+	HC3N	→	HC5N+	1.170E-09
C3HN+	+	H2O	→	C3H2N+	6.700E-10
C3HN+	+	C4H2	→	C4H2+	8.900E-10
C3HN+	+	NH3	→	NH4+	1.700E-09
C3HN+	+	NH3	→	NH3+	1.700E-09
C3HN+	+	C8H2	→	NH3+	1.700E-09
C3H2N+	+	C2H4	→	C5H5N+	1.300E-09
C3H2N+	+	C2H4	→	C4H5NH+	1.000E-11
C3H2N+	+	NH3	→	NH4+	2.000E-09
C3H2N+	+	CH2NH	→	CH2NH2+	2.400E-09
C3H2N+	+	CH3CN	→	CH3CNH+	1.280E-09
C3H2N+	+	CH3CN	→	C5H4N+	3.200E-10
C3H2N+	+	C2H5CN	→	C2H5CNH+	1.900E-09
C3H2N+	+	C6H6	→	CH3NH3+	1.600E-09
C4H2+	+	CH4	→	C5H5+	5.000E-10
C4H2+	+	CH4	→	CH3C4H+	2.000E-10
C4H2+	+	N	→	CH2N+	9.000E-12
C4H2+	+	N	→	C3H+	1.620E-10
C4H2+	+	N	→	HC4N+	9.000E-12
C4H2+	+	C2H2	→	C6H3+	1.400E-11
C4H2+	+	C2H4	→	C3H2N+	7.350E-10
C4H2+	+	C2H4	→	C6H5+	7.600E-10
C4H2+	+	C2H4	→	C7H3+	2.200E-09
C4H2+	+	C2H4	→	C4H4+	7.050E-10
C4H2+	+	H	→	C4H3+	7.000E-11
C4H2+	+	HC3N	→	H3C7N+	1.700E-09
C4H2+	+	C3H4	→	C7H5+	1.170E-09
C4H2+	+	C3H4	→	CH3C4H+	1.300E-10

C4H2+	+	C4H2	→	C8H3+	1.000E-09
C4H2+	+	C3H2	→	C7H3+	2.200E-09
C4H2+	+	O	→	C3H2+	1.080E-10
C4H2+	+	O	→	HC3O+	1.350E-11
C4H3+	+	CH4	→	C5H5+	5.000E-10
C4H3+	+	C2H2	→	C6H5+	2.200E-10
C4H3+	+	C2H4	→	C6H5+	1.200E-10
C4H3+	+	H	→	C4H4+	6.000E-14
C4H3+	+	C3H4	→	C5H5+	1.400E-09
C4H3+	+	C3H4	→	C6H5+	4.000E-11
C4H3+	+	C3H4	→	C7H5+	1.000E-09
C4H3+	+	C4H2	→	C6H3+	7.400E-10
C4H3+	+	C4H2	→	C8H5+	1.000E-13
C4H3+	+	C3H2	→	C7H4+	1.500E-09
C4H3+	+	CH2NH	→	CH2NH2+	1.920E-09
C4H3+	+	C6H6	→	C6H7+	1.300E-09
C4H3+	+	C6H6	→	CH2NH2+	5.000E-10
C4H3+	+	C6H6	→	CH3NH2+	2.000E-10
C4H3+	+	C6H6	→	CH3NH3+	1.300E-09
C4H3+	+	C6H2	→	C8H3+	7.400E-10
CNC+	+	CH4	→	CH2N+	2.100E-10
CNC+	+	CH4	→	C2H3+	4.200E-10
CNC+	+	CH4	→	C3H2N+	7.000E-11
CNC+	+	H2	→	CH2N+	8.100E-10
CNC+	+	H2	→	CH2CN+	9.000E-11
CNC+	+	N	→	CH2N+	1.280E-10
CNC+	+	N	→	C3H+	1.470E-09
CNC+	+	C2H2	→	C3H+	8.000E-10
CNC+	+	C2H2	→	C4H2+	4.000E-10
CNC+	+	C2H4	→	C2H4+	1.300E-10
CNC+	+	C2H4	→	lC3H3+	1.950E-10
CNC+	+	C2H4	→	cC3H3+	1.950E-10
CNC+	+	C2H4	→	CH2CN+	6.500E-10
CNC+	+	C2H6	→	C2H5+	3.000E-10
CNC+	+	C2H6	→	C2H3+	1.200E-10
CNC+	+	C2H6	→	lC3H3+	1.800E-10
CNC+	+	C2H6	→	C3H5+	1.200E-10
CNC+	+	C2H6	→	cC3H3+	1.800E-10
CNC+	+	C2H6	→	C3H2N+	3.000E-10
CNC+	+	C2H6	→	CH2CN+	3.000E-10
CNC+	+	HC3N	→	C3H+	3.300E-09
CNC+	+	H2O	→	CH2N+	1.300E-10
CNC+	+	H2O	→	C2HN+	1.750E-11

CNC+	+	H2O	→	HCO+	1.500E-09
CNC+	+	C4H2	→	C4H2+	2.600E-10
CNC+	+	C4H2	→	CNC+	2.600E-10
CNC+	+	NH3	→	CH2N+	1.900E-09
CNC+	+	CH3CN	→	C2H3+	4.100E-09
C6H5+	+	CH4	→	C7H7+	7.500E-11
C6H5+	+	H2	→	C6H7+	6.000E-11
C6H5+	+	N	→	CH3C4H+	3.700E-11
C6H5+	+	C2H2	→	C8H6P	7.800E-11
C6H5+	+	C2H2	→	C8H7P	5.200E-11
C6H5+	+	C2H4	→	C6H7+	1.020E-10
C6H5+	+	C2H4	→	C8H7P	6.800E-11
C6H5+	+	C2H4	→	C8H8P	6.000E-11
C6H5+	+	C2H6	→	C6H7+	1.260E-10
C6H5+	+	C2H6	→	C7H7+	3.900E-12
C6H5+	+	C3H4	→	C7H7+	4.140E-11
C6H5+	+	C3H4	→	C9H7+	1.790E-10
C6H5+	+	C3H4	→	C9H8P	1.150E-11
C6H5+	+	C3H6	→	C7H7+	3.400E-10
C6H5+	+	C6H6	→	C9H7+	2.820E-11
C6H5+	+	C6H6	→	C10H9+	2.330E-11
C6H5+	+	C6H6	→	C12H9+	2.300E-10
C6H5+	+	C6H6	→	C12H10+	5.170E-11
C6H5+	+	C6H6	→	C10H8P	1.410E-11
C6H5+	+	C6H6	→	C8H5+	8.460E-11
NH4+	+	CH3NH2	→	CH3NH3+	1.400E-09
CH2NH2+	+	CH3NH2	→	CH3NH3+	1.400E-09
CH3CN+	+	H2	→	CH3CNH+	5.700E-10
CH3CN+	+	CO	→	HCO+	2.000E-09
CH3CNH+	+	CH2NH	→	CH2NH2+	2.500E-09
CH3CNH+	+	C2H5CN	→	C2H5CNH+	4.090E-09
CH3CNH+	+	C6H6	→	CH3NH3+	1.800E-09
HC2N2+	+	C2H4	→	C2H5+	5.600E-10
HC2N2+	+	HCN	→	CH2N+	2.000E-09
HC2N2+	+	H2O	→	H3O+	5.100E-10
HC2N2+	+	NH3	→	NH4+	2.000E-09
C2H3CN+	+	CH4	→	CH3CN+	1.820E-11
C2H3CN+	+	CH4	→	C2H3CNH+	6.500E-12
C2H3CN+	+	CH4	→	C4H5NH+	1.300E-12
C2H3CN+	+	H2	→	C2H3CNH+	1.200E-11
C2H3CN+	+	C2H2	→	lC3H3+	3.720E-11
C2H3CN+	+	C2H2	→	cC3H3+	3.720E-11
C2H3CN+	+	C2H2	→	C6H5+	5.100E-10

C2H3CN+	+	C2H2	→	C5H4N+	1.490E-10
C2H3CN+	+	C2H2	→	C4H4+	5.120E-10
C2H3CN+	+	NH3	→	NH4+	1.900E-10
C2H3CN+	+	C2H3CN	→	C2H3CNH+	2.500E-09
C2H3CNH+	+	NH3	→	NH4+	1.700E-09
C2H3CNH+	+	CH2NH	→	CH2NH2+	2.400E-09
C2H3CNH+	+	C6H6	→	CH3NH3+	1.700E-09
C6H3+	+	O	→	HCO+	2.000E-10
C7H5+	+	N	→	H3C7N+	1.000E-10
C8H3+	+	O	→	HCO+	2.000E-10
C9H7+	+	C2H2	→	C9H8P	1.250E-10
C9H7+	+	C2H2	→	C9H9P	1.250E-10
C9H7+	+	C2H2	→	C10H8P	5.000E-10
C9H7+	+	C2H4	→	C9H8P	1.250E-10
C9H7+	+	C2H4	→	C9H9P	1.250E-10
C9H7+	+	C2H4	→	C10H8P	5.000E-10
C9H7+	+	C3H4	→	C8H5+	2.800E-09
C10H9+	+	C2H2	→	C11H9+	5.000E-11
C10H9+	+	C2H2	→	C10H10P	5.000E-10
C10H9+	+	C2H2	→	C11H10P	5.000E-11
C10H9+	+	C2H4	→	C11H9+	5.000E-11
C10H9+	+	C2H4	→	C10H10P	5.000E-10
C10H9+	+	C2H4	→	C11H10P	5.000E-11
C10H9+	+	C2H6	→	C11H9+	5.000E-11
C10H9+	+	C2H6	→	C11H10P	5.000E-11
C10H9+	+	C2H6	→	C11H11P	5.000E-11
C7H6P	+	C2H4	→	C8H8P	1.000E-09
C7H6P	+	C2H6	→	C7H7+	2.000E-10
C7H6P	+	C2H6	→	C7H8P	2.000E-10
C7H6P	+	C3H4	→	C10H9+	5.000E-10
C7H6P	+	C3H4	→	C8H8P	1.000E-09
C7H6P	+	C3H4	→	C10H8P	5.000E-10
C8H6P	+	C2H4	→	C8H7P	5.000E-10
C8H6P	+	C2H4	→	C8H8P	5.000E-10
C8H7P	+	C2H2	→	C6H5+	1.700E-10
C8H7P	+	C2H4	→	C6H5+	4.800E-11
C8H7P	+	C2H4	→	C8H8P	5.000E-10
C8H7P	+	C2H4	→	C9H9P	4.000E-10
C8H7P	+	HCN	→	C11H9+	5.000E-11
C8H7P	+	HCN	→	C11H8P	5.000E-11
C8H7P	+	HCN	→	C11H10P	5.000E-11
C8H7P	+	C2H6	→	C9H9P	4.000E-10
C8H7P	+	C3H4	→	C9H8P	5.000E-10

C8H7P	+	C3H4	→	C9H9P	5.000E-10
C8H8P	+	C2H2	→	C10H9+	5.000E-10
C8H8P	+	C2H2	→	C10H10P	5.000E-10
C8H8P	+	C2H4	→	C10H9+	5.000E-10
C8H8P	+	C2H4	→	C10H10P	5.000E-10
C8H8P	+	C2H6	→	C9H9P	4.000E-10
C8H8P	+	C3H4	→	C11H9+	5.000E-11
C8H8P	+	C3H4	→	C11H10P	5.000E-11
C8H8P	+	C3H4	→	C11H11P	5.000E-11
C9H8P	+	C2H2	→	C10H9+	5.000E-10
C9H8P	+	C2H2	→	C9H9P	5.000E-10
C9H8P	+	C2H4	→	C10H9+	5.000E-10
C9H8P	+	C2H4	→	C9H9P	5.000E-10
C9H9P	+	C2H2	→	C10H9+	5.000E-10
C9H9P	+	C2H2	→	C10H10P	5.000E-10
C9H9P	+	C2H4	→	C10H9+	5.000E-10
C9H9P	+	C2H4	→	C10H10P	5.000E-10
C9H9P	+	C2H6	→	C10H9+	5.000E-10
C9H9P	+	C2H6	→	C10H10P	5.000E-10
C10H8P	+	C2H2	→	C11H9+	5.000E-11
C10H8P	+	C2H2	→	C11H8P	5.000E-11
C10H8P	+	C2H4	→	C11H9+	5.000E-11
C10H8P	+	C2H4	→	C11H8P	5.000E-11
C10H8P	+	C2H6	→	C11H9+	5.000E-11
C10H8P	+	C2H6	→	C11H10P	5.000E-11
C10H8P	+	C2H6	→	C11H11P	5.000E-11
C10H10P	+	C2H2	→	C11H10P	5.000E-11
C10H10P	+	C2H2	→	C11H11P	5.000E-11
C10H10P	+	C2H4	→	C11H10P	5.000E-11
C10H10P	+	C2H4	→	C11H11P	5.000E-11
C10H10P	+	C2H6	→	C11H9+	5.000E-11
C10H10P	+	C2H6	→	C11H10P	5.000E-11
C10H10P	+	C2H6	→	C11H11P	5.000E-11
C7N+	+	H2	→	HC7N+	1.500E-09
HC7N+	+	H2	→	H2C7N+	5.000E-12
C7H+	+	H2	→	C7H2+	1.000E-17
C7H+	+	N	→	C7N+	2.000E-10
C7H+	+	O	→	HCO+	2.000E-10
C7H2+	+	N	→	HC7N+	2.000E-10
C7H2+	+	C2H2	→	C9H2+	3.000E-10
C7H2+	+	O	→	HCO+	2.000E-10
C7H3+	+	N	→	H2C7N+	2.000E-10
C7H3+	+	O	→	HCO+	2.000E-10

C7H4+	+	N	→	H3C7N+	1.000E-10
CH3C4H+	+	N	→	C5H3N+	1.000E-10
C5H3N+	+	C2H4	→	C7H5N+	1.000E-10
C7H5N+	+	C2H4	→	C9H7N+	1.000E-10
C9H7N+	+	C2H4	→	C11H9N+	1.000E-10
C11H9N+	+	C2H4	→	C13H11N+	1.000E-10
C9N+	+	H2	→	HC9N+	1.500E-09
HC9N+	+	H2	→	H2C9N+	5.000E-12
C9H+	+	N	→	C9N+	2.000E-10
C9H+	+	O	→	HCO+	2.000E-10
C9H2+	+	N	→	HC9N+	2.000E-10
C9H2+	+	O	→	HCO+	2.000E-10
C9H3+	+	O	→	HCO+	2.000E-10
H3CO+	+	H2	→	H3O+	2.300E-10
H3CO+	+	HCN	→	CH2N+	1.300E-09
H3CO+	+	H2O	→	H3O+	2.300E-10
H3CO+	+	C4H2	→	C4H3+	9.300E-10
H3CO+	+	NH3	→	NH4+	2.300E-09
C4N+	+	CH4	→	C2H3+	1.430E-10
C4N+	+	CH4	→	C3H2N+	2.000E-10
C4N+	+	CH4	→	C4H3+	1.710E-10
C4N+	+	CH4	→	HC5NH+	2.850E-11
C4N+	+	H2	→	C3H+	2.200E-11
C4N+	+	H2O	→	HCO+	7.500E-10
C2N2+	+	H2	→	HC2N2+	8.800E-10
C2N2+	+	C2H2	→	C2H2+	1.000E-10
C2N2+	+	C2H2	→	C4H2+	3.000E-11
C2N2+	+	C2H4	→	C2H4+	1.300E-09
C2N2+	+	HCN	→	CHN+	5.400E-10
C2N2+	+	HCN	→	HC2N2+	2.030E-09
C2N2+	+	H	→	CHN+	4.960E-10
C2N2+	+	H	→	C2H+	1.240E-10
C2N2+	+	HC3N	→	C3HN+	1.600E-09
C2N2+	+	H2O	→	H2O+	2.340E-10
C2N2+	+	H2O	→	HC2N2+	2.370E-09
C2N2+	+	C4H2	→	C4H3+	1.080E-09
C3+	+	CH4	→	C3H+	2.380E-10
C3+	+	CH4	→	C4H2+	3.610E-10
C3+	+	CH4	→	C4H3+	3.520E-10
C3+	+	H2	→	C3H+	2.400E-10
C3+	+	C2H4	→	C2H4+	3.960E-10
C3+	+	C2H4	→	C3H2+	1.350E-10
C3+	+	C2H4	→	C5H3+	1.350E-10

C3+	+	C2H4	→	C5H2+	2.340E-10
C3+	+	HCN	→	C3H+	2.600E-10
C3+	+	HCN	→	C4N+	1.040E-09
C3+	+	HCN	→	C4H+	1.040E-09
HC5N+	+	H2	→	HC5NH+	1.000E-09
HC5N+	+	C2H4	→	HC5NH+	9.000E-10
HC5N+	+	C2H4	→	C7H5N+	2.400E-10
HC4N+	+	H2	→	HC5NH+	1.000E-09
NH3+	+	CH4	→	NH4+	4.800E-10
NH3+	+	H2	→	NH4+	4.400E-13
NH3+	+	NH	→	NH4+	7.100E-10
NH3+	+	C2H4	→	NH4+	1.400E-09
NH3+	+	H2O	→	NH4+	2.500E-10
NH3+	+	NH3	→	NH4+	2.100E-09
NH2+	+	CH4	→	NH3+	9.200E-10
NH2+	+	H2	→	NH3+	1.950E-10
NH2+	+	N	→	HN2+	9.100E-11
NH2+	+	C2H4	→	C2H4+	4.500E-10
NH2+	+	C2H4	→	C2H3+	3.000E-10
NH2+	+	C2H4	→	CH2NH2+	4.500E-10
NH2+	+	HCN	→	CH2N+	1.200E-09
NH2+	+	H2O	→	H3O+	2.730E-09
NH2+	+	H2O	→	NH4+	1.160E-10
NH2+	+	H2O	→	NH3+	8.700E-11
NH2+	+	NH3	→	NH4+	1.610E-09
NH2+	+	NH3	→	NH3+	6.900E-10
CO+	+	CH4	→	CH4+	8.980E-10
CO+	+	CH4	→	HCO+	3.750E-10
CO+	+	H2	→	HCO+	1.400E-09
CO+	+	N	→	NO+	8.200E-11
CO+	+	NH	→	HN+	3.200E-10
CO+	+	NH	→	HCO+	3.200E-10
CO+	+	C2H2	→	C2H2+	4.100E-10
CO+	+	HCN	→	CHN+	3.060E-09
CO+	+	HCN	→	HCO+	3.400E-10
CO+	+	C2H6	→	CH3+	2.780E-11
CO+	+	C2H6	→	C2H5+	5.000E-10
CO+	+	C2H6	→	C2H4+	8.620E-10
CO+	+	H	→	H+	4.000E-10
CO+	+	HC3N	→	C3HN+	3.100E-09
CO+	+	H2O	→	H2O+	1.560E-09
CO+	+	H2O	→	HCO+	8.400E-10
CO+	+	C3H8	→	C2H5+	6.600E-10

CO+	+	C3H8	→	C2H4+	1.800E-10
CO+	+	C3H8	→	C3H6+	3.000E-11
CO+	+	C3H8	→	C3H7+	1.300E-10
CO+	+	NH3	→	NH3+	2.020E-09
CO+	+	NH3	→	HCO+	4.080E-11
CO+	+	CH3CN	→	CH3CN+	2.250E-09
CO+	+	CH3CN	→	CH2CN+	7.500E-10
HCO+	+	N2	→	HN2+	6.600E-10
HCO+	+	CH4	→	CH3+	1.100E-09
HCO+	+	H2	→	HCO+	3.800E-10
HCO+	+	NH	→	NH2+	6.400E-10
HCO+	+	C2H2	→	C2H3+	1.360E-09
HCO+	+	C2H4	→	C2H5+	1.400E-09
HCO+	+	HCN	→	CH2N+	3.500E-09
HCO+	+	C2H6	→	C2H7+	1.200E-10
HCO+	+	HC3N	→	C3H2N+	3.800E-09
HCO+	+	C3H4	→	C3H5+	1.400E-09
HCO+	+	H2O	→	H3O+	2.600E-09
HCO+	+	C4H2	→	C4H3+	1.400E-09
HCO+	+	CO	→	HCO+	4.000E-10
HCO+	+	C2N2	→	HC2N2+	1.300E-09
HCO+	+	C3H2	→	cC3H3+	1.400E-09
HCO+	+	C3H2	→	C3H4+	1.400E-09
HCO+	+	NH3	→	NH4+	2.200E-09
HCO+	+	CH2NH	→	CH2NH2+	1.000E-09
HCO+	+	CH3CN	→	CH3CNH+	4.100E-09
HCO+	+	C2H3CN	→	C4H3NH+	4.000E-09
HCO+	+	C6H6	→	C6H7+	1.600E-09
HCO+	+	C6H2	→	C6H3+	1.400E-09
HCO+	+	C7H4	→	HN2+	2.000E-09
HCO+	+	C7H4	→	C7H5+	2.000E-09
HCO+	+	C8H2	→	C8H3+	1.400E-09
HCO+	+	HC5N	→	HC5NH+	8.000E-09
HCO+	+	C6H3N	→	C6H3NH+	4.000E-09
C5H2+	+	CH4	→	C6H5+	8.000E-10
C5H2+	+	N	→	HC5N+	2.000E-10
C5H2+	+	C2H4	→	C7H5+	5.000E-10
C5H2+	+	C2H4	→	C7H4+	5.000E-10
C5H2+	+	C4H2	→	C7H3+	6.000E-10
C5H2+	+	C3H2	→	C8H3+	1.200E-09
C5H2+	+	O	→	HCO+	2.000E-10
C2H7+	+	HCN	→	CH2N+	1.980E-09
C2H7+	+	HCN	→	CH3CNH+	2.200E-10

C2H7+	+	NH3	→	NH4+	2.000E-09
C4H+	+	CH4	→	C5H3+	1.100E-09
C4H+	+	H2	→	C3H+	2.200E-11
C4H+	+	H2	→	C4H2+	1.650E-10
C4H+	+	C2H4	→	C4H3+	7.500E-10
C4H+	+	HCN	→	C4H2+	9.450E-11
C4H+	+	HCN	→	HC5N+	1.230E-09
C4H+	+	C3H4	→	C7H4+	1.200E-09
C4H+	+	H2O	→	C3H2N+	7.500E-10
C4H+	+	H2O	→	HCO+	7.500E-10
C4H+	+	C4H2	→	C9H2+	1.500E-09
C4H+	+	C3H2	→	C7H2+	2.000E-09
C4H+	+	O	→	HCO+	2.000E-10
C4H4+	+	C2H2	→	C6H5+	8.800E-11
C8H5+	+	C3H4	→	C5H7+	7.000E-10

A.2 Electron Dissociative Recombination Parameters

Table A.2 Electron dissociative recombination coefficients and temperature dependencies.

Ion	α (cm^{3}s^{-1})	β
N2+	1.70E-07	0.3
N+	4.00E-12	0.58
CH5+	6.20E-07	0.52
CH4+	3.50E-07	0.5
CH3+	2.97E-07	0.5
CH2+	6.40E-07	0.6
CH+	1.50E-07	0.42
C+	4.67E-12	0.6
H3+	6.70E-08	0.52
H2+	1.60E-08	0.43
H+	3.50E-12	0.75
HN+	4.30E-08	0.5
HN2+	4.00E-07	0.92
CN+	1.80E-07	0.5
CHN+	3.90E-07	1
CH2N+	2.80E-07	0.65
C2H6+	3.00E-07	0.5
C2H5+	8.00E-07	0.79
C2H4+	5.00E-07	0.76
C2H3+	5.00E-07	0.84

C2H2+	2.70E-07	0.5
C2H+	2.69E-07	0.76
lC3H3+	4.00E-07	0
C3H5+	1.00E-06	0
cC3H3+	4.00E-07	0
H3O+	4.40E-07	0.5
H2O+	4.30E-07	0.5
C3H+	3.00E-07	0.7
C3H2+	3.00E-07	0.7
C3H4+	1.00E-06	0
C3H6+	1.00E-06	0
C3H7+	1.00E-06	0
C4H5+	1.00E-06	0.7
C4H7+	1.00E-06	0.7
C5H3+	9.00E-07	0.5
C5H5+	1.00E-06	0.7
C6H7+	2.80E-06	1.3
C7H7+	2.80E-06	1.3
C11H9+	1.10E-06	0.5
C3HN+	1.38E-06	0.6
C3H2N+	1.30E-06	0.58
CnHm+	1.10E-06	0.5
ZLo+	1.10E-06	0.5
ZHi+	1.10E-06	0.5
C5H5N+	1.10E-06	0.5
C4H2+	1.00E-06	0.79
C4H3+	6.20E-07	0.7
C5H7+	1.00E-06	0.7
C5H9+	1.00E-06	0.7
CNC+	3.00E-07	0.5
C6H5+	2.80E-06	1.3
NO+	4.30E-07	0.37
NH4+	9.38E-07	0.6
CH2NH2+	3.00E-06	0.7
CH3NH2+	3.00E-07	0.7
CH3CN+	6.00E-07	0.7
CH3CNH+	8.13E-07	0.69
HC2N2+	9.40E-07	0.7
C2H3CN+	1.00E-07	0.5
C2H3CNH+	1.78E-06	0.8
C2H5CNH+	1.50E-06	0.76
CH3NH3+	9.00E-07	0.79
C6H3+	2.00E-06	0.3

C7H5+	7.00E-07	0.3
C7H9+	3.80E-07	0.7
C8H3+	2.00E-06	0.3
C4H3NH+	1.30E-06	0.58
C4H5NH+	4.00E-07	0.7
HC5NH+	3.50E-07	0.7
C7H7NH+	3.50E-07	0.7
C6H3NH+	2.00E-06	0.3
C5H6N+	8.50E-07	0.7
C5H4N+	3.00E-07	0.7
CH3C5H5N+	2.83E-07	0.7
C9H7+	1.00E-06	0.7
C10H9+	1.00E-06	0.7
C12H9+	1.00E-06	0.7
C12H10+	1.00E-06	0.7
C7H6P	1.00E-06	0.7
C7H8P	1.00E-06	0.7
C8H6P	1.00E-06	0.7
C8H7P	1.00E-06	0.7
C8H8P	1.00E-06	0.7
C9H8P	1.00E-06	0.7
C9H9P	1.00E-06	0.7
C10H8P	1.00E-06	0.7
C10H10P	1.00E-06	0.7
C11H8P	1.00E-06	0.7
C11H10P	1.00E-06	0.7
C11H11P	1.00E-06	0.7
C7N+	2.00E-06	0.3
HC7N+	2.00E-06	0.3
H2C7N+	2.00E-06	0.3
H3C7N+	2.00E-06	0.3
C7H+	2.00E-06	0.3
C7H2+	2.00E-06	0.3
C7H3+	2.00E-06	0.3
C7H4+	2.00E-06	0.3
CH3C4H+	2.00E-06	0.3
C5H3N+	2.00E-06	0.3
C7H5N+	1.00E-06	0.7
C9H7N+	1.00E-06	0.7
C11H9N+	1.00E-06	0.7
C13H11N+	1.00E-06	0.7
C9N+	2.00E-06	0.3
HC9N+	2.00E-06	0.3

H2C9N+	2.00E-06	0.3
C9+	2.00E-06	0.3
C9H+	2.00E-06	0.3
C9H2+	2.00E-06	0.3
C9H3+	2.00E-06	0.3
HC3O+	3.00E-07	0.5
OCN+	3.00E-07	0.5
C3H3N2+	6.00E-07	0.5
H3CO+	6.00E-07	0.5
C4N+	3.00E-07	0.5
CH2CN+	3.00E-07	0.5
C2HN+	3.00E-07	0.5
C2N2+	3.00E-07	0.5
C3+	3.00E-07	0.5
HC5N+	3.00E-07	0.5
HNCO+	3.00E-07	0.5
HC4N+	3.00E-07	0.5
NH3+	3.10E-07	0.5
NH2+	3.05E-07	0.9
CO+	2.00E-07	0.48
HCO+	2.00E-07	0.79
C5H2+	3.00E-07	0.5
C2H7+	9.00E-07	0.79
C4H+	3.00E-07	0.5
C4H4+	3.30E-07	0.5
C8H5+	3.00E-07	0.5
C8H9+	2.00E-06	0.3
C8H11+	2.00E-06	0.3
C9H11+	2.00E-06	0.3
C12H11	2.00E-06	0.3

Appendix B IES Instrument

This appendix includes a table of full resolution IES energy bin. Table B.1 lists the sequence and starting energy of each bin. This energy bin structure is the same ion and electron sensors.

Table B.1 – IES energy bin structure.

Bin number	Starting energy (eV)
1	4.32
2	8.63
3	12.95
4	17.26
5	21.58
6	25.89
7	30.21
8	34.52
9	38.84
10	43.15
11	47.47
12	51.78
13	56.1
14	60.41
15	64.73
16	69.04
17	73.36
18	77.67
19	81.99
20	86.3
21	90.62
22	94.93
23	99.25
24	103.56
25	107.88
26	116.51
27	120.82

28	129.45
29	133.77
30	142.4
31	151.03
32	155.34
33	163.97
34	172.6
35	185.55
36	194.18
37	202.81
38	215.75
39	224.38
40	237.33
41	250.27
42	263.22
43	276.16
44	293.42
45	306.37
46	323.63
47	340.89
48	358.15
49	375.41
50	396.99
51	418.56
52	440.14
53	461.71
54	487.6
55	513.49
56	539.38
57	569.59
58	599.79
59	630
60	664.52
61	699.04
62	733.56
63	772.4
64	811.23
65	854.36
66	901.85
67	949.31
68	996.78

69	1052.88
70	1104.66
71	1165.07
72	1225.48
73	1290.21
74	1359.25
75	1428.29
76	1505.96
77	1583.63
78	1669.93
79	1756.23
80	1848.85
81	1946.1
82	2049.66
83	2157.53
84	2269.73
85	2390.55
86	2515.68
87	2645.14
88	2787.53
89	2943.25
90	3089.59
91	3249.25
92	3421.85
93	3603.08
94	3792.94
95	3991.44
96	4202.88
97	4422.94
98	4655.96
99	4901.92
100	5156.51
101	5428.35
102	5713.15
103	6015.2
104	6334.52
105	6666.78
106	7016.3
107	7387.39
108	7775.75
109	8185.68

110	8617.19
111	9070.27
112	9544.93
113	10049.79
114	10576.23
115	11137.19
116	11719.72
117	12336.78
118	12988.35
119	13670.13
120	14390.75
121	15150.2
122	15948.49
123	16785.61
124	17670.2